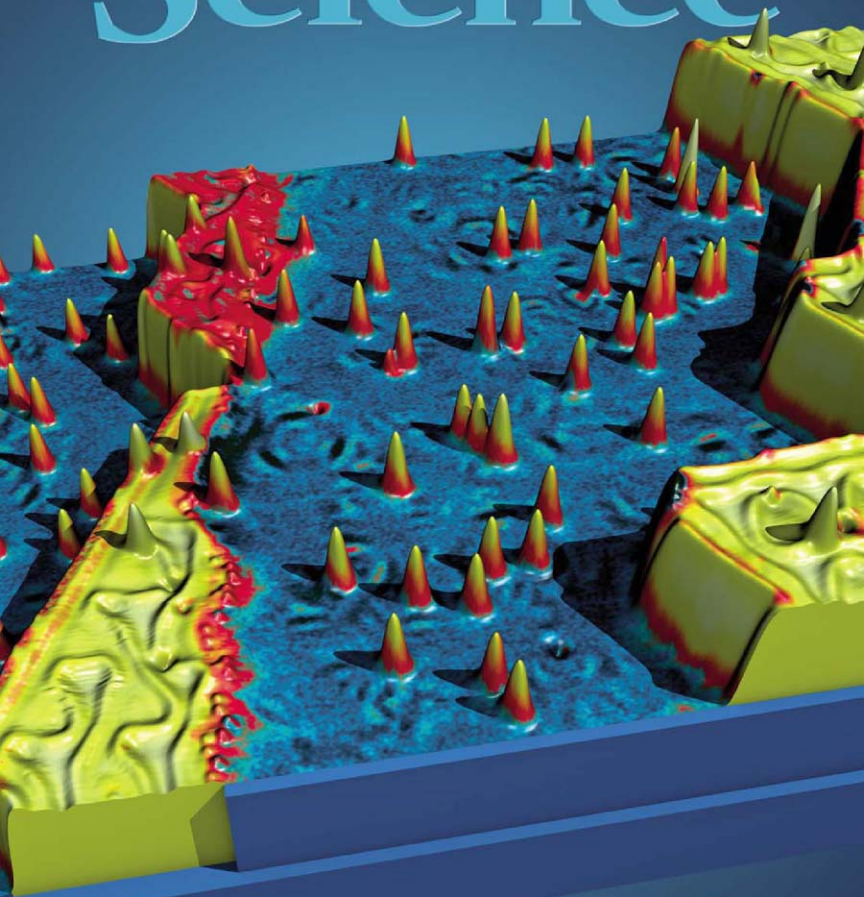
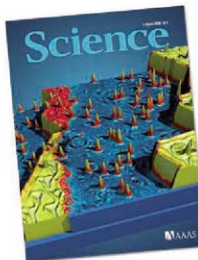


4 April 2008 | \$10

# Science





## COVER

Single cobalt atoms (cones) on a stepped platinum substrate (blue), with attached stripes of one atomic layer of cobalt, magnetized up (yellow) or down (red), as imaged by spin-polarized scanning tunneling microscopy. Recording such images at successive magnetic fields enables measurement of the magnetic properties of individual atoms. See page 82.

Image: F. Meier et al.  
(Illustration: F. Marczinowski)

## DEPARTMENTS

- 13 Science Online
- 15 This Week in Science
- 21 Editors' Choice
- 24 Contact Science
- 27 Random Samples
- 29 Newsmakers
- 120 New Products
- 121 Science Careers

## EDITORIAL

- 19 The Promise of Cancer Research  
by Bruce Alberts

## NEWS OF THE WEEK

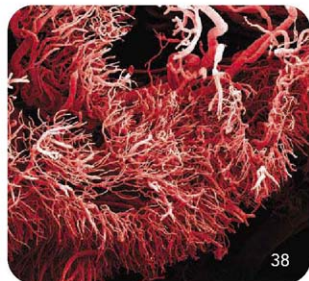
- Review of Vaccine Failure Prompts a Return to Basics 30
- NASA's Stern Quits Over Mars Exploration Plans 31
- Germes Take a Bite Out of Antibiotics 33
- >> Report p. 100

## SCIENCESCOPE

- China's LAMOST Observatory Prepares for the Ultimate Test 34
- U.S. Asked to Bolster Ties With China 35
- DNA From Fossil Feces Breaks Clovis Barrier 37
- >> Science Express Report by M. T. P. Gilbert et al.

## NEWS FOCUS

- All in the Stroma: Cancer's Cosa Nostra 38
- American Physical Society Meeting 42
- Magnetic Measurements Hint at Toastier Superconductivity
- Laser Plays Chemical Matchmaker
- Squeeze: Play Makes Solid Helium Flow
- Puzzling Over a Steller Whodunit 44



38

## LETTERS

- Conserving Top Predators in Ecosystems 47
- G. Chapron, H. Andr n, O. Liberg
- The Role of Fisheries-Induced Evolution
- H. I. Broman, R. Law, C. T. Marshall, A. Kuparinen
- and J. Meril  Response C. J rgensen et al.
- Tips for NIH M. Aickin

## CORRECTIONS AND CLARIFICATIONS

## BOOKS ET AL.

- Violence A Micro-sociological Theory 51
- R. Collins, reviewed by D. D. Laitin
- BROWSEINGS 52

## POLICY FORUM

- A Case Study of Personalized Medicine 53
- S. H. Katsanis, G. Javitt, K. Hudson

## PERSPECTIVES

- Toward Understanding Self-Splicing 56
- J. A. Piccirilli
- >> Research Article p. 77
- Blooms Like It Hot 57
- H. W. Paerl and J. Huisman
- Deconstructing Pluripotency 58
- A. G. Bang and M. K. Carpenter
- >> Report p. 97
- Tel2 Finally Tells One Story 60
- M. Chang and J. Lingner
- Small-Scale Observations Tell a Cosmological Story 61
- P. A. Bland
- >> Report p. 91
- Creating Musical Variation 62
- D. S. Dabby



51

CONTENTS continued >>

## SCIENCE EXPRESS

www.sciencexpress.org

## ANTHROPOLOGY

## DNA from Pre-Clovis Human Coprolites in Oregon, North America

M. T. P. Gilbert et al.

Fossil human feces from an Oregon cave predate the Clovis culture by about 1000 years, and DNA from the feces marks the presence of Native Americans in North America.

&gt;&gt; News story p. 37

10.1126/science.1154116

## PHYSICS

## BREVIA: Fine Structure Constant Defines Visual Transparency of Graphene

R. R. Nair et al.

The transparency of sheets of graphene is quantized in a way that allows a simple determination of the fine structure constant, which relates light and relativistic electrons.

10.1126/science.1156965



## REVIEW

## DEVELOPMENTAL BIOLOGY

## Stochasticity and Cell Fate

R. Losick and C. Desplan

65

## BREVIA

## ECOLOGY

## Bats Limit Insects in a Neotropical Agroforestry System

K. Williams-Guillén, I. Perfecto, J. Vandermeer

Exclusion experiments show that bats contribute to the reduction of insects on coffee plants more than has been appreciated and to a comparable degree as birds.

70

## ECOLOGY

## Bats Limit Arthropods and Herbivory in a Tropical Forest

M. B. Kalka, A. R. Smith, E. K. V. Kalka

In a lowland tropical forest, bats consume insect herbivores on understory plants at least as much as birds do, thereby also indirectly limiting damage to the plants.

71



## MEDICINE

## ROS-Generating Mitochondrial DNA Mutations Can Regulate Tumor Cell Metastasis

K. Ishikawa et al.

Mutations in mitochondrial DNA that cause enhanced production of reactive oxygen species can increase the propensity of tumor cells to metastasize.

10.1126/science.1156906

## RESEARCH ARTICLES

## ARCHAEOLOGY

## Aztec Arithmetic Revisited: Land-Area Algorithms and Acolhua Congruence Arithmetic

B. J. Williams and M. del Carmen Jorge y Jorge

Analysis of ancient property records shows that the Aztecs used common algorithms and a distance standard for calculating land area and specific symbols to represent fractions.

72

## BIOCHEMISTRY

## Crystal Structure of a Self-Spliced Group II Intron

N. Toor, K. S. Keating, S. D. Taylor, A. M. Pyle

The autocatalytic group II intron contains a network of unusual tertiary RNA interactions that form a metalloprotein active site with parallels to eukaryotic spliceosomes.

&gt;&gt; Perspective p. 56

77

## REPORTS

## APPLIED PHYSICS

## Revealing Magnetic Interactions from Single-Atom Magnetization Curves

F. Meier, L. Zhou, J. Vliebe, R. Wiesendanger

A scanning tunneling microscope with a spin-polarized tip can characterize the magnetic properties of single atoms on a nonmagnetic surface.

82

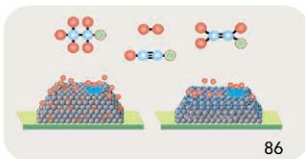
## CHEMISTRY

## The Roles of Subsurface Carbon and Hydrogen in Palladium-Catalyzed Alkyne Hydrogenation

D. Teschner et al.

The population of hydrogen and carbon within a palladium catalyst governs the hydrogenation of alkynes on its surface.

86



## REPORTS CONTINUED...

### GEOCHEMISTRY

- The Electrical Conductivity of Post-Perovskite in Earth's D" Layer** 89  
*K. Ohta et al.*

A major silicate mineral deep in Earth's mantle has a high electrical conductivity, causing a sufficiently strong coupling with the core to explain variations in Earth's rotation.

### ASTRONOMY

- Graphite Whiskers in CV3 Meteorites** 91  
*M. Fries and A. Steele*

Graphite whiskers, a naturally occurring allotrope of carbon, have been found in primitive grains in several meteorites and may explain spectral features of supernovae.

>> *Perspective p. 61*

### CLIMATE CHANGE

- Covariant Glacial-Interglacial Dust Fluxes in the Equatorial Pacific and Antarctica** 93  
*G. Winckler et al.*

A 500,000-year record shows that more dust, which provides iron and other nutrients, was blown into the equatorial Pacific during glacial periods than during warm periods.

### MOLECULAR BIOLOGY

- Selective Blockade of MicroRNA Processing by Lin-28** 97  
*S. R. Viswanathan, G. Q. Daley, R. I. Gregory*

A protein necessary for reprogramming skin fibroblasts to pluripotent stem cells is an RNA-binding protein that normally inhibits microRNA processing in embryonic cells.

>> *Perspective p. 58*

### MICROBIOLOGY

- Bacteria Subsisting on Antibiotics** 100  
*G. Dantas et al.*

A wide range of bacteria in the environment, many related to human pathogens, are both resistant to antibiotics and consume them as their only source of carbon for growth.

>> *News story p. 33*

### CELL BIOLOGY

- Reversible Compartmentalization of de Novo Purine Biosynthetic Complexes in Living Cells** 103  
*S. An, R. Kumar, E. D. Sheets, S. J. Benkovic*

The enzymes needed for purine biosynthesis cluster in the cytoplasm when cells are depleted of purine but dissociate when the demand for purine is low.

### BIOCHEMISTRY

- Single-Molecule DNA Sequencing of a Viral Genome** 106  
*T. D. Harris et al.*

The M13 viral genome has been resequenced by a single-molecule method that allows simultaneous sequencing of 280,000 DNA strands of 25 bases with 100 percent coverage.

### NEUROSCIENCE

- Entrainment of Neuronal Oscillations as a Mechanism of Attentional Selection** 110  
*P. Lakatos et al.*

In monkeys that are paying attention to a rhythmic stimulus, brain oscillations become tuned to the stimulus so that the response in the visual cortex is enhanced.

### NEUROSCIENCE

- Episodic-Like Memory in Rats: Is It Based on When or How Long Ago?** 113  
*W. A. Roberts et al.*

Unlike humans, who can place past events within a temporal framework, rats can only remember when an event happened by tracking the time elapsed since its occurrence.



113



**Change of address:** Allow 4 weeks, please old and new addresses and 8-digit account number. **Postmaster:** Send change of address to AAAS, P.O. Box 96178, Washington, DC 20090-6178. **Single-copy sales:** \$10.00 current issue, \$15.00 back issue prepaid includes surface postage bulk rates on request. **Authorizations to photocopy material for internal or personal use, and/or for specific internal or personal use, is granted by AAAS for libraries and other users registered with the Copyright Clearance Center (CCC) Transactional Reporting Service, provided that \$20.00 per article is paid directly to CCC, 222 Rosewood Drive, Danvers, MA 01923. The identification code for Science is 0036-8075. Science is indexed in the Reader's Guide to Periodical Literature and in several specialized indexes.**

SCIENCE (ISSN 0036-8075) is published weekly on Friday, except the last week in December, by the American Association for the Advancement of Science, 1200 New York Avenue, NW, Washington, DC 20005. Periodicals Mail postage (publication no. 4344-60) paid at Washington, DC, and additional mailing offices. Copyright © 2008 by the American Association for the Advancement of Science. This title is a registered trademark of the AAAS. Circulation: Institutional membership and subscription (53 issues): \$144 (\$74 allocated to subscription). Domestic institutional subscription (53 issues): \$770. Foreign postage extra: Mexico, Caribbean (surface mail): \$55; other countries (air mail delivery): \$85. First class, airmail, student, and emeritus rates on request. Canadian rates with GST available upon request. GST #R12314R822. Publications Mail Agreement Number 856894. Printed in the U.S.A.

CONTENTS continued >>>





Gorgeous trains get no love from peahens.

## SCIENCE NOW

[www.sciencenow.org](http://www.sciencenow.org) DAILY NEWS COVERAGE

### Peacock Feathers: That's So Last Year

Some female birds have lost interest in flashy males.

### Traffic Jams Happen, Get Used to It

Physics helps explain bunch-ups on the highway.

### Organics in the Mist

Astronomers find an amino acid precursor lurking in an interstellar cloud.



Networking among polar scientists.

## SCIENCE CAREERS

[www.sciencereers.org/career\\_development](http://www.sciencereers.org/career_development)  
CAREER RESOURCES FOR SCIENTISTS

### Taken for Granted: Help is on the Way (for Some)

*B. Benderly*

A flurry of activity on workforce issues in early March did little to ease the problems of young scientists.

### A Competitive Fellowship

*J. Mervis*

Next year, NSF officials hope to launch a novel training program connected to the president's American Competitiveness Initiative.

### Networking Group Seeks to Bridge the Poles

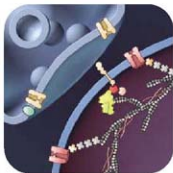
*C. Reed*

A fledgling organization connects polar scientists.

### April 2008 Funding News

*J. Fernández*

Learn about the latest in research funding opportunities, scholarships, fellowships, and internships.



Calpain cleaves postsynaptic proteins.

## SCIENCE SIGNALING

[www.stke.org](http://www.stke.org) THE SIGNAL TRANSDUCTION KNOWLEDGE ENVIRONMENT

### REVIEW: Calpain in the CNS—From Synaptic Function to Neurotoxicity

*J. Liu, M. Cheng Liu, K. K. W. Wang*

Physiological activation of calpains may play a role in memory, whereas pathological activation leads to cell death.

### PODCAST

*E. M. Adler and J. F. Foley*

Mutations in the IGF-1 receptor are associated with longer life span in humans.



## SCIENCE PODCAST

Download the 4 April Science Podcast to hear about DNA evidence of pre-Clovis people in the Americas, bacteria subsisting on antibiotics, Aztec arithmetic, and more.

[www.sciencemag.org/about/podcast.dtl](http://www.sciencemag.org/about/podcast.dtl)

Separate individual or institutional subscriptions to these products may be required for full-text access.



## << Yummy Antibiotics

As a food source, antibiotics would seem to be a poor choice for bacteria. However, Dantas *et al.* (p. 100) readily cultured bacteria from the soil that can consume antibiotics as sole carbon sources. Importantly, these bacteria are from several genera, some of which are closely allied to human and livestock pathogens, and are also generally extremely resistant to many antibiotics. Consumption is not restricted to antibiotics derived from natural products but also includes synthetic ones, as well as new-generation molecules, such as levofloxacin.

This heretofore unrecognized source of antibiotic-metabolizing bacteria represents a potential reservoir of antibiotic resistance genes for pathogenic bacteria.

## Aztecs' Lay of the Land

Just as modern governments require careful land surveys and records of value for taxation, the Aztecs were diligent bookkeepers when it came to landholdings and real estate transactions. How exactly did the Aztecs calculate land parcel areas from the recorded dimensions of the plots?

Williams and del Carmen Jorge y Jorge (p. 72) examined the records of the Codex Vergara and were able to determine the indigenous computational techniques used by the Aztecs to calculate land area.

## Chance Aspects of Cell Fate

Ranging from bacteria to humans, cell fate is generally reached through a hard-wired program.

However, in a review on stochasticity and cell fate, Losick and Desplan (p. 65) describe how the surroundings and cell lineage may have a lesser impact on cell fate than normally assumed.

Instead, the differentiation pathway may be stochastically or randomly attained. Examples are seen in the entry of *Bacillus subtilis* into a state of competence or the generation of alternative color-vision photoreceptors in *Drosophila melanogaster*. There are varied reasons as to why a cell lacks a deterministic program, for example, "bet hedging" in bacteria to anticipate adverse changes in the environment. A stochastic mechanism for cell fate may be advantageous or, in some cases, necessary for the organism's or species survival.

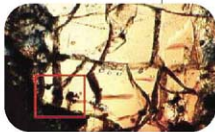
## Cobalt Atoms Singled Out

Magnetization curves, the response of a magnetic material to an applied magnetic field, have

long been used to characterize sample properties that determine a material's usefulness in applications such as memory storage. Characterization techniques have had to develop in parallel to the miniaturization of magnetic memory, even down to the single magnetic atom adsorbed on a surface (an adatom). However, previous work looked at the adatoms in a somewhat artificial environment in which they are strongly coupled to a magnetic surface. Meier *et al.* (p. 82; see the cover) have now developed a spin-polarized scanning tunneling microscopy system to probe the magnetization of single cobalt adatoms on the more technologically relevant system of a nonmagnetic, metallic surface.

## Early Condensation of Graphite Whiskers

Graphite whiskers can be condensed from high-temperature plasmas in the laboratory but have not been seen naturally. These whiskers have been postulated to be responsible for affecting the brightness of type 1a supernovae (used as a distance measure in astronomy) and the cosmic microwave background. Fries and Steele (p. 91; see the Perspective by Bland) have found several graphite whiskers in some of the most primitive and highest-temperature grains in several



meteorites. They identified the whiskers using Raman imaging and electron microscopy. Thus, these whiskers likely condensed from the early hot solar nebula and may be expected in other stellar systems.

## Probing Post-Perovskite Conductivity

Deep in Earth's mantle, near the core, silicate perovskite transforms to post-perovskite. Understanding the properties of post-perovskite is critical to inferring the nature of the deep mantle and the flow of heat, magnetic flux, and momentum from the core to the mantle. Using a diamond anvil cell, Ohta *et al.* (p. 89) show that the electrical conductivity of post-perovskite at deep mantle pressures and temperatures is much higher than for most oxide insulators.

These results imply that there is a strong electromagnetic coupling between the core and mantle, which affects the rotation of Earth, as observed in decadal changes in the length of the day.

## Working Back to Pluripotency

Recent studies have shown that adult mouse and human fibroblasts can be reprogrammed to a pluripotent state after the viral integration of four transcription factors. However, questions remained as to the origin of those cells, whether

*Continued on page 17*

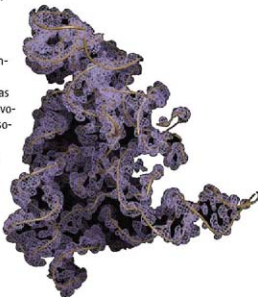
specific genomic integration sites are needed, and how tumorigenicity might be reduced (see the Perspective by **Bang and Carpenter**). Embryonic stem cells and cells of human malignancies are characterized by low levels of let-7 microRNAs (miRNAs), a phenomenon thought to be functionally linked to pluripotency and oncogenesis. In both cases, precursors of let-7 are detectable but processing to the miRNA mature form is inhibited. **Viswanathan et al.** (p. 97, published online 21 February) identify Lin28 as an RNA binding protein that selectively inhibits let-7 miRNA processing. Lin28 was recently shown to function with three other factors to reprogram human fibroblasts to pluripotent stem cells. This work suggests that the regulation of miRNA processing may be critical in the dedifferentiation that occurs in both reprogramming and oncogenesis.

## Organizing Purine Biosynthesis

How primary metabolic enzymes are organized in living cells has long been a topic of discussion. There have been suggestions that multienzyme complexes may facilitate flux through the pathway, but scant evidence in support of such organization. **An et al.** (p. 103) use fluorescence microscopy to show that enzymes in the purine biosynthesis pathway colocalize to form clusters in the cytoplasm of HeLa cells. Formation of these "purinosomes" is regulated by changes in purine levels and results suggest that purinosomes form to satisfy a cellular demand for purine. Similar dynamic regulation may apply to other metabolic enzyme complexes.

## Structure for Self-Splicing

Splicing by autocatalytic group II introns is essential for gene expression in plants, fungi, and yeast. Group II introns are also of great interest as model systems because they are thought to be evolutionary predecessors of the eukaryotic spliceosomal apparatus. **Toor et al.** (p. 77; see the perspective by **Piccirilli**) describe the structure of an intact, self-spliced group II intron at 3.1 angstrom resolution. The structure is consistent with a two-metal ion mechanism for catalysis and, together with previous biochemical studies, supports the hypothesis that group II introns and the spliceosome share a common ancestor.



## I've Got Rhythm

Low-frequency electroencephalogram oscillations are very common in the cortex, but their functional significance has largely been unclear. In most studies low frequencies are desynchronized by attention. Now, however, **Lakatos et al.** (p. 110) present data from area V1, the primary visual cortex, that indicate a potential mechanism behind selective attention in the case of rhythmic stimuli. When stimuli are presented at a predictable, low-frequency rate, the low-frequency oscillations entrain to the low-frequency stimulus, and the higher frequencies, the so called gamma band oscillations, are modulated in phase with the low frequencies. Cells then become most excitable at times when the stimulus is expected. During visual attention, ongoing entrainment and incoming stimulation support each other and lead to particularly strong responses.

## Mental Time Travel in Rats?

The notion of how time is represented in episodic memory is an elusive concept. In work on scrub jays, episodic-like memory has been tested by tasking the birds to remember whether one of two food items appeared 4 hours previously or 4 days previously. Now, in experiments with rats, **Roberts et al.** (p. 113) sought to learn whether the "when" component of episodic-like memory really is a sense of "when," or if it is merely a sense of elapsed time. They contrasted scenarios in which the animals were required to remember exactly when the food item event occurred or, in a different condition, how long ago the food item event occurred. Their results show that the rats can only remember elapsed time and are consistently subject to chance when required to remember precisely when an event happened. The authors thus argue that episodic-like memory in rats is very different from human episodic recall.

# More Advanced LCM



MDS Analytical Technologies introduces the next generation ArcturusXT<sup>™</sup> microdissection instrument. The ArcturusXT system takes advantage of the latest advances in microscope technology by employing the all-new Nikon Eclipse Ti-E inverted research microscope as its base.

- Unique IR-enabled LCM—never lose contact with the sample!
- Optional UV Laser Cutting and Epi-Fluorescence
- Phase contrast and DIC options—ideal for live-cell applications
- AutoScanXT automated LCM image analysis
- Second camera with MetaVue<sup>®</sup> software for high-resolution imaging
- Full range of objective offerings—2x to 100x
- Fully modular, upgradeable and extendable platform
- Compatible with glass or membrane slides

The updated ArcturusXT system maintains the greatest flexibility in microdissection by combining gentle LCM with rapid UV laser cutting. Together with our Arcturus<sup>®</sup> microgenomics reagents and Axon GenePix<sup>®</sup> microarray systems, we provide a more complete solution for microarray research. Visit [www.moleculardevices.com/lcm](http://www.moleculardevices.com/lcm) for more information.

Expect more. We'll do our very best to exceed your expectations.

See us at AACR '08  
Booth #1617



Analytical Technologies

tel. +1 800 435-0377 | [www.moleculardevices.com](http://www.moleculardevices.com)



Bruce Alberts is  
Editor-in-Chief of *Science*.

## The Promise of Cancer Research

IN RECENT YEARS, I HAVE HEARD THE ARGUMENT THAT WE ALREADY KNOW ENOUGH about fundamental biological mechanisms to cure cancer, and that the best way to improve cancer outcomes would be to focus nearly all of our cancer research resources on applying what we know to develop therapies. This would be a mistake. To make my point, I describe two of many examples where a much deeper understanding of fundamental mechanisms seems almost certain to improve cancer treatments. Of necessity, I omit many other promising ways of attacking this disease.

Cancer arises when the descendants of just one of our more than ten thousand billion cells proliferate out of control, eventually interfering with normal body functions. Since so many cells are at risk, the most amazing thing about cancer to me is how many years it usually takes to develop the disease. One major obstruction to the proliferation of cancerous cells is the phenomenon of apoptosis, which causes nearly all of our cells to kill themselves whenever they start to behave aberrantly.

A complicated cellular signaling network determines the balance between the pro-apoptotic and anti-apoptotic proteins inside animal cells. Each of our many cells is constantly sensing its external and internal environment and will sacrifice itself (for our own good) if it is either not correctly located or not behaving normally. Without mechanisms of this type, the evolution of large complex organisms such as ourselves would probably not have been possible, because the tumors caused by cancerlike diseases would have overtaken us early in life.

Tumors arise after a long process of random mutation followed by multiple rounds of selection for those cells able to proliferate best. One change selected for is in apoptotic mechanisms, which will be altered in different ways in different tumors. Imagine that we could determine why the cells in an individual's tumor incorrectly compute that they need not kill themselves, as normal cells would do in their condition. If we understood the fundamental mechanisms by which cells make these decisions, we would stand an excellent chance of creating a tailored mixture of drugs that causes the tumor cells to compute differently, so that they commit suicide without harming normal cells.

Another promising strategy takes advantage of the fact that essentially all cancer cells have acquired a defect in some aspect of their "DNA metabolism," often some aspect of DNA repair that causes them to become highly mutable. This genetic instability of cancer cells is selected for early in tumor development, because only such cells can evolve the multiple additional changes, including defects in apoptosis, that are necessary for most cell types to become malignant.

Cells that are too genetically unstable will die. Therefore, a treatment that blocks a particular DNA repair process can be lethal for a cancer cell, while sparing normal cells. If we could determine why the cells in a particular individual tumor are genetically unstable (for example, which DNA repair protein has been altered during the evolution of that tumor), we might be able to design drugs that kill the cells in that cancer highly selectively, with little harm to normal cells.

These examples of rational approaches to cancer therapy were only a dream until recently. But by targeting these types of alterations in cancer cells, researchers have made impressive progress and are thus much closer to being able to design highly selective therapies based on the critical molecular defects in an individual tumor. But for most tumors, this type of approach is still hit or miss, because oncologists are severely hampered by an inadequate understanding of the fundamental processes that are altered in a particular tumor. My conclusion: If I were the czar of cancer research, I would give a higher priority to recruiting more of our best young scientists to decipher the detailed mechanisms of both apoptosis and DNA repair, and I would give them the resources to do so.

— Bruce Alberts



10.1126/science.1158084





ECOLOGY

## Third-Party Parasitism

For more than 50 million years, Agaonidae wasps have laid their eggs in the ovules of the enclosed flowers, or syconia, of fig trees. The grubs stimulate the formation of a small gall and feed on the plant's tissue. The payoff for the loss of reproductive power to the fig tree occurs when the young wasps emerge and carry their host's pollen to other trees. Fortunately for the trees, wasps don't lay eggs in every ovule in a syconium, even though in evolutionary terms this might seem a good strategy for the wasp; rather than being deterred by the tree itself, the fig wasps are in fact preyed on by another wasp. The parasitoid's ovipositor is just long enough to penetrate the wall of the fig and reaches only the outermost ovules. Dunn *et al.* show that thanks to the packing architecture of the ovules within the syconium, the fig wasps predominantly use inner ovules that are out of range of the parasitoid, allowing the other ovules to mature into fig seeds and thereby stabilizing this mutualism. — CA

PLoS Biol. 6, e59 (2008).

## CLIMATE SCIENCE

### Catching a Cold

Earth has wandered in and out of periods of extensive glaciation for hundreds of millions of years. The oxygen isotopic record of seawater indicates that the current Antarctic ice sheet began to form about 34 million years ago, across the Eocene-Oligocene transition. In contrast, extensive permanent ice sheets are thought not to have appeared in the Northern Hemisphere for another 25 million years. However, oxygen isotope ratios are affected by temperature as well as the isotopic composition of the water itself (which in turn is controlled mostly by the amount of ice that exists in the environment), so the cooling inferred from that record was not unequivocally established. Earlier work to construct a pure temperature record by measuring Mg/Ca ratios in foraminifera actually seemed to show that there was no appreciable ocean cooling 34 million years ago, implying that the drop in temperature believed to have occurred then was instead due to an earlier appearance of ice in the Northern Hemisphere. Now, Lear *et al.* report results from Mg/Ca measurements of exceptionally well-preserved samples that show a 2.5°C tropical sea

surface temperature drop across the Eocene-Oligocene boundary. This finding at last provides direct evidence of the cooling that had previously been so difficult to demonstrate. — HJS  
*Geology* 36, 251 (2008).

## EVOLUTION

### Crop Rotation

Humans, attine ants, termites, and bark beetles have one thing in common—they all practice agriculture. The attine ants are found in the neotropics in South America; they grow and harvest fungal cultivars;



Ant farmers

and they co-opt a filamentous bacterium, which produces an antibiotic, to help control a parasitic fungal "crop disease." Schultz and Brady have calculated a fossil-calibrated molecular phylogeny of the attine ants and suggest that agriculture arose only once, as it did in termites, and unlike in humans or bark beetles, where it evolved independently several times. From this single emergence, five distinct agricultural systems developed, with the most primitive appearing roughly 50 million years ago. A radically dif-

ferent fungal cultivar, coral fungus, was adopted later by some ant species, and in a third offshoot, the normally filamentous Leucocoprineae fungi, common to most of the attines, were instead grown as nodules of single-celled yeast by select species. Further evidence for adaptive domestication of their fungal crop is seen in the ant species (including the leaf-cutter ants) that carry out higher agriculture: These fungal cultivars cannot survive independently of the ants, unlike those cultivated under the other systems, and these fungi produce gongyliidia—swollen nutritious hyphal tips harvested by their caretakers. — GR

*Proc. Natl. Acad. Sci. U.S.A.* 105, 10.1073/pnas.0711024105 (2008).

## PHYSICS

### Downsizing Synchrotrons

Particle accelerators and synchrotron light sources qualify as big science, not just in the questions they strive to answer but also in their sheer physical size. At the same time, focusing petawatt laser pulses into gas samples can produce a plasma capable of generating and accelerating ions and electrons up to energies of several hundred MeV. Whereas such electrons might traditionally be directed down an undulator—a linear chicane of alternating magnetic fields—to produce synchrotron radiation, Knip *et al.* show that the self-

Continued on page 23



Continued from page 21

generated magnetic and electric fields present in the plasma channel can themselves be used as a miniature undulator. X-rays with energies up to 50 keV can thereby be produced, offering the possibility of reducing large-scale, national facility apparatus to instruments of more modest size. — ISO

*Phys. Rev. Lett.* **100**, 105006 (2008).

## MATERIALS SCIENCE

## Inching up the Wall

The sight of ivy clinging to a wall may evoke serene contemplation, but for the plant, wending up there takes some work. How do the slender stems scale a sheer surface without slipping back down to the ground? More than 100 years ago, Darwin noted a yellow secretion accompanying the climbing process. Zhang *et al.* have now taken a closer look and observed a multitude of nanoparticles emanating from disks that the ivy stems pressed against silicon or mica substrates as they grew. After pulling away the branches, the authors used atomic force microscopy to characterize the fairly uniform distribution of ~70-nm-diameter parti-



cles. Chemical analysis by extraction into organic solvent and subsequent high-performance liquid chromatography revealed a complex composition,

of which the 19 most prominent components were characterized by mass spectrometry. These compounds ranged in molecular weight from ~300 to ~700, comprising 18 to 38 carbons together with hydrogen, nitrogen, oxygen, and sulfur. The precise adhesion mechanism remains unclear, but the authors highlight the high surface area of contact fostered by nanoparticle secretion. — JSY

*Nano Lett.* **8**, 10.1021/nl0725704 (2008).

## BIOCHEMISTRY

## Distinctive Individualism

Single-molecule studies have shown that enzyme activities can differ substantially from the average measured in ensemble experiments and that rates of a single enzyme can vary because of conformational fluctuations. Most experiments, however, have not looked at a large enough number of molecules to characterize the stochastic nature of enzyme kinetics. Rissin *et al.* use an array of 50,000 40-fl reaction chambers in which most chambers were empty but approximately 5% contained a single molecule of  $\beta$ -galactosidase. Hydrolysis of a nonfluorescent substrate to a fluorescent product was monitored simultaneously for about 200 enzyme molecules. Averaged single-molecule turnover velocities agreed well with bulk measures, but there was a wide distribution in activities, confirming the heterogeneity within enzyme populations observed previously. The variability in rate was independent of substrate concentration, suggesting that it arises from variability in  $k_{cat}$ . The effect of enzyme activity distribution on metabolic pathways remains to be determined. — VV

*J. Am. Chem. Soc.* **130**, 10.1021/ja711414f (2008).

## Science Signaling



## &lt;&lt; An Inside Job?

Toll-like receptor (TLR) 4, which recognizes bacterial cell wall components, interacts with the TIRAP-MyD88 pair of adaptor proteins to stimulate the production of type I interferons. Curious about how TLR4 coordinates activation of these two signaling pathways, Kagan *et al.* analyzed TLR4 location in macrophages and found that it was present both at the plasma membrane and in early endosomes. Inhibition of dynamin-dependent endocytosis prevented lipopolysaccharide (LPS)-induced internalization of endogenous TLR4 and blocked TRAM-TRIF-dependent phosphorylation of the transcription factor IRF3 (and the expression of target genes) whereas TIRAP-MyD88-dependent phosphorylation of p38 mitogen-activated protein kinase and I $\kappa$ B $\alpha$  degradation were unaffected. Although TIRAP localized to the plasma membrane, TRAM was present at both the plasma membrane and in early endosomes. Analyses of LPS-induced cytokine production by TRAM localization mutants indicated that TLR4 signaling through TRAM-TRIF took place in endosomes. Noting that no known TLRs stimulate type I interferon production from the plasma membrane (TLR4 had been thought to be the lone exception), the authors propose that TLR4 stimulates TIRAP-MyD88 signaling from the cell surface and initiates TRAM-TRIF signaling only after internalization. — EMA

*Nat. Immunol.* **9**, 361 (2008).



Order today,  
oligos tomorrow

Next-Day Service for  
custom DNA oligos

Invitrogen's new U.S.  
express service allows you to order  
oligos and receive them the next  
business day. Just order online  
before 2 p.m. eastern time.

Get 2 OD units guaranteed minimum yield  
(25 nmol scale) for tube DNA oligos 7 to 40  
bases in length, with the same quality control  
as our standard oligos.

On-time shipment is guaranteed—if we  
don't ship your full order on time, the \$1995  
Next-Day Service fee will be credited back  
to you. Next-Day Service is available in the  
United States only.

Place your order now at  
[www.invitrogen.com/oligos](http://www.invitrogen.com/oligos).



[www.invitrogen.com](http://www.invitrogen.com)

©2008 Invitrogen Corporation. All rights reserved. Service for U.S. customers only.  
These products may be covered by one or more Limited Use Label Licenses (see  
Invitrogen catalog or [www.invitrogen.com](http://www.invitrogen.com)).



## It's in His Kiss

About 600 species of bacteria live in human mouths. Some cause cavities or periodontal disease, whereas others keep breath smelling fresh—but most have unspecified roles and are known only as DNA sequences. “All this myriad of data has been sort of dumped in GenBank,” says Floyd Dewhirst, a microbiologist at the Forsyth Institute in Boston, Massachusetts. “It’s become a meaningless Tower of Babel.”

But no longer. Dewhirst and a team of scientists funded by the National Institute of Dental



Plaque

and Craniofacial Research in Bethesda, Maryland, organized all the sequences in the Human Oral Microbiome Database, which went online 25 March (hmd.org). Based on a new evolutionary tree, each species has been

neatly assigned to a genus, numbered, and linked to bibliographic references. The entire database is searchable by key words and DNA sequences.

Paul Lepp, a microbiologist at Minot State University in North Dakota, says the database will help generate an ecological perspective of disease, encouraging researchers to study how interactions among microbes foster health or disorder. The oral biome is the first of a series of microbiomes to go online; similar databases are in the works for skin, gut, and vaginal microbes.

## Gamblers Bad at Cards

Why do gamblers on a losing streak keep playing till they go bust? Because their minds aren't flexible enough to change course, a recent study concludes.

Psychiatric researchers at the University of Pisa in Italy compared how well 20 recovering gambling addicts and a healthy control group matched for IQ performed on the Wisconsin Card Sorting Test. WCST measures “executive function” such as planning and shifting cognitive strategies. Subjects learn to sort cards (see illustration) according to a particular rule, which the experimenter then covertly changes; participants are judged by how well they pick up on the shifts. In the Pisa study, the



## Living Off the Air

Aeroponics—cultivating plants without soil or water—started to take off in 1983 when Rick Stoner of Agrihouse, a company in Berthoud, Colorado, patented a water-conserving, pesticide-free way to grow crops. NASA chipped in funding for application to potential future space colonies.

The colonies are still beyond the horizon, but commercial production of air-grown veggies is becoming a reality. Optometrist Larry Forrest of Frederick, Colorado, has expanded his aeroponic greenhouse to about 150 square meters, which may make him the world's largest aeroponic farmer. His company, Grow Anywhere Air-Foods, grows tiny seedlings of mesclun and other greens for restaurants, misting their roots with a nitrogen- and calcium-rich spray every 20 minutes. Forrest's equipment involves several thousand nozzles, pipes, and other parts. But he says he is working on a simpler, cheaper 500-part system to sell to like-minded growers.

“This is the first I’ve seen someone else trying to make a go of it,” says Edward Hanwood, who patented an aeroponic system with a cloth conveyor belt but couldn't make it pay. As far as the U.S. growers know, the technique hasn't caught on anywhere else in the world. But Stoner sees a big potential: The technology “can be set up anywhere, including Iceland or Antarctica,” he says.

gamblers had much more difficulty adapting to new rules and, unlike the healthy people, actually got worse with practice. The results, the scientists reported last week in the journal *Clinical Practice and Epidemiology in Mental Health*, indicate “a sort of cognitive ‘rigidity’” that prevents people from looking for alternative solutions to problems and fosters the kind of “perseverating” thinking that gamblers indulge in.

Yale University gambling researcher Marc Potenza says the study is interesting, but the results are uncertain given the small number of subjects and the fact that they suffer from other additions and mental problems. Nonetheless, psychiatrist Jon Grant of the University of Minnesota, Minneapolis, says the study underscores that gambling, unlike, say, drinking, “is a cognitive task.” And it raises the question of whether such flaws in

thinking are there all along but “don’t show up until [people] get into gambling.”



## << Astronaut Family Humor

When the second Skylab crew lifted off in May 1973, the astronauts carried, unbeknownst to them, copies of this patch sent by their wives. It's a takeoff on the mission logo, adapted from the famous drawing by Leonardo da Vinci.

Last week, one of the 320 original parody patches was sold for \$388.38 at an auction of space artifacts in Dallas, Texas. One item still awaiting a buyer: a moon dust scoop used during the 1971 Apollo 14 flight and presented to backup commander Eugene Cernan, who became the last human to walk on the moon the following year. It was expected to fetch as much as \$300,000, but no one picked it up, so it's now on sale for \$161,325.



Press 1-4 to sort card





## Collections

**THERMOMETER KINGS.** As a child, Joel Myers was entranced by the meter-tall "Prestone Antifreeze" thermometer across the street from his Philadelphia, Pennsylvania, home. Now, he owns the world's largest collection of thermometers, and he's looking for a place to house them.

Myers, 68, earned a Ph.D. in meteorology and founded AccuWeather, a \$100 million company in State College, Pennsylvania, that provides weather forecasts to media outlets. That made him the logical person for Richard Porter to seek out when the retired science teacher decided to sell his collection of 4000-plus thermometers, including an earring thermometer from a 1650 whaling ship. "It's been a labor of love," says Porter, 79, who dedicated his collection to his daughter, a teacher's aide who died in 1990, to honor girls who pursue careers in science.

Myers bought the lot for about \$20,000 and plans to combine it with his own collection of 300 antique barometers. He hopes the instruments will inspire weather and history buffs.

## AWARDS

**James Galloway and Harold Mooney** have won the \$200,000 Tyler Prize for Environmental Achievement, administered by the University of Southern California in Los Angeles. Galloway, a researcher at the University of Virginia, Charlottesville, wins the honor for pioneering work describing how nitrogen affects the environment. Mooney, an environmental biologist at Stanford University in Palo Alto, California, is being recognized for helping to make ecological studies a global discipline by starting or helping to launch efforts such as the Global Invasive Species Programme and the Global Biodiversity Assessment.

## MOVERS

**HEAVYWEIGHT HIRE.** Mark Yudof, a law professor who has led the University of Texas (UT) since 2002, was last week named president of the University of California (UC). Yudof takes over the 10-campus system from physicist

Robert Dynes, who last year announced his decision to step down following a series of controversial decisions including the approval of questionable salaries and perks for some top-level UC employees.

Yudof, 63, was president of the University of Minnesota for 5 years before taking charge of the UT system. In his new position, Yudof will receive a compensation package of \$828,000, nearly twice as much as what Dynes was making but close to Yudof's current UT salary of \$790,000. "He's expensive but worth it," Richard Blum, president of the UC Board of Regents, told the *San Jose Mercury News*. Yudof starts this summer; Dynes will return to being a professor at UC San Diego.

## RISEING STARS

**BEATING BACTERIA.** Timothy Lu's new approach to eradicating biofilms has won him this year's \$30,000 Lemelson-MIT Student Prize for innovation.

Biofilms are layers of bacteria embedded in a protective matrix that makes them 1000 times more resistant to antibiotics than free-living bacteria. As a Ph.D. student in the lab of Boston University biomedical engineer James Collins, Lu engineered a bacteriophage to help eliminate the films, which contaminate food-processing equipment, pipes, and medical implants. Ordinary phages destroy bacteria but can't penetrate the biofilm matrix. Lu's modified phage forces infected bacteria to manufacture an extra enzyme that breaks down the matrix as well.

Collins calls Lu, now in medical school, an "exceptionally creative entrepreneurial young scientist" and notes that Lu's work represents one of the first practical applications to arise from the new field of synthetic biology. Lu plans to use his prize money to help commercialize the engineered viruses.



## Three Q's

Black seas, glowing icebergs, and moody skies now dominate the roundtable at the U.S. National Academy of Sciences in Washington, D.C. *Science* talked with California-based photographer **Camille Seaman** about her exhibit, "The Last

Iceberg," based on several trips to the Arctic and Antarctica since 2003.

**Q: What do you want your audience to experience?**

It's very important that people feel what I felt when I was there: a sense of awe, of isolation,



and a bit of sadness but also profound beauty. I want them to understand that our planet is beautiful, that the process of living can be really beautiful.

**Q: How has climate change influenced the way you look at icebergs?**

When I was in the Arctic in 2003, the ice was really significant. I went back on the same ship in 2006 to the same area, and there was nothing. I

understood just how much we stand to lose and the importance of a visual record.

**Q: Is there one iceberg that was most memorable?**

The worst situation was at Grand Pinnacle [Greenland]. It was so cold, and I was the only one out on deck. I used a beautifully German camera, but it's completely metal, and it's not friendly to load. I literally almost lost my fingertips. I learned the hard way that was not the right camera.

Got a tip for this page? E-mail [people@aaas.org](mailto:people@aaas.org)



China's innovative  
new telescope

34

DNA from  
the earliest  
Americans?

37

## AIDS RESEARCH

## Review of Vaccine Failure Prompts a Return to Basics

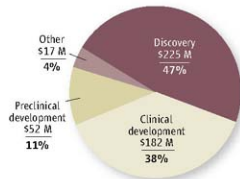
**BETHESDA, MARYLAND**—It may be a stretch to call it a turning point, as one optimist did, but a 1-day AIDS vaccine meeting held here last week undoubtedly marked a low point. Some of the more than 200 gloomy researchers gathered in a hotel conference room were grumbling about a recent newspaper story in which AIDS researcher Robert Gallo compared last year's failure of a major AIDS vaccine trial to the Challenger space shuttle disaster. During lunch, an AIDS activist group called for an end to all AIDS vaccine research and testing.

The summit's convener, meanwhile, National Institute of Allergy and Infectious Diseases (NIAID) Director Anthony Fauci, cheered the troops on: "Not only will we not cut it; wherever possible, we will increase" funding for vaccine research, he declared. But he agreed that NIAID needs to set a new course for a field that seems to have hit a brick wall.

NIAID called for a summit earlier this year following the suspension in September of an international trial of a Merck AIDS vaccine, which failed to protect against HIV infection and may even have made some people more susceptible (*Science*, 16 November 2007, p. 1048). The devastating news led the National Institutes of Health (NIH) in Bethesda, Maryland, to suspend plans for a trial of a similar vaccine of its own (*Science*, 21 December 2007, p. 1852). In January, 14 investigators wrote Fauci urging NIAID to rethink its funding priorities and put less money into testing. The chief author, Ronald Desrosiers, director of the New England Regional Primate Research Center in Southborough, Massachusetts, told an AIDS conference in February that no vaccine in the pipeline has a chance of success and that NIAID has "lost its way" (*ScienceNOW*, 5 February:

scienecow.sciencemag.org/cgi/content/full/2008/205/1).

Fauci said he agrees that NIAID needs to "torque" the \$476 million AIDS vaccine extramural portfolio, to shift away from prod-



Total NIAID extramural funding for HIV vaccine research: \$476 M



**Midcourse correction.** NIAID chief Anthony Fauci says that the institute needs to increase the share of vaccine research that goes for "discovery," or basic research (now 47%), and spend less on testing candidate vaccines in the lab and in clinical trials.

uct development and toward "discovery research." "We really do need new and novel ideas," agreed Carl Dieffenbach, director of the NIAID Division of AIDS. Although few specifics were offered, participants agreed on worthy avenues of study. They include finding antibodies that thwart HIV; investigating the mucosal immune system, where the virus usually gets a foothold; and studying African monkey species that carry simianlike HIV but don't get sick, as well as rare people who become infected with HIV but stay healthy without drugs.

The summit also considered another problem: the need for a predictive animal model. Participants agreed that the rhesus macaque system now used to test potential vaccines isn't working well. They would like to create more simian strains of the AIDS virus and develop standard testing protocols, as well as explore basic biology questions. Such plans will be constrained, however, by the high cost of animal studies and shrinking budgets of primate centers, noted speakers. "It's going to be a cost-benefit analysis," said pathologist Louis Picker of Oregon Health and Science University in Portland.

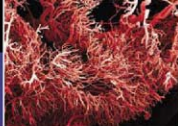
The emphasis on discovery does not mean abandoning clinical studies, participants observed. "Human data trumps" other kinds of data, said Jerald Sadoff, president of the Aeras Global TB Vaccine Foundation in Rockville, Maryland. But decisions about testing products should be made only with "broad input," concluded Scott Hammer of Columbia University. In the meantime, smaller human studies can be used to answer fundamental questions, he and others said.

Others emphasized the need to mine data from existing trials. The Merck trial "could be a sterling scientific success if in fact we can decipher" what went wrong, said virologist Warner Greene of the University of California, San Francisco, co-chair of the summit, which he hoped would be a historic "turning point."

How will NIAID fund more discovery research when NIH's budget is stagnant and competition for grants is more intense than ever? Fauci said he wants to set aside funds for AIDS vaccine research but make the request for proposals "broad" to stimulate creativity. He would also give priority to new investigators. He says he may start with \$10 million in 2009, part from the

COURTESY: NIAID





proposed \$130 million trial of NIH's vaccine, which if it happens may be downsized from 8500 patients to 2000. Dieffenbach says the agency "could move some money" to this pot from its international clinical trials network.

Although the summit did not produce a detailed plan, Desrosiers, for one, seemed encouraged. Testing vaccine products is "no longer going to be the emphasis. Tony [Fauci] said it. That's a huge deal," he said. Exactly

what that means will become clear in coming months, others note. "It will require some bold and creative administration leadership," says University of Pennsylvania professor emeritus and AIDS researcher Neal Nathanson, who signed the letter to Fauci but was unable to attend the summit.

The most urgent issue—one not addressed at this meeting—is whether to go ahead with the trial of NIH's vaccine. Fauci thinks the

study still has merit because the vaccine's design is "not the exact same" one as Merck's. He also points to a suggestion at the summit that the Merck vaccine might have protected a subgroup of patients—although he adds that such post hoc analysis of a small group is not statistically significant. Fauci expects to decide the fate of the NIH trial after the NIH AIDS vaccine advisory committee meets in late May.

—JOCELYN KAISER

## SPACE SCIENCE

# NASA's Stern Quits Over Mars Exploration Plans

The twin Mars rovers have spent more than 4 years trundling across the surface of the Red Planet. Last week, however, they created a stir back home—the resignation of S. Alan Stern as NASA's science chief after a running dispute with his boss, Administrator Michael Griffin, over how to manage the financial squeeze on NASA's \$4.6 billion science effort.

Stern's abrupt departure from NASA headquarters, effective next week, underscores how serious that crisis has become. Griffin has decreed that NASA's science budget will remain flat to accommodate a new launcher capable of taking humans to the moon despite rising costs for a host of projects, including the \$2 billion Mars Science Laboratory (MSL). But cutting existing missions to make up for the growing shortfall is no simple matter.

Last month, Stern's office tried to offset a tiny fraction of a \$200 million MSL overrun by ordering a \$4 million cut to the rovers project, managed by NASA's Jet Propulsion Laboratory (JPL) in Pasadena, California. Faced with the budget reduction, JPL said it would have to mothball one of the rovers. When Griffin found out about the decision from media accounts, he reversed it in a move that reflected the lab's political clout and the public's fascination with the intrepid robots, Opportunity and Spirit. The decision "was not coordinated with the administrator's office," a NASA spokesperson said. Within hours, Stern announced his resignation, effective 11 April.

Sources close to NASA headquarters say that Griffin feels Stern, a planetary scientist who came to Washington, D.C., 1 year ago, has repeatedly failed to tell him about major decisions and that the plan to shut down one of the rovers—which outraged congressional

supporters and made headlines around the country—was the last straw. Other managers, however, say that Stern believes Griffin has tied his managerial hands by blocking efforts to cut or delay politically sensitive projects.

NASA officials say Griffin favors cutting less popular parts of the budget, including funding for science grants, but that Stern has resisted that approach. "Mike didn't like Alan's solutions," explains one NASA official. "Mike told him how to fix it. Alan didn't like the solution and resigned."

Stern told *Science* that he's leaving because he does not want to make cuts to healthy projects and research grants to cover overruns in other programs. The rover is just a symptom of a larger problem, he says. Griffin praised Stern in a terse statement and named Goddard Space Flight Center Director Edward Weiler—a former science chief himself—as temporary replacement.

Stern has said that the overall Mars program should shoulder the burden of the overruns in the MSL project. NASA's 2009 budget request, for example, cut in half the planned funding for Mars exploration during the next 5 years (*Science*, 29 February, p. 1174). That decision prompted an outcry from both scientists and lawmakers. "[Stern] wanted to strangle Mars to pay for other things," says John Mustard, a planetary scientist at Brown University, who heads a key Mars advisory committee.

Weiler says he's aware of the difficult problems facing the science office, which he headed from 1998 to 2004, and that he is not afraid of killing a project if NASA can't afford it: "I canceled seven missions. I'm no pushover." He notes that he scrapped and



**Quick exit.** S. Alan Stern is leaving NASA after 1 year as science chief.

rebuild the entire Mars program in 1999 after the failure of two Mars missions. He promises to revisit the 2009 budget plan, given "all the criticism" from the science community. He says he will consult with scientists about whether to focus resources on a single Mars sample-return project—a highlight of the 2009 plan—or use the money to fund several missions. And he promises to find the resources to push for smaller and cheaper missions using modest launchers.

Weiler has also had an unfortunate encounter with a beloved program. His proposal to cancel a 2004 mission to service the Hubble Space Telescope created a public furor and eventually led NASA to reverse itself. "There are three things you don't do at NASA," he jokes. "That is cancel Spirit, Opportunity, or Hubble." —ANDREW LAWLER

## MICROBIOLOGY

## Germs Take a Bite Out of Antibiotics

As far as patients and doctors are concerned, bacteria are supposed to do one thing when they encounter antibiotics: drop dead. But a broad survey of soil microbes shows that numerous species devour even the most potent drugs. The craving for antibiotics is widespread across environments and bacterial groups, researchers report on page 100, fueling worries about the dwindling power of our main weapons against infections.

Although a few previous studies had identified antibiotic-eating strains, "nobody had done a systematic search like this," says chemical biologist Gerry Wright of McMaster University in Hamilton, Canada.



**Taste test.** Harvard University researchers Morten Sommer and Gautam Dantas and colleagues used soil samples from a Massachusetts forest and a cornfield (inset) to screen for antibiotic-eating microbes.

"It's one of those papers that unveils a whole new area of research."

Eighty years after Alexander Fleming discovered penicillin on a moldy culture dish, the battle against killer bugs is faltering. More and more bacteria—including insidious tuberculosis strains that have cropped up (*Science*, 15 February, p. 894)—now shrug off almost all antibiotics. Meanwhile, few new antibiotics are reaching the clinic. Medicine is on the defensive, says microbiologist and physician Stuart Levy of Tufts University School of Medicine in Boston. "We are not keeping up with the bacteria."

Geneticist George Church of Harvard Medical School in Boston and colleagues had not planned to dig up more grim news about antibiotics. These researchers were hunting for microbes that could convert agricultural waste into biofuels and were using antibiotics in their control studies. But for some bacteria, they learned, anti-

biotics provide a meal.

The team gathered soil from 11 sites that have varying degrees of exposure to human-made antibiotics—from a cornfield that had been fertilized with manure from cows fed antibiotics to an untouched patch of temperate forest. Every locale harbored bacteria that could survive with nothing to eat but antibiotics.

The diners hailed from 11 orders of bacteria and included relatives of pathogens such as the gut invader *Shigella flexneri* and the noxious *Escherichia coli* strain O157:H7. Compared with "conventional" antibiotic-resistant bacteria, the drug-eaters were "uberbugs." They could tolerate antibiotic concentrations 50 times higher than what qualifies a bacterium as resistant. Moreover, each of the 18 medicines the team tested—including pharmacy staples such as penicillin, ciprofloxacin, and kanamycin—could provide nourishment for at least one type of bug.

"Almost all the drugs that we consider as our mainline defense against bacterial infections are at risk from bacteria that not only resist the drugs but eat them for breakfast," says Church. He doesn't yet know how bacteria turn these supposedly lethal compounds into a meal.

The medical importance of these consumers is also unknown. In principle, the germs could cause trouble in two ways, says Wright. Microbes that are usually innocuous might pick on people, such as AIDS patients, who have crippled immune systems. Moreover, soil bacteria pass around resistance-conferring genes like teenagers swap downloaded music files, and pathogenic bacteria could likewise pick up antibiotic-digesting genes, particularly from a closely related microbe.

However, nobody has identified a pathogenic bacterium that can chow down on the drugs, Church notes. And bacteriologist Jo Handelsman of the University of Wisconsin, Madison, thinks it's unlikely that disease-causing bugs would switch to an antibiotic diet: "There are much yummier and easier things to eat in the human body."

—MITCH LESLIE

## Chimp Center Proposed

A Louisiana-based foundation wants to build a facility to house as many as 250 great apes in a setting that would be part tourist attraction, part sanctuary, and part research center.

The National Chimpanzee Observatory and Great Ape Zoological Gardens would "allow chimps to seamlessly participate in behavioral and cognitive research and have a naturalistic outdoor environment," says psychologist Daniel Povinelli of the University of Louisiana, Lafayette, who directs the foundation behind the concept. He says the 120-hectare center, near Lafayette, Louisiana, would help maintain genetic viability in the captive chimpanzee population despite a U.S. moratorium on breeding chimps for research.

Supporters have asked the Louisiana legislature for a \$10 million down payment on a \$256 million investment, hoping that admissions and concessions will cover operating costs. "There's the potential for this to have enormous benefit to chimpanzees," says primatologist Rob Shumaker of the Great Ape Trust of Iowa in Des Moines.

—ELSA YOUNGSTADT

## Second Chance for Your Euros

**PARIS**—Young researchers in four European countries who miss out on the first Starting Grants from the European Research Council (ERC) may get a second chance. In a move that expands ERC's clout, France, Italy, Switzerland, and Spain have announced plans to make special funding available for those who meet ERC's criteria but end up missing the cut.

Out of more than 9000 proposals in biomedicine, physics, engineering, and social sciences, ERC has selected 430 as worthy of funding; but although its €290 million budget for this round may yet increase somewhat, it will suffice for only the best 300 or so. (The first contracts will be signed soon.) Recently, however, Italy's Ministry of University and Research promised €30 million to support Italian researchers likely to lose out, and France's national research agency, CNRS, will pony up €10 million for its nation's scientists. The Swiss National Science Foundation has similar plans. The Spanish science and education ministry will offer 25 candidates a 1- or 2-year "bridge fund" to set up shop while they reapply to ERC or secure funding elsewhere.

The country-level support is "an early acknowledgment of the intrinsic quality of the ERC's peer-review evaluation mechanisms," ERC President Fotis Kafatos said in a statement.

—MARTIN ENSERINK

## ASTRONOMY

# China's LAMOST Observatory Prepares for the Ultimate Test

**XINGLONG, CHINA**—The towering white edifice on the ridge looks like a futuristic missile site pointed at Beijing or a marvel of constructivist architecture. Last year, when astronomer Donald York of the University of Chicago in Illinois laid eyes on the sleek structure perched above the town of Xinglong, 170 kilometers northeast of Beijing, “I was, frankly, stunned,” he says. That’s a reaction Chu Yaoquan expects from the uninitiated when the Large Sky Area Multi-Object Fiber Spectroscopic Telescope (LAMOST) comes into view after rounding a bend on the road to Xinglong Observing Sta-

tion,” says Chu.

Engineers this month are installing LAMOST’s eyes and optic nerves: 1-meter-wide hexagonal sections of its two mirrors and the 4000 optical fibers on its focal surface that will feed starlight into a battalion of spectrographs. Viewing conditions at Xinglong, in China’s industrialized north, are not ideal: Independent experts say that siting the scope in western China would have been better. Every week, dust and sand blown in from the Gobi Desert have to be

images a spectroscopic area of 7 square degrees of sky, about 28 full moons. “We took a different approach,” says Chu.

In 1994, two senior astronomers—Wang Shouquan and Su Dingqiang—along with Chu, Cui, and Wang Yanan unveiled a concept for a telescope that can see both far and wide. A 4-meter Schmidt correcting mirror—the largest of its kind—tracks the motion of objects and reflects their light onto a fixed 6-meter primary mirror. A key innovation is an active optics system that deforms the correcting mirror’s 24 plates individually, compensating for the spherical aberration of the primary mirror and bringing both mirrors into focus simultaneously. The primary mirror focuses light from the 4-meter flat mirror onto the focal surface, forming an image of the sky spanning 20 square degrees, or 80 full moons.

At the focal surface, light from individual objects streams into individual optical fibers feeding into the spectrographs, which parse the light into spectra with wavelengths ranging from 370 to 900 nanometers. The dispersed light is collected on charge-coupled device detectors. “It’s groundbreaking in its elegant optics and the number of fibers simultaneously placed on the sky,” says York.

LAMOST came along at an auspicious time, as astronomers were emerging from the Cultural Revolution. “I saw it as a project that could rally the community,” says Douglas Lin, an astronomer at the University of California, Santa Cruz, and director of the Kavli Institute for Astronomy and Astrophysics in Beijing. China approved LAMOST as a major project in 1996. At the time, Chu says, many skeptics doubted whether the team could pull off the active optics system, which uses 34 actuators to deform each of the correcting mirror’s 1.1-meter segments and to position the 4000 fibers during observations. “This was the most challenging part of the design,” says Cui. In 2005, on the eve of construction, China’s National Astronomical Observatories asked York and Richard Ellis, an astronomer at the California Institute of Technology in Pasadena, to co-chair a panel of foreign experts to review LAMOST. Their report identified engineering and management issues that project manager Zhao Yongheng says have mostly been put to rest. Last year, Cui and her staff installed and tested portions of the two segmented mirrors, along with the focal surface. “The test demonstrated that the design works,” she says.

Once Cui’s team wraps up the engineering, it will be up to Chu’s team to come up with the discoveries. They have three main objectives. One is to acquire spectra from hundreds of thousands of galaxies to shed light on



**LAMOST leaders.** Cui Xiangqun (right) heads the telescope’s engineering team; astrophysicist Chu Yaoquan leads the scientific group that plans to begin spectral surveys next year.

tion. “It’s totally unlike any other telescope in the world,” says Chu. LAMOST’s project scientist and an astrophysicist at the University of Science and Technology of China in Hefei.

The science should be out of this world, too. LAMOST is designed to peer deeper into space and measure more spectral emissions than the project that inspires it, the Sloan Digital Sky Survey (SDSS). Perhaps the most ambitious astronomical survey ever undertaken, SDSS has imaged 300 million celestial objects and measured spectra of 800,000 galaxies, 300,000 stars, and 104,000 quasi-stellar objects (QSOs), bright galactic cores harboring black holes. “LAMOST goes well beyond SDSS,” says York, the Sloan survey’s founding project director. LAMOST’s spectral deluge of tens of millions of galaxies and stars should offer new insights into galaxy formation, including our own Milky Way. “We know how stars form and how our universe formed. But we still don’t know how galaxies

brushed off the correcting mirror. On the bright side, Xinglong, in the foothills of the Yanshan Mountains, gets an average of 270 clear nights of viewing each year. The whole system—which has cost \$40 million so far to build—should be in place by fall, when final testing will begin, says LAMOST’s chief engineer, Cui Xiangqun, director of Nanjing Institute of Astronomical Optics and Technology. Data collection should begin in earnest next year.

For Cui and Chu, first light will mean the end of a long journey to bring LAMOST into this world. Broadly speaking, optical telescopes come in two flavors: those with a large aperture that gaze deep into space—and deeper into the past—but are confined to a field of view that’s smaller than the full moon, and those that take in many moons’ worth of sky. “It’s difficult to get both area and depth at the same time,” says Cui. At any moment, the SDSS’s 2.5-meter telescope in New Mexico



universe structure and, for instance, the role of enigmatic dark energy. LAMOST should be able to peer twice as deep into space and time as the Sloan survey, says Chu. It should also find scads of QSOs. A QSO influences star formation throughout its galaxy, but how it does so is a mystery. "LAMOST can make great headway on this problem," says York.

A second aim is to scrutinize our own galaxy. "We still don't have a clear idea about our galaxy's structure," Chu says. SDSS pioneered the use of color filters for the classification of star types. LAMOST should be able to extend this work by finding dispersed families

of stars. By parsing spectra of millions of stars in the Milky Way, "we can get the whole history of our galaxy," Chu says. A third objective is to unmask anomalous objects found in radio, infrared, and other surveys by analyzing their optical spectra.

Because of the daunting technical challenges, not everybody in China's scientific community is enamored of LAMOST. But York, for one, is a fan. LAMOST, he says, "is very beautiful and seems to be accomplishing its [engineering] goals." Its potential for groundbreaking science will soon be put to the test.

—RICHARD STONE

## DEFENSE RESEARCH

# U.S. Asked to Bolster Ties With China

The U.S. military has more to gain than lose by working with Chinese scientists on fundamental research. So says the Pentagon's former director of basic research, William Berry, in arguing for the removal of obstacles to scientific cooperation between the U.S. Department of Defense (DOD) and China despite the military rivalry between the two countries.

Berry, now a researcher at the Center for Technology and National Security Policy at the National Defense University in Washington, D.C., writes with colleague Cheryl Loeb in a working paper published by his center last week that collaborating with Chinese researchers at a time of rapid growth in China's science and technology investment will help DOD stay on the cutting edge of materials, biotechnology, energy sciences, and other disciplines relevant to long-term U.S. security interests. "It would also help the U.S. military learn more about China's scientific capabilities," says Berry, who was wowed by a visit to Shanghai's Fudan University last fall. As first steps toward fostering these links, the authors want DOD to encourage its program managers and scientists to travel to Chinese universities, establish a liaison office in China, and sponsor visits by Chinese academics to U.S. institutions.

It's a controversial idea among defense policy analysts. "A number of people at the agency are receptive to having a more open exchange with China," says Alan Shaffer, director of plans and programs within the

Defense Research and Engineering office. "But there is also concern about giving away too much information. ... We are going through those debates right now." Shaffer agrees that the benefits of collaboration would outweigh the risks to national security as long as there are "checks and balances."

Others are not so sure. Larry Wortzel, chair of the U.S.-China Economic and Security Review Commission, a federal advisory body that monitors the security implications of U.S.-China trade, says any research, no matter

how fundamental, could ultimately help strengthen the Chinese military. "Science is not neutral, and it eventually has application," says Wortzel, who calls the idea a dangerous mix of "scientific tourism" and "the desire to link hands in the name of science and sing 'Kum Ba Yah.'" In its most recent annual report to the U.S. Congress, the commission advised caution in all S&T engagements with China, including collaborative projects funded by the National Science Foundation (NSF) and the departments of Energy and Health and Human Services. NSF and DOE have both established offices in Beijing in the past 3 years, and an official at the Office of Naval Research says ONR is exploring the idea.

A Hill staffer familiar with the debate thinks that Berry is walking a political tightrope. "It may be hard for DOD to make the case that the collaborations will somehow have value for DOD but not the Chinese military," says the aide.

—YUDHIJIT BHATTACHARJEE



**China watcher.** Berry says research is a two-way street.

## After the Nobel

The Intergovernmental Panel on Climate Change (IPCC) has demonstrated the tremendous value in exhaustive studies on the state of climate science. But after delivering its fourth such assessment last year and then picking up a Nobel Prize for its 2 decades of labor, some scientists are thinking that more frequent, shorter special reports on how to fix the problem might better serve policymakers. "Do we need to say we are now really, really, really certain that human influence is changing climate? No, the questions have changed. So should IPCC," says Kevin Trenberth of the National Center for Atmospheric Research in Boulder, Colorado.

Next week, the panel will meet in Budapest, Hungary, to take up that issue and other matters, including how to spend its \$876,000 Nobel windfall. One idea is student scholarships.

—ELI KINTISCH

## Popping the Question

The National Science Foundation (NSF) is on the verge of adding a question to the U.S. census that will help it paint a clearer picture of the technological skills of the U.S. workforce. Pending White House approval this spring, the U.S. Census Bureau will ask college graduates responding to its American Community Survey about their major field of study. The annual 70-question survey provides data on income, housing, and other matters needed to run various mandated government programs.

Residents are currently asked only about their highest level of education attained, giving NSF no clue to their scientific savvy.

—JEFFREY MERVIS

## Radiation Risks Neglected

NASA needs to pay more attention to radiation risks facing astronauts on extended missions to the moon and Mars, warns a U.S. National Academies panel. The report urges NASA to beef up its space radiation research program, in which grants have dropped by half in the past 2 years to \$15 million. NASA is building a new launcher capable of taking astronauts beyond low-Earth orbit, the panel notes, without knowing how much shielding is necessary to protect astronauts from potentially deadly cosmic rays and solar particles, which can cause short-term damage and long-term injury. The report calls for NASA to work with other agencies, such as the Department of Defense or the National Oceanic and Atmospheric Agency, to better understand space-radiation hazards.

—ANDREW LAWLER

## ARCHAEOLOGY

## DNA From Fossil Feces Breaks Clovis Barrier

Who were the first Americans? A decade ago, most archaeologists bestowed this distinction upon the so-called Clovis people, who left elegantly fluted projectile blades across the United States and Central America beginning about 13,000 years ago. But since the late 1990s, evidence for an earlier peopling of the Americas has steadily accumulated.

Now, in a *Science* paper published online ([www.sciencemag.org/cgi/content/abstract/1154116](http://www.sciencemag.org/cgi/content/abstract/1154116)) this week, an international team reports what some experts consider the strongest evidence yet against the "Clovis First" position: 14,000-year-old ancient DNA from fossilized human excrement (coprolites), found in caves in south-central Oregon. "This is the smoking gun" for an earlier colonization of the Americas, says molecular anthropologist Ripan Malhi of the University of Illinois, Urbana-Champaign. The new work, combined with recent finds at even earlier sites in Florida, Wisconsin, and elsewhere (*Science*, 14 March, p. 1497), "add up to a human presence on the continent by 15,000 years ago," says geochronologist Michael Waters of Texas A&M University in College Station. (All dates are given in calibrated calendar years.)

But some members of both camps caution that the team has not entirely ruled out the possibility of modern contamination—or that the feces were left by dogs rather than people. There is "an element of doubt," says anthropologist Thomas Dillehay of Vanderbilt University in Nashville, Tennessee, whose excavations at a 14,600-year-old Chilean site also challenge the Clovis First paradigm.

The 14 coprolites were found in 2002 and 2003 during excavations in Oregon's Paisley Caves, led by archaeologist Dennis Jenkins of the University of Oregon, Eugene. From the size, shape, and color of the coprolites, Jenkins's team concluded that they had been produced by humans. The researchers then joined up with ancient DNA specialists Eske Willerslev and Thomas Gilbert of the University of Copenhagen in Denmark (*Science*, 6 July 2007, p. 36). The pair succeeded in extracting human mitochondrial DNA (mtDNA) with genetic signatures typical of Native Ameri-

cans—and not shared by any other population groups—from six of the coprolites.

Because the coprolites were not excavated under sterile conditions, the team was not surprised to find modern mtDNA contamination from people of European origin. To ensure that the Native American DNA was not from similar contamination, researchers analyzed the mtDNA of all 55 people present at the dig, plus all 12 scientists at the Copenhagen lab. None had the Native

dogs, coyotes, or wolves—or canids may have urinated on the human feces. But if these were actually canid rather than human coprolites, some researchers say, it might be the other way around: The DNA could be from the urine of humans who ventured into the caves long after the coprolites were deposited. "The coprolites are the same size and shape as both human and canid feces, and less than half of the [14] coprolites had human DNA in them," notes anthropologist Gary Haynes of the University of Nevada, Reno.

Team members reject this explanation and offer yet more data as evidence: They tested for and found human proteins in three coprolites, including two dated to about 14,000 years ago. "This nongenetic test requires more human protein than can be expected from urination," explains Willerslev. Jenkins adds that human hair was found in the coprolites too. "Whether the coprolites are human or canine is irrelevant, since for a canine to swallow human hair people had to be present in that environment," he says. "People eat canines, canines eat people, and

canines eat human feces. Any way you cut the poop, people and dogs would have to be at the site within days of each other 14,000 years ago."

Such an early date nixes any claims of Clovis priority, because demographic studies have shown that early colonizers could have fanned out across the

United States in as little as 100 years. "The Clovis First argument is pretty much dead in the water," says archaeologist Jon Erlandson of the University of Oregon, Eugene. "But our knowledge of what came before is still very sparse."

Erlandson, Waters, and others say the coprolite data bolster the idea that when the first Americans came east from Asia, they arrived on the Pacific Coast rather than taking an inland route. At 14,000 years ago, ice sheets would have mostly blocked the inland path. The coastal theory is attractive to many, but archaeological details have been scarce. Says Jenkins: "We may not know much about the first Americans, but if we are going to search for [them], we need to be working beyond the 13,000-year Clovis barrier."

—MICHAEL BALZER



**Prehistoric poop.** Coprolites from Oregon's Paisley Caves (inset) push back dates for the first Americans.



American signatures. Next, the team called in two other well-known ancient DNA labs, which each independently verified the findings. Finally, two leading labs radiocarbon-dated the coprolites and found that at least three were 14,000 years or older.

"This is an excellent paper that will set the agenda for future research," says ancient DNA researcher Terry Brown of the University of Manchester, U.K. "I am convinced that the [human] DNA they detected is not modern contamination." Adds anthropologist David Smith of the University of California, Davis: "If this doesn't convince what's left of the Clovis First people, it should."

However, Brown, along with leading pre-Clovis skeptics such as Stuart Fiedel of the Louis Berger Group in Washington, D.C., says that the coprolites do not make an airtight case for pre-Clovis occupation. That's because the team also reported finding canid DNA in three coprolites. The co-authors suggest that humans might have eaten canids—



# All in the Stroma: Cancer's Cosa Nostra

**After focusing for decades on what happens within tumor cells to make them go wrong, biologists are turning to the tumor environment and finding a network of coconspirators**

As several spectacular cases have shown, corporate criminals can operate for years, bending office systems to their needs and co-opting others into their nefarious deeds. Eventually, the malfeasance can threaten the entire company. So it is with cancer cells. Cancer biologists have recently been coming to grips with the fact that tumor cells get a lot of help from the cells around them. Such collusion is not the source of disease: More than 30 years of research have shown that mutations in a cell's own DNA initiate the changes that put it on its destructive path. But "people are realizing that the tumor environment is a coconspirator," says Zena Werb of the University of California, San Francisco (UCSF). "There's been a clear shift in interest."

A variety of cells in and around tumors help cancer cells survive, grow, and then spread to new locations where they seed metastases. Investigators are beginning to trace out the biochemical lines of communication that enable this aberrant behavior—information that could help drug developers devise new strategies for combating cancer. "People are excited about potential new [drug] targets in the tumor microenvironment," says Lynn Matrisian of

Vanderbilt University School of Medicine in Nashville, Tennessee.

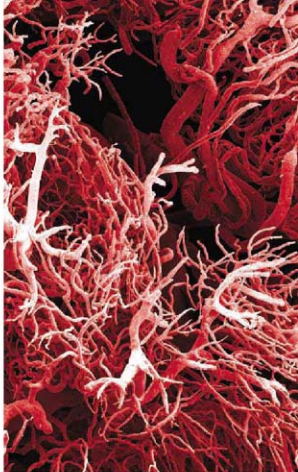
Although this work is still in its early stages, researchers have identified some key molecules in communication pathways that could serve as targets. These include some relatively unfamiliar characters as well as some old friends, such as the protein VEGF, which stimulates angiogenesis, the formation of the new blood vessels that tumors must acquire as they grow. Drugs that inhibit VEGF's action are already in use in the clinic. Their effects are relatively modest, but they do indicate that targeting the tumor environment has promise.

## Trouble in the stroma

Researchers have known for many years that a tumor is more than a homogeneous mass of cancer cells. It incorporates several other cells, including fibroblasts, inflammatory immune cells such as macrophages, and the smooth muscle and endothelial cells of the blood vessels—all imbedded in an extracellular matrix that fibroblasts produce. Cancer researchers paid little attention to this tumor microenvironment, or stroma, until the mid- to late 1990s.

At the time, one of the few investigators

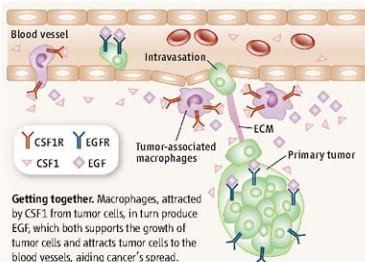
systematically pursuing the question of how the tumor microenvironment influences cancer development was Mina Bissell of Lawrence Berkeley National Laboratory in Berkeley, California. Bissell's team got interested in cell surface proteins called integrins that help assemble organized tissues by forming contacts between cells and



with the basement membrane. In 1997, Bissell and her colleagues reported that treating human breast cancer cells with an antibody directed at an integrin caused them to behave more like normal cells. In mice, for example, they formed fewer tumors than untreated cancer cells.

Conversely, antibodies directed against a different integrin could make normal cells behave like cancer cells. These results showed that simply disturbing cellular interactions, and thus tissue architecture, can dramatically alter cell behavior. Bissell says this is evidence for what she has long argued: "Structural integrity needs to be maintained for signaling to be maintained," she says. "When that doesn't happen, you get tumors."

Other research in the late 1990s implicated so-called tumor-associated fibroblasts (TAFs) as important coconspirators in the development of the common solid tumors, such as those of the breast, prostate, lung, and colon. These cancers originate in epithelial cells, which form the inner linings of the intestines and lungs and of the ductwork of the mammary and prostate glands. In 1999, Gerald Cunha and colleagues at UCSF showed that nonmalignant prostate epithelial cells grown in culture with prostate TAFs acquired the ability to form tumors when transplanted into mice. The researchers concluded that TAFs had undergone changes that resulted in their production



**Getting together.** Macrophages, attracted by CSF1 from tumor cells, in turn produce EGF, which both supports the growth of tumor cells and attracts tumor cells to the blood vessels, aiding cancer's spread.

CREDITS: CLOUDS HILL IMAGING LTD. PHOTO RESEARCHERS INC./A. MORRIS/SCIENCE SOURCE; CONSIDER ET AL./NATURE REVIEWS CANCER 1 (2003)



**Support system.** Promoting new blood vessel growth is one of many ways that tumor cells can make the microenvironment more hospitable to cancer.

of growth factors or other substances that can make cells cancerous.

Since then, cancer biologists have been finding that essentially all components of the tumor stroma contribute to cancer's growth and spread. This includes the cells involved in forming the tumor blood vessels, the focus of pioneering work begun more than 2 decades ago by the late Judah Folkman. More recently, the role of macrophages and other inflammatory cells in promoting cancer has come in for a lot of attention (*Science*, 5 November 2004, p. 966).

### Cancer stimuli

With the role of the microenvironment now well established, researchers are investigating how the various stromal components interact with cancer cells to promote growth and metastasis. "The question now is how do these things talk to each other," Werb says. Matrisian cautions, however, that answering that question won't be easy. "There's incredible complexity," she says. "For 35 years, we've been working on the tumor cells. Now we're adding five to six cell types."

One of the important communication molecules to emerge from this jumble is transforming growth factor- $\beta$  (TGF- $\beta$ ), a protein best known as a suppressor of tumor growth. About 4 years ago, Harold Moses and colleagues at Vanderbilt University School of Medicine provided evidence that TGF- $\beta$  doesn't have to act directly on can-

cer cells to inhibit their growth. As described in the 6 February 2004 issue of *Science* (p. 848), when the Vanderbilt team inactivated the receptor through which TGF- $\beta$  exerts its effects in mouse fibroblasts, the animals developed early signs of prostate cancer and also more advanced invasive carcinomas of the stomach.

Turning to a different form of cancer, Moses and his colleagues transplanted mammary carcinoma cells, together with the fibroblasts lacking the TGF- $\beta$  receptor, into mice. Those animals, Moses says, "got more aggressive cancers and many more metastases" than when normal fibroblasts were used. The altered fibroblasts appear to stimulate cancer growth by producing transforming growth factor- $\alpha$  and hepatocyte growth factor. Loss of the ability to respond to TGF- $\beta$  might therefore be one of the changes that cause fibroblasts to stimulate cancer growth.

The conspiracy hatched in the stroma does more than help cancer cells grow; it can also help them move—and metastasize. More than 20 years ago, a group of enzymes called the

matrix metalloproteinases (MMPs) came in for a lot of attention as researchers found that some of them could help cancer cells spread by breaking down the extracellular matrix (ECM) and other barriers that would otherwise hold the cells in place. This early work culminated in clinical trials conducted primarily in the 1990s to test whether MMP inhibitors could extend life in human patients. But the trials "were spectacular failures," says Matrisian, an early MMP pioneer.

Now, however, MMPs have been identified as mediators of the communication between tumors and their microenvironment. Matrisian and others have found that MMPs are largely produced by various stromal cells rather than by the tumor cells themselves. The enzymes can appear early in tumor development and may contribute to tumor growth and spread in several ways.

About 4 years ago, for example, work by Douglas Hanahan's team at UCSF implicated MMP-9 produced by macrophages in the so-called angiogenic switch: the activation of the machinery that produces the blood vessel tumors need to grow and metastasize. Working with a mouse model of cervical cancer, the researchers found that macrophages in the tumors began producing the enzyme just at the time new blood vessels began to form. In addition, the drug zoledronic acid, a nonspecific MMP-9 suppressor, inhibited angiogenesis and slowed tumor growth. Later research suggests MMP-3 inhibition results in suppression of the pro-angiogenic protein VEGF.

The finding that MMPs can work early to promote tumor progression may help explain why inhibitors of the enzymes worked so poorly in clinical trials: Therapy may have come too late for these patients who had advanced disease.

The MMP situation is complicated, however; not all of the enzymes foster cancer development. Matrisian and her colleagues have found that stroma-derived MMP-12 actually protects against the development of non-small cell lung cancer. And even MMP-9 can



**Trojan horses.** When carried in by MSCs, IFN- $\beta$  inhibits the growth of metastatic tumors in lungs (top row), whereas the interferon alone has little or no effect (second row) as shown by comparison to untreated controls (third row). Normal lungs are in the bottom row.

be protective very early in the development of melanoma tumors in mice, says Raghu Kalluri of Harvard's Beth Israel Deaconess

Medical Center in Boston. "We're not just talking about positive influences on tumor growth," Kalluri says. "Some cancers can be held in check by the stroma."

### More conspirators

Macrophages are apparently essential for the angiogenic switch. As Jeffrey Pollard and his colleagues at Albert Einstein College of Medicine in New York City reported in the 1 December 2006 issue of *Cancer Research*, the onset of the switch was greatly delayed in mouse mammary tumors that can't accumulate the cells. Indeed, in more than 40% of the animals with such tumors, the angiogenic switch had not been turned on by the time they were 16 weeks old; in all of the normal mice of that age, the tumors had progressed to advanced metastatic disease.

But macrophages and other inflammatory factors do more than just foment angiogenesis. They actively aid the cell movements that produce metastases. John Condeelis and his colleagues at Albert Einstein College of Medicine have devised methods that allow them to visualize cell movements in mammary tumors growing in live mice. Using these methods, the Condeelis team, working with Pollard's team, observed a few years ago that mammary tumor cells migrate very quickly along the fibers of ECM to blood vessels.

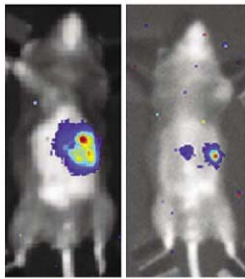
The Condeelis-Pollard team has found that tumor cells are called to the vessels by macrophages. The specific lure is epidermal growth factor, a protein produced by macrophages that can stimulate both the growth and the movement of cancer cells. More recently, the Condeelis-Pollard team showed that tumor cells escape into the blood vessels in direct association with macrophages. "They follow the macrophages like little trained dogs," is how Condeelis describes it. (The results appeared in the 15 March 2007 issue of *Cancer Research*.)

Macrophages are not alone in their ability to stimulate metastasis. Researchers have recently discovered that a group of immunosuppressive cells called MDSCs can promote cancer development (*Science*, 11 January, p. 154). Earlier this year, Moses and his colleagues found that these cells contribute to cancer spread. Inactivation of the gene for one of the receptors through which TGF- $\beta$  exerts its effects in mouse mammary tumor cells resulted, they found, in an influx of MDSCs that ended up primarily at the invasive edges of the tumors.

Moses and his colleagues identified what they consider to be a trigger for the influx: increased production of two

chemokines (SDF-1 and CXCL5) by the receptor-deficient mammary cancer cells. Drawn by the chemokines, MDSCs promote tumor metastases by producing at least three MMPs that stimulate the migration of cancer cells, presumably by digesting the extracellular matrix.

Several research groups have identified still another type of cell—the mesenchymal stem cell (MSCs)—as a prominent component of the tumor microenvironment. Last fall, a team led by Robert Weinberg of the Massachusetts Institute of Technology (MIT) in Cambridge reported evidence that these cells can also promote metastasis. The researchers injected mice with human breast cancer cells labeled with green fluorescent protein either with or without



**Aiding cancer spread.** Normal mice show much greater growth of liver metastases (left) than mice lacking the enzyme MMP-9.

MSCs. Mice given both cell types developed many more lung metastases—up to seven times more—than animals injected with only the cancer cells.

MSCs rev up the metastatic potential of the breast cancer cells by secreting the cytokine CCL5, which triggers a signaling pathway that sparks the cancer cells' migratory abilities. This change is not permanent, however. When the MIT team isolated cancer cells from lung metastases and injected them into new mice, the cells formed no more lung metastases than did the original cells injected without MSCs. "They're educated to be metastatic," Weinberg says. "But when they're moved, they forget that education." The discovery suggests that it might be possible to develop a therapy that blocks the metastatic changes.

There may be another way to enlist MSCs in the fight against cancer. Because the cells

concentrate in tumors, researchers are trying to turn them into Trojan horses. "Tumors recruit these cells from the circulation," says Frank Marini of the University of Texas M. D. Anderson Cancer Center in Houston. "That means we do have access to the tumor" through MSCs. It may be possible to use them to deliver drugs or cancer-fighting cytokines.

For example, Marini, working with M. D. Anderson colleague Michael Andreeff, has genetically engineered MSCs to produce interferon- $\beta$ . In mice carrying either melanoma or breast cancer tumors, the engineered cells proved much more effective at suppressing lung metastases and extending life than did simple injections of the interferon- $\beta$  protein. Mice given the protein by itself lived no longer than controls, whereas those that received the cells lived roughly twice as long as the controls. Marini hopes to begin clinical trials of the engineered cells in a year.

It may even be possible to control cancer growth by targeting the stroma rather than the cancer cells themselves. Hans Schreiber's team at the University of Chicago in Illinois has been trying to develop immunotherapies but, like other investigators in that field, has often been thwarted by cancer cells' propensity for losing their antigens. When that happens, they can escape detection by immune cells that have been trained to recognize them.

About a year ago, Schreiber and his colleagues showed that by targeting stroma cells, they could eradicate well-established tumors in mice even though the tumor cells expressed little antigen. The researchers first treated the tumors with local radiation or chemotherapy. Although this won't eliminate the tumors, it apparently killed enough cells so that their antigens were picked up by the stroma. Subsequent injection of killer T cells finished off both the stroma and the tumor cells, which apparently succumbed to a "bystander effect."

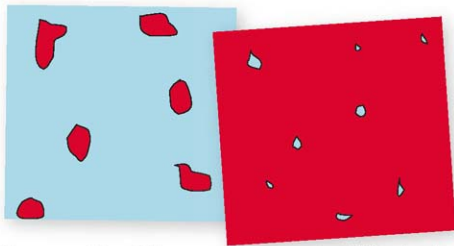
In a paper out last month in *Cancer Research*, the Chicago team reported that immune cells directed against the stroma alone halt tumor growth, although in this case, the tumor cells weren't killed. "When you just target the stroma, tumors stay in long-term equilibrium—close to a year—without relapse," Schreiber says.

At this point, it's too early to tell whether strategies directed at the stroma will pay off in better cancer therapies. But evidence is building that it will be necessary to corral the entire cancer gang to truly get the cancer problem under control.

—JEAN MARX

This article is Jean Marx's 610th in a 35-year career. Sadly, she has decided it will be her last as a staff writer.





## Magnetic Measurements Hint at Toaster Superconductivity

Twenty-two years after the discovery of high-temperature superconductors, theorists continue to disagree about how the complex materials conduct electricity without resistance at temperatures as high as 138 K. Meanwhile, experimenters are cranking out reams of intriguing data. At the meeting, Jeff Sonier of Simon Fraser University in Burnaby, Canada, reported evidence that superconductivity might persist in the materials to even higher temperatures—at least 200 K—albeit in tiny, disconnected patches.

The result implies that current materials may not have reached the ultimate limits, says Eduardo Fradkin, a theorist at the University of Illinois, Urbana-Champaign. “In principle, it seems that if you knew how to do it, you could get an even higher temperature superconductor,” he says.

In superconductors, electrons pair and the

pairs “condense” into a single quantum wave to flow without resistance. In a conventional superconductor, all this happens simultaneously when the material is cooled below a single “critical temperature.” Numerous experiments hint that things are more complicated in high-temperature superconductors. In those materials, electrons appear to pair at temperatures above the superconducting transition. The pairs then condense at the critical temperature, or so some theorists argue.

Sonier and colleagues are suggesting an even more tantalizing alternative. Their data indicate that at very high temperatures, the pairs do condense but into disconnected nanometer-sized puddles of superconductivity. Presumably, the puddles proliferate as the temperature decreases, and the free flow of current sets in when they overlap.

Evidence for such patchiness comes from

**Patchwork.** Islands of superconductivity (red, left) may grow and merge as temperature drops.

measurements of the magnetic fields within the materials. Sonier and colleagues fired subatomic particles called antimuons into samples of two different high-temperature superconductors—lanthanum strontium copper oxide and yttrium barium copper oxide—while they applied a strong external magnetic field. An antimuon acts like a little gyroscope whose axis sweeps around until the particle decays into a positron, which shoots out of the material in the direction the antimuon was pointing. How far the muon turns depends on the strength of the magnetic field at its position. By measuring the decay of many muons, the researchers found that the field varied dramatically within the materials, even at the highest temperatures they could measure.

Tiny patches of superconductivity could produce just such variations because they would expel the magnetic field, shoving it into the surrounding areas. The researchers performed checks to rule out other possibilities. For example, they “doped” the materials with more oxygen atoms to add electrical charges and found that the variations remained. That indicates that the effect is not produced by the magnetism of copper nuclei, which the mobile charges would obscure.

But although the patches may react unusually to the magnetic field, Sonier and colleagues have no direct proof that they contain coherent quantum waves, notes Ali Yazdani, an experimenter at Princeton University. “I would be a little bit cautious about claiming” that, he says. Still, last year, Yazdani used a device called a scanning tunneling

## Laser Plays Chemical Matchmaker

Typically, a molecule can break into several different combinations of fragments. In the past decade, physicists and chemists have exploited ultrashort pulses of laser light and the quirks of quantum mechanics to force molecules to split one way and not another. More recently, such “quantum control” schemes have also been used to manipulate the shapes of molecules. Now, Gustav Gerber, a physicist at the University of Würzburg, Germany, reports that he and colleagues have extended quantum control to the synthesis of molecules, too.

“I think it’s fair to say that he’s opened up a new direction,” says Herschel Rabitz, a chemist at Princeton University. But others question whether Gerber has truly manipulated the forming of chemical bonds.

Quantum control exploits the fact that, even when a molecule splits into specific fragments or twists into a particular shape, there’s more than one way to get from the beginning of the process to the end. That’s because the bonds between atoms in the molecule may break or stretch in different sequences to

arrive at the same result. In quantum theory, each sequence is described by an “amplitude,” and like waves, amplitudes can reinforce or cancel one another.

In fact, researchers can use a femtosecond-long pulse of laser light to make the amplitudes leading to the desired combination of fragments or shapes bolster one another and those for other outcomes add to naught. The trick is to apply an automated feedback system that tracks the molecules produced by each light pulse and then adjusts subsequent pulses’ properties to optimize the results, as Rabitz and a colleague proposed in 1992.

In 1998, Gerber and colleagues used the scheme to guide the cleaving of an organometallic molecule in a gas. Others have used quantum control in liquids to select one of several different molecular shapes, or “isomers.”

Now Gerber says his team has controlled the formation of chemical bonds as well. The researchers exposed a palladium surface to molecular hydrogen ( $H_2$ ) and carbon monoxide (CO) and zapped the surface with femtosecond pulses of laser light. That produced ions such as  $CH^+$ ,  $OH^+$ ,  $HCO^+$ , and  $H_2CO^+$ . When the researchers turned on the feedback, they found that they could

microscope to measure the pairing in barium strontium calcium copper oxide and found that it persisted in patches above the superconducting transition. That result jibes with Sonier's data, and Yazdani says, "It's nice to see things hanging together."

## Squeeze Play Makes Solid Helium Flow

Can ultracold, highly pressurized solid helium flow like the thinnest possible liquid? For 4 years, physicists have debated that question. Now, preliminary data from Robert Hallock of the University of Massachusetts (UMass), Amherst, and his team provide the most direct evidence yet for such flow.

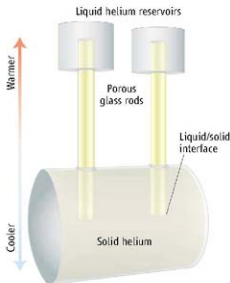
"It's a very, very clever experiment," says Moses Chan of Pennsylvania State University in State College. But all agree it hasn't solved the mystery of solid helium.

In 2004, Chan and Eunseong Kim, now of the Korea Advanced Institute of Science and Technology in Daejeon, South Korea, reported that crystalline helium appeared to flow through itself without resistance (*Science*, 1 July 2005, p. 38). They set a small can filled with solid helium twisting back and forth atop a thin metal shaft. At temperatures near absolute zero—below about 0.2 K—the frequency of twisting increased, suggesting that some helium had let go of the can and was standing stock-still while the rest moved back and forth. That implied that the helium was flowing through itself.

Others questioned Chan and Kim's interpretation of a flowing perfect crystal. Two years ago, John Reppy and Ann Sophie Rittner of Cornell University found that the effect went away if they gently heated and

cooled their solid helium to eliminate fault-like defects in the crystal (*Science*, 24 March 2006, p. 1693). That suggested that the flow involved the seeping of more conventional "superfluid" liquid helium along the defects.

A few months later, Sébastien Balibar of the École Normale Supérieure in Paris showed that crystalline helium could flow under the pull of gravity but only if it con-



**Throughput.** Physicists forced superfluid liquid helium through a solid squeezed too tightly to melt.

tained imperfections called grain boundaries (*Science*, 4 August 2006, p. 603). Balibar, however, studied solid helium held at its melting point and immersed in liquid. Under those conditions, the solid could contain macroscopic holes like those in Swiss cheese—and, other scientists noted, the flow could be produced not by atoms creeping through the solid but simply by liquid sluicing through the holes. Last November, Balibar reported in *Physical Review Letters*

that he had spotted such pipeline channels where grain boundaries meet the walls of the container holding the helium.

Hallock and colleagues devised a clever way to avoid that end run. They confined their solid helium in a cylindrical chamber. Two posts of glass riddled with nanometer-sized pores jutted into the chamber and connected it to reservoirs of superfluid liquid helium. The helium in the pores could only solidify at a much higher pressure than the helium in the chamber. So the arrangement enabled the team to inject superfluid liquid into a solid squeezed too tightly to melt.

The physicists applied a pressure difference between the two reservoirs of liquid and saw it decrease steadily over time. That shows that helium atoms flow through the chamber, says Nikolay Prokof'ev, a theorist at UMass who presented the data for Hallock. The atoms must move through the solid helium, he says, because "it's so far away from melting that liquid channels cannot survive."

Balibar is not so sure. Such channels remain open at pressures up to 35 times atmospheric pressure—far above the 25 atmospheres needed to solidify helium—says Balibar, who was not at the meeting but has seen the UMass data. However, Chan notes that one feature of the new experiment suggests that the flow isn't through large channels: The signal goes away when experimenters raise the temperature to 0.4 K. Higher temperatures ought to widen macroscopic channels; they should also eliminate superfluid flow along defects.

Oddly, although most physicists agree that the flow involves defects in the crystal, the new experiment shows flow only when the helium is solidified in a way that should reduce the number of imperfections. That puts another twist in the already convoluted tale of solid helium.

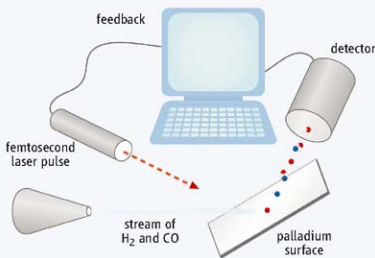
—ADRIAN CHO

increase the ratio of  $\text{CH}^+$  to  $\text{C}^+$  by a factor of 10 or boost the ratio of  $\text{CH}^+$  to  $\text{H}_2\text{O}^+$  by nearly as much. That shows that the laser pulses control the bonding of oxygen to hydrogen and carbon to hydrogen, Gerber says.

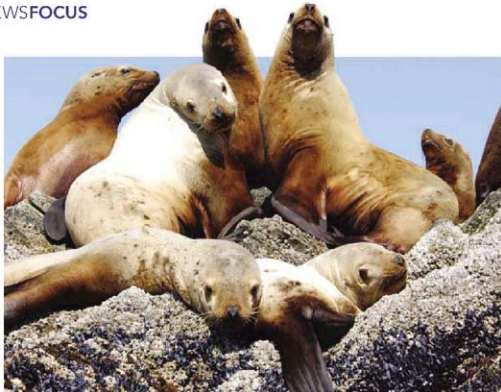
But the striking effect may have a simpler, less promising explanation, says Robert Levis, a physicist at Temple University in Philadelphia, Pennsylvania. Palladium makes an excellent catalyst, he notes, so the hydrogen and carbon monoxide may spontaneously form all sorts of compounds on the surface. "The alternative explanation is that there is this whole gemisch [of molecules] on the surface and that you're just selectively liberating them" by heating the surface with the laser pulse, Levis says.

Gerber counters that the laser must be doing something more, as the ability to alter the ratios goes away when he uses light with half the wavelength, which would also heat the surface. Rabitz says that although it's not clear precisely what's happening on the surface, the feedback appears to be working. "He's seeing a real controlled effect," Rabitz says. "What the mechanism is, that's an open question."

—A.C.







## CONSERVATION BIOLOGY

## Puzzling Over a Steller Whodunit

What plunged the North Pacific's Steller sea lions into a catastrophic decline, and why are numbers still low? After \$190 million worth of research, scientists aren't sure

Every other summer for more than a decade, biologists have boarded a twin-engine plane in Anchorage, Alaska, to skim above the rocky rookeries and haul-outs of one of the state's most endangered marine mammals: the massive Steller sea lion (*Eumetopias jubatus*). From the air, the team photographs mothers and pups to tally their populations, which took a horrific plunge some 30 years ago. The researchers hope to fathom an enduring mystery about these jeep-sized marine mammals: Why did their numbers plummet in the first place, and why is a population in southeastern Alaska recovering while numbers west of Prince William Sound stay very low? Most importantly to the state, which manages a billion-dollar fishery in these icy waters: Is the fishing industry to blame?

Now, after 16 years and \$190 million worth of studies (not to mention several lawsuits, charges of animal cruelty, and intense political attention), a team of scientists at the National Marine Fisheries Service (NMFS) in Seattle, Washington, has summarized various researchers' findings in the *Final Revised Steller Sea Lion Recovery Plan*. The 325-page document, released last month, updates a 1992 plan and will help guide NMFS's management of the sea lions.

Yet the 17-member team (which included

fishing industry representatives and environmentalists as well as scientists) was unable to solve the key mysteries behind the species' troubles, despite the generous pot of federal funds. Some scientists on the team say that the "consensus" document was anything but, with various factions arguing that the document doesn't go far enough in fingering the fishery and others complaining that alternative ideas were given too short shrift.

Still, the NMFS scientists involved say the document achieves what is needed to secure the future of the Steller sea lions, identifying a trio of most probable causes for the animals' ongoing problems. The chief suspects: competition with the fishery, which expanded by an order of magnitude at the time of the decline; environmental changes; and perhaps predation by killer whales. The *Plan* suggests possibly removing the eastern population (which is increasing at a healthy 3% a year) from the Endangered Species List but advises retaining the western population on the list at least until 2030. "The *Plan* defines recovery for a species thought to compete with a major fishery, which is a big deal in Alaska," says Douglas DeMaster, director of NMFS's Alaska Fisheries Science Center. "Some people have wanted to pin the sea lions' problems entirely on the fishery,

On the edge. Scientists aren't sure why Steller sea lions in the western Pacific are still struggling.

but the data [to do this] aren't as clear as some might expect."

### Plummeting populations

Steller sea lions, named for naturalist Georg Steller, who described them in 1741, numbered close to 250,000 in the North Pacific until the 1960s. Over the next 2 decades, their population declined by a staggering 80%. In 1990, they were declared threatened and placed on the federal endangered species list. Seven years later, the struggling western population, once the largest in the world, was declared endangered. It now numbers about 45,000, up from a nadir of 33,000. "But the birth rate is lower than expected," says DeMaster, "and our model predicts this population will begin to decline again." Curiously, the eastern population regained ground quickly, increasing by 225% over the last 25 years and establishing four new rookeries. Scientists remain as baffled by the discrepancy between the populations, which inhabit similar, heavily fished areas, as they are by the initial catastrophic plunge.

In 1992, researchers set out to test potential causes for the decline. They soon discovered that other marine species, including seals, sea otters, and diving sea ducks, had suffered similar precipitous drops. But, as with the sea lions, there was no single smoking gun. Some hypothesize that climate-driven changes in currents and ice cover altered the behavior, composition, or nutritional quality of the sea lions' prey. But others note that the sea lions, which have lived in the region for millions of years, must have weathered similar changes in the past and that proving such a broad-brush idea is unlikely. Other researchers have targeted killer whales, arguing that the orcas upped their take of Stellers after whale calves became scarce due to whaling, although evidence for this is controversial.

Humans are prime suspects too. "When a large, long-lived mammal [more than 15 years] declines that rapidly, you have to consider anthropogenic factors," says DeMaster. The team first thought that intentional shooting along with entanglement in fishing nets most likely triggered the initial decline. Before 1972, some 45,000 Stellers were killed in Alaska in legal harvests and predator-control programs. Until 1990, fishers were allowed to shoot interfering sea lions. But despite concerted efforts, "we couldn't confirm how many bullets flew,"

CREDIT: GARDEN J. GUNNISON, NATIONAL MARINE MAMMAL LIAISON, ALASKA FISHERIES SCIENCE CENTER, NMFS

says Shannon Atkinson of the University of Alaska, Fairbanks, lead author on a study trying to document these numbers in the April issue of *Mammal Review*.

Nor do scientists know how many sea lions ended up as by-catch or died entangled in fishing nets. Nevertheless, when the shooting stopped and netting practices changed, the eastern Steller sea lions recovered. But those in the west kept declining until 2000, when they eked out a slight increase.

### A problem of proof

Just before the sea lions' population plunge, another dramatic change occurred in their environment: NMFS upped the annual limits on the catch of groundfish—pollock, Pacific cod, and Atka mackerel—in the Bering Sea from 175,000 metric tons in 1964 to more than 1.5 million metric tons by 1972. That exponential increase turned the region into the world's largest commercial fishery; it annually trawls more than 1.4 million metric tons from the ocean, in a catch worth more than \$1 billion. This year's catch was reduced to 1 million metric tons because surveys found fewer maturing fish (*Science*, 21 December 2007, p. 1853).

Groundfish are Steller sea lions' primary prey. Researchers hypothesize that dwindling groundfish numbers—and perhaps sizes, as commercial operations take adult fish—mean that pregnant and nursing female sea lions are simply not getting enough to eat and so have fewer surviving pups.

"What is the impact on hunters like Steller sea lions and northern fur seals of removing 60% of their prey?" asks Timothy Ragen, a marine mammalogist and executive director of the Marine Mammal Commission in Bethesda, Maryland. "That's the hard and fundamental question, which still hasn't been fully addressed. ... It's a problem of proof."

"That's true," agrees NMFS marine mammalogist Lowell Fritz. "But the *Plan* says fishing is a 'potentially high threat' to recovery, which is of course controversial."

Indeed, the possible competition between sea lions and commercial fishers has been controversial for years. In 1998, environmental groups led by Greenpeace alleged in a lawsuit that NMFS had violated the Endangered Species Act by not assessing the groundfish fishery's effects on the sea lions. The judge hearing the case blocked trawlers from fishing in critical Steller sea lion habitat in the summer of 2000.

That's when Alaska's powerful Republican senator, Ted Stevens, stepped in. Then

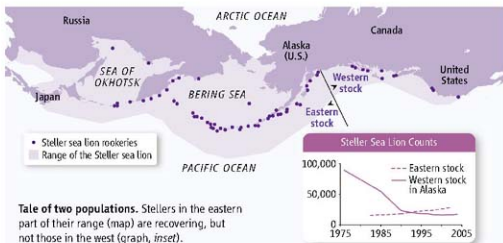
chair of the Senate Appropriations Committee, Stevens held up the entire federal budget for a week in December 2000 until he brokered a deal: The fishery would continue as long as fishers kept away from areas close to sea lion rookeries and haul-outs. Stevens argued that scientists had unfairly targeted the fishing industry when there were other possible causes for the sea lions' decline. In what some saw as a delaying tactic, he turned on the money tap, prodding Congress to approve the Steller Sea Lion Research Initiative. Congress gave scientists 13 topics to study, only one of which was the impact of the commercial fishery, and pumped in more than \$40 million in the first year. Since then, another \$150 million has poured in and more millions are promised.

Some researchers contend that the flood of money and the requirement to spend it

Statement, the Humane Society pounced. Its lawsuit halted several research programs on females. "It's tragic that we haven't been allowed to do this and don't have these data," says DeMaster. "It has not helped the recovery of Steller sea lions."

In 2009, NMFS will be allowed to reap for a research permit to put transmitter tags on adult females in the western population to find out where they are foraging and to collect blood and tissue samples from them. Those data may at last reveal whether the females are not getting enough to eat and so test the link between fishing and the Stellers' troubles.

Another way to investigate such a link is to compare sea lion health in fished and unfished areas. One \$200,000 study found that the Stellers' population had declined fastest in the most heavily fished areas,



**Tale of two populations.** Stellers in the eastern part of their range (map) are recovering, but not those in the west (graph, inset).

quickly on specific topics have watered down the research. DeMaster counters that "we've learned a lot about Steller sea lions' vital rates and food habits." But he concedes that they don't know why the western population has not recovered. "The key is their reproductive rate, which is lower and declining. And it's why we are concerned about the possible competition ... with the fisheries."

Still, DeMaster and others note that scientists have yet to prove a one-to-one relationship between the western population's fertility troubles and a presumed lack of prey. One reason: The scientists are not allowed to handle adult females, the result of a successful 2005 Humane Society lawsuit. "We don't have any data on the reproductive health of the females" in parts of the western region, says DeMaster. The Humane Society and Marine Mammal Commission have regularly questioned the NMFS scientists' practices of sedating and hot-branding pups in order to identify them. When NMFS failed to write a required Environmental Impact

Statement, the Humane Society pounced. Its lawsuit halted several research programs on females. "It's tragic that we haven't been allowed to do this and don't have these data," says DeMaster. "It has not helped the recovery of Steller sea lions."

Even without such data, next month NMFS will issue a draft Biological Opinion (BiOp) on the sea lions. "This is where the rubber meets the road," says Fritz. "The BiOp has to decide whether fishing, as currently allowed, is adversely affecting the recovery of the sea lions." Small adds that "because we don't understand the cause of the severe decline, or the prolonged decline that followed, we can't say that it won't happen again. ... So we have to find ways to assure that the population at least stabilizes." For Steller sea lions, even that would be good news.

—VIRGINIA MORELL



## LETTERS

edited by Jennifer Sills

## Conserving Top Predators in Ecosystems



THE NEWS FOCUS STORY "WOLVES AT THE DOOR OF A MORE dangerous world" (V. Morell, 15 February, p. 890) discusses whether the proposed delisting target for the Northern Rockies wolf population will ensure its long-term demographic and genetic viability. We would like to add that viability should not be the sole objective of a species-conservation plan. Another objective—often overlooked—should be to restore and maintain the ecological functionality of the species in its ecosystem.

Recent results from long-term research [including some following the wolf reintroduction in Yellowstone (1)] have shown that top predators can play some unexpected but nevertheless crucial roles in ecosystems. For example, by checking the densities of abundant generalist mesopredators, they can indirectly support species at lower trophic levels (2), and

by preventing irruptions of ungulate populations, they can help restore vegetation (3). Top predators can also buffer some effects of climate change (4), drive senescence of prey (5), and frame river channel dynamics (6).

Conservation plans for predators should take this broader view of ecological roles into account instead of focusing solely on a species' viability by numbers.

GUILLAUME CHAPRON, HENRIK ANDRÉN, OLOF LIBERG

Grimsö Wildlife Research Station, Swedish University of Agricultural Sciences, Riddarhyttan 73091, Sweden.

## References

1. C. C. Wilmer *et al.*, *J. Anim. Ecol.* **72**, 909 (2003).
2. C. N. Johnson, J. L. Isaac, D. O. Fisher, *Proc. R. Soc. London Ser. B* **274**, 341 (2006).
3. W. J. Ripple, R. L. Beschta, *Biol. Conserv.* **138**, 514 (2007).
4. C. C. Wilmer, W. M. Getz, *PLoS Biol.* **3**, 571 (2005).
5. S. M. Carlson, R. Hilborn, A. R. Hendry, T. P. Quinn, *PLoS ONE* **2**, e1286 (2007).
6. R. L. Beschta, W. J. Ripple, *Earth Surf. Process. Landforms* **31**, 1525 (2006).

## The Role of Fisheries-Induced Evolution

IN THEIR POLICY FORUM "MANAGING EVOLVING fish stocks," 23 November 2007, p. 1247, C. Jørgensen *et al.* propose evolutionary impact assessments (EvoIAs) as a general tool for managing evolving resources. The basis for their proposal is that fisheries-induced evolution (FIE) is the most important driver of changes in life-history characteristics of heavily exploited marine fishes. Although Jørgensen *et al.* give the impression that this is well established, the evidence supporting FIE unfortunately remains circumstantial and is

often open to alternative interpretations (1).

To make the case for EvoIAs, Jørgensen *et al.* present a selective set of studies—those concluding that FIE was a likely cause of the observed changes, after considering some environmental effects (see their table S2). In doing this, they excluded results that do not support their case [e.g., (2, 3)]. Furthermore, because FIE is often a matter of interpretation [e.g., (3, 4)] and the authors of the Policy Forum are strong advocates of FIE, the majority of the studies on life-history traits included in table S2 were their own. Their analysis does not represent a consensus opinion developed from critical scrutiny of the studies currently available.

Some component of phenotypic change is undoubtedly genetic and caused by fishing. The challenge remains to determine how important this is relative to other environmental and trophic drivers. A truly precautionary approach to fisheries management must allow for FIE in the longer term. However, EvoIA should be one of several tools used to address the many pressing problems facing fisheries managers.

HOWARD I. BROWMAN,<sup>1</sup> RICHARD LAW,<sup>2</sup>  
C. TARA MARSHALL<sup>3</sup>

<sup>1</sup>Austevoll Research Station, Institute of Marine Research, Storebø 5392, Norway. <sup>2</sup>Department of Biology, University of York, York YO10 5YW, UK. <sup>3</sup>School of Biological Sciences, University of Aberdeen, Aberdeen AB24 2TZ, UK.

## References

1. C. T. Marshall, H. I. Browman, *Mar. Ecol. Prog. Ser.* **335**, 249 (2007).
2. K. Morita, M. Fukunaka, *Evolution* **60**, 1516 (2006).
3. A. D. Rijnsdorp, R. E. Grift, S. B. M. Kraak, *Can. J. Fish. Aquat. Sci.* **62**, 833 (2005).
4. G. H. Engsthaler, M. Heino, *Mar. Ecol. Prog. Ser.* **272**, 245 (2004).

IN A RECENT POLICY FORUM, "MANAGING evolving fish stocks" (23 November 2007, p. 1247), C. Jørgensen *et al.* propose that evolutionary impact assessment should be adopted as a tool to manage evolving fish stocks. This is a well-motivated idea in principle, but their reasoning relies entirely on the assumptions that fisheries-induced evolution (FIE) occurs commonly and that it is an undisturbable fact. Neither of these assumptions is true. None of the studies of exploited fish populations in their article have provided genetic evidence for the observed phenotypic changes. Because evolution is by definition a change in the genetic constitution of a population, an evolutionary change cannot be postulated without demonstrating a genetic basis for the observed phenotypic shift. In fact, phenotypic changes in mean trait values due to simple environmental inductions are common (1), as are cases where populations are not evolving despite strong directional selection acting on heritable traits (2). Furthermore, several studies have shown that observed phenotypic shifts in exploited fish popula-



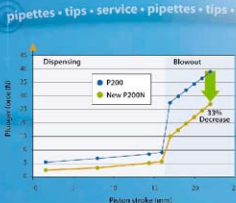
We are inclined to believe that some of the case studies listed in the Jørgensen *et al.* Policy Forum might indeed turn out to be cases of FFI if genetic data were to become available. However, until that proof is provided, the claims about FIE are nothing but "adaptive storytelling" (5). As pointed out by S. J. Gould and R. C. Lewontin three decades ago (5), unwillingness to consider alternatives to adaptive stories, reliance on plausibility as a criterion for accepting speculative tales, and failure to consider adequately competing themes are

Letters (~300 words) discuss material published in *Science* in the previous 3 months or issues of general interest. They can be submitted through the Web ([www.submit2science.org](http://www.submit2science.org)) or by regular mail (1200 New York Ave., NW, Washington, DC 20005, USA). Letters are not acknowledged upon receipt, nor are authors generally consulted before publication. Whether published in full or in part, letters are subject to editing for clarity and space.

While we agree with Kuperinen and Merilä that direct genetic evidence for FIE in the wild

Pipetman® has been the name of the world's most innovative pipette brand for more than 30 years and has become the world's best known pipette trademark. We are driven by the idea that quality, robustness and precision should always lead our way to delivering innovative pipettes to the scientific community around the world. Pipetman® Neo continues the tradition.

# Neo





is highly desirable and practically nonexistent, we must take issue with their claim that "an evolutionary change cannot be postulated without demonstrating a genetic basis for the observed phenotypic shift." This claim questions the fundamental assumption that scientists can make inferences about genotypes by studying phenotypes. It is worth remembering that Darwin formulated his theory of evolution with a similar assumption—that traits are heritable—nearly a century before DNA was found to carry hereditary information. Without such assumptions, evolutionary ecology could not operate. Moreover, Kuparinen and Merilä now seem to contradict their recent conclusion that "[t]heory, phenotypic observations and modelling studies all suggest that fisheries are capable of inducing evolutionary changes in life histories in harvested populations" (2).

Like Kuparinen and Merilä, we look forward to the day when direct genetic evidence can decisively determine the extent of FIE. At a practical level, however, traits affected by FIE are likely polygenic and involve unexplored genotype-to-phenotype relations. Even where changing allele frequencies are found, it might take a long time before such changes

are robustly linked to phenotypic effects.

FIE is not a universal explanation for phenotypic changes in harvested fish populations. The importance of FIE relative to other processes that induce phenotypic change will need to be evaluated case by case. One must expect, as Kuparinen and Merilä suggest, that sometimes "observed phenotypic shifts in exploited fish populations are fully consistent with simple environmentally induced changes." For this reason, researchers of FIE have made considerable efforts to account for environmental effects and phenotypic plasticity before ascribing residual trends to FIE (e.g., (3)). Of the two studies Kuparinen and Merilä highlighted, one kept open the possibility of FIE (4), while the other even concluded that FIE played a role (5).

Kuparinen and Merilä also refer to a famous argument from the 1970s (6) that did not stand up to scrutiny (7) and had few implications for mainstream evolutionary biology. Furthermore, Kuparinen and Merilä overlook the many, mutually complementary sources of evidence for FIE: expectations from life-history theory and quantitative evolutionary models of exploited fish; statistical analyses

of scientific-survey and fisheries time series that consider phenotypic plasticity; comparative studies of populations experiencing different fishing pressures; demonstrations of FIE in laboratory experiments; and successful engineering of life-history traits in breeding programs. Together, this is much more than "adaptive storytelling."

CHRISTIAN JØRGENSEN,<sup>1,\*</sup> KATJA ENBERG,<sup>1,2</sup> ERIN S. DUNLOP,<sup>2,3</sup> ROBERT ARLINGHAUS,<sup>3,4</sup> DAVID S. BOUKAL,<sup>2,3</sup> KEITH BRANDER,<sup>5</sup> BRUNO ERNANDE,<sup>6,7</sup> ANNA GÄRDMARK,<sup>8</sup> FIONA JOHNSTON,<sup>7,9</sup> SHUICHI MATSUMURA,<sup>7,3</sup> HEIDI PARDOE,<sup>9,10</sup> KRISTINA RAAB,<sup>11</sup> ALEXANDRA SILVA,<sup>12</sup> ANSSI VAINIKKA,<sup>8</sup> ULF DIECKMANN,<sup>7</sup> MIKKO HEINO,<sup>2,3,7</sup> ADRIAAN D. RIJNSDOORP<sup>13</sup>

<sup>1</sup>Department of Biology, University of Bergen, N-5020 Bergen, Norway. <sup>2</sup>Institute of Marine Research, Bergen, Norway. <sup>3</sup>Department of Biology and Ecology of Fishes, Leibniz-Institute of Freshwater Ecology and inland Fisheries, Berlin, Germany. <sup>4</sup>Humboldt-University of Berlin, Institute of Animal Sciences, Berlin, Germany. <sup>5</sup>DTU-Aqua, Charlottenlund, Denmark. <sup>6</sup>Laboratoire Ressources Halieutiques, Institut Français de Recherche pour l'Exploitation de la Mer (IFREMER), Port-en-Bessin, France. <sup>7</sup>Evolution and Ecology Program, International Institute for Applied Systems Analysis (IIASA), Laxenburg, Austria. <sup>8</sup>Institute of Coastal Research, Swedish Board of Fisheries, Öregrund, Sweden. <sup>9</sup>Marine Research Institute, Reykjavik, Iceland. <sup>10</sup>University of Iceland, Institute of

Same quality. Same price. Lower spring forces.



800-445-7661  
www.pipetman.com



Gilson, Inc. | 3000 Parmenter Street | Middleton, WI 53562-0027, USA | Tel: 800-445-7661 | Fax: 608-821-4403

Biology, Sturlugata 7, Reykjavik, Iceland. <sup>11</sup>Wageningen Institute for Marine Resources and Ecosystem Studies (IMARES), IJmuiden, Netherlands. <sup>12</sup>INRA-IPIMAR National Institute for Agriculture and Fisheries, Lisboa, Portugal.

\*Author for correspondence. E-mail: christian.jorgensen@bio.uib.no

#### References

1. J. A. Hutchings, D. J. Fraser, *Mol. Ecol.* **17**, 294 (2008).
2. A. Kuparinen, J. Merilä, *TREE* **22**, 652 (2007).
3. U. Dieckmann, M. Heino, *Mar. Ecol. Prog. Ser.* **335**, 253 (2007).
4. K. Morita, M. Fukuwaka, *Mar. Ecol. Prog. Ser.* **335**, 289 (2007).
5. S. B. H. Kaak, *Mar. Ecol. Prog. Ser.* **335**, 295 (2007).
6. S. J. Gould, R. C. Lewontin, *Proc. R. Soc. London Ser. B* **205**, 581 (1979).
7. D. C. Dennett, *Darwin's Dangerous Idea* (Penguin, London, 1995), chap. 10.

## Tips for NIH

THERE ARE TWO USEFUL THINGS THE NIH could do to disseminate science information. First, NIH could ensure that every NIH-funded study had to produce some public report. This would provide an outlet for results that had not been published through conventional channels within a reasonable time. Second, NIH could make

publicly available the raw data of all funded studies, within a reasonable time after the end of funding, and with all appropriate documentation and protection of confidentiality. Instead, the NIH chooses to require collection and redundant dissemination of already-published articles and to provoke copyright battles between scientists and journals, such as those discussed in J. Kaiser's News of the Week story, "Uncle Sam's biomedical archive wants your papers" (18 January, p. 266). Future historians of science may wonder what we were thinking.

MIKEL AICKIN

Department of Family and Community Medicine, University of Arizona, Tucson, AZ 85724, USA.

## CORRECTIONS AND CLARIFICATIONS

**Random Samples:** "Genes and humor" (21 March, p. 1595). The item confused the data and conclusions of two studies. The 2008 Twin Research and Human Genetics study of U.K. twins involved close to 2000 twin pairs, not 456 as reported. The 2008 Personality and Individual Differences study covered 456 U.S. twin pairs. In addition, the U.K. study showed substantial heritability for negative as well as positive humor styles, while genetic effects for negative humor in the U.S. sample were not significant.

**Table of Contents:** (14 March, p. 1449). In the description of the Report "Amyloid fibrils of the HET-s(218-289) prion form a  $\beta$  selenoid with a triangular hydrophobic core" by C. Wamser et al., "yeast prion" should have been "fungal prion."

**News of the Week:** "\$300 million in private money for new investigators" by J. Kaiser (14 March, p. 1469). The statement that the new HHMI awards for early career scientists are "twice the size of an NIH R01 grant" could be misinterpreted. The research portion of the HHMI award rises over 6 years from \$150,000 per year to \$300,000 per year, which is roughly equal to the average NIH R01 grant. The remainder is for salary, benefits, and funds paid to the host institution to cover occupancy costs for the scientist's space.

**News of the Week:** "Physicist wins open Illinois seat" by E. Kintisch (14 March, p. 1470). The article incorrectly described the position of the previous holder of the seat, Representative Dennis Hastert (R-IL). He was Speaker of the House.

**News Focus:** "Dueling visions for a hungry world" by E. Stokstad (14 March, p. 1474). Emile Frison's institution is named Bioversity International, not Biodiversity International.

**Editors' Choice:** "Picking O over N" (29 February, p. 1163). The doi for the referenced paper should have been 10.1021/az11349r. The complete citation for the paper is T. Ohshima, T. Iwasaki, Y. Maegawa, A. Yoshiyama, K. Mashima, *J. Am. Chem. Soc.* **130**, 2944 (2008).

**Random Samples:** "Mastodon on the block" (1 February, p. 551). The article stated that all male mastodons had four tusks. In fact, in some adult male mastodons there is no evidence of lower tusks.

## Lambda DG-4 High-speed wavelength switcher

### Intense!

And versatile! The Lambda DG-4 offers real-time video and dual wavelength ratio imaging with uniform spatial illumination and integral neutral density filtering.

#### Features:

- Up to 4 interference filters (5 available on DG-5)
- 1 msec filter to filter switching
- Pre-aligned 175W xenon light source
- Programmable attenuation for each filter
- Adaptable to most microscopes



SUTTER INSTRUMENT

PHONE: 415.883.0128 | FAX: 415.883.0572

EMAIL: INFO@SUTTER.COM | WWW.SUTTER.COM

## YOUNG INVESTIGATOR AWARD

The Society for Neuroscience is pleased to announce the Call for Nominations for the Young Investigator Award to recognize a young neuroscientist's outstanding achievements. The award is presented at the Society's annual meeting to a young scientist who has received an advanced professional degree within the past 10 years. The award is \$15,000.



Deadline for nomination packages:  
Monday, April 28, 2008.

For more information about this award,  
please visit [www.sfn.org/yaia](http://www.sfn.org/yaia).

## SOCIOLOGY

## Confronting Violence Face to Face

David D. Laitin

Social science research on violence has flourished since the mid-1980s, when the Harry Frank Guggenheim Foundation (HGF)—whose basic mission has been the study of dominance, aggression, and violence—changed its strategy. Turning from support for biology (in the search for the chemical sources of violence), where the returns to investment were disappointing, the foundation funded work investigating the social bases of violence.

In *Violence*, Randall Collins makes an important contribution to this literature, but not by extending theories associated with the HGF initiative. These theories built on field work observations and statistical analysis of data, seeking to understand the sources of variation in the production of violence—for example, differentiating cases of civil wars with both high and low levels of violence (1, 2). Ignoring that work, Collins (a sociologist at the University of Pennsylvania) extends a microsociological research program only indirectly concerned with violence into a new substantive realm.

Microsociology focuses not on grand causal factors such as societal modernization but rather on the everyday methods ordinary folk use to get through daily interactions smoothly (and, by so doing, to produce social order). Collins builds on the work of Erving Goffman, the brilliant founder of interactional sociology, who cataloged the tactics for successfully escaping humiliation during the uncountable incidents that people weather in their daily lives (3). Goffman and his successors have not previously focused on explanations of violence (4), so Collins's application of microsociological techniques to examine violence provides a fresh outlook on violence in everyday life.

Collins's starting point is the observation that humans are not good at conflictual interactions at a face-to-face level. From readings in psychology and empirical accounts of violent interactions, he infers that humans

encounter a barrier of confrontational tension in conflict situations and that for violence to erupt, those who are not psychically injured from confrontational fear must find a pathway around that barrier. The pathways include attacking a physically or emotionally weak victim, performing in front of an audience that provides emotional support, and belonging to a violence-enforcing organization (a product of civilization) that makes its members pay heavy costs for refusing to surmount confrontational barriers. Even though sophis-

**Violence**  
A Micro-sociological Theory  
by Randall Collins  
Princeton University Press,  
Princeton, NJ, 2008. \$79 pp. \$45,  
£26.95. ISBN 9780691133133.



ticated armies have a difficult time inducing soldiers to kill, Collins provides evidence that as violence-enforcing organizations, they are best at overcoming confrontational fear.

Most everyday violence is episodic and rarely sustained. A common form is typified by episodes of "forward panic," in which the weak are mercilessly attacked. Here, tension and fear drive people into a breakdown of constraint. Collins takes readers through a dangerous police chase to exemplify this pathway,

and we see how the supercharged pursuers, once they have their victim, release their tension in a paroxysm of gratuitous violence.

Collins's examples of everyday violence abound. In contradiction to the representations in the movies, we see that real instantiations of human violence are short, usually ineffective, and rare. Even serial killers spend nearly all their time in a nonviolent state. Collins infers from an accumulation of vignettes that humans are hard wired to abjure combat. This inference ignores the rational foundations of intraspecies nonviolence as theorized by biologists such as John Maynard

Smith and Richard Dawkins (5, 6). Nonviolence for them is learned behavior that sustains an evolutionarily stable equilibrium. Their rational models seem far more compelling than an ad hoc assumption about human wiring.

Nonetheless, the payoff from microsociology is high, as its adherents highlight the obvious, that which is often missed in highly abstracted sociological theories. Collins observes inter alia that today, due to lack of audience support, American sports fans (unlike Europeans) don't provoke violence through hurling racial epithets at a rival team's black players; that suicide missions attract a distinct personality type (those who fear interpersonal confrontations) in contrast with combat missions; and that fair fights are fought in view of audiences, whereas unfair fights typically avoid public viewing.

In more direct support of his theory, photos of gang scenes reveal most gang members huddled on the periphery, too scared to punch or be punched. Soccer hooligans are in truth far more bluff and bluster than predators running amok. When violence does erupt, people in these situations are embarrassingly incompetent at combat and are more likely to run from the scene than to pursue their fight.

Although these observations are insightful, sticking to one's microsociological guns has its costs. Take Collins's stunning observations of tension and fear "entraining" pursuers into "tunnels" that leave them no escape from unmitigated violence. Examples from English troops at the battle of Agincourt, the Kent State killings amid the Vietnam protests, and the Los Angeles police in the capture of Rodney King are vivid. But suspicions are raised. What are the coding rules for the presence of this

The reviewer is at the Department of Political Science, 100 Encina Hall, Stanford University, Stanford, CA 94305-6044, USA. E-mail: daitin@stanford.edu



panic? (In the Kent State case, the high ratio of shots fired to casualties leads Collins to infer that the National Guard was in such a panic, but this rule is hard to generalize, as you would need to control for the difficulty of hitting the target.) If we examined a large number of militia assaults, would the level of gratuitous violence be greater where forward panic was present? Controlling for the symmetry of force levels, how much more violence can we expect if the perpetrators of the violence suffer from forward panic? Are panics observationally distinguishable from the appearances of frenzy that Caesar sought, in the battles against Pompey, to instill in his troops to signal commitment? And if capture of the enemy after high levels of tension and fear can lead to "post-victory letdown," the theory can explain both heightened violence and quiescent relaxation. With both high and low levels of violence predicted by theory, it cannot be disconfirmed. Although he piles up example after example—and despite incessant repetitions, they make for riveting reading—Collins never addresses these difficult issues of theory confirmation.

The range of conditions under which the author's theory applies is vague. The theory is one of face-to-face confrontation.

Because such conditions hold for nearly all of human history, we can see how confrontational tension has culturally evolved to make us bad at violence more generally. Collins's framework also helps us make sense of why long-distance violence (for example, dropping bombs from 35,000 feet) would not be subject to the cultural constraints he highlights in the book. Yet the African genocides in Rwanda and Darfur, which were taking place at the time the research for the book was conducted, are ignored. In his one mention of the 1994 Rwanda genocide, Collins claims that this sustained violence was due mostly to deliberate orders from higher authority and can therefore be blamed on civilization. This is partly true, but the sustained and sadly competent killings did have a face-to-face quality (often neighbor on neighbor) that doesn't follow from Collins's theory. Rwanda in 1994 certainly did not have the modern organizational apparatus that the Nazis had to reduce confrontational fear. In short, even if the theory is intended for face-to-face conditions, clearer limits need to be set or else the unspeakable surfeit of violence in Rwanda and Darfur cannot so easily be written off.

The theory itself, without any formalization of its propositions, allows for contradic-

Visit our Books *et al.* home page  
[www.sciencemag.org/books](http://www.sciencemag.org/books)

tory claims to slip through unacknowledged. We are told that it is an entertainment myth to think of killers smiling as they rampage since they are typically weighed down by fear. But elsewhere we read of the "joy" involved in ethnic rioting. Forward panic is said to lead to overkill, but some of the same emotional background occurs with fighter pilots, for whom the violence is self-limiting. Collins's theory of violence is based on fear and tension, but to explain the absence of combatant violence in tennis he points to low levels of anger, a variable that has no place in the causal theory. Although terms such as "entrainment" and "tunnels" are neat metaphors that help us picture how violence-fearing individuals become grotesque killers—even if reading about "pits" inside "tunnels" while being "entrained" makes the process hard to picture—a formalized model of the conditions to lead folk down different paths would allow testing and refinement of the provocative perspective Collins offers in the book. Such formalizations have led Maynard Smith and his followers to "hawk-dove" games. These indeed describe a nonviolent equilibrium, but they also can specify the conditions for off-the-equilibrium-path violence. Had Collins subjected his data to such formal analysis, the conditions under which pathways to violence are traveled would be more clearly mapped.

The bedrock of the behavioral sciences remains observation. Despite the isolation of the author's microsociology from statistical and formal analyses and the failure to specify the conditions under which the theory applies, Collins's *Violence* is a sourcebook for the oft-ignored and usually unseen obvious: We humans are bad at violence, even if civilization makes us a bit better at it.

## BROWSINGS

**Four Laws That Drive the Universe.** Peter Atkins. Oxford University Press, Oxford, 2007. 141 pp. \$19.95, £9.99. ISBN 9780199232369.

In the 19th century, considerations of the behavior of ideal steam engines led to the recognition of four fundamental laws: If two thermal systems are in equilibrium with a third, they are in equilibrium with each other. The internal energy of an isolated system is constant. Any spontaneous change increases the entropy of the universe. No finite number of steps can cool a body to absolute zero. Atkins's presentation of these four laws stresses the logical and physical structure of classical thermodynamics—the world of macroscopic, isolated, near-equilibrium systems. His engaging account is almost free of equations, but the lucid text and clear figures offer readers a firm understanding of energy and entropy.

**Symmetry. A Journey into the Patterns of Nature.** Marcus du Sautoy. Harper, New York, 2008. 384 pp. \$25.95, £27.95. ISBN 9780060789404. **Finding Moonshine. A Mathematician's Journey Through Symmetry.** Fourth Estate, London, 2008. 384 pp. £18.99. ISBN 978000714617.

The author (an Oxford professor known for his radio and newspaper presentations of mathematics to the general public) weaves this engaging and informative account from three strands. The personal describes his research, his interactions with colleagues, and his own life. The problem that has obsessed him is far from famous, and the book offers a realistic picture of what it is like to be a mathematician. The historical strand follows group theory from its origins in the early 19th-century work of Niels Abel and Évariste Galois to the 1980s completion of the classification of finite simple groups. The third strand comprises the mathematics itself. Du Sautoy provides elementary but accurate explanations of the basic concepts of symmetry and groups. Early in the book, readers are introduced to the "monster," the largest of the 26 "sporadic" groups, whose representation requires a 196,883-dimensional space. Close to the end, they find "moonshine"—the name John Conway gave to the connection between the monster and the sequence of numbers in the modular function.

## References and Notes

1. S. N. Kalyvas, *The Logic of Violence in Civil War* (Cambridge Univ. Press, Cambridge, 2006).
2. J. M. Weinstein, *Inside Rebellion: The Politics of Insurgent Violence* (Cambridge Univ. Press, Cambridge, 2007).
3. For a comprehensive treatment of the move from macro to microsociology and the works of Goffman, see R. Collins, *M. Makowsky, The Discovery of Society* (Random House, New York, 1972), ch. 11, ch. 13.
4. Jack Katz is one of the few microsociologists who has investigated violence, as in J. Katz, *Seductions of Crime: Moral and Sensual Attractions in Doing Evil* (Basic, New York, 1988).
5. J. Maynard Smith, in *On Evolution*, J. Maynard Smith, Ed. (Edinburgh Univ. Press, Edinburgh, 1972), pp. 8–28.
6. R. Dawkins, *The Selfish Gene* (Oxford Univ. Press, Oxford, 1976).

10.1126/science.1156187

## PUBLIC HEALTH

# A Case Study of Personalized Medicine

S. H. Katsanis, G. Javitt, K. Hudson\*

Personalized medicine through pharmacogenetics promises to revolutionize health care by harnessing individual genetic information to improve drug safety and efficacy. Under a personalized medicine scheme, drug prescribing and dosing no longer would be “one size fits all” but would be carefully tailored to a patient’s individual genetic variants. To date, there have been only a few genetic biomarkers whose clinical validity in predicting drug response has been clearly established: HER2-positive breast cancer as a predictor of response to the drug Herceptin being perhaps the best known. However, some foresee the emergence of many more such tests (1).

Pharmacogenetic testing presupposes the availability of validated genetic tests, i.e., tests for which there are data linking the presence or absence of specific variants with a specific outcome, such as improved therapeutic response or reduction in adverse events (see figure). Furthermore, it requires that information about the connection between genetic variation and drug response is accurately and truthfully communicated to both health-care providers and patients. As the case study below describes, several barriers currently impede the success of personalized medicine. Today, there is no mechanism to ensure that genetic tests are supported by adequate evidence before they are marketed or that marketing claims for such tests are truthful and not misleading. Misleading claims about tests may lead health-care providers and patients to make inappropriate decisions about whether to test or how to interpret test results (2). Misleading marketing claims are particularly troubling when tests are sold directly to consumers (DTC), because there is no health-care provider to serve as a “gatekeeper” to prevent inappropriate test ordering or misinterpretation of test results (2). For example, a patient informed of his or her cytochrome P-450 (CYP450) profile might independently change the dose of antidepressant medication with adverse health outcomes. The current situation also could lead both providers and

patients to lose trust in the value of genetic testing to improve drug-prescribing decisions (3, 4).

## CYP450 Genetic Testing for SSRIs

Many drugs, including the commonly prescribed class of antidepressants, selective serotonin reuptake inhibitors (SSRIs), are either metabolized by CYP450 enzymes or inhibit the activity of these enzymes (5, 6).



Genotyping of variants in the CYP450 genes can be used to predict the metabolizing strength of the cytochrome enzymes, defined as ultrarapid, extensive, intermediate, or poor. In theory, the profile of genotypic variants can be used to determine a dosage specific to a patient more efficiently than the traditional trial-and-error approach (7, 8). An individual's genotypic profile also may predict whether a particular medication interferes with the activity of another prescribed medication. Hence, there has been interest in genotyping CYP450 genes as a means to better guide SSRI prescribing and dosing. A CYP450 genotyping test cleared by the U.S. Food and Drug Administration (FDA) is available for two genes.

Marketing of unproven tests shows the need for regulatory action to protect public health.

In Fall 2004, the Centers for Disease Control and Prevention (CDC) commissioned an independent, nonfederal expert panel, the EGAPP (Evaluation of Genomic Applications in Practice and Prevention) working group, to examine the validity and utility of genotyping for SSRI prescription. The review of the evidence found convincing data that SSRIs are metabolized by and inhibit the function of CYP450 enzymes and that polymorphisms in

CYP450 enzymes are associated with the function and strength of SSRI metabolism (7, 9). However, EGAPP found “no evidence was available showing that the results of CYP450 testing influenced SSRI choice or dose and improved patient outcomes...” (9). EGAPP's conclusion “discourages use of CYP450 testing for patients beginning SSRI treatment until further clinical trials are completed” (9).

Despite the EGAPP conclusions, at least 15 businesses currently offer CYP450 genotyping services, with four companies making specific claims about the benefit of such testing for SSRI prescribing or dosing. Seryx and DNA Direct outsource the test to LabCorp and provide only interpretation of the genotypes, whereas

Genelex provides both the test and interpretation. Both DNA Direct and Genelex offer this test DTC, rather than through a medical provider. All four businesses offer CYP450 genotyping services for a range of pharmaceuticals, not only antidepressants. Some Web sites make explicit claims about the utility of CYP450 testing for particular drugs, such as the claim by Genelex that pharmacogenetic testing is “required to effectively prescribe Paxil” (10). Other Web sites are less direct, including information about SSRIs within tables that describe the relations between CYP450 genes and a number of different medications (11–13). Among the four Web sites surveyed, there were inconsistencies regarding which genes are genotyped for each

Genetics and Public Policy Center, the Johns Hopkins University, Washington, DC 20036, USA.

\*Author for correspondence. E-mail: khudson5@jh.edu

of five SSRIs, a finding that shows the lack of consensus within the community as to what genes are relevant to test for each SSRI. This lack of consensus is likely confusing to both patients and doctors.

### Current Regulatory Environment

In most states, laboratories are not required to demonstrate clinical validity before offering new genetic tests to health-care providers and the public. Although clinical laboratories must be certified under the Clinical Laboratory Improvement Amendments of 1988 (CLIA) (14), laboratories do not have to demonstrate the clinical validity of the tests they provide to obtain certification. In addition, although FDA regulates manufactured test kits as medical devices, FDA does not regulate most laboratory-developed tests (LDTs). In the case of CYP450 testing, a laboratory may purchase the Roche Amplichip, which is regulated by FDA as a medical device, or it may create an LDT for CYP450 that receives no FDA scrutiny.

Perhaps an even more relevant limitation is that FDA's oversight is limited to the specific uses for which the manufacturer intends the device. Thus, if the manufacturer does not claim that the test is beneficial in selection and dosing of SSRIs, FDA does not require clinical evidence of such benefit from the manufacturer. In the case of the Roche Amplichip test, for example, the intended use cleared by FDA does not refer to any specific drug, but rather states that information about the CYP2D6 and CYP2C19 genotypes "may be used as an aid to clinicians in determining therapeutic strategy and treatment dose for therapeutics that are metabolized" by products of these genes (15).

Although FDA could, in theory, require manufacturers to demonstrate a test's efficacy for a specific intended use (e.g., CYP450 testing for fluvoxamine) as a condition of test approval, the agency instead has cleared CYP450 tests without clinical studies demonstrating that using these tests is beneficial in the selection or dosing of any particular SSRI. This is consistent with FDA's approach to some other diagnostic devices (such as magnetic resonance imaging machines), where it has left determinations of clinical validity and utility to clinicians and payers.

Finally, although the Federal Trade Commission Act prohibits businesses from making false or misleading claims about their products, the Federal Trade Commission (FTC) has not undertaken enforcement activities against false and misleading claims made by genetic test providers. In July 2006, in response to a U.S. Government Accountability Office investigation and subsequent Senate

hearing on the value of genetic tests sold directly to consumers, FTC issued a consumer alert publicizing the questionable claims made for some DTC genetic tests (16). As described in this case study, this indirect approach has had no apparent effect on the availability of tests with questionable clinical validity.

### Policy Options and Prospects

Federal advisory committees, lawmakers, and stakeholder groups have made recommendations about enhancements in the oversight of genetic testing (17–23) and the Department of Health and Human Services has made "ensuring that genetic tests are accurate, valid and useful" a critical element of its personalized health-care initiative (24). However, to date, the government has not taken meaningful steps to enhance the oversight of genetic testing. Three key policy changes are needed.

**Enhanced enforcement by FTC in oversight of misleading claims.** FTC has the authority to prohibit misleading advertising claims, but enforcement of this authority with respect to genetic tests has not been a priority for the agency. FTC should use the data analysis generated by EGAPP and others to take decisive action against companies making false or misleading claims about the benefit of genetic testing.

**Development of a mandatory registry.** Those offering genetic tests, whether DTC or through health-care providers, should first be required to submit information about the test and data supporting the intended use of the tests to a registry that would be accessible to the public. The availability of this information would aid doctors and patients in test selection and interpretation and afford a degree of transparency that currently is absent from the genetic-testing marketplace. Stakeholders representing industry, patients, and consumers support the development of a genetic test registry (17–19).

**FDA oversight of LDTs.** When the results of a genetic test will be used to take specific action regarding drug selection or dosing, FDA should first ensure that the test accurately and reliably detects a variant that correlates with drug response and that the claims made by those selling the test are supported by the evidence. Such review is essential for public health protection whether the test in question is based on a "test kit" or an LDT; FDA's review thus should not depend on the testing platform used by the laboratory. Expanding FDA to include those tests that will form the bedrock of personalized medicine will better protect the public against tests that lack adequate evidence of clinical benefit and whose

use could lead to selection of ineffective medications, adverse drug reactions, or failure to take a drug that would be effective.

At this early stage of personalized genomic medicine, it is essential to be certain that the regulatory infrastructure is tailored in a manner beneficial to public health.

### References and Notes

1. S. B. Shurin, E. G. Nabel, *N. Engl. J. Med.* **358**, 1061 (2008).
2. L. L. McCabe, E. R. McCabe, *Genet. Med.* **6**(1), 58 (2004).
3. D. J. Hunter, M. J. Khoury, J. M. Drazen, *N. Engl. J. Med.* **358**, 105 (2008).
4. K. Hudson et al., *Am. J. Hum. Genet.* **81**, 635 (2007).
5. H. P. Eugster, M. Probst, F. E. Würgler, C. Sengstag, *Drug Metab. Dispos.* **21**, 43 (1993).
6. P. Wei et al., *Nature* **407**, 920 (2000).
7. D. B. Matchar et al., *Evid. Rep. Technol. Assess. (Full Rep.)* **1**(46), 1 (2007).
8. D. R. Nelson et al., *Pharmacogenetics* **14**, 1 (2004).
9. EGAPP, *Genet. Med.* **9**, 819 (2007).
10. Genetix Corporation, "Pharmacogenetics of Paxil (paroxetine)" (Genetix Corp., Seattle, WA, 2007); [www.healthanddrug.com/professional/paxil.html](http://www.healthanddrug.com/professional/paxil.html), accessed 19 November 2007.
11. Laboratory Corporation of America, Inc., "LabCorp capsule: Cyclochrome P450 2D6 and 2C19" (LabCorp, Burlington, NC, 2006); [www.labcorp.com/pdf/gen\\_labcapsule\\_CYP450\\_2D6\\_2C19.pdf](http://www.labcorp.com/pdf/gen_labcapsule_CYP450_2D6_2C19.pdf), accessed 19 November 2007.
12. DNA Direct, Inc., "Drugs to test for" (DNA Direct, San Francisco, CA, 2007); [www.dnadirect.com/patients/test/drug\\_response/drugs\\_to\\_test\\_for.jsp](http://www.dnadirect.com/patients/test/drug_response/drugs_to_test_for.jsp), accessed 19 November 2007.
13. Serxys, Inc., "Drug Gene Report" (Serxys, Montreal, Quebec, Canada, 2007); [www.signaturgenetics.com/public/411.html#21112](http://www.signaturgenetics.com/public/411.html#21112), accessed 19 November 2007.
14. Clinical Laboratory Improvement Amendments of 1988, U.S. Code, Publ. Law No. 100-578.
15. Roche Molecular Systems, Inc., *Amplichip CYP450 Test for In Vitro Diagnostic Use* (Roche Diagnostics, North America, Indianapolis, IN, 2006); [www.amplichip.us/documents/CYP450\\_P1\\_US-IVD\\_Sept\\_15\\_2006.pdf](http://www.amplichip.us/documents/CYP450_P1_US-IVD_Sept_15_2006.pdf).
16. Federal Trade Commission (FTC), "FTC Factions for Consumers: At-Home Genetic Tests: A Healthy Dose of Skepticism May Be Best Prescription" (FTC, Washington, DC, 2006).
17. Secretary's Advisory Committee on Genetics, Health, and Society (SACGHS), "U.S. System of Oversight of Genetic Testing: SACGHS' Draft Response to the Charge of the Secretary of HHS" (National Institutes of Health (NIH), Bethesda, MD, 2007).
18. G. Javitt, *Food Drug Law J.* **62**, 617 (2007).
19. D. E. Dyer, "Public comment on behalf of the Coalition for 21st Century Medicine on the HHS' System of Oversight of Genetic Testing: SACGHS' Draft Response to the Charge of the Secretary of HHS" (NIH, Bethesda, MD, 2007).
20. Enhancing the Oversight of Genetic Tests: Recommendations of the Secretary's Advisory Committee on Genetic Testing (SACGT) (NIH, Bethesda, MD, 2008); [http://www.od.nih.gov/ohba/sacgt/reports/oversight\\_report.pdf](http://www.od.nih.gov/ohba/sacgt/reports/oversight_report.pdf).
21. K. Hudson, *Science* **313**, 1853 (2006).
22. Laboratory Test Improvement Act, S. 736, introduced 1 March 2007.
23. G. Javitt, E. Stanley, K. Hudson, *Oklahoma Law Rev.* **57**, 251 (2004).
24. "HHS Secretary Leavitt Announces Steps Toward a Future of 'Personalized Health Care'"; [www.hhs.gov/news/press/2007pres/20070323a.html](http://www.hhs.gov/news/press/2007pres/20070323a.html).
25. We acknowledge the support of the Pew Charitable Trusts.

10.1126/science.1156604



## BIOCHEMISTRY

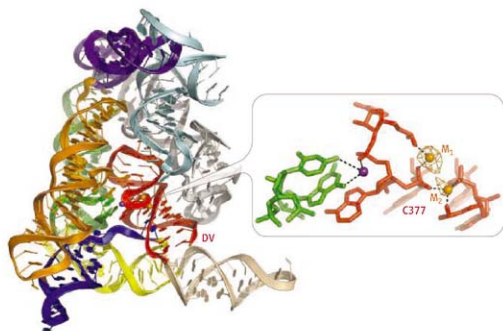
# Toward Understanding Self-Splicing

Joseph A. Piccirilli

Group II introns are a type of RNA enzyme (ribozyme) that catalyze their own excision from RNA transcripts. They hold profound significance for biological evolution, because some can insert themselves into DNA targets, providing a possible pathway for genome diversification (1, 2). Furthermore, group II introns probably represent the molecular ancestors of the spliceosome, a complex assembly of five RNA molecules and many proteins that removes introns from many eukaryotic RNA transcripts (1, 2). On page 77 of this issue (3), Toor *et al.* describe the crystal structure of a self-spliced group II intron at 3.1 Å resolution, revealing for the first time the molecular details of this versatile catalytic RNA.

Cells express their genes by first copying DNA into RNA transcripts, which serve as messenger molecules that code for proteins or as non-messengers that perform other cellular functions. Many genes contain intervening sequences (introns) that interrupt the coding regions (exons) of the DNA. During gene expression, the entire length of the gene (introns and exons) is copied into RNA. But to express the gene correctly, cells must remove the introns from the RNA transcript and arrange the exons contiguously. This happens through a process known as RNA splicing, which involves catalysis of phosphoester transfer reactions at the exon/intron boundaries. Some introns, known as self-splicing introns, catalyze their own removal. Others require more specialized machinery, such as the spliceosome, for removal.

Group II introns are widespread, occurring in organisms from all three branches of life. They contain a well-preserved secondary structure, organized into six domains (I to VI). Biochemical, phylogenetic, and computational analysis has provided important insights into the three-dimensional arrangement of the domains, the catalytic mechanism of the intron, and the mode of substrate recognition (1, 2). However, no high-resolution crystal structures of group II introns have been reported.



**Molecular architecture of an RNA group II intron.** The intron organizes domain V into a binuclear metal center (DV, shown in red). The bound metal ions mediate catalysis of splicing chemistry.

In the new work, Toor *et al.* screened extremophilic bacteria and identified a group II intron from the deep sea microbe, *Oceanobacillus iheyensis*. This intron has two properties usually considered favorable for RNA crystallization. It retains splicing activity at relatively high temperatures, implying structural stability, and splices during enzymatic synthesis in the test tube to produce a conformationally homogenous RNA, thereby precluding the denaturation steps that usually accompany RNA purification.

In the structure, domains I to IV surround the highly conserved domain V, the long-suspected catalytic center of the intron (see the figure). In domain V, a 2-nucleotide (nt) bulge separates an upper hairpin from a lower helical stem that contains the "catalytic triad" (usually AGC, but often CGC, as is the case here). Domains I to IV (including the highly conserved junction between domains II and III) organize the domain V bulge and the triad into a platform for binding two  $Mg^{2+}$  ions ( $M_1$  and  $M_2$ ) that are spaced 3.9 Å apart (see the figure). A third metal ion resides 6 Å from  $M_1$  and  $M_2$ . The crystallographic data lack density for domain VI and some other regions, but the structure contains many of the contacts

The crystal structure of a group II intron shows a complex architecture with metal ions at the catalytic center.

previously implicated in functional studies (1, 2), suggesting that the overall arrangement of the domains closely resembles that of the active structure.

The 3.9 Å distance between  $M_1$  and  $M_2$  matches that between the two metal ions observed at the active sites of the *Azoarcus* group I intron (4) and many protein enzymes that catalyze phosphoester transfer reactions (5). This configuration of metal ions presumably facilitates splicing chemistry by providing electrostatic complementarity to changes in atomic charge that occur along the reaction pathway. Biochemical experiments also support the functional relevance of the binuclear metal center in the group II structure. Structural studies and terbium probing experiments implicate metal-ion binding in the bulge (6, 7), and phosphates in both the bulge and the catalytic triad are sensitive to sulfur substitution (8). Metal-ion rescue experiments further show that at least two distinct metal ions participate directly in catalysis (9). Atomic mutagenesis combined with quantitative analysis (8) identified the interaction corresponding to  $M_2$  and the phosphate at C377 (see the figure).

The U6 small nuclear RNA, one of the five

Department of Biochemistry and Molecular Biology, and Department of Chemistry, Howard Hughes Medical Institute, The University of Chicago, Chicago, IL 60637, USA. E-mail: jpiccir@uchicago.edu

RNA pieces in the spliceosome, has a domain V counterpart, containing a 2-nucleotide bulge located 5 base pairs away from an AGC triad (10). Formation of an analogous metal-binding platform in this region of U6 (11) may explain the apparent ability of spliceosomal RNAs to retain catalytic activity in the complete absence of the many protein components that usually accompany splicing (12). A domain V-like element could have played a major role during the RNA world era of evolution, serving as the catalytic center for RNA cleavage, transesterification, and polymerization reactions.

The new structure provides a powerful starting point for future investigations of group II introns and the spliceosome. The

lack of electron density for domain VI, which is important for the first step of splicing in many group II introns, and the absence of exons from the structure preclude us from seeing how these elements dock onto the surface created by domains I to V. Thus, the structural details of substrate recognition and catalysis remain undefined. The nature of the conformational change known to separate the two steps of splicing (13) also remains unclear. Finally, it will be important for our understanding of group II intron self-splicing to capture the structures of the other intermediates along the splicing pathway and to pursue experiments that link features of these structures with functionally defined interactions.

## References

1. A. M. Pye, *Ribozymes and RNA Catalysis* (Royal Society of Chemistry, Cambridge, UK, ed. 2, 2008).
2. A. M. Pye, A. M. Lambowitz, *The RNA World* (Cold Spring Harbor Laboratory, Cold Spring Harbor, NY, ed. 3, 2006).
3. N. Toot, K. N. Keating, S. D. Taylor, A. M. Pye, *Science* **320**, 77 (2008).
4. M. Stähle, S. Strobel, *Science* **309**, 1587 (2005).
5. T. Steitz, J. Steitz, *Proc. Natl. Acad. Sci. U.S.A.* **90**, 6498 (1993).
6. L. Zhang, J. A. Doudna, *Science* **295**, 2084 (2002).
7. R. Sigel et al., *Nat. Struct. Mol. Biol.* **11**, 187 (2004).
8. P. Gordon, J. Piccirilli, *Nat. Struct. Mol. Biol.* **8**, 893 (2001).
9. P. Gordon, R. Fong, J. Piccirilli, *Chem. Biol.* **14**, 607 (2007).
10. G. Shukla, R. Padgett, *Mol. Cell* **9**, 1145 (2002).
11. S. Yoon, G. Wüenscheil, J. Termini, R. Lin, *Nature* **408**, 881 (2000).
12. S. Valadkhan, J. Manley, *Nature* **413**, 701 (2002).
13. G. Chamfron, A. Jacques, *EMBO J.* **15**, 3466 (1996).

10.1126/science.1156721

## CLIMATE

# Blooms Like It Hot

Hans W. Paerl<sup>1</sup> and Jef Huisman<sup>2</sup>

Nutrient overenrichment of waters by urban, agricultural, and industrial development has promoted the growth of cyanobacteria as harmful algal blooms (see the figure) (1, 2). These blooms increase the turbidity of aquatic ecosystems, smothering aquatic plants and thereby suppressing important invertebrate and fish habitats. Die-off of blooms may deplete oxygen, killing fish. Some cyanobacteria produce toxins, which can cause serious and occasionally fatal human liver, digestive, neurological, and skin diseases (3–6). Cyanobacterial blooms thus threaten many aquatic ecosystems, including Lake Victoria in Africa, Lake Erie in North America, Lake Taihu in China, and the Baltic Sea in Europe (3–6). Climate change is a potent catalyst for the further expansion of these blooms.

Rising temperatures favor cyanobacteria in several ways. Cyanobacteria generally grow better at higher temperatures (often above 25°C) than do other phytoplankton species such as diatoms and green algae (7, 8). This gives cyanobacteria a competitive advantage at elevated temperatures (8, 9). Warming of surface waters also strengthens the vertical stratification of lakes, reducing vertical mixing. Furthermore, global warming causes

lakes to stratify earlier in spring and destratify later in autumn, which lengthens optimal growth periods. Many cyanobacteria exploit these stratified conditions by forming intracellular gas vesicles, which make the cells buoyant. Buoyant cyanobacteria float upward when mixing is weak and accumulate in dense surface blooms (1, 2, 7) (see the figure). These surface blooms shade underlying nonbuoyant phytoplankton, thus suppressing their opponents through competition for light (8).

Cyanobacterial blooms may even locally increase water temperatures through the intense absorption of light. The temperatures of surface blooms in the Baltic Sea and in Lake IJsselmeer, Netherlands, can be at least 1.5°C above those of ambient waters (10, 11). This positive feedback provides additional competitive dominance of buoyant cyanobacteria over nonbuoyant phytoplankton.

Global warming also affects patterns of precipitation and drought. These changes in the hydrological cycle could further enhance cyanobacterial dominance. For example, more intense precipitation will increase surface and groundwater nutrient discharge into water bodies. In the short term, freshwater discharge may prevent blooms by flushing. However, as the discharge subsides and water residence time increases as a result of drought, nutrient loads will be captured, eventually promoting blooms. This scenario takes place when elevated winter-spring rainfall and flushing events are followed by protracted periods of summer drought. This sequence of

A link exists between global warming and the worldwide proliferation of harmful cyanobacterial blooms.



**Undesired blooms.** Examples of large water bodies covered by cyanobacterial blooms include the Neuse River Estuary, North Carolina, USA (top) and Lake Victoria, Africa (bottom).

<sup>1</sup>Institute of Marine Sciences, University of North Carolina at Chapel Hill, Morehead City, NC 28557, USA. E-mail: hpaerl@emil.unc.edu <sup>2</sup>Institute for Biodiversity and Ecosystem Dynamics, University of Amsterdam, 1018 WS Amsterdam, Netherlands. E-mail: jef.huisman@science.uva.nl

events has triggered massive algal blooms in aquatic ecosystems serving critical drinking water, fishery, and recreational needs. Attempts to control fluctuations in the discharge of rivers and lakes by means of dams and sluices may increase residence time, further aggravating cyanobacteria-related ecological and human health problems.

In addition, summer droughts, rising sea levels, increased withdrawal of freshwater for agricultural use, and application of road salt as a deicing agent have led to rising lake salinities in many regions. Several common cyanobacteria are more salt-tolerant than freshwater phytoplankton species (12, 13). This high salt tolerance is reflected by increasing reports of toxic cyanobacterial blooms in brackish waters (2, 6).

Some cyanobacteria have substantially expanded their geographical ranges. For example, *Cylindrospermopsis raciborskii*—the species responsible for “Palm Island mystery disease,” an outbreak of a severe hepatitis-like illness on Palm Island, Australia (4)—was originally described as a tropical/subtropical genus. The species appeared in southern Europe in the 1930s and colonized higher lat-

itudes in the late 20th century. It is now widespread in lakes in northern Germany (14). Similarly, the species was noted in Florida almost 35 years ago and is now commonly found in reservoirs and lakes experiencing eutrophication in the U.S. southeast and midwest (2). It is adapted to the low-light conditions that typify eutrophic waters, prefers water temperatures above 20°C, and survives adverse conditions through the use of specialized resting cells (14). These bloom characteristics suggest a link to eutrophication and global warming.

More detailed studies of the population dynamics in cyanobacterial blooms are needed. For example, competition between toxic and nontoxic strains affects the toxicity of cyanobacterial blooms (15). Furthermore, viruses may attack cyanobacteria and mediate bloom development and succession (16). It is unclear how these processes are affected by global warming. What is clear, however, is that high nutrient loading, rising temperatures, enhanced stratification, increased residence time, and salination all favor cyanobacterial dominance in many aquatic ecosystems. Water managers will have to accommodate the effects

of climatic change in their strategies to combat the expansion of cyanobacterial blooms.

#### References

1. J. Huisman, H. C. P. Matthijs, P. M. Visser, *Harmful Cyanobacteria* (Springer, Dordrecht, Netherlands, 2005).
2. H. W. Paerl, R. S. Fulton III, in *Ecology of Harmful Marine Algae*, E. Granéli, J. Turner, Eds. (Springer, Berlin, 2006), pp. 95–107.
3. A. Chorus, J. Bartram, *Toxic Cyanobacteria in Water* (Epon, London, 1999).
4. W. W. Carmichael, *Human Ecol. Risk Assess.* **7**, 1393 (2001).
5. L. Guo, *Science* **317**, 1166 (2007).
6. S. Suikkanen, M. Laamanen, M. Huhtanen, *Estuar. Coast. Shelf Sci.* **71**, 580 (2007).
7. C. S. Reynolds, *Ecology of Phytoplankton* (Cambridge Univ. Press, Cambridge, 2006).
8. K. D. Jöhnk et al., *Global Change Biol.* **14**, 495 (2008).
9. J. A. Elliott, I. D. Jones, S. J. Thackeray, *Hydrobiologia* **559**, 401 (2006).
10. M. Kahru, J.-M. Leppänen, O. Rud, *Marine Ecol. Prog. Ser.* **101**, 1 (1993).
11. B. W. Ibelings, M. Vonk, H. F. J. J. van der Molen, W. M. Mooij, *Ecol. Appl.* **13**, 1456 (2003).
12. L. Tonk, K. Bosch, P. M. Visser, J. Huisman, *Aquat. Microb. Ecol.* **46**, 117 (2007).
13. P. H. Moisan, E. McCrindle III, H. W. Paerl, *Microb. Ecol.* **43**, 432 (2002).
14. C. Wiedner, J. Rüdiger, R. Brüggemann, B. Nordor, *Oecologia* **152**, 473 (2007).
15. W. A. Kardinal et al., *Aquat. Microb. Ecol.* **48**, 1 (2007).
16. M. Hwang et al., *J. Plankton Res.* **28**, 407 (2006).

10.1126/science.1155398

#### DEVELOPMENT

## Deconstructing Pluripotency

Anne G. Bang and Melissa K. Carpenter

In 2006, Yamanaka and colleagues (1) discovered that mouse fibroblasts could be reprogrammed to a pluripotent, embryonic stem (ES) cell-like state by the simple introduction of four transcription factors, Oct4, Sox2, Klf4, and c-Myc. This finding has since been reproduced (2–6) and extended to human fibroblasts using the same cocktail of genes (7, 8) or one composed of Oct4, Sox2, Nanog, and Lin28 (9). These so-called “induced pluripotent stem cells” (iPS cells) appear similar to ES cells in that they can give rise to all the cells of the body and display fundamental genetic and morphologic ES cell characteristics (see the figure). The concept of an iPS cell brings together decades of work in the fields of ES cell biology and nuclear reprogramming that predicted it might be possible to impose pluripotency upon a somatic cell (10). iPS cells not only have the potential to produce patient-specific stem cells, but they also provide a platform to study the biology

of pluripotency and cell reprogramming. In *Science Express*, Aoi et al. (11) broaden the application of iPS cell methodology to murine epithelial cell types, highlighting differences when compared with reprogramming of fibroblasts. And on page 97 of this issue, Viswanathan et al. (12) address the role of one of the reprogramming factors, Lin28, in regulating microRNAs (miRNAs) in ES cells. The findings of Viswanathan et al., and recent work by Benetti et al. (13) and Sinkkonen et al. (14), advance our knowledge of the little-understood roles of miRNAs in ES cells. Collectively, these studies take us closer to understanding how ES cells maintain an undifferentiated, self-renewing, and pluripotent state, and to defining how pluripotency can be imposed on other cell types.

To date, fibroblasts and mesenchymal stem cells have been used to generate iPS cells (1–9). A next step is to determine whether other cell types are susceptible to reprogramming. Toward this end, Aoi et al. produced iPS cells from two epithelial cell populations, adult mouse hepatocytes and gastric epithelial

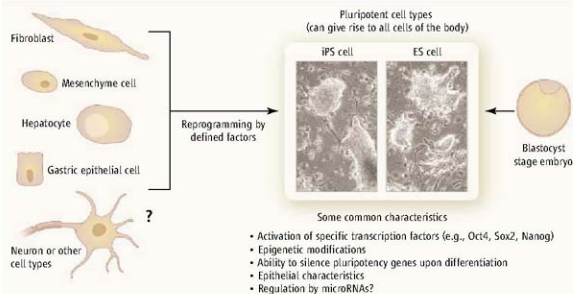
The requirements for reprogramming different somatic cell types to a pluripotent state may not be equivalent.

cells, by expressing Oct4, Sox2, Klf4, and c-Myc. Like iPS cells generated from fibroblasts (iPS-fibroblast), those from primary hepatocytes (iPS-Hep) and gastric epithelial cells (iPS-Stm) were pluripotent and gave rise to adult and germline chimeras. However, iPS-Hep and iPS-Stm differ from iPS-fibroblast cells in several important respects, indicating that the dynamics of reprogramming may not be equivalent in these cell types. For instance, although c-Myc was used, iPS-Hep and iPS-Stm cell-derived chimeric mice did not display the c-Myc-dependent tumorigenicity observed in iPS-fibroblast-derived chimeric mice. In addition, iPS-Hep and iPS-Stm cells could be generated using less stringent selection conditions. Thus, epithelial cell types may be more prone to reprogramming than fibroblasts.

How do these differences inform us about the mechanism of reprogramming? Given that ES cells are an epithelial population, characterized by cell adhesion (mediated by the membrane protein E-cadherin), one possibility is that epithelialization is an event required

Novocell Inc., 3550 General Atomics Court, San Diego, CA 92121, USA. E-mail: mcarpenter@novocell.com





**Look alike?** Induced pluripotent stem (iPS) cells can be derived from different cell types and share characteristics with embryonic stem (ES) cells. Whether other somatic cell types, like neurons, can be reprogrammed is unknown. MicroRNAs have yet to be examined in iPS cells. Microphotographs from (17).

for generating iPS cells. Reprogrammed fibroblasts begin to morphologically resemble ES cells before they express endogenous Oct4, which allows iPS cells to be isolated solely on the basis of morphology (4, 6–9). Does the epithelial state of the liver and stomach cells give them a “leg up” relative to fibroblasts such that they are more susceptible to reprogramming? Are there other intrinsic distinctions between these cell types that could explain the apparent reprogramming differences? Two recent papers (15, 16) break down reprogramming in fibroblasts into sequential events characterized by the expression of various markers, leading to the activation of Oct4. It will be interesting to compare the timing and sequence of events leading to reprogramming in fibroblasts versus epithelial cells to determine whether the kinetics of reprogramming differ in these cell types.

The discovery of iPS cells, together with advances in our understanding of the molecular mechanisms that regulate ES cells, raise the prospect that the puzzle of pluripotency may one day be solved. Recent studies highlight the importance of miRNAs in the regulatory circuitry that controls pluripotency (17). Functional miRNAs are generated by processing primary miRNA (pri-miRNA) to a pre-miRNA and then to a mature miRNA that controls gene silencing through RNA interference. Mouse ES cells mutant for miRNA-processing genes (*Dgcr8* or *Dicer*), do not proliferate normally, and upon differentiation fail to completely down-regulate Oct4 expression and display severe defects in their ability to differentiate (17). Mutant phenotypes of ES cells lacking DICER can be

rescued by expressing the miR-290 cluster miRNAs and by de novo DNA methyltransferases (Dnmts) (13, 14). The authors propose that miR-290 cluster miRNAs regulate the expression of Dnmts, in part through targeting the transcriptional repressor Rbl2. Sinkkonen *et al.* describe rescue of the stable repression of Oct4 upon differentiation, whereas Benetti *et al.* propose that through indirect regulation of Dnmts, miR-290 cluster miRNAs control telomere recombination. These data support a model in which miRNAs maintain ES cells by controlling telomere homeostasis and, upon differentiation, repress the self-renewal program by modulating the epigenetic status of pluripotency genes. Although miRNAs are yet to be examined in iPS cells, it seems likely that they will play similarly important roles.

Viswanathan *et al.* provide further evidence for the potential importance of miRNAs in ES cells. Because the let-7 family of miRNAs is not processed in mouse ES cells, but processing is observed by 10 days of embryogenesis, let-7 maturation was presumed to be blocked in ES cells (18). Viswanathan *et al.* have identified Lin28 as a pri-let-7g binding protein in ES cell extracts and show that Lin28 specifically blocks the processing of pri-let-7g to pre-let-7g. This discovery may correlate with the recent finding that Lin28 enhances the recovery of iPS cell clones from human fibroblasts (9). It is intriguing that let-7g has been implicated as a tumor suppressor. Putative targets of let-7g include Hmg2a, c-Myc, and K-Ras, which suggests possible mechanisms of action (19, 20). Thus, inclusion of Lin28 in the factor cocktail to make

iPS cells may be a double-edged sword because it could participate in self-renewal but could also have oncogenic potential. Lin28 may also regulate the translation of mRNA, as observed in myoblasts (21). What role does Lin28 play in ES and iPS cells and why is let-7 expressed but not processed? Does Lin28 promote the undifferentiated state? Answers to these questions await future studies examining the phenotypic consequences of let-7 miRNA maturation or loss of Lin28 function in ES and iPS cells.

The promise of iPS cells is that they are pluripotent and potentially patient-specific. The therapeutic application of iPS

cells will require demonstrating that these cells are stable and show an appropriate safety profile in preclinical studies. An in-depth understanding of the molecular mechanisms that underlie pluripotency and reprogramming is crucial to harness iPS cell technology and develop viral-free methods to produce these cells. The studies by Aoi *et al.* and Viswanathan *et al.* are a step toward deconstructing pluripotency and open many new questions regarding reprogramming and the nature of the embryonic stem cell.

## References

1. K. Takahashi, S. Yamanaka, *Cell* **126**, 663 (2006).
2. K. Okita, T. Ichisaka, S. Yamanaka, *Nature* **448**, 313 (2007).
3. M. Wernig *et al.*, *Nature* **448**, 318 (2007).
4. A. Meissner, M. Wernig, R. Jaenisch, *Nat. Biotechnol.* **25**, 1177 (2007).
5. N. Maherali *et al.*, *Cell Stem Cell* **1**, 55 (2007).
6. M. Nakagawa *et al.*, *Nat. Biotechnol.* **26**, 101 (2008).
7. K. Takahashi *et al.*, *Cell* **131**, 861 (2007).
8. L. H. Park *et al.*, *Nature* **451**, 141 (2008).
9. J. Yu *et al.*, *Science* **318**, 1917 (2007); published online 19 November 2007 (10.1126/science.1151526).
10. R. Jaenisch, R. Young, *Cell* **132**, 567 (2008).
11. T. Aoi *et al.*, *Science*, 14 February 2008 (10.1126/science.1154884).
12. S. R. Viswanathan, G. Q. Daley, R. L. Gregory, *Science* **320**, 97 (2008); published online 21 February 2008 (10.1126/science.1154040).
13. R. Benetti *et al.*, *Nat. Struct. Mol. Biol.* **15**, 268 (2008).
14. L. Sinkkonen *et al.*, *Nat. Struct. Mol. Biol.* **15**, 259 (2008).
15. J. Brumbrink *et al.*, *Cell Stem Cell* **2**, 151 (2008).
16. M. Stadler, N. Maherali, D. T. Brault, K. Hochdinger, *Cell Stem Cell* **2**, 230 (2008).
17. B. M. Stadler, H. Ruchoux-Bakus, *Cell* **132**, 563 (2008).
18. J. M. Thomson *et al.*, *Genes Dev.* **20**, 2202 (2006).
19. M. S. Kumar *et al.*, *Proc. Natl. Acad. Sci. U.S.A.* **105**, 3903 (2008).
20. F. Yu *et al.*, *Cell* **131**, 1109 (2007).
21. A. Pokesskaya *et al.*, *Genes Dev.* **21**, 1125 (2007).

10.1126/science.1157042

## CELL SIGNALING

## Tel2 Finally Tells One Story

Michael Chang<sup>1,2</sup> and Joachim Lingner<sup>1,2</sup>

The recently published work by Takai *et al.* (1) on the protein TEL2 is reminiscent of the tale in which six blind men were each asked to describe an elephant by touching it. Each one touched a different part, and thus each provided a strikingly different description of what an elephant is like. One touched the elephant's broad and sturdy side and thought it felt like a wall. Another touched its tusk, which felt like a spear. A third touched its trunk, which felt like a snake. The fourth, fifth, and sixth men touched its knee, ear, and tail, which were mistaken for a tree, a fan, and

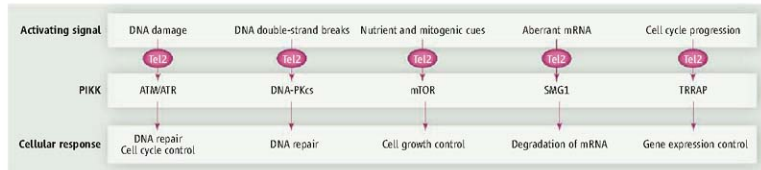
reacting to DNA double-strand breaks by eliciting a DNA damage response.

By contrast, the functional role of Tel2 has been a more difficult puzzle to solve. Tel2 is a well-conserved protein that is essential for yeast viability. Determining the precise role of Tel2 has been complicated by its many apparently nonoverlapping functions reported in various organisms. In addition to maintaining telomere length in *S. cerevisiae*, it functions in the DNA replication checkpoint in the fission yeast *Schizosaccharomyces pombe* and in humans, coupling the onset of cell division

The ability of a protein to interact with an entire family of phosphorylating enzymes explains its diverse functions across species.

physical association between Tel2 and PIKKs was also recently observed in fission yeast (11), the function of Tel2 as a stabilizer of these kinases may also be conserved.

PIKKs are a family of enzymes with diverse functions. There are six PIKKs in mammals: ATM, ATM and Rad3 related (ATR), DNA-dependent protein kinase catalytic subunit (DNA-PKcs), mammalian target of rapamycin (mTOR), suppressor with morphological effect on genitalia 1 (SMG1), and transformation/transcription domain-associated protein (TRRAP). ATM is the human ortholog of *S. cerevisiae*



**Diverse roles.** The protein Tel2 interacts with phosphatidylinositol 3-kinase-related protein kinases (PIKKs) in mammalian cells, each of which functions in a different

signaling pathway that responds to a specific cellular stress. How Tel2 function is coordinated among these pathways remains to be determined.

a rope, respectively. The story illustrates the importance of getting the whole picture, which is what the new study provides about TEL2, whose many, seemingly unrelated functions have been puzzling.

The Tel2 story begins in 1986, when Lustig and Petes discovered mutant strains of the budding yeast *Saccharomyces cerevisiae* that had abnormally short telomeres (2), the physical ends of eukaryotic chromosomes. They named the two identified strains *tel1* and *tel2*, whose mutated genes were cloned 10 years later (3, 4). Much is now known about the yeast gene *TEL1*. It encodes an evolutionarily conserved enzyme that localizes to short telomeres, where it phosphorylates protein substrates and increases the activity of telomerase, the ribonucleoprotein complex that lengthens telomeres. Ataxia telangiectasia mutated (ATM), the human ortholog of Tel1, is well known for

with the successful replication of DNA (5–7). In the nematode *Caenorhabditis elegans*, however, hypomorphic alleles (forms of a gene in which the encoded protein has reduced function compared with the wild-type allele) of *clk-2/rad-5* (the *TEL2* ortholog in *C. elegans*) not only can cause stress during DNA replication and hypersensitivity to DNA double-strand breaks, but also can increase life span and reduce the rate of numerous physiological processes, including embryonic and postembryonic development, and reproduction (8–10).

The work by Takai *et al.* provides a unifying model for all the reported functions of mammalian Tel2 and its orthologs. Through a very careful and systematic analysis of the phenotype of Tel2-null mouse cells and biochemical protein interaction studies, the authors discovered that TEL2 directly interacts with all six of the mammalian phosphatidylinositol 3-kinase-related protein kinases (PIKKs). Absence of TEL2 substantially reduced the expression level of all PIKKs in mouse cells, impinging on their function (see the figure). Because a direct

Tel1, which explains the short telomeres seen in budding yeast *tel2* mutants in which Tel1 may be unstable. ATM and ATR are key regulators in the DNA damage response, accounting for the hypersensitivity to DNA damage and DNA replication checkpoint defects in humans, fission yeast, and *C. elegans* *tel2* mutants. mTOR has an essential role in cell growth by regulating the cellular response to changes in environmental cues, mitogenic signals, and nutrient availability, offering an explanation for the pleiotropic phenotypes seen in *clk-2/tel2* mutants in *C. elegans*.

However, much remains unknown about what exactly Tel2 is doing and how it is doing it. Note that the mechanisms by which Tel2 stabilizes PIKKs and the process through which PIKK degradation occurs in *Tel2*-deficient cells have yet to be elucidated. Inhibition of the proteasome did not affect PIKK degradation, and Takai and colleagues speculate that Tel2 may protect PIKKs from cleavage by a specific protease. Perhaps most intriguing is why Tel2 should impinge on so many apparently disconnected signaling pathways that respond to very different envi-

<sup>1</sup>École Polytechnique Fédérale de Lausanne, Swiss Institute for Experimental Cancer Research (USREO), CH-1066 Epalinges, Switzerland; <sup>2</sup>Frontiers in Genetics National Center for Competence in Research, CH-1211 Geneva, Switzerland; E-mail: michael.chang@epfl.ch, joachim.lingner@epfl.ch

ronmental cues. It seems unlikely that all PIKKs should be regulated by Tel2 in a coordinated fashion. A more attractive hypothesis is that the interaction of Tel2 with PIKKs is regulated individually, to provide a fast switch to turn signaling pathways on or off in response to changes in the environment. Of course, this opens up many questions about regulatory mechanisms, and the yeast and nematode model systems may be powerful tools to explore this area.

It also remains to be seen if Tel2 influences the enzymatic or cellular properties of PIKKs. Indeed, recent work by Anderson *et al.* (12) shows that the *tel2-1* mutant allele in *S. cerevisiae* not only causes a decrease in the amount of Tel1 protein (the yeast ortho-

log of mammalian ATM) expressed, but that Tel2 may also help Tel1 to associate with DNA double-strand breaks in this organism. Notwithstanding, by providing one model by which all the *tel2* phenotypes could potentially be satisfyingly explained, Takai and colleagues have given researchers a foundation for future hypotheses and experiments. They have allowed us to see the entire Tel2 elephant.

#### References and Notes

1. H. Takai, R. C. Wang, K. K. Takai, H. Yang, T. de Lange, *Cell* **131**, 1248 (2007).
2. A. J. Lustig, T. D. Petes, *Proc. Natl. Acad. Sci. U.S.A.* **83**, 1398 (1986).
3. P. W. Greenwell *et al.*, *Cell* **82**, 823 (1995).
4. K. W. Runge, V. A. Zakian, *Mol. Cell. Biol.* **16**, 3094 (1996).

5. M. Shikata, F. Ishikawa, J. Kanoh, *J. Biol. Chem.* **282**, 5346 (2007).
6. N. Jiang, C. Y. Benard, H. Kibir, E. A. Shoubridge, S. Hekimi, *J. Biol. Chem.* **278**, 21678 (2003).
7. S. J. Collins *et al.*, *Nat. Cell Biol.* **9**, 391 (2007).
8. S. Ahmed, A. Alpi, M. O. Hengartner, A. Gartner, *Curr. Biol.* **11**, 1934 (2001).
9. C. Benard *et al.*, *Development* **128**, 4045 (2001).
10. T. Garcia-Muse, S. J. Boulton, *EMBO J.* **24**, 4345 (2005).
11. T. Hayashi *et al.*, *Genes Cells* **12**, 1357 (2007).
12. C. M. Anderson *et al.*, *Genes Dev.*, published 11 March 2008; 10.1101/gad.1644208.
13. M. C. is supported by a Human Frontier Science Program (HFS) postdoctoral fellowship. Work in the laboratory is supported by grants from the Swiss Cancer League, the Swiss National Science Foundation, the HFS Program, and the European Union 6th and 7th Framework Programmes.

10.1126/science.1155132

#### ASTRONOMY

## Small-Scale Observations Tell a Cosmological Story

Philip A. Bland

Meteorites are the oldest rocks to which we have access, dating back 4567 million years (1), to an epoch before planets, when our solar system was nothing more than a disk of dust and gas. They contain a record of that earliest period of solar system history, including the variety of local stellar sources that contributed to our protoplanetary disk and the physical and chemical processes that occurred within it. On page 91 of this issue, Fries and Steele (2) report their discovery of graphite whiskers (GW) in meteorites. Their observation has importance for our understanding of the environment of the early solar system, and GWs may have broader astrophysical and cosmological implications as well.

The most primitive meteorites—with textures, mineralogy, and chemistry comparatively unmodified since their accretion—are known as carbonaceous chondrites. These rocks have a composition approaching that of the Sun (for elements other than the noble gases and H, C, N, and O) (3). They are also hugely heterogeneous, containing spherical igneous inclusions known as chondrules, which probably formed by localized heating events in the body of the disk (4), and occasional calcium-aluminum-rich inclusions

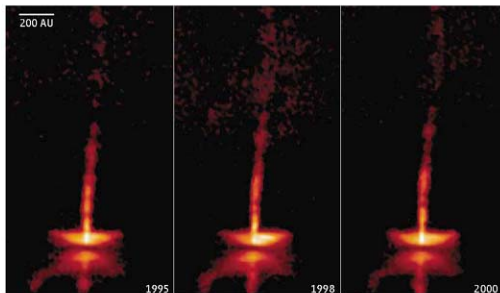
(CAIs) that may have formed very close to the proto-Sun (4). All of this is bound together with a fine-grained “matrix” that is likely (at least in part) a remnant of the disk itself (5). The matrix contains presolar material: micrometer- and submicrometer-sized grains, formed in the atmospheres of other stars, which we can analyze in the lab (6).

Studies of carbonaceous chondrites are relevant to questions beyond the origins of our own solar system, complementing astronomical observations of protoplanetary disks and

Graphite whiskers found in meteorites provide clues to the chemical environment in the early solar system.

young stellar objects and (in the case of presolar grains) astrophysical models of stellar nucleosynthesis and the chemical and dynamic evolution of the Galaxy (6). Fries and Steele present a Raman imaging spectroscopy study of three carbonaceous chondrites in which they find a highly unusual carbon allotrope in the form of graphite whiskers, which have never before been observed in meteorites or cosmic dust.

Graphite whiskers are postulated to be a component of the interstellar (and intergalac-



**Growing whiskers.** A protoplanetary disk showing bipolar outflows: A potential mechanism for launching graphite whiskers, condensing close to the young star, into interstellar space.

Impacts and Astromaterials Research Centre, Department of Earth Science and Engineering, Imperial College London, London SW7 2AZ, UK. E-mail: p.a.bland@imperial.ac.uk



tic) medium and have found a home in a variety of astrophysical models (7–10). One fascinating possibility is that GWs in the intergalactic medium may explain the observed dimming of supernovae at high redshift. Astronomers use measurements of the brightness and redshift of distant objects to determine how quickly the universe is expanding. Observational evidence of the apparent luminosities of supernovae at high redshift (11, 12) have been taken to suggest an accelerated expansion of the universe, driven by “dark energy”—a concept that has recently revolutionized cosmology.

However, there are a number of potential explanations for these observations that would remove the need for “dark energy,” among them models that explain supernova dimming through particles in intergalactic space that absorb or scatter light (9, 10). Graphite whiskers are an ideal candidate for this material for two reasons: These grains change the spectrum of incident light very little, consistent with the apparent colors of the high redshift supernovae, and they are very efficient absorbers, so they could be preferentially ejected from the formation sites within galaxies by radiation pressure. Although early models (9) are difficult to reconcile with more recent supernova data (13), new, more detailed models (10) are compatible with current data.

With the potential to study extraterrestrial GWs in the lab, Fries and Steele have shown that analysis of meteorites can provide “ground truth” data for the models discussed above. Before the current study, only one other form of mineral needle or whisker had been discovered in extraterrestrial materials: enstatite, a magnesium silicate (13). It was suggested, based on the unusual crystal morphology and microstructure of the enstatite needles, that they were vapor-phase condensates and that they might have formed either in the solar nebula or in a presolar environment (13). Similarly, Fries and Steele note that all known GW synthesis methods involve deposition from a vapor at high temperature. GWs appear to be commonly associated with CAIs (2); thus, Fries and Steele propose that, because CAIs are thought to form close to the young Sun, and GWs are condensing there, GWs could easily have been launched into interstellar space from the disk by bipolar outflows, a common feature of protoplanetary disks (see the figure).

Bringing the discussion closer to home, what are the implications for our understanding of processes occurring in the early solar system? GWs are observed in three settings: within a chondrule, inside several CAIs (and also at the CAI/matrix boundary), and associated with a rim around a piece of altered

matrix-like material. Many CAIs show evidence for formation by condensation, so it is not unexpected to find evidence for another condensed phase there. More surprising are the GWs associated with the fragment of matrix-like material, which, with associated minerals, suggests high-temperature formation of these fragments at asteroidal distances.

The GWs described by Fries and Steele clearly have a solar system origin. The abundance of presolar GWs may be very low compared with other presolar grains found in meteorites, but if Fries and Steele are correct, then bona fide presolar GWs should also be there. Although bipolar outflows are a reasonable mechanism by which to launch GWs into interstellar space, it is clearly a priority now to confirm whether GWs are indeed a component of the interstellar medium. Meteorite analysis can answer that question. CV chondrites—the type of meteorite studied here (2)—are arguably the least primitive of all the carbonaceous chondrites. Therefore, a necessary next step would be to extend the search to fine-grained materials in the most primitive meteorites, cosmic dust, and cometary samples to identify graphite

whiskers that exhibit the type of isotopic anomalies characteristic of formation in the atmosphere of stars other than the Sun.

## References

1. Y. Amelin, A. N. Krot, I. D. Hutcheon, A. A. Ulyanov, *Science* **297**, 1678 (2002).
2. M. Fries, A. Steele, *Science* **320**, 91 (2008).
3. E. Anders, N. Grevesse, *Geochim. Cosmochim. Acta* **53**, 197 (1989).
4. S. S. Russell et al., in *Chondrites and the Protoplanetary Disk*, A. N. Krot, E. R. D. Scott, B. Reipurth, Eds., ASP Conference Series 341 (Astronomical Society of the Pacific, San Francisco, 2005), pp. 317–350.
5. G. R. Huss, C. M. O'D Alexander, H. Palme, P. A. Bland, J. T. Wasson, in *Chondrites and the Protoplanetary Disk*, A. N. Krot, E. R. D. Scott, B. Reipurth, Eds., ASP Conference Series 341 (Astronomical Society of the Pacific, San Francisco, 2005), pp. 701–731.
6. E. K. Zinner, in *Meteorites, Comets and Planets: Treatise on Geochemistry*, A. M. Davis, Ed. (Elsevier, London, 2005), pp. 17–39.
7. N. C. Wickramasinghe, H. Okuda, *Nature* **368**, 695 (1994).
8. E. Dwek, *Astrophys. J.* **611**, L109 (2004).
9. A. N. Aguirre, *Astrophys. J.* **512**, L19 (1999).
10. R. Robaina, J. Cepa, *Astron. Astrophys.* **464**, 465 (2007).
11. A. G. Reiss et al., *Astrophys. J.* **116**, 1009 (1998).
12. S. Perlmutter et al., *Astrophys. J.* **517**, 565 (1999).
13. A. G. Riess et al., *Astrophys. J.* **607**, 665 (2004).

10.1126/science.1155284

## MUSIC THEORY

# Creating Musical Variation

Diana S. Dabby

Inspiration for composition may come from natural sounds, chance, and methods based on chaos theory.

In the 21 letters that Mozart wrote to his friend Michael Puchberg between 1788 and 1791, there exist at least 24 variants of the supplication “Brother, can you spare a dime?” Mozart ornaments his language to cajole, flatter, and play on Puchberg’s sympathies (1, 2). He varies his theme of “cash needed now” in much the same way an 18th-century composer might dress a melody in new attire by weaving additional notes around its thematic tones in order to create a variation. Such ornamentation could enliven and elaborate one or more musical entities, as can be heard in the Haydn F Minor Variations (1793) (3). The Haydn represents one of the most popular forms of the 18th and 19th centuries—variations on original or borrowed themes. Yet myriad variation techniques existed besides ornamentation, including permutation and combination, as advocated by a number of

18th-century treatises. More recently, fields such as chaos theory have allowed composers to create new kinds of variations, some of which are reminiscent of earlier combinatorial techniques.

In a broad context, variation refers to the technique of altering musical material to create something related, yet new. Recognizing its importance to composers, the 20th-century composer and teacher Arnold Schoenberg defined variation as “repetition in which some features are changed and the rest preserved” (4). He wrote numerous examples showing how a group of four notes, each having the same duration, can be varied by making rhythmic alterations, adding neighboring notes, changing the order of the notes, and so on (see the figure, panels A to C) (5). Changing the order of the notes reflects the 18th-century practice of *ars combinatoria*. Joseph Riepel advocated a similar approach (see the figure, panel D) (6). How might a composer use such ordering techniques?

Franklin W. Olin College of Engineering, Needham, MA 02492, USA. E-mail: diana.dabby@olin.edu



## ARNOLD SCHOENBERG



## JOSEPH RIEPEL



## JOHANN SEBASTIAN BACH



**Idea and variations.** Variation techniques illustrated by Schoenberg, Riepel, and a chaotic mapping example. Schoenberg offers numerous ways to vary a given four-note group, shown in the first measure of each line. (A) Rhythmic changes. (B) Addition of neighboring notes. (C) Changing the original order. (D) One of many examples given by Riepel of *ars permutatoria*, a branch of *ars combinatoria*, where six permutations of the notes A B C are given (15). Note that Riepel writes above the staff the German musical spelling of the notes so that “B” translates to B-flat. (E) The first measure of a Bach prelude (pitches only) followed by the first measure of a variation generated by the chaotic mapping.

Igor Stravinsky offers one of many possible examples in his *Variations: Aldous Huxley in Memoriam* for Orchestra (1964): “My Variations were composed on the following pitch series, a succession of notes that came to my mind as a melody: D C A B E A# G# C# D# G F# F. After writing it out, I gradually discovered the possibilities in it as material for variations. ... Veränderungen—alterations or mutations, Bach’s word for *The ‘Goldberg’ Variations*—could be used to describe my Variations as well, except that I have altered or diversified a series, instead of a theme or subject...” (7).

Stravinsky derived additional material from his array of notes to produce 12 variations by, for instance, taking his original series and reversing the order to generate a second row of notes: F F# G D# C# G# A# E B A C D. He then rotated this row to create five more rows by placing the first note at the end to generate a second row. To construct the third row, he rotated the second, and so on. Clearly Stravinsky built a  $6 \times 12$  matrix of notes. He then exploited the rows and columns to construct his variations of the original series by, for example, deriving the opening chords of his *Variations* from the first six columns of the matrix (8).

Yet an array of material does not have to consist of single notes, as demonstrated by Pierre Henri in his 48-minute *Variations pour*

*une porte et un soupir* (“Variations for a Door and a Sigh,” 1963). Using recordings of a breathed sigh, the sung sigh of a musical saw, and a squeaking door, Henri created his variations by mixing, then transforming these sounds in their entirety and in fragments, while varying rhythm and intensity (9).

Flash forward to 1987 when DJ Lil’ Louis, using much more sophisticated analog equipment, produced *French Kiss*, the first house music hit to sell a million copies in Europe and North America. House music typically features a sampled audio clip that undergoes successive transformations, engineered through electronic effects and instruments. Louis started with a simple repetitive array of rhythms heard on kick drum, synthesizer, and hi-hat, which he gradually varied by adding shakers, electronic brass instruments, hand claps, and more (10, 11).

John Cage broke with tradition by leaving the elemental material of the array and its order unspecified. The “score” for his *Variations IV* consists of handwritten instructions providing a schematic that enables chance not only to decide the musical material but also to determine its order. Cage allows “any number of players, any sounds or combinations of sounds produced by any means, with or without other activities” (12). Cage’s piece will drastically change from performance to performance—much more so than, say, Stravinsky’s *Variations*—by virtue of the

chance and randomness he deliberately inserts into his score.

However, if a composer wants to vary an entire work from one hearing to the next, and even from performance to performance, without Cage’s randomness, a different kind of variation technique has been helpful—one that uses a chaotic mapping to make musical variations of the entire work (13). Such a technique harnesses a natural mechanism for variability found in the science of chaos—that is, the sensitivity of chaotic trajectories to initial conditions. Two chaotic trajectories map the pitch sequence of a musical score into a variation where the same set (or subset) of pitches appear, but in modified order (see the figure, panel E). Virtually infinite in number, these variations can be close to the original, diverge from it substantially, or achieve degrees of variability between these two extremes. Unlike the above methods, the technique offers a post-compositional process in which a composer can go on a journey to someplace new or unimagined with an already completed piece (14).

The several music files available online (3, 11, 14) are intended to serve as only a sampling of the richness of musical variations. Just opening one’s ears makes it possible to hear the variations that pervade our musical lives, from jazz improvisations on popular songs to the tinkling pitches caused by rain on a tin roof.

## References and Notes

1. *The Letters of Mozart and His Family*, E. Anderson, Ed. (Norton, New York, 1985).
2. E. R. Sisman, *Haydn and the Classical Variation* (Harvard Univ. Press, Cambridge, 1993).
3. Audio example 1: Haydn theme 1, variation 1 (tracks 1 and 2).
4. A. Schoenberg, *Fundamentals of Musical Composition*, G. Strang, L. Stein, Eds. (Belmont, Pacific Palisades, CA, 1967).
5. Even if one does not read musical notation, the variations in Schoenberg’s examples can be understood “graphically.”
6. J. Riepel, *Anfangsgründe zur musicalischen Setzkunst* (Regensburg, 1752–1768).
7. I. Stravinsky, R. Craft, *Themes and Episodes* (Knopf, New York, 1966).
8. P. S. Phillips, *Mus. Anal.* 3, 69 (1984).
9. P. Henri, liner notes, *Variations for a Door and a Sigh* (Limelight, 1963).
10. S. Hawkins, in *Analyzing Popular Music*, A. F. Moore, Ed. (Cambridge Univ. Press, Cambridge, 2003), pp. 80–102.
11. Audio example 2: Lil’ Louis, *French Kiss*, [www.youtube.com/watch?v=kBnBLfAdBY&feature=related](http://www.youtube.com/watch?v=kBnBLfAdBY&feature=related). This piece includes explicit content.
12. J. Cage, *Variations IV* (Peters/Henmar, New York, 1963).
13. D. S. Dabby, *Chaos* 6, 2 (1996).
14. Audio examples 3 to 5: Original Bach Prelude in C (track 3), chaotic mapping-generated variation of the Bach (track 4), composed variation based on the chaotic mapping-generated variation (track 5).
15. N. Reed, thesis, Eastman School of Music, 1983.
16. Supported by the Research Fund of Olin College.

## Supporting Online Material

[www.sciencemag.org/cgi/content/full/320/5872/62/DC1](http://www.sciencemag.org/cgi/content/full/320/5872/62/DC1)  
Audios S1 to S5

10.1126/science.1153825



# Stochasticity and Cell Fate

Richard Losick<sup>1</sup> and Claude Desplan<sup>2</sup>

Fundamental to living cells is the capacity to differentiate into subtypes with specialized attributes. Understanding the way cells acquire their fates is a major challenge in developmental biology. How cells adopt a particular fate is usually thought of as being deterministic, and in the large majority of cases it is. That is, cells acquire their fate by virtue of their lineage or their proximity to an inductive signal from another cell. In some cases, however, and in organisms ranging from bacteria to humans, cells choose one or another pathway of differentiation stochastically, without apparent regard to environment or history. Stochasticity has important mechanistic requirements. We speculate on why stochasticity is advantageous—and even critical in some circumstances—to the individual, the colony, or the species.

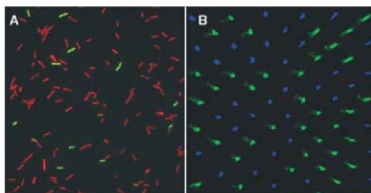
"I, at any rate, am convinced that He does not play dice."

Albert Einstein, 1926

Classic model systems for the study of development offer numerous examples of cellular differentiation in which cell fate is not left to chance. The generation of progeny with distinct cell fates is hard-wired into the cell cycle of *Caulobacter crescentus* (1). Likewise, *Saccharomyces cerevisiae* switches mating types (2) and *Drosophila melanogaster* generates neurons and glial cells by intrinsically asymmetric processes of cell division (3). Also not left to a roll of the dice is the decision to become a photoreceptor in the fly eye, which is determined by the proximity of a precursor cell to a signaling peptide (4).

In striking contrast are entry into the state of competence by *Bacillus subtilis* and the generation of alternative color vision photoreceptors in *D. melanogaster* (Fig. 1). Although these systems could not be more different, they have in common that the choice of fate is made stochastically. Figure 1A shows a field of *B. subtilis* cells containing DNA encoding green fluorescent protein fused to the promoter of a gene that is under the control of the DNA-binding protein ComK, the master regulator for competence (5). Competence is a specialized state involving the expression of about 100 genes. In competence, growth ceases and the cells become capable of taking up DNA from the environment and incorporating it into the chromosome by recombination. About 20% of the cells are active for ComK and the rest are not.

Each cell makes a binary choice between these two states randomly (5–7). Presumably, competence imparts a fitness advantage that outweighs the cost of producing cells that temporarily stop growing. Whereas the choice to enter competence is made stochastically, exit from competence and resumption of growth occur after a relatively fixed period of time (8). Thus, competence exhibits both nondeterministic and deterministic features.



**Fig. 1.** Stochastic distribution of cell fates in bacteria and in insect photoreceptors. (A) Fluorescence micrograph of *B. subtilis* cells containing the coding sequence for GFP fused to the promoter for a gene under the control of the competence regulator ComK. The cells were visualized with a red stain; the green fluorescence reveals the subpopulation of cells that are ON for ComK. The cells are 1 to 2  $\mu$ m in length. (B) Photograph of a whole adult *Drosophila* retina whose R8 photoreceptors were stained with antibodies to the green-sensitive photopigment Rh6 (green) and the blue-sensitive photopigment Rh5 (blue). The horizontal distance between photoreceptors is about 10  $\mu$ m.

Figure 1B shows the retina of *Drosophila*, which has a compound eye composed of multiple-unit eyes known as ommatidia. In each ommatidium, a stochastic choice is made in one of the eight photoreceptor cells (called R7) to become one of two possible cell types (9). Once this choice is made, the R7 cell instructs the photoreceptors lying underneath it (called R8) to express either a blue-sensitive or a green-sensitive rhodopsin photopigment (10). Here too, the choice is made randomly: Each ommatidium makes its choice independently (11).

In both examples, the choice is not simply the equivalent of flipping a coin. Instead, it is biased: For the bacteria, the ratio of competent to noncompetent cells is about 20:80, whereas for the ommatidia, the ratio of blue to green subtypes is 30:70. Interestingly, the 30:70 ratio is conserved between *Drosophila* and the house fly (*Musca*) despite more than 120 million years of evolution (12).

## Noise and Bistability

Stochasticity requires both a means to generate noise and mechanisms to stabilize decisions reached in response to it. Noise can arise from multiple sources, such as variations in the activity of individual genes, cell-to-cell variations in metabolic activity, or fluctuating levels of an external signal (13). For example, a *B. subtilis* cell might enter competence as a response to noise in the intrinsic transcription of the gene encoding ComK (6).

Noise alone is insufficient to create binary switches between alternative cell fates. Fluctuations due to noise are generally small and transient; what is also needed are mechanisms to amplify these fluctuations and then to stabilize one choice or another. Systems of this kind are said to be bistable; that is, the system has two

stable states, each of which is resistant to small perturbations and hence can persist for prolonged periods of time (14). Bistable systems often exhibit a kind of memory known as hysteresis: When a switch is thrown in one direction, it does not readily switch back when the signal is removed. Bistability ensures that once the switch is thrown, the circuit remains locked. Bistability can be achieved by positive autoregulatory loops (Fig. 2A), by double-negative loops (Fig. 2B), or by complex circuits comprising several intermediary loops (Fig. 2C) (15). A classic example is the alternative lytic and lysogenic states of the bacterial virus lambda (16). The virus is locked into lytic or lysogenic modes by mutually antagonistic repressors that inhibit each other's synthesis. When one repressor takes over, even weakly, the system switches for long periods of time in one direction (Fig. 2D).

Bistability requires mechanisms to render the switch hypersensitive, allowing a rapid response once a threshold has been attained. In phage lambda, this is achieved by cooperative DNA-binding interactions among repressor molecules. For *B. subtilis* competence, production of ComK is controlled by a positive feedback loop in which ComK stimulates its own synthesis (5). Hypersensitivity is achieved by cooperative binding of ComK to its promoter. What these systems have

<sup>1</sup>Department of Molecular and Cellular Biology, Harvard University, Cambridge, MA 02138, USA. <sup>2</sup>Center for Developmental Genetics, Department of Biology, New York University, New York, NY 10003, USA.



in common is a hypersensitive switch that is poised on a knife edge and can flip in one direction or the other when pushed by noise.

### Cell-Autonomous Choices

Why is stochastic choice of cell fate advantageous? We address this question first in the case of stochastic choices that are made cell-autonomously. Perhaps the most attractive explanation comes from studies of stochastic switches in bacteria. Bacteria respond to adverse environmental conditions by inducing the expression of adaptive genes. Stochasticity allows bacteria to deploy specialized cells in anticipation of possible adverse changes in the environment. A striking example is the persister state, which is observed in many bacteria (17, 18). Populations of *Escherichia coli* cells are found to contain a tiny subpopulation of cells that have temporarily entered nongrowing or slow-growing states in which they can elude the action of antibiotics that can only kill actively growing bacterial cells. Thus, when a population of *E. coli* cells is treated with (for example) ampicillin, the persister cells survive by virtue of their quiescence. Cells that exit the persister state after the antibiotic treatment has ended resume growth. An appealing interpretation of this phenomenon is that *E. coli* is hedging its bets against the future possibility of encountering antibiotics. If it waited to respond until after the antibiotic was present, it would be too late to adapt and the entire population would die. Indeed, modeling shows that stochastic switching can be favored over mechanisms based on sensing when the environment changes infrequently (19, 20). The mechanism that causes cells to enter the persister state stochastically involves an imbalance between a toxin and its antitoxin encoded by a two-gene module. Normally, the antitoxin is in excess and neutralizes the toxin. However, when the toxin is in excess, cell growth is arrested but the cells are not killed. Rather, they are in stasis.

Another example of apparent bet-hedging is swimming and chaining in *B. subtilis*. Bacterial cells in exponential-phase growth are a mixture of unicellular, motile cells and long chains of nonmotile cells (21). The swimming cells are active for the transcription factor  $\sigma^D$ , which governs motility and the production of enzymes (autolysins) that allow newly divided cells to separate from each other. Conversely, the chains of nonmotile cells are inactive for  $\sigma^D$ . How the cells interconvert between the  $\sigma^D$ -ON and  $\sigma^D$ -OFF states is not known.

What is the biological importance of the alternative swimming and chaining states? An appealing possibility is that the swimmers are nomadic cells in search of new food sources, whereas the chains are sessile cells that exploit the current niche. Thus, *B. subtilis* would appear to hedge its bets against the likelihood that its current food source will be exhausted while at the same time taking full advantage of existing food.

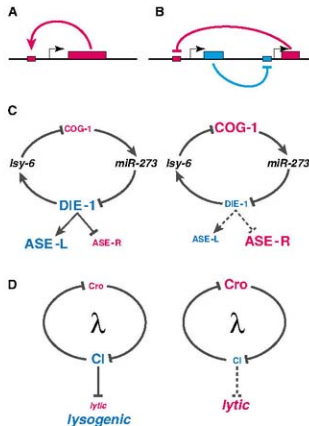
When it comes to cell fate in metazoans, interpretations other than bet-hedging must be in-

voked to explain stochastic choices because all cells depend on one another. Consider the case of olfactory receptors in mammals (22). As for most sensory systems, only one type of olfactory receptor protein is produced in any given olfactory receptor neuron so as to avoid the sensory confusion that would occur if the same cell expressed more than one receptor gene. As the genome of the mouse devotes 4% of its protein-coding sequences to olfactory receptors, representing 1000 genes, the task of achieving this sensory exclu-

sion is formidable. To meet the challenge, each neuron chooses to express one olfactory receptor gene in a stochastic manner and prevents expression of all other olfactory receptor genes in that cell (22). Thus, only one of the 1000 olfactory receptor genes (actually 2000, each gene being represented by two alleles) is randomly activated in any one cell (Fig. 3A). Here, the explanation for using stochasticity is economy: A regulatory circuit designed to choose among 2000 genes in a directed manner would need to be extraordinarily complex.

The olfactory receptor decision is made in a cell autonomous manner (22), but its mechanism remains poorly understood. A similar stochastic choice exists in the distribution of green (M) and red (L) cones in the human retina, which express the genes encoding M and L opsin, respectively. These two genes are located near each other (23). A unique locus control region (LCR) located upstream of both genes is required for their expression, but it can only activate one gene at a time (24). When the LCR connects to the L gene, the connection is stabilized and the cell becomes an L cone for the life of the cell: The M gene cannot be expressed. If the LCR associates by chance with the M gene, the M gene is expressed and the L gene is off (Fig. 3B). Given the diploid nature of mammalian cells, how does the cone cell ensure that only one gene (M or L) is expressed? The answer is that the LCR-L-M cluster is located on the X chromosome. Only one X chromosome is expressed in females because of X chromosome inactivation; males, of course, have only one X chromosome. Interestingly, the system has a built-in way to control the proportion of M/L cones: The gene closest to the LCR has more chances to be chosen by the LCR.

A parallel can be made between the human and *Drosophila* color vision systems. R7 cone photoreceptor cells exist in alternative states that either express *rh3* or *rh4*, which encode rhodopsin molecules that are sensitive to different hues of UV light. The *rh3* and *rh4* genes are not clustered on the chromosome near a common LCR. Rather, the basis for stochasticity is attributed to the expression of a transcription factor called Spineless (9). Somehow, the regulatory protein is only present in a subset of R7 cells and directs these cells to express *rh4* rather than *rh3*. Just how Spineless becomes ex-



**Fig. 2.** Regulatory circuits exhibiting bistability. (A and B) Two kinds of regulatory circuits that can exhibit bistability. (A) Positive feedback loop in which an activator (e.g., ComK) stimulates the transcription of its own gene. Hypersensitivity is achieved by cooperativity among activator molecules in binding to the promoter region for the gene (not illustrated). (B) Double-negative regulatory circuit in which two repressors (e.g., the phage lambda CI and Cro repressors) antagonize the transcription of each other's gene. Hypersensitivity is achieved by cooperativity among repressor molecules in binding to operator sites in DNA. (C) An example of a double-negative regulatory circuit that governs the alternative neuronal ASE-L and ASE-R fates in *C. elegans*. In this case, the two transcriptional regulators (COG-1 and DIE-1) antagonize each other's synthesis indirectly through the action of the microRNAs *Isy-6* and *miR-273*, which block the translation of the mRNAs for COG-1 and DIE-1, respectively. Neurons have the ASE-L fate when DIE-1 levels are high and COG-1 levels are low (left panel) and the ASE-R fate when the opposite is the case (right panel). (D) The classic example of the double-negative circuit [as in (B)] governing the alternative lytic and lysogenic states of phage lambda. When the lambda repressor CI is at high levels, it represses the gene encoding the Cro repressor and genes involved in lytic growth (left panel). Hence, the phage is held in the dormant, lysogenic state. Conversely, when Cro is at high levels, it represses the gene encoding CI, and consequently genes involved in lytic growth are freely expressed (right panel).

pressed exclusively in a subset of R7 cells is not understood.

What is the meaning of stochasticity in the choice of photoreceptor cells in the eye of the fly or of a human? Because the retina in these two very different eyes is composed of many photoreceptors of different types, stochasticity is a simple mechanism to distribute two kinds of photoreceptors (in a particular ratio) across a large field and to avoid repetitive patterns that might limit the ability of the eye to perceive corresponding patterns in the visual field.

### Nonautonomous Choices

In the preceding examples, a cell decides its fate stochastically in a manner that is independent of other cells. In some cases, the choice the cell makes influences the fate of other nearby cells. Nonetheless, the original cell fate decision is made independently of its neighbors. But not all stochastic decisions are cell-autonomous; sometimes the decision is the result of back-and-forth interactions between two (or more) cells. In animals, the simplest system of cell-nonautonomous decision-making is the choice between the anchor cell (AC) and the ventral uterine (VU) cell fates in the nematode *Caenorhabditis elegans* (25). Two neighboring precursor cells of the gonad can choose either fate. The two cells are the products of two parallel lineages that arose from a common ancestor several divisions earlier. However, small differences in the cell cycle of cells in these lineages lead one or the other of the two precursors to be born first. The first-born cell is biased to become the VU cell, but it does not make this decision alone. Rather, the decision-making process involves inhibitory lateral interactions between the two cells via the LIN-12 signaling pathway (known as the Notch pathway in flies and vertebrates).

LIN-12 is a receptor. Its ligand LAG-2 stimulates the activity of the LIN-12 pathway, resulting in the production of additional LIN-12 receptors. This causes the cell to become hypersensitive to the ligand. Meanwhile, high levels of LIN-12 activity decrease the production of the ligand (Fig. 4A). Therefore, a cell that is activated for LIN-12 has diminished capacity to stimulate its neighbor (25). As with the paradigm of bistable processes that are noise-driven, stochasticity in birth order (developmental noise) tips the switch in one direction or the other. This bias is then amplified and locked in by lateral actions between the two cells. The first-born cell

exhibits somewhat higher LIN-12 activity than its neighbor and hence has diminished levels of the LAG-2 ligand. LAG-2 signaling from the second-born neighbor results in yet higher levels of LIN-12 and yet lower levels of ligand in the first cell (25). This sets up a self-reinforcing cycle of lateral inhibition in which the first-born cell achieves higher and higher levels of LIN-12 and the second-born cell, not receiving any stimulation from its neighbor, has lower and lower LIN-12 activity. High LIN-12 activity leads to the VU fate and low activity to the AC fate.

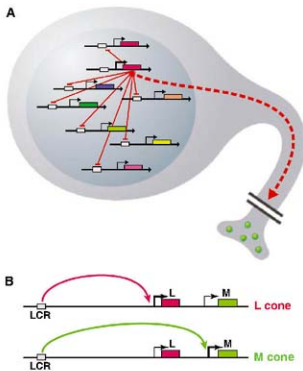
Lateral inhibition is also the basis for non-autonomous cell fate determination in the epidermis of *Drosophila*. One cell in a proneural cluster of equivalent cells becomes a neuroblast, and it must do so to the exclusion of all the other cells in the cluster, which become epidermal cells (3, 26). Flies use the same system as worms to achieve this (Fig. 4A). Notch is the LIN-12 equivalent in flies and its ligand is called Delta, the equivalent of worm LAG-2. The neuroblast fate arises stochastically by transcription noise leading to a very

small increase in the capacity of one cell in the cluster to produce more Delta and hence stimulate the Notch pathway a little more in all of its neighbors. This signaling stimulates Notch production in the neighbors, increasing their sensitivity to Delta and, as in the AC/VU example, setting up a self-reinforcing cycle (Fig. 4A). Meanwhile, the cell that, as a result of noise, exhibited an elevated capacity to signal attains a state of low Notch activity and hence becomes a neuroblast. Each cell in the cluster is competent to become a neuroblast, because killing the neuroblast—and thereby relieving lateral inhibitory signaling—allows another random cell to start the bistable loop again and to adopt the neuroblast fate (3, 26).

An equivalent example of cell-nonautonomous decision making is not known in bacteria. But the phenomenon of "cannibalism" combines stochastic decision-making with reciprocal intercellular interactions (27). When grown under conditions of nutrient limitation, *B. subtilis* enters an elaborate developmental process that culminates in the formation of a dormant spore. Entry into sporulation is governed by the regulatory protein Spo0A, whose activation is governed by a bistable switch (28). Thus, only some cells in the population (about half) are ON for Spo0A and the others are OFF. The Spo0A-ON cells produce toxins that kill the Spo0A-OFF siblings. The dying siblings, in turn, release nutrients that limit further Spo0A activation in the Spo0A-ON cells, thereby arresting sporulation or even reversing it. This phenomenon can also be interpreted as bet-hedging: Uncertain as to whether they are experiencing a temporary shortage of nutrients or the onset of a prolonged famine, the bacteria stall for as long as possible before committing to spore formation, even at the expense of fratricide. In the Notch signaling systems, intercellular interactions reinforce alternative cell fate decisions. By contrast, in the cannibalistic bacterial system, the reverse is true, as the remaining cells are delayed in committing to the spore fate.

### Bistable-Like Switches That Are Hard-Wired by Upstream Events

Not all switches that exist in alternative stable states are driven by noise. Hypersensitive switches that include loops can also be used to lock a cell into one or another fate, but the decision is not left to chance. This is often the case when the deterministic signal is very weak and needs to be reinforced. For instance, in the fly eye, the photoreceptors R3 and R4 are derived from seemingly identical cells. Once again, competition for Notch activation leads to a critical distinction between the R3 or R4 fates, and this distinction is crucial to promote the correct orientation of the ommatidium (29). However, in each of the 800 ommatidia, it is always the cell closer to the equator that becomes R3, the polar one becoming R4 (Fig. 4B). This is because gradients of signaling proteins (e.g., Wnt) that drive the decision to the R4 fate are superimposed on circuitry that, in

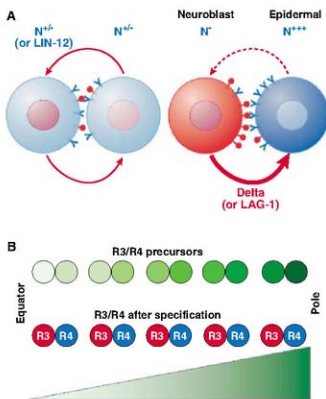


**Fig. 3.** Cell-autonomous cell fate decisions. **(A)** Cell-autonomous stochasticity in a mouse olfactory neuron. The neuron expresses one olfactory receptor gene (red) to the exclusion of all others (blue, brown, dark or light green, yellow, or pink), including the other allele of the "red" gene. The olfactory neuron somehow instructs its target neuron in the olfactory bulb of its choice (dashed arrow). **(B)** Cell-autonomous stochasticity in an Old World primate color vision cone photoreceptor. The choice of a cone photoreceptor to become M (green-sensitive) or L (red-sensitive) depends on the ability of a single locus control region (LCR) located upstream of the L and M genes to contact one of the two genes. If the LCR contacts the M gene, the cone becomes an M cone, and similarly for the L gene. This ensures that only one gene is expressed in each cone. As the LCR-M-L cluster is located on the X chromosome, only one copy is present in males and only one is active in females because of X-chromosome inactivation.

other contexts (e.g., the choice between VU and AC fates in worms; neuroblast commitment in flies), is noise-driven (29, 30). The Wnt protein is at its highest concentration at the north and south poles and at its lowest at the equator. Interestingly, it is not the absolute value of Wnt that matters. Rather, it is the relative difference in the level of signaling perceived, directly or indirectly, between the precursors of R3 and R4 that determines the outcome (29). Thus, for each ommatidium, the precursor cell closest to the pole (where Wnt levels are higher) becomes R4, and the one closest to the equator (where Wnt is relatively lower) becomes R3 (Fig. 4B).

Another example of a bistable-like switch in which the outcome is hard-wired is the establishment of left-right asymmetry between the two neurons (ASE) that sense either Na<sup>+</sup> or Cl<sup>-</sup> in *C. elegans* (15). The switch consists of a complex regulatory loop in which a microRNA (*miR-273*) inhibits translation of the mRNA for a transcription factor (DIE-1), which itself turns on the synthesis of another microRNA (*miR-6*) (Fig. 2C). Closing the loop, *miR-6* blocks the synthesis of the transcription factor (COG-1) that is responsible for directing *miR-273* synthesis. The left and right fates of ASE are specified by DIE-1 and COG-1, respectively (Fig. 2C). The ASE switch has the same logic as the double-negative loop that governs the alternative lytic and lysogenic states of phage lambda (Fig. 2D). Thus, when COG-1 is ON, the synthesis of *miR-273* blocks the production of the transcription factor (DIE-1) for the opposite cell fate (Fig. 2C), just as one lambda repressor blocks the synthesis of the other repressor. Conversely, when DIE-1 is ON, it determines the right-hand fate and induces the synthesis of *miR-6* that prevents the accumulation of the transcription factor COG-1. In contrast to the stochasticity that drives the phage lambda double-negative loop, the choice between the left-hand (ASE-L) and right-hand (ASE-R) fates is instructed by the lineage of the two neurons; ASE-R is always on the right and ASE-L always on the left (15).

Why, then, have a system that resembles a bistable switch? Perhaps the ASE system derives from an ancestral world that made the choice between the right- and left-hand fates stochastically.



**Fig. 4.** Cell-nonautonomous cell fate decisions. **(A)** Lateral inhibition by the Notch (LIN-12) regulatory system in which a stochastic decision by one cell prevents its neighbor(s) from making the same decision. Two neighboring epidermal cells of *Drosophila* start with the same potential to become neuroblasts, both initially exhibiting low Notch activity ( $N^{++}$ ) (left panel). Variations in gene expression in the precursor cells lead one cell (dark pink nucleus) to increase production of the Notch ligand Delta (red lollipop) and to decrease production of the Notch receptor (blue Y) (right panel). This asymmetry sets in motion a self-reinforcing cycle in which one cell ( $N^{-}$ ) becomes less and less sensitive to the Delta ligand and more and more active in producing ligand, whereas the other cell ( $N^{+++}$ ) becomes more and more sensitive to ligand but less active in producing it. The  $N^{-}$  cell becomes a neuroblast while the  $N^{+++}$  cell remains an epidermal cell. **(B)** A Notch-Delta regulatory switch that is biased in one direction by gradients of signaling molecules. Two neighboring photoreceptor cells, R3 and R4, in the fly compete as in (A) to acquire their cell fate. High Notch leads to the R4 cell fate; low Notch leads to the R3 fate. Pairs of R3/R4 precursors are in a gradient of a signaling molecule (e.g., wingless, green). In each pair, the cell positioned at the polar side receives more signal than its more equatorial neighbor, thus biasing it to becoming R4. The decision is then reinforced by lateral inhibition; all equatorial cells become R3 and all polar cells become R4.

If so, only half of the ancestral animals would have had both ASE-R and ASE-L. If having a given neuron on the left, or on the right, proved advantageous, the system might have evolved through "genetic assimilation" into directional asymmetry, in which it is always the same cell type that is on the right, and the other on the left (31). Even though upstream signals dictate the outcome in the contemporary nematode, the circuity of what once was a noise-driven switch might have been maintained in evolution as a way to lock in the decision robustly.

# Conclusions

Most organisms exhibit characteristics that are reproducibly inherited from generation to gener-

ation, which strongly implies that development is hard-wired. However, certain developmental decisions are left to chance, sometimes out of necessity (when the choices are too many to be tightly controlled), or sometimes when it benefits the community to hedge its bets. In yet other cases, particular developmental outcomes are imposed on systems that are otherwise intrinsically stochastic. Nature knows how to make deterministic decisions, but, in contrast to Einstein's view of the universe, she also knows how to leave certain decisions to a roll of the dice when it is to her advantage.

# References and Notes

1. J. Holtzendorff et al., *Science* **304**, 983 (2004); published online 15 April 2004 (10.1126/science.1095191).
2. J. Rine, R. Jensen, D. Hagen, L. Blair, I. Herskowitz, *Cold Spring Harb. Symp. Quant. Biol.* **45**, 951 (1981).
3. J. A. Campos-Ortega, *Curr. Biol.* **7**, R276 (1997).
4. M. Freeman, *Cell* **87**, 651 (1996).
5. H. Masmar, D. Dubnau, *Mol. Microbiol.* **56**, 615 (2005).
6. H. Masmar, A. Raj, D. Dubnau, *Science* **317**, 526 (2007); published online 13 June 2007 (10.1126/science.1140818).
7. G. M. Suel, J. Garcia-Ojalvo, L. M. Liberman, M. B. Dowitz, *Nature* **440**, 545 (2006).
8. G. M. Suel, R. P. Kulkarni, J. Dworkin, J. Garcia-Ojalvo, M. B. Dowitz, *Science* **315**, 1716 (2007).
9. M. F. Wernet et al., *Nature* **440**, 174 (2006).
10. T. Mikkelsson-Davall et al., *Cell* **122**, 775 (2005).
11. M. L. Bell, J. B. East, S. G. Britt, *J. Comp. Neurol.* **502**, 75 (2007).
12. N. Franceschini, K. Kirschfeld, B. Mink, *Science* **213**, 1264 (1981).
13. J. M. Raver, E. K. O'Shea, *Science* **309**, 240 (2005).
14. J. E. Ferrell Jr., *Curr. Opin. Cell Biol.* **14**, 210 (2002).
15. R. J. Johnston Jr., S. Chung, J. F. Eubberger, C. O. Ortiz, O. Hobert, *Proc. Natl. Acad. Sci. U.S.A.* **102**, 12449 (2005).
16. M. Plush, *Curr. Biol.* **17**, R233 (2007).
17. K. Lewis, *Nat. Rev. Microbiol.* **5**, 48 (2007).
18. N. Q. Balaban, J. Merrin, R. Chait, L. Kowalik, S. Leibler, *Science* **305**, 1622 (2004); published online 12 August 2004 (10.1126/science.1099390).
19. M. Thattai, A. van Oudenaarden, *Genetics* **167**, 523 (2004).
20. E. Kowalik, S. Leibler, *Science* **309**, 2075 (2005); published online 25 August 2005 (10.1126/science.1114383).
21. D. S. Kearns, R. Losick, *Genes Dev.* **19**, 3083 (2005).
22. P. Mombaerts, *Curr. Opin. Neurobiol.* **14**, 31 (2004).
23. J. Nathans, *Neuron* **24**, 299 (1999).
24. P. M. Smallwood, Y. Wang, J. Nathans, *Proc. Natl. Acad. Sci. U.S.A.* **99**, 1008 (2002).
25. I. Greenwald, *Genes Dev.* **12**, 1751 (1998).
26. C. Q. Doe, J. B. Skeath, *Curr. Opin. Neurobiol.* **6**, 18 (1996).
27. J. E. González-Pastor, E. C. Hobbs, R. Losick, *Science* **301**, 510 (2003); published online 19 June 2003 (10.1126/science.1086462).
28. J. W. Wessling, I. W. Hannon, O. P. Kuipers, *Mol. Microbiol.* **56**, 1481 (2005).
29. M. Wohlt, A. Tomlinson, *Development* **121**, 2451 (1995).
30. C. H. Yang, J. D. Axelrod, M. A. Simon, *Cell* **108**, 675 (2002).
31. A. R. Palmer, *Proc. Natl. Acad. Sci. U.S.A.* **93**, 14279 (1996).
32. We thank J. Hahn and D. Dubnau for the image of Fig. 1A, D. Vasilakos for the image of Fig. 1B, and J. Blau, D. Dubnau, M. Elowitz, O. Hobert, R. Johnston, E. Kowalik, E. O'Shea, A. Schier, L. Shapiro, G. Suel, E. Tomlinson, and G. Yuan for comments on the manuscript. Supported by NIH grants GM18568 (R.L.) and EY13010 (C.D.).

10.1126/science.1147888



# Bats Limit Insects in a Neotropical Agroforestry System

Kimberly Williams-Guillén,<sup>1,2</sup> Yvette Perfecto,<sup>1</sup> John Vandermeer<sup>1,2</sup>

**T**op-down limitation of herbivores is an important ecosystem service that facilitates agricultural production (1). Several experiments in natural and managed ecosystems demonstrate the importance of avian predators in arthropod control (2). Although insectivorous bats are ex-

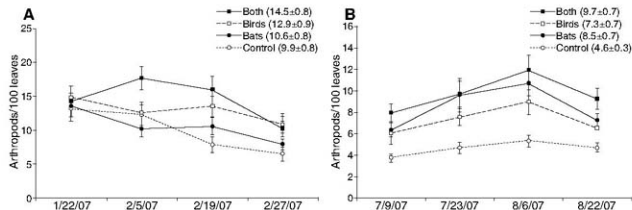
cluded for an 8-week period beginning June 2007 (wet season).

Exclusion of birds and bats resulted in significant increases in total arthropods on experimental plants, although a significant amount of variation was also explained by foliage biomass

solute density of bats versus birds; however, at our site the capture rates (and presumably abundance) and reproductive activity of bats increased during the wet season. Bats' relatively higher surface area may result in greater heat loss and concomitantly higher energy requirements (5), and reproduction increases females' energetic needs; thus, increased bat abundance and reproduction in the wet season may result in an increased impact of bat predation on understory arthropods.

Our results are consistent with arguments that functional diversity is central to the maintenance of ecosystem services (6). In this case, the presence of these two vertebrate taxa maintains a functional difference that enhances the efficacy of arthropod reduction. Previous ex-

closure studies have not differentiated between diurnal and nocturnal predators, attributing observed changes to birds. We suggest that these studies of the impacts of "bird" predation may have underestimated the importance of bats in limiting insects. Bat populations are declining worldwide (7), but monitoring programs and conservation plans for bats lag far behind those for birds. Declining bat populations may compromise critical ecosystem services, making



**Fig. 1.** Mean number of arthropods  $\pm$  SEM per 100 coffee leaves in four enclosure treatments in (A) dry season and (B) wet season. "Both" indicates birds and bats excluded ( $\blacksquare$ ); "Birds," only birds excluded ( $\square$ ); "Bats," only bats excluded ( $\bullet$ ); and "Control," no predators excluded ( $\circ$ ). Numbers after treatment name in legends indicate mean number of arthropods  $\pm$  SEM per 100 leaves across all counts.  $N = 88$  for each season.

pected to have major impacts on arthropods (3), few studies have quantified the effects of bats on standing crops of arthropods. Because all previous enclosure-based studies of avian insectivory have left enclosures up during the night, it is possible that a proportion of predation attributed to birds may represent predation by foliage-gleaning bats. Here, we report an enclosure experiment conducted in a Mexican coffee agroforest, in which we directly measured the impact of predation by foliage-gleaning birds and bats on arthropods found on coffee plants.

We used enclosures made of agricultural netting erected around individual coffee plants in Finca Irlanda, an organic shade coffee plantation harboring abundant populations of  $\geq 120$  bird species and  $\geq 45$  bat species. We established 22 blocks of four treatments: birds-only excluded (enclosure netting in place only during the day), bats-only excluded (netting in place only during the night), both excluded (netting in place day and night), and control (no netting). We visually censused noncolonial arthropods (primarily insects, but also spiders, harvestmen, and mites) on all plants at the beginning of the experiments, every 2 weeks thereafter, and at the end of the experiment. We conducted the experiment for a 7-week period beginning January 2007 (dry season)

and initial arthropod density (table S1). On average, total arthropod densities on plants from which both predators were excluded were 46% higher than those observed on control plants. There was a clear seasonal effect with regard to bats: Although bats did not have significant effects on arthropod densities in the dry season, their impacts were highly significant in the wet season, with an 84% increase in arthropod density in bat-only enclosures, exceeding the effects of birds (Fig. 1). In neither season was there a significant interaction between bats and birds, indicating an additive effect. Regardless of season, arthropod densities increased the most on plants from which both birds and bats were excluded (Fig. 1). These seasonal and additive patterns held for various arthropod taxa (table S2), although only birds significantly reduced spiders. Although predator exclusions resulted in increased arthropod density, no significant differences were seen between treatments in the prevalence or the intensity of leaf damage.

At our site, bats were as important as birds in regulating insect populations across the course of the year. We suspect that increased impacts of birds in the dry season may result from an influx of insectivorous overwintering migrants from North America (4). We have no data on the ab-

an improved understanding of their conservation status vital.

## References and Notes

- G. D. Quilley et al., *Islands Ecol.* **2**, 2 (1997).
- J. Schmitz, P. A. Hambark, A. P. Beckerman, *Am. Nat.* **155**, 141 (2000).
- C. J. Cleveland et al., *Front. Ecol. Environ.* **5**, 238 (2006).
- R. Greenberg, *J. Avian Biol.* **26**, 260 (1995).
- G. L. Graham, *J. Biogeogr.* **17**, 657 (1990).
- D. Tilman et al., *Science* **277**, 1300 (1997).
- A. M. Hutson, S. P. Mickleburgh, P. A. Racey, Eds., *Microchiroptera: Global Status Survey and Conservation Action Plan* (International Union for Conservation of Nature Species Survival Commission IUCN/SSC Chiroptera Specialist Group, Gland, Switzerland, 2001).
- We thank G. Martinez and C. Rossa for field assistance and W. Peters for permission to work in Finca Irlanda. Research supported by NSF grant no. DBI-0610473 to K.W.-G., Bat Conservation International, and NSF grant no. DEB-0349388 to J.P.

## Supporting Online Material

www.sciencemag.org/cgi/content/full/320/S8/7270/DC1  
Tables S1 and S2

13 November 2007; accepted 12 February 2008  
10.1126/science.1152944

<sup>1</sup>School of Natural Resources and Environment, University of Michigan, Ann Arbor, MI 48109, USA. <sup>2</sup>Department of Ecology and Evolutionary Biology, University of Michigan, Ann Arbor, MI 48109, USA.

\*To whom correspondence should be addressed. E-mail: kimw@umich.edu

# Bats Limit Arthropods and Herbivory in a Tropical Forest

Margareta B. Kalka,<sup>1\*</sup> Adam R. Smith,<sup>1</sup> Elisabeth K. V. Kalko<sup>1,2</sup>

Bats are diverse and abundant insectivores that consume many herbivorous insects (1, 2). Insect herbivory, in turn, constrains plant reproduction and influences plant diversity and distribution (3). However, the impact of bat insectivory on plants has never been studied. Previous studies measuring top-down reduction of insect herbivory focused on birds (4–6) but actually measured the combined impact of birds and bats because predator exclosures were left in place day and night. Partitioning the effects of each predator group is essential for both basic ecological questions, such as the top-down maintenance of tropical diversity (3), and applied studies, such as the biological control of agricultural pests (2, 6). We experimentally separated the ecological effects of insectivorous birds from those of insectivorous bats in a tropical lowland forest in Panama.

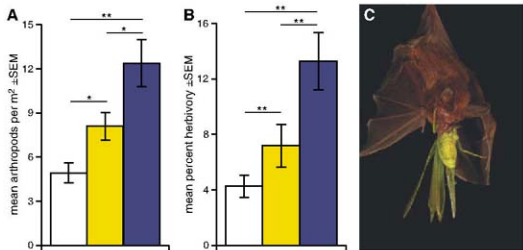
We covered plants with mesh exclosures that permitted access to arthropods but prevented birds or bats from gleaning them off of the plants. However, we left our exclosures in place only during the day or night, allowing us to compare arthropod abundance and herbivory on plants inaccessible to bats (nocturnal exclosures,  $N = 42$ ), plants inaccessible to birds (diurnal exclosures,  $N = 35$ ), and uncovered controls ( $N = 43$ ) in a randomized block design using five common understory plant species. We visually censused arthropods throughout the 10-week study to test the direct effect of treatment (i.e., absence of bats or birds) on insect and other arthropod abundance and measured leaf damage incurred during the study to test the indirect effect of treatment on herbivory (7).

Nocturnal (bat) and diurnal (bird) exclosures each directly increased arthropod abundance on

plants, and nocturnal exclosures had a significantly stronger effect than diurnal exclosures (table S1 and Fig. 1A) [repeated measures generalized linear

and indirectly reduces herbivory. We also show that the ecological effects of insectivorous gleaning bats can be considerably stronger than those of birds. Our estimates of the direct and indirect impacts of both groups are likely conservative because (i) predation away from exclosures also reduces herbivory (2), (ii) very large arthropods may have been excluded along with bats and birds, (iii) predatory arthropods in the exclosures may have mitigated the effect of bird or bat exclusion (table S1), and (iv) top-down reduction of herbivory may be greater in the more-productive

forest canopy (5). Gleaning insectivorous bats are common in tropical and temperate lowland forests; thus, it is likely that bat predation of herbivorous insects reduces herbivory in the temperate zone as well (7). Given their ecological importance, bats should be included in future conservation plans aimed at preserving the integrity of tropical forests and also considered in agricultural management strategies based on natural pest control (2, 6).



**Fig. 1.** (A) Mean number of arthropods per  $m^2$  per census. (B) Mean herbivory as percent of total leaf area. White bars represent controls (birds and bats present); yellow bars, diurnal exclosures (birds absent and bats present); and blue bars, nocturnal exclosures (bats absent and birds present). \* $P < 0.05$  and \*\* $P < 0.005$  according to Tukey's HSD. (C) A bat (*Microcyrtus microtis*) consuming a katydid, Barro Colorado Island, Panama. [Photo: C. Ziegler]

model (GLM) treatment  $F_{2,75} = 17.11$ ,  $P < 0.001$ ; all Tukey's honestly significantly different (HSD) posthoc pairwise comparisons between treatments,  $P < 0.05$ . Control plants averaged  $4.9 \pm 0.7$  (SEM) arthropods per  $m^2$  of leaf area per census; bird-exclosures plants,  $8.1 \pm 1.0$ ; and bat-exclosures plants,  $12.4 \pm 1.6$ . Nocturnal and diurnal exclosures also each indirectly increased herbivory, and nocturnal exclosures again had a significantly stronger effect than diurnal exclosures (Fig. 1B; univariate GLM treatment  $F_{2,75} = 41.89$ ,  $P < 0.001$ , all Tukey's HSD posthoc pairwise comparisons between treatments  $P < 0.005$ ). Control plants averaged  $4.3 \pm 0.8\%$  leaf area lost to herbivory; bird-exclosures plants,  $7.2 \pm 1.6\%$ ; and bat-exclosures plants,  $13.3 \pm 2.1\%$  (7).

Treatment effects on both arthropod abundance and herbivory were consistent across plant species, and potential confounding variables such as light intensity, number of new leaves emerged during the study, and total leaf area neither differed between treatments nor interacted with treatment in either GLM (7).

Our data suggest that bat predation both directly reduces arthropod abundance on plants

## References and Notes

1. M. Kalka, E. K. V. Kalko, *J. Trop. Ecol.* **22**, 1 (2006).
2. C. J. Cleveland et al., *Front. Ecol. Environ.* **4**, 238 (2006).
3. P. V. A. Fine, L. Mesones, P. D. Coley, *Science* **305**, 663 (2004).
4. R. T. Holmes, J. C. Schultz, P. Nothnagle, *Science* **206**, 462 (1979).
5. A. Van Bant, J. D. Braun, S. K. Robinson, *Proc. Natl. Acad. Sci. U.S.A.* **100**, 8304 (2003).
6. R. Greenberg et al., *Ecology* **81**, 1750 (2000).
7. Materials and methods are available on Science Online.
8. M.B.K. was supported by STRI and Bat Conservation International, A.R.S. by SENACYT Panama, and E.K.V. by Deutsche Forschungsgemeinschaft Germany and STRI.
9. A. van Bael and S. A. Mangan assisted with experimental design and data analysis, respectively.

## Supporting Online Material

www.sciencemag.org/cgi/content/full/320/S8/72/1/DC1

Materials and Methods

Table S1

References

26 November 2007; accepted 12 February 2008

10.1126/science.1153352

<sup>1</sup>Smithsonian Tropical Research Institute, Apdo. 0843-03092, Balboa, Ancón, Panama. <sup>2</sup>Institute of Experimental Ecology, University of Ulm, Albert-Einstein-Allee 11, 89069 Ulm, Germany.

\*To whom correspondence should be addressed. E-mail: mbkalka@gmail.com

# Aztec Arithmetic Revisited: Land-Area Algorithms and Acolhua Congruence Arithmetic

Barbara J. Williams<sup>1</sup> and María del Carmen Jorge y Jorge<sup>2\*</sup>

Acolhua-Aztec land records depicting areas and side dimensions of agricultural fields provide insight into Aztec arithmetic. Hypothesizing that recorded areas resulted from indigenous calculation, in a study of sample quadrilateral fields we found that 60% of the area values could be reproduced exactly by computation. In remaining cases, discrepancies between computed and recorded areas were consistently small, suggesting use of an unknown indigenous arithmetic. In revisiting the research, we discovered evidence for the use of congruence principles, based on proportions between the standard linear Acolhua measure and their units of shorter length. This procedure substitutes for computation with fractions and is labeled "Acolhua congruence arithmetic." The findings also clarify variance between Acolhua and Tenochca linear units, long an issue in understanding Aztec metrology.

The largest extant corpus of indigenous written data pertaining to native arithmetic in the Americas is of Aztec origin. Two pictorial manuscripts, the *Códice de Santa María Asunción* (1) and the *Códice Vergara* (2), treat an important bookkeeping matter in Aztec imperial society, that of measuring and recording household landholdings for tribute and other purposes. In an initial study of these codices, Harvey and Williams (3) demonstrated that Aztec property descriptions included the concept of areal as well as linear measures, but they did not pursue the question of how the area values might have been determined. We addressed this issue in a partial study of the *Códice Vergara* (4), finding that recorded areas for ~60% of the sample quadrilateral fields could be obtained by Length times Width and Surveyors' Rule algorithms. Although exact recorded areas were not obtained in the residual cases, discrepancies were consistently small, suggesting an unknown indigenous calculation procedure. Here we report findings from an expanded and more detailed analysis of the *Códice Vergara*, using etic (cultural outsider) and emic (cultural insider) perspectives (5). The etic analysis (framed by modern mathematics reflecting an outsider's view of Aztec culture) concerns evidence for land-area calculation with algorithms and computation with fractions. The emic analysis (framed by concepts with meaning internal to Aztec culture) focuses on interpreting indigenous knowledge and procedures embodied in metrological categories expressed by surveyors and painters in their writings. The results show patterns suggesting principal logical components of Aztec surveyor metrology

and computation. Furthermore, the new analysis provides an important independent basis to interpret and clarify often confusing Colonial-period Spanish and Nahuatl alphabetic texts.

**Data.** Of the extant indigenous land documents, many pertain to the Basin of Mexico, heartland of the Aztec empire constituted by a confederation of three powerful kingdoms (6). When interpreting these manuscripts, it is important to distinguish between two distinct "Aztec" cultural traditions present at European contact, that of the Tenochca (Mexico) of Tenochtitlan and the Acolhua of Texcoco. Each produced land documents that are somewhat different in graphic style (7), in turn reflecting underlying variations in metrology.

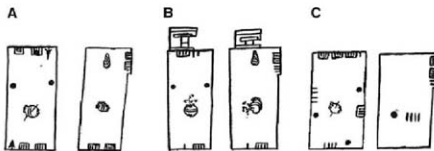
The *Códice de Santa María Asunción* and the *Códice Vergara* are Acolhua pictorials depicting land and population records for two wards in Tepetlaoztoc, an Aztec-period city-state 6 km northeast of Texcoco in the northeastern Basin.

Together they record over 2000 drawings of agricultural properties pertaining to households in 16 named communities as they existed around 1540 to 1544 CE. Below we summarize the records, which are described and analyzed in greater detail elsewhere (8).

*Milcolli* and *tlahuemantli* drawings. Agricultural fields of each property holder are depicted twice, once with field sidelengths in a section labeled *milcolli*, and again in a section labeled *tlahuemantli*, which records field areas. *Milcolli* drawings are either quadrilaterals or irregular, often many-sided polygons. On each field side, painters indicated sidelength distances in standard linear measures with number glyphs (Fig. 1). The Acolhua did not express the standard unit glyphically, but Nahuatl texts attest that it was the *tlahuemantli*, hereafter referred to as "land rod/s" (T) (9). According to the Acolhua native chronicler Alva Ixtlilxochitl (10), this measure equaled three Spanish *varas* (taken here to be 0.83 m  $\times$  3, ~2.5 m). Sometimes a glyph for arrow, heart, or hand follows the standard "land rods." These refer to a distance remaining on a field side that is shorter than one "land rod." We label them "monads" because they are neither subdivided nor do they appear as multiples. No more than one monad glyph occurs on the same field side (11).

Other than sidelengths, the *milcolli* sections in the codices provide little data relevant to etic analysis of area calculation. The properties are not drawn to scale, and we find no direct evidence of angle measurement. If other measurements such as height and triangular subdivisions of quadrilaterals were made (which we suspect), they were not recorded in these codices.

In the *tlahuemantli* registers, area values in "land rods" (T<sup>2</sup>) are framed by an abstract rectangle, usually with a protruding tab in the upper right corner. The frame provides three places in which to register numbers in base-20 positional notation. The values of the number



**Fig. 1.** Paired drawings of perimeter dimensions (*milcolli*) and RAs (*tlahuemantli*) of fields in the *Códice Vergara*. Sidelengths are in standard "land rods" (T); lines equal 1T and solid circles equal 20T. Monad units shorter than 1T are represented by hand, heart, and arrow glyphs. One of these (arrow) appears in A. Abstract frames record RAs in T<sup>2</sup>. Lines in the upper right tab equal 1T<sup>2</sup>, lines on the bottom margin and in the center equal 20T<sup>2</sup>, solid circles equal 400T<sup>2</sup>. (A) The RA = 210T<sup>2</sup>, computed exactly by multiplying length times width with ACA for 2 arrows = 1T (Loc. 1-142). (B) Applying the Surveyors' Rule and ACA for 5 hearts = 2T yields the RA of 128T<sup>2</sup> (Loc. 1-73). (C) The RA of 492T<sup>2</sup> is obtained by using ACA for 5 hands = 3T and the Surveyors' Rule (Loc. 2-30). Besides number symbols, drawings usually display a soil glyph in the center, and on the top margin of abstract frames a concomb glyph flags areas less than 400T<sup>2</sup>.

<sup>1</sup>Department of Geography and Geology, University of Wisconsin-Rock County, Janesville, WI 53546, USA. <sup>2</sup>Instituto de Investigaciones en Matemáticas Aplicadas y en Sistemas, FENOMEC, Universidad Nacional Autónoma de México, Ciudad Universitaria, 04510 México D.F., México.

\*To whom correspondence should be addressed. E-mail: mcj@myim.unam.mx.



glyphs depend on their placement within the frame line (Fig. 1). Monads do not occur on any *tlahuemantli* drawings, signifying that area values were recorded only as  $T^2$  integers.

**Method.** We examined the 408 *milcoicoli* quadrilateral fields of all five Codex Vergara localities and eliminated 41 from further consideration as detailed in table S1. The resultant Vergara database consists of 367 *milcoicoli* and matching *tlahuemantli* fields (90% of the quadrilateral universe). In our calculations (table S2), field sides are labeled  $a, b, c$ , and  $d$  proceeding clockwise from the left side of each quadrilateral. Given field sidelengths in “land rods,” we tested area algorithms from simple to complex (ranked by the number of operations required) and compared our computed area (CA) with the Acolhua recorded area (RA). Initially we ignored monads and used only integer sidelengths. A test algorithm was deemed successful if the error ( $E$ ) = 0 ( $E = CA - RA$ ). If test algorithms failed, we sought new rules by selecting the factors that could reproduce the RAs resulting from their prime number decomposition. If these two procedures failed, in a final step we integrated monads into calculations.

Our method presupposes that surveyor arithmetic was practical, simple, and efficient. Faced

with procedural choices, we presumed that surveyors tended to use rounding in order to work with integers of standard linear distance, and that they utilized algorithms that squared up field shapes or balanced one operation with another. Anecdotal evidence suggests such practices are quite natural, and they are readily observable in everyday measuring procedure.

**Acolhua area algorithms.** We obtained most Acolhua RAs by applying one of five area algorithms. The most frequent, and least complex arithmetically, is multiplication of two adjacent sides (Rule 1). Nearly one-third of the quadrilaterals in the Vergara database have adjacent sides measuring either 20T by 20T or 20T by 10T ( $n = 108$  of 367). For all of these fields, multiplication of adjacent sides yields the exact RA, suggesting that the field side angles are 90° and that the field shapes approximate squares and rectangles. For irregular quadrilaterals, where length is defined as side  $a$  or  $c$ , and width as side  $b$  or  $d$ , multiplication of a set of adjacent sides also may produce  $E = 0$ . More complex is a related algorithm in which RAs are obtained by multiplication of the average length of one set of opposite sides by an adjacent side (Rule 2), thus introducing the operations of addition and division.

If these algorithms failed to produce the RA, we then applied the Surveyors' Rule (Rule 3), a method of area computation used by Sumerians and later by Romans (12, 13). It approximates quadrilateral area by multiplication of the average lengths of opposite sides:  $A = (a + c)/2 \times (b + d)/2$ .

Some Acolhua RAs are prime numbers ( $n = 17$ ). These can result only if area computation couples addition or subtraction with multiplication operations; otherwise, multiplication involves a fractional number. In analyzing primes, it became apparent that some RAs of quadrilaterals with unequal sides are obtained by what we call the Triangle Rule (Rule 4). In this procedure, a given quadrilateral is divided by a diagonal, whereby the quadrilateral area equals the sum of half the product of adjacent sides:  $A = ab/2 + cd/2$ , or  $A = ad/2 + bc/2$ , using the right or left diagonal, respectively (14).

Prime number decomposition also reveals that some areas are derived by adding/subtracting the same unit (1T or 2T) to/from adjacent sides and multiplying the modified sidelength numbers. Operations with this Plus-minus Rule (Rule 5) balance each other, and although not always, tend to square-up field shapes. Finally, a category of miscellaneous rules applies to a small number of fields where areas are obtained with low frequency or unique algorithms (see sample calculations for Rules 1 to 5 in Table 1 and miscellaneous rules in table S2).

Whether our methods successfully reconstruct Acolhua area algorithms is debatable, because at present we lack indigenous worksheets or other evidence of Acolhua calculations “in progress.” It is noteworthy, however, that usually only one algorithm results in  $E = 0$  for a given set of sidelengths. For example, the Triangle Rule gives the same results as the Surveyors' Rule only if one pair of opposite sides is equal. Similarly, when applying the Length times Width Rule to irregular quadrilaterals, multiplication of each possible set of adjacent sides often results in large variances in area values. Thus, exactly obtained RAs strongly suggest that our computation method is the same as (or functionally equivalent to) indigenous arithmetic procedures.

**Monads, Acolhua congruence arithmetic, and metric equivalents.** Using sidelength integers, we obtain exact RAs for 218 fields with the five described algorithms and miscellaneous category (Table 2). In many other instances ( $n = 69$ ), our results closely, but not precisely, match those of the Acolhua surveyors. These small discrepancies between RAs and CAs appear to relate to the use of distance monads.

**Arrow: Cenmil.** We achieved the RAs for most quadrilaterals without considering sidelength monads; therefore, we expected that Acolhua surveyors did likewise. One special field, however, demonstrated otherwise. A rectangle with length 20T and width 10T plus an arrow has a RA of 210T<sup>2</sup>, which is exactly obtained by ascribing a value of 0.5T to the arrow monad:

**Table 1.** Calculation examples of algorithms yielding Acolhua recorded areas.

Field id.*	Sidelengths <i>a, b, c, d</i> in (T) "land rods" and monads†				Recorded area (T <sup>2</sup> )	Calculated area (T <sup>2</sup> )‡
<i>Multiplication of two adjacent sides</i>						
1-207-31	20 + ht	19 + hd	20 + ht	19 + a	380	20 × 19 = 380
3-50-7	17	23	16	24	391	17 × 23 = 391
<i>Average length of one pair of opposite sides times an adjacent side</i>						
4-27-16	42	12	40	11	451	11 × (42 + 40)/2 = 11 × 41 = 451
5-12-2	52	21	56	13	884	13 × (21 + 13)/2 = 52 × 17 = 884
5-145-31	40	8	27	24	432	27 × (8 + 24)/2 = 27 × 16 = 432
<i>Surveyors' Rule, <math>A = (a + c)/2 \times (b + d)/2</math></i>						
5-111-21	26	32	30	10	588	(26 + 30)/2 × (32 + 10)/2 = 28 × 21 = 588
5-46-4	23	15 + hd	25 + hd	11	312	(23 + 25)/2 × (15 + 11)/2 = 24 × 13 = 312
1-2-1	16	10	11	9	126	(16 + 11)/2 = 13.5ru = 14, (10 + 9)/2 = 9.5rd = 9, 14 × 9 = 126
<i>Triangle Rule, <math>A = (a \times b)/2 + (c \times d)/2</math>, or <math>(a \times d)/2 + (b \times c)/2</math></i>						
2-2-1	41	11	35	8 + a	366	(41 × 11)/2 = 225.5ru = 226, (35 × 8)/2 = 140, 226 + 140 = 366
2-30-6	24	16	25	24	492	(24 + 16)/2 × (24 + 25)/2 = 192 + 300 = 492
5-34-3	49	14	47	12 + a	623	(49 × 12)/2 + (14 × 47)/2 = 294 + 329 = 623
<i>Plus-minus Rule, one sidelength +1 or +2 times another sidelength -1 or -2</i>						
1-106-25	16	8	16	7	126	(16 - 2) × (7 + 2) = 14 × 9 = 126
5-139-30	18	19	13	13 + a	252	(19 - 1) × (13 + 1) = 18 × 14 = 252
1-189-27	14	6	13	6	75	(14 + 1) × (6 - 1) = 15 × 5 = 75

\*Field id.: locality number 1 to 5-field number consecutive within locality-household number consecutive within locality.

†Sidelengths clockwise from left field margin; monads: a, arrow; ht, heart; hd, hand representing distances shorter than (T).

‡Monads are not required in these computations. Abbreviations: ru, round up to integer; rd, round down to integer.

RA =  $20T \times 10.5T = 210T^2$  (Fig. 1A). This case provides empirical indigenous evidence, later confirmed by many other RA computations, that the arrow in the Tepetlaoztoc data has a value of  $\frac{1}{2}$  "land rod." The computationally derived value is consistent with dictionaries and Colonial-period land documents in which an arrow glyph, or its gloss *cenmitl*, is often translated into Spanish as *media de la brazza*, " $\frac{1}{2}$  a standard linear measure" (15). The relation between arrows and "land rods" thus defines a 2:1 proportion; that is, if  $a$  is an arrow, then  $2 \times a = 1T$  (Fig. 2). This proportion is used to compute areas, just as in an analogous way congruence classes are found if  $(2 \times \text{arrow})$  were the modulus (16). In other words,

for the above-mentioned rectangle, the RA is calculated as

$$\begin{aligned} RA &= 20T \times (10 + a)T \\ &= 200T^2 + (20 \times a)T^2 \\ &= 200T^2 + 10 \times (2 \times a)T^2 \\ &= (200 + 10)T^2 \\ &= 210T^2 \end{aligned} \quad (1)$$

This type of computation we call "Acolhua congruence arithmetic" (hereafter ACA).

The 2:1 proportion of arrows to "land rods" also applies in a different and very important operational context. For example, one field has sidelengths of 13, 7, 12, and 6: No monads

are depicted in the perimeter (Loc. 4, 43). The area by the Surveyors' Rule is  $(13T + 12T)/2 \times (7T + 6T)/2 = (12.5T) \times (6.5T) = 81.25T^2$ . The RA of  $81T^2$  results by including  $0.5T$  in the calculations and rounding down. In ACA the area is


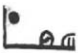



$$\begin{aligned} (13T + 12T)/2 &= 12T + a, (7T + 6T)/2 \\ &= 6T + a, \\ RA &= (12 + a)T \times (6 + a)T \\ &= (72 + 18a + a^2)T^2 \\ &= 81T^2 + 9 \times (2 \times a)T^2 + a \times a - (72 + 9)T^2 \\ &= 81T^2 \end{aligned} \quad (2)$$

Because Acolhua areas were recorded only as  $T^2$  integers, the  $a^2$  term is dropped. Even though perimeter sidelengths did not include arrows, this example and others provide direct evidence that a proportion of 2 arrows = 1T was used arithmetically in computation (see sample calculations with monads in Table 3 and table S2).

**Heart: Cenyllotli.** Evidence that Acolhua surveyors used an arrow when averaging sidelengths clarifies possible derivations of other indigenous area values. One frequently replicated pattern is illustrated by a quadrilateral whose sidelengths are 20, 7, 20, and 6 and RA =  $128T^2$  (Fig. 1B). According to the Surveyors' Rule, area is  $(20T + 20T)/2 \times (7T + 6T)/2 = (20T) \times (6.5T) = 130T^2$ . However, the RA is obtained exactly by multiplying  $20T$  by  $6.4T$ , instead of  $6.5T$ . Assuming  $0.4T$  ( $\frac{2}{5}T$ ) represents a monad other than an arrow, of the two other monads depicted in field perimeters—hands and hearts—the heart is the likely pictograph, because in other sources it is similarly defined as  $\frac{2}{5}$  of a *brazza*. Applying a proportion of 5 hearts to 2 "land rods,"  $5 \times ht = 2T$ , where  $ht$  is heart, in this case ACA for the RA is

$$\begin{aligned} (20T + 20T)/2 &= 20T, (7T + 6T)/2 \\ &= 6T + a - \frac{6T}{5} + ht, \\ RA &= 20T \times (6 + ht)T \\ &= 120T^2 + 20 \times htT^2 \\ &= 120T^2 + 4 \times (5 \times ht)T^2 \\ &= (120 + 4 \times 2)T^2 \\ &= 128T^2 \end{aligned} \quad (3)$$

**Hand: Cemmatl.** When averaging, in some cases substitution of  $0.5T$  by  $0.6T$  yields the RA. Assuming  $0.6T$  is also monad, it would be longer than an arrow and probably corresponds to the hand glyph, the other of the three monads depicted in *milcochilli* perimeters. The hand glyph usually is translated into Spanish as a *brazza de medir*, "a unit of measure." However, the hand glyph does not symbolize the standard land measure in the Tepetlaoztoc codices because the hand is depicted rarely and is placed at the end of the circle-and-line number sequence denoting "land rods." Rather,  $hd = 0.6T = \frac{3}{5}T$ , where  $hd$  is hand. A proportion of 5 hands equal 3 "land rods," ( $5 \times hd = 3T$ ), applies for example in a quadrilateral whose sidelengths are 24, 16, 25, and 24 and RA =  $492T^2$  (Fig. 1C). The Surveyors' Rule gives  $(24T + 25T)/2 \times (16T + 24T)/2 =$

Monad glyphs in Acolhua land documents	Glosses Nahuatl	Proportion of monads to standard "land rods" (T)	Fractional equivalent of (T)	Metric equivalent (1T equals 2.5 m)
	Cemmatl one hand	5 : 3	3 / 5	1.5 m
	Cenyllotli one heart	5 : 2	2 / 5	1.0 m
	Cemomilt one bone	5 : 1	1 / 5	0.5 m
	Cemacolli one arm	3 : 1	1 / 3	0.83 m
	Cemmitl one arrow	2 : 1	1 / 2	1.25 m

**Fig. 2.** Acolhua equivalences inferred from computation of RAs. Illustrations of hand, heart, and arrow are from (2). Bone and arm from (17) are tentatively proposed glyphic referents for proportions 5:1 and 3:1. Alternate reading of the arm glyph may be *cenciacatl* (21, 22).

**Table 2.** Quadrilateral frequency where CA = RA, by algorithm.

Algorithm	Computation requiring integers only	Computation requiring monads					Totals
		Arrow	Heart	Hand	Bone	Arm	
Rule 1: Multiplication of two adjacent sides	139	2	0	0	0	0	141
Rule 2: Average length of one pair of opposite sides times an adjacent side	9	4	3	1	0	4	21
Rule 3: Surveyors' Rule	33	19	8	1	3	5	69
Rule 4: Triangle Rule	6	6	4	1	0	0	17
Rule 5 Plus-minus Rule	12	0	0	0	0	0	12
Rule 6: Miscellaneous, unique, or low frequency algorithms	19	6	0	1	1	0	27
Totals (Vergara database $n=367$ )	218	37	15	4	4	9	287

**Table 3.** Examples of algorithm calculations with monad ACA where CA = RA.

Field id.*	Sidelengths $a, b, c, d$ in (T) "land rods" and monads†				Recorded area (T <sup>2</sup> )	Calculated area (T <sup>2</sup> )‡
3-26-5	19	20	18	20	372	<i>cemmatt</i> : 5 hands = 3 "land rods" <i>Surveyors' Rule</i> $(19 + 18)/2 = 18 + a - 18 + \text{hd}, 20 \times (18 + \text{hd}) = 360 + 20 \times \text{hd}$ $= 360 + 4 \times (5 \times \text{hd}) = 360 + 4 \times 3 = 360 + 12 = 372$
3-86-5	15	25	17	34	470	<i>Triangle Rule</i> $(34 \times 15)/2 = 255, (25 \times 17)/2 = 212.5 \rightarrow 212 + 5 = 217$ $= 200 + 25 \times \text{hd} = 200 + 5 \times (5 \times \text{hd}) = 200 + 5 \times 3$ $= 215, 255 + 215 = 470$
5-120-23	22	17	19	18	350	<i>Average of one pair of opposite sides times an adjacent side</i> $(22 + 19)/2 = 20 + a - 20 + \text{hd}, 17 \times (20 + \text{hd}) = 340 + 3 \times (5 \times \text{hd}) +$ $2 \times \text{hd} = 340 + 3 \times 3 + 2 \times \text{hd} = 349 + 2 \times \text{hd} \text{ ru} = 350$
3-10-2	42	17	41	9	538	<i>Surveyors' Rule</i> $(42 + 41)/2 = 41 + a - 41 + \text{ht}, (17 + 9)/2 = 13, (41 + \text{ht}) \times 13$ $= 533 + 13 \times \text{ht} = 533 + 2 \times (5 \times \text{ht}) + 3 \times \text{ht} = 533 +$ $2 \times 2 + 3 \times \text{ht} = 533 + 4 + 3 \times \text{ht} = 537 + 3 \times \text{ht} \text{ ru} = 538$
4-47-11	16	10	15	15	191	<i>Triangle Rule</i> $(16 \times 10)/2 = 80, (15 \times 15)/2 = 112.5 \rightarrow 112 + 5 = 117$ $= 105 + 15 \times \text{ht} = 105 + 3 \times (5 \times \text{ht}) = 105 + 3 \times 2 = 111,$ $111 + 80 = 191$
5-144-31	22	20	23	21	448	<i>Average of one pair of opposite sides times an adjacent side</i> $(22 + 20)/2 = 20 + a - 20 + \text{ht}, 22 \times (20 + \text{ht}) = 440 + 22 \times \text{ht}$ $= 440 + 4 \times (5 \times \text{ht}) + 2 \times \text{ht} = 440 + 4 \times 2 + 2 \times \text{ht} \text{ rd} = 448$
1-179-28	22	6	21	12	191	<i>Surveyors' Rule</i> $(22 + 21)/2 = 21 + a - 21 + \text{bn}, (12 + 6)/2 = 9, (21 + \text{bn}) \times 9$ $= 189 + 9 \times \text{bn} = 189 + 5 \times \text{bn} + 4 \times \text{bn} = 189 + 1 + 4 \times \text{bn}$ $= 190 + 4 \times \text{bn} \text{ ru} = 191$
4-21-4	20	20	21	16	364	<i>Average of two adjacent sides times another side</i> $(21 + 16)/2 = 18 + a - 18 + \text{bn}, 20 \times (18 + \text{bn}) = 360 + 20 \times \text{bn}$ $= 360 + 4 \times (5 \times \text{bn}) = 360 + 4 = 364$
5-170-36	37	30	38	28	1079	<i>Surveyors' Rule</i> $(37 + 37)/2 = 37 + a - 37 + \text{bn}, (30 + 28)/2 = 29, (37 + \text{bn}) \times 29$ $= 1073 + 29 \times \text{bn} = 1073 + 5 \times (5 \times \text{bn}) + 4 \times \text{bn}$ $= 1073 + 5 + 4 \times \text{bn} = 1078 + 4 \times \text{bn} \text{ ru} = 1079$
1-60-14	34	20	25	20	586	<i>Surveyors' Rule</i> $(34 + 25)/2 = 29 + a - 29 + \text{am}, (20 + 20)/2 = 20,$ $(29 + \text{am}) \times 20 = 580 + 20 \times \text{am} = 580 + 6 \times (3 \times \text{am}) + 2 \times \text{am}$ $= 580 + 6 + 2 \times \text{am} = 586 + 2 \times \text{am} \text{ rd} = 586$
1-182-29	5 + a	9	36	8	300	<i>Average of one pair of opposite sides times an adjacent side</i> $(9 + 8)/2 = 8 + a - 8 + \text{am}, 36 \times (8 + \text{am}) = 288 + 36 \times \text{am}$ $= 288 + 12 \times (3 \times \text{am}) = 288 + 12 = 300$
2-16-5	29	13 + a	30 + a	14	400	<i>Average of one pair of opposite sides times an adjacent side</i> $(13 + 14)/2 = 13 + a - 13 + \text{am}, 30 \times (13 + \text{am}) = 390 + 30 \times \text{am} =$ $390 + 10 \times (3 \times \text{am}) = 390 + 10 = 400$
2-14-5	36	12	37	12	438	<i>Surveyors' Rule</i> $(36 + 37)/2 = 36 + a, (12 + 12)/2 = 12, (36 + a) \times 12 = 432 +$ $12 \times a = 432 + 6 \times (2 \times a) = 432 + 6 = 438$
3-61-7	17	11	19	14	227	<i>Triangle Rule</i> $(17 \times 11)/2 = 93.5 \rightarrow 93 + 5 = 98$ $= 85 + 8 + 1 \times a = 93 + 1 \times a \text{ ru} = 94, (19 \times 14)/2 = 133,$ $94 + 133 = 227$
5-140-30	28	11	27	9 + a	257	<i>Multiplication of two adjacent sides</i> $27 \times (9 + a) = 243 + (27 \times a) = 243 + 13 \times (2 \times a) + 1 \times a$ $= 243 + 13 + 1 \times a = 256 + 1 \times a \text{ ru} = 257$

\*Field id: See Table 1.

†Sidelengths: See Table 1.

‡Monads: See Table 1. In addition: bn, bone; am, arm. In averaged sidelengths, 0.5 = a. Abbreviations: See Table 1.



$24.5T \times 20T = 490T^2$ . In ACA for hands, the exact RA for this field is computed as

$$\begin{aligned}(24T + 25T)/2 &= 24T + a - \\ 24T + hd, (16T + 24T)/2 &= 20T, \\ RA &= (24 + hd)T \times 20T \\ &= 480T^2 + (20 \times hd)T^2 \\ &= 480T^2 + 4 \times (5 \times hd)T^2 \\ &= (480 + 4 \times 3)T^2 \\ &= 492T^2\end{aligned}\quad (4)$$

**Bone:** *Cemomil*. Some RAs are obtained arithmetically by substituting  $0.2T$  ( $\frac{1}{5}T$ ) for  $0.5T$ . For example, for sidelengths  $21 + a$ ,  $12 + a$ ,  $19$ , and  $17$ , and an RA =  $284T^2$ , the Surveyors' Rule (ignoring sidelength monads) gives  $(21T + 19T)/2 \times (12T + 17T)/2 = 20T \times 14.5T = 290T^2$ . In ACA with a proportion of 5:1, the RA is calculated as

$$\begin{aligned}(21T + 19T)/2 &= 20T, (12T + 17T)/2 \\ &= 14T + a - 14T + \frac{1}{5}T, \\ RA &= 20T \times (14 + \frac{1}{5})T \\ &= 280T^2 + 20 \times \frac{1}{5}T^2 \\ &= 280T^2 + 4 \times (5 \times \frac{1}{5})T^2 \\ &= (280 + 4)T^2 \\ &= 284T^2\end{aligned}\quad (5)$$

Although undepicted in the Tepetlaozotoc codices, we suspect  $\frac{1}{5}T = \frac{1}{5} \times 2.5 \text{ m} = 0.5 \text{ m}$  and represents a monad unit in Acolhua metrology. As evidence, another Acolhua document of the same vintage, the Oztotitlac Land Map (17), pictures not only hands, hearts, and arrows but also monad glyphs that unambiguously read "bone" (*omil*) in Nahuatl epigraphy. The reading is confirmed by *cemomil* glosses for bone glyphs in Tenochca documents. Thus, we tentatively identify the unknown Tepetlaozotoc monad as an Acolhua "bone" equivalent to  $0.5 \text{ m}$ , a length slightly longer than what Cline (18) and Hayes (19) suggest for the Oztotitlac bone glyph (20).

**Arm:** *Cemacoli*. In addition to the bone, heart, hand, and arrow (fractions  $\frac{1}{5}T$ ,  $\frac{2}{5}T$ ,  $\frac{3}{5}T$ , and  $\frac{4}{5}T$ , respectively), another monad is suggested by nine quadrilaterals in which exact RAs are obtained by replacing  $0.5T$  with  $\frac{1}{5}T$ , a length equivalent to  $\frac{1}{5} \times 2.5 \text{ m} = 0.83 \text{ m}$  (one *vara*). Probably this fraction represents computation with "one-arm," *cemacoli*. A drawing of a bent arm from the shoulder to the tips of outstretched fingers typically reads "acoli" in Acolhua and Tenochca epigraphy, and one such monad glyph appears on the Oztotitlac Land Map mentioned above. The arm glyph in Tenochca texts is often glossed "media braza," i.e., one-half of the two-*vara* "braza":  $\frac{1}{2} \times 1.67 \text{ m} = 0.83 \text{ m}$ , a metric distance that coincides with the Tepetlaozotoc  $\frac{1}{5}T$ . In this instance, the Acolhua and Tenochca "arm" distances coincide because the relations 3:1 and 2:1 establish proportions vis a vis the 3-*vara* braza and the 2-*vara* braza. The CA of a quad-

rilateral with sidelengths  $32, 11 + ht, 31, 12$ , and  $RA = 351T^2$  exemplifies application of the 3 arms to 1 "land rod" in ACA. Where arm is arm and rd is round down to integer, multiplication of the average length of one pair of opposite sides by an adjacent side gives

$$\begin{aligned}(11T + 12T)/2 &= 11T + a - 11T + am, \\ RA &= 31T \times (11 + am)T \\ &= 341T^2 + (31 \times am)T^2 \\ &= 341T^2 + 10 \times (3 \times am)T^2 + 1 \times am \\ &= (341 + 10)T^2 + 1 \times am \text{ rd} \\ &= 351T^2\end{aligned}\quad (6)$$

**Discussion and conclusions.** The logic of Acolhua land measurement is based on units of standard length and monad distances shorter than the standard. Using an etic perspective, 16th-century Spanish and subsequent scholars often defined monads in terms of fractional parts of Spanish *varas* and *brazas*. In contrast, from the Acolhua (and most likely Tenochca) emic view, each monad was conceptualized as a unitary entity unto itself, not a fraction of a larger unit.

The metrological role of monads generally is presumed to indicate only native concern with precise measurement. This study suggests a considerably more complex function than surveyed-distance units. Our calculations provide strong evidence that the Acolhua computed field areas with ACA based on proportions between monads and the standard linear unit. Long debated, proposed metric equivalents of monads inferred from Colonial-period texts are testable for Acolhua units by computing with ACA applied to their field area records. Our research suggests that among the most commonly used monads, the Acolhua hand measured 1.5 m, the arrow 1.25 m, and the heart 1.0 m. More problematic, the arm may have equaled 0.83 m and the bone 0.5 m.

Except for the 3 arms:1T equivalence, the symmetry of the most frequent proportions is consistent with Mesoamerican metrics in that they are submultiples of 20—2:1, 5:3, 5:2, and possibly 5:1. They resonate with emic emphasis on vigesimal numerology seen in cosmovision, divisions of time, and groupings of objects or people. In Mesoamerica, congruence principles had long been used in calendars to synchronize solar, lunar, and Venus cycles. It is therefore not unexpected that the Acolhua would use ACA in their everyday arithmetic. What is unexpected is to find documentary evidence of such procedures. A persistent question in etic evaluation of Aztec arithmetical accomplishments is whether they used fractions. We suggest that the Acolhua solved the arithmetic problem in an alternate manner by using ACA, thus rendering the etic question moot.

Because hundreds of Acolhua RAs can be replicated through computation, it seems highly improbable that areas were derived by laying out quadrilaterals on fields or by some other physical means, especially given long distances and un-

even terrain. Calculations with the simplest algorithm require multiplication; more complex ones use addition and division as well. Computations yielding the exact RAs imply that the Acolhua approximated areas by rounding and averaging. The algorithms that successfully yield Acolhua RAs are commonly applied in western utilitarian metrology, which suggests that Acolhua categories of field shapes (squares, rectangles, and right-triangles) and their ascribed geometric properties were not unlike European ones.

Among many unresolved questions suggested by this research is an emic explanation for the choice of monads substituting for  $\frac{1}{5}T$  in averaging procedures. More broadly, we wonder what factors determined the choice of algorithms to use in the first place. How accurate Acolhua area values were, while emically satisfactory for their purposes, nevertheless stirs etic curiosity.

## References and Notes

1. Located in the Fondo reservado No. 1497bis, Biblioteca Nacional de México, Universidad Nacional Autónoma de México (UNAM), Mexico City.
2. Located in the Bibliothèque Nationale de France, Ms. Mexicain 37-39, Paris.
3. H. R. Harvey, B. J. Williams, *Science* **210**, 499 (1980).
4. B. J. Williams, A. C. Jorge y Jorge, *Symmetry* **Sci. Sci.** **12**, 185 (2001).
5. T. N. Hoad, K. L. Pike, M. Harris, Eds., *Emics and Etics: the Insider/Outsider Debate* (Sage, Beverly Hills, CA, 1990).
6. P. Carrasco, *The Tenochca Empire of Aztec Mexico: The Triple Alliance of Tenochtitlan, Texcoco, and Tlacopan* (University of Oklahoma Press, Norman, OK, 1999).
7. D. Robinson, *Mexican Manuscript Painting of the Early Colonial Period: The Metropolitan Schools* (Yale Univ. Press, New Haven, CT, 1959).
8. B. J. Williams, H. R. Harvey, *El Códice de Santa María Acapulco: Huastolatl and Lands in Sixteenth Century Tepicostotl* (Univ. of Utah Press, Salt Lake City, UT, 1977).
9. *Papeles de la embajada americana*, Museo Nacional de Antropología, Archivo Histórico, Instituto Nacional de Antropología e Historia, Mexico City.
10. F. de Alva Ixtlilxochitl, *Obras históricas de Don Fernando de Alva Ixtlilxochitl, publicadas y anotadas por Alfredo Chavero* (Editorial Nacional, Mexico City, 1952).
11. With some exceptions, Tenochca and Acolhua property plans share similar numerical symbols, but with differing values. The *cemomil*, "one hand," is the Tenochca standard linear measure and equals two Spanish varas ( $0.83 \text{ m} \times 2 = 1.67 \text{ m}$ ). Thus, it is shorter than the Acolhua three-*vara* "land rod." Unlike the "land rod," the Tenochca *cemomil* is typically glyphed by a hand symbol.
12. H. J. Nissen, P. Damerow, R. K. Englund, *Archaic Bookkeeping: Early Writing and Techniques of Economic Administration in the Ancient Near East*, trans. P. Larsen (Univ. of Chicago Press, Chicago, IL, 1993).
13. E. Robson, *Mesopotamian Mathematics, 2100–1600 BC: Technical Constants in Bureaucracy and Education* (Clarendon, Oxford, UK, 1999).
14. Examples of triangular-shaped field area calculations are found in 6a.
15. Unless otherwise noted, Spanish translations and metric equivalents of native measures not based on Tepetlaozotoc data are drawn from 21–23.
16. Two integer numbers are congruent "modulus  $n$ ," where  $n$  is an integer, if their remainders are the same when



$\theta$ - $\theta'$  interaction. Domains III and IV are also coaxially stacked, as are stems IA and IB in DI.

**Long-range tertiary interactions.** Most of the tertiary interactions proposed for group IIB introns also exist or have an analog in IIC introns. Some of these include  $\alpha$ - $\alpha'$  (25), EBS1-IBS1 (8), EBS3-IBS3 (9),  $\gamma$ - $\gamma'$  (26),  $e$ - $e'$  (26),  $\lambda$ - $\lambda'$  (27),  $\theta$ - $\theta'$  (28),  $\kappa$ - $\kappa'$  (29), and  $\zeta$ - $\zeta'$  (30). Some of these interactions, such as  $\theta$ - $\theta'$ , form a structure exactly as predicted from previous biochemical data (28). In contrast, other predicted interactions, such as  $\alpha$ - $\alpha'$  and  $\zeta$ - $\zeta'$ , have an unexpected structural form (see below). There are also some tertiary contacts that are missing in IIC introns. For example,  $\mu$ - $\mu'$  (31) and the

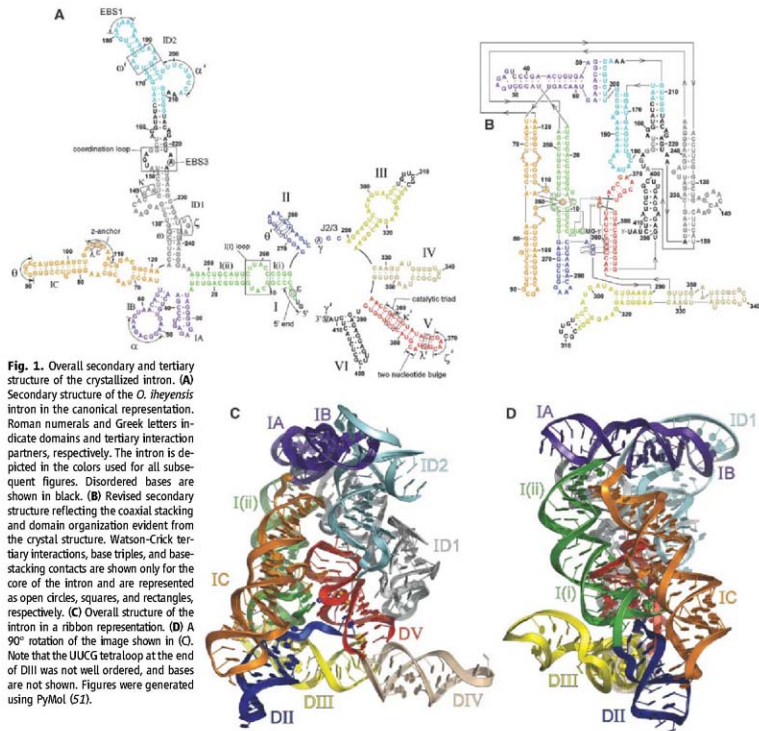
EBS2-IBS2 pairing are absent (18). In addition, there is a new long-range contact,  $\omega$ - $\omega'$ , that only seems to exist in this primitive class of introns.

DI contains numerous conserved sequences and tertiary interactions that are important for maintaining the overall fold of the ribozyme. Consistent with previous folding studies, DI is structured as an autonomous scaffold that appears to organize the other domains (32). The most dominant long-range interaction within DI is the kissing loop between  $\alpha$  and  $\alpha'$  (Fig. 3A). This is a helix of seven consecutive Watson-Crick base pairs, followed and reinforced by a Watson-Crick pair (A50-U198) that points away from the  $\alpha$ - $\alpha'$  helix. The coaxial stacking of stems

IA and IB is essential for properly positioning the  $\alpha$  sequence and for stabilizing the five-way junction in DI. This junction is reinforced by multiple stacking and pairing interactions between stem IA and the junction nucleotides (Fig. 3B and fig. S7B).

The  $\theta$ - $\theta'$  interaction consists of a GCGA tetraloop from stem IC that docks into a receptor at the base of DI. This is a canonical GNRA tetraloop-receptor interaction (30) that positions the conserved  $e'$  sequence within the core of the intron.

An unexpected interaction within DI, designated as  $\omega$ - $\omega'$  (Fig. 3C), places EBS1 near catalytically essential motifs in DV and posi-



**Fig. 1.** Overall secondary and tertiary structure of the crystallized intron. (A) Secondary structure of the *O. iheyensis* intron in the canonical representation. Roman numerals and Greek letters indicate domains and tertiary interaction partners, respectively. The intron is depicted in the colors used for all subsequent figures. Disordered bases are shown in black. (B) Revised secondary structure reflecting the coaxial stacking and domain organization evident from the crystal structure. Watson-Crick tertiary interactions, base triples, and base-stacking contacts are shown only for the core of the intron and are represented as open circles, squares, and rectangles, respectively. (C) Overall structure of the intron in a ribbon representation. (D) A 90° rotation of the image shown in (C). Note that the UUCG tetraloop at the end of DIII was not well ordered, and bases are not shown. Figures were generated using PyMol (52).



tions the 5' splice junction within the intron active site. The  $\omega$ - $\omega'$  interaction involves the formation of a ribose zipper (33) between a small, conserved internal loop ( $\omega'$ ) near EBS1 and stem ID1 ( $\omega$ ).

**Interactions between DI and DV.** The active site is constructed through a network of interactions between the DI scaffold and DV. One of the most important contacts between these do-

main is  $\zeta$ - $\zeta'$ , which consists of a GAAC tetraloop from DV interacting with a receptor in DI (Fig. 1, A and C). This tetraloop-receptor interaction is conformationally unusual and consists only of base stacking between the AAC of the tetraloop and a single, bulged guanine within the receptor. Indeed, this interaction seems to be a new class of tetraloop receptor interaction found only in IIC introns and is identifiable by

a GANC tetraloop sequence, in which the third nucleotide is variable.

Another important connection between DV and DI is  $\kappa$ - $\kappa'$ , which serves to anchor DV within the DI scaffold (29). Although poor density in the  $\kappa$  loop prevents a detailed analysis of molecular features, the two elements of  $\kappa$ - $\kappa'$  are close together and thus consistent with an interaction (Fig. 1C).

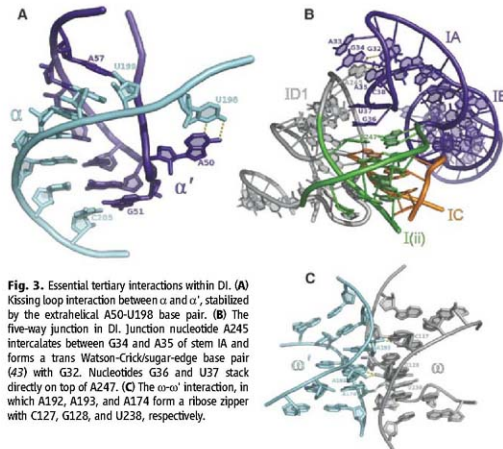
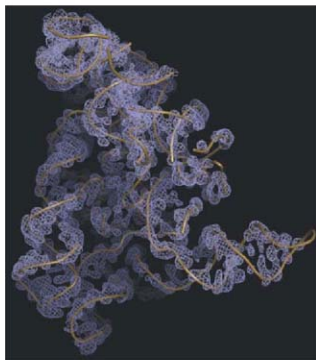
**The z-anchor mediates structural integrity of the core.** Nucleotides 106 to 111, from sub-domain IC, form a series of base pairs, triples, and stacking interactions with three different regions of the intron. Two 160° kinks in the backbone, between nucleotides 109 to 111, cause nucleobases in this region to alternate from side to side (Fig. 4A), forming interactions with disparate parts of the intron and assembling them into a scaffold for the active site. The known  $e$ - $e'$  and  $\lambda$ - $\lambda'$  interactions are components of this larger, functional substructure, which we have named the "z-anchor." The z-anchor has a form and function that is reminiscent of J8/7 in group I introns (34).

The z-anchor makes multiple contacts with the I(i) loop of DI and with the 5' end of the intron. For example, residues G108 and A110 form Watson-Crick pairs with nucleotides C11 and U259 of the I(i) loop (Figs. 1B and 4, A and B), whereas G107 forms a wobble pair with U4 (analogous to  $e$ - $e'$ ), thereby placing the z-anchor near the 5' splice site. In addition to these contacts, the I(i) loop and the 5' end of the intron interact directly through a set of Watson Crick/sugar-edge pairs (Figs. 1B and 4A).

The z-anchor ties this complex of DI constituents to DV via a base triple involving A106 and a base quartet involving G107. The base triple is analogous to the  $\lambda$ - $\lambda'$  interaction that was chemogenetically identified in IIB introns (27). The sugar-edge of A106 forms multiple base and 2'-OH contacts to the sugar-edges of both C367 and G374 in DV (Fig. 4C). The unusual base quartet connects nucleobase and sugar functional groups of G107, U4, A366, and U375 (Fig. 4D). In addition, the I(i) loop and the 5' end of DI each make direct contacts with DV. The highly conserved G5 residue interacts with A376 in the DV bulge, allowing that nucleotide to extrude from the DV helix and thereby support the active-site structure. This elaborate network of tertiary contacts is crucial for intron function because it places the 5' splice site near the bulge of DV and mediates most of the interactions surrounding the DV bulge, thereby stabilizing the catalytic core of the intron.

J2/3 and bulge base C377 form a triple helix with the DV catalytic triad. J2/3 is a highly conserved linker region between domains II and III. Enzymological investigations have shown that J2/3 is important for efficient splicing by group II introns (11, 12), and photo-crosslinking studies have repeatedly placed J2/3 near the catalytic triad (16, 35). In the *O. iheyensis* intron, J2/3 is composed of nucleotides A287, G288,

**Fig. 2.** Experimental, unbiased electron density map at 1.3 $\sigma$ . The structure is slightly rotated from Fig. 1C to better illustrate the quality of the map. A trace of the intron backbone is shown in beige.



**Fig. 3.** Essential tertiary interactions within DI. (A) Kissing loop interaction between  $\alpha$  and  $\alpha'$ , stabilized by the extrahelical A50-U198 base pair. (B) The five-way junction in DI. Junction nucleotide A245 intercalates between G34 and A35 of stem IA and forms a trans Watson-Crick/sugar-edge base pair (43) with G32. Nucleotides G36 and U37 stack directly on top of A247. (C) The  $\omega$ - $\omega'$  interaction, in which A192, A193, and A174 form a ribose zipper with C127, G128, and U238, respectively.

and C289. Nucleobases G288 and C289 insert into the major groove of DV, where they stack directly beneath bulge base C377 (Fig. 5, A and B, and fig. S7C). Each nucleotide of this stacked array (i.e., G288, C289, and C377) forms a base triple with the three nucleotides of the catalytic triad located in DV (residues 358 to 360, Fig. 5B). In essence, the J2/3 strand and the DV stem completely merge, forming a triple helix that brings together catalytically essential residues of the intron (the catalytic triplex).

**The bulge of DV forms an unusual helix.** Base-stacking interactions between the DV bulge and residues G5, G288, and C289 distort the bulge region and induce formation of a short, single-stranded helical structure that spans nucleotides 375 to 379 (Fig. 5A and fig. S7C). This "mini-helix" is comparable in radius and pitch to the  $\alpha$  helices commonly found in proteins.

This structure of DV differs greatly from the conformation of this domain when it is studied in isolation. Previous nuclear magnetic resonance (36) and crystallographic (37) data have indicated that the upper and lower stems of DV are essentially coaxial. However, in the intact intron, these two stems are at an angle of  $\sim 45^\circ$  with respect to each other. This bend serves to move the backbones of the bulge and catalytic triad closer together, to a distance of  $\sim 3$  Å. In addition to the angular orientation of the two helices, the bulge region of DV also differs from previous models in that it is extensively distorted by other intron components. This demonstrates that the entire group II intron structure is essential for inducing a catalytically relevant fold in DV.

**DV is a metal ion-binding platform.** The proximity of backbone moieties in the bulge and the catalytic triad results in the formation of a negatively charged pocket that binds two metal ions ( $M_1$  and  $M_2$ ) (Fig. 6). These two sites were assigned as  $Mg^{2+}$  ions on the basis of  $Yb^{3+}$  soaks.  $Yb^{3+}$  mimics the coordination state of  $Mg^{2+}$  and exhibits strong anomalous scattering, which allows its position to be easily identified within the structure.

$Yb^{3+}$  was observed to bind at only four positions within the intron, three of which were located near the bulge of DV. Two of the  $Yb^{3+}$  sites correspond to electron density observed in the native map and were assigned as the aforementioned  $Mg^{2+}$  ions (Fig. 6). These two positions ( $M_1$  and  $M_2$ ) have very large anomalous signals of 75 $\sigma$  and 57 $\sigma$ . The other two sites do not correspond to any density in the native map and have smaller anomalous signals of only 7 $\sigma$  and 5 $\sigma$ . The third  $Yb^{3+}$  site is near the bulge, where it is located  $\sim 6$  Å from  $M_1$  and  $M_2$ , while the fourth site is located outside the core of the intron altogether. The latter ions may represent low-occupancy  $Mg^{2+}$  sites or they may be specific only for  $Yb^{3+}$ .

Within the metal ion-binding pocket (Fig. 6),  $M_1$  is bound by two inner-sphere ligands, consisting of the O1P of U375 and the O2P of C377.  $M_2$

is bound by three inner-sphere contacts to the O1P of C358, the O2P of G359, and the O1P of C377. Previous biochemical studies on the  $\alpha 5\gamma$  IIB intron have indicated that nonbridging phosphoryl oxygens at the corresponding DV positions are essential for both steps of splicing and, in at least one case, direct binding to metal ions (29, 38, 39), thereby providing functional evidence for the assignment of  $M_1$  and  $M_2$  as catalytic metal ions. The distance between metals  $M_1$  and  $M_2$  is 3.9 Å, which matches the ideal distance of 3.9 Å invoked for the classic two-metal ion reaction mechanism of the group I intron and protein phosphotransferases such as DNA and RNA polymerase (40, 41). These two metal ions reside on the surface of DV and are therefore accessible to both the 5' and 3' splice sites (fig. S8).

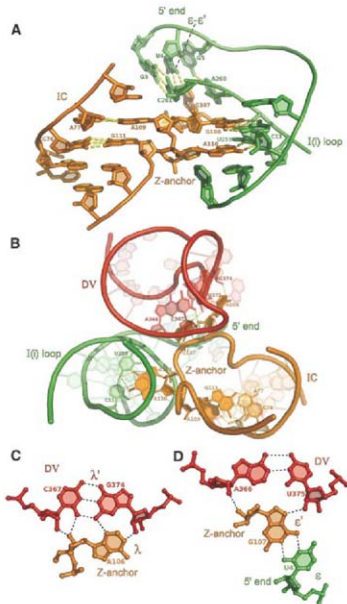
#### Evidence that DIII is an allosteric effector.

DIII contains a conserved, purine-rich internal loop that forms a curved, tightly wound RNA helix that is similar to loop motifs containing sheared G-A and A-A pairs (42). Density for many nucleobases in this region is weak, so a

precise description of the pairing is not warranted. However, nucleotides in the conserved internal loop of DIII are in a position to form multiple base pairs and 2'-OH contacts with the basal regions of subdomain I(i) and DII. This is consistent with previous biochemical data indicating that DII helps position DIII (10). There is good base density for G320, indicating that it forms a trans sugar-edge/sugar-edge base pair (43) with G267, resulting in stacking of G320 upon A268 at the bottom of the DII stem. Thus, DIII is tied rigidly to the junction between DII and DIII, which serves to position the adjacent J2/3 nucleotides within DV. Notably, a  $140^\circ$  kink in the backbone between the A290 of DIII and C289 of J2/3 (Fig. 5A) assists the insertion of J2/3 into DV. DIII also appears to stabilize the I(i) loop, which helps create a foundation for the active site through interactions with the z-anchor.

Enzymological studies have shown that DIII is not strictly required for catalysis, but it greatly accelerates the rate constants for splicing and for ribozyme reactions of the intron (44). The struc-

**Fig. 4.** The z-anchor and its network of interactions with D(i) and DV. (A) Nucleotides 108 to 111 form an alternating "zig-zag" pattern which, together with 106 and 107, assemble the I(i) loop, the 5' end of the intron, and DV. (B) Top view of the z-anchor, illustrating its role in assembling multiple intron substructures. (C) Base triple between A106 and the C367-G374 base pair of DV (equivalent to  $\lambda$ - $\lambda'$ ). (D) Nucleotide quartet between G107, the 5' end, and DV.



ture explains these observations by showing that DIII helps to organize the active site indirectly through its proximity to J2/3 and the 5' end of the intron. DIII is therefore an allosteric effector of catalysis and influences intron reactivity despite its distance from active-site moieties in DV.

**Lack of electron density for domain VI.** DVI contains the bulged adenosine that provides the 2'-OH nucleophile during lariat formation by group II introns (1). The crystal structure lacks electron density for DVI, even though this domain was included within the crystallization construct. Although DVI could not be visualized

with the existing data, there is ample space for this domain within the structure, and it is likely to lie within the open cleft next to DV (fig. S8). This position would be consistent with biochemical evidence indicating that domains V and VI exist in a side-by-side arrangement (45).

**Implications for catalysis.** Group II introns have an absolute requirement for either  $Mg^{2+}$  (1) or  $Mn^{2+}$  (18) in order to catalyze both steps of splicing. The two-metal ion mechanism for RNA catalysis postulates that two divalent metal ions, located 3.9 Å apart, catalyze phosphotransfer reactions in self-splicing ribozymes

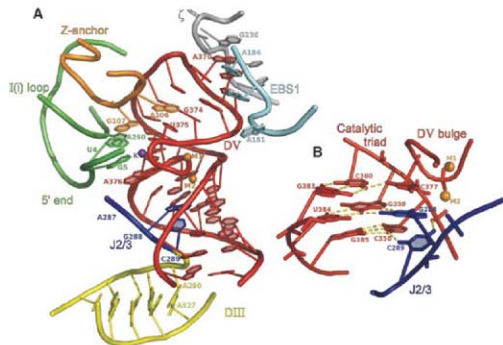
(40). Crystallographic evidence indicates that this is the mechanism for group I intron splicing (41), and our structure suggests that a similar mechanism is also used in group II introns, consistent with biochemical data (46).

It is clear that the exon recognition machinery and the metal-binding pocket of DV are in close proximity within the ribozyme core. The 5' end of the intron and EBS1 are both located near the DV bulge (Fig. 5A), thereby placing the 5' splice site in the active site. In addition, the  $\gamma$  nucleotide (A287), which pairs to the 3' terminal uridine ( $\gamma'$ ) of the intron, is located near the DV bulge (Fig. 5A), thereby positioning the 3' splice site for catalysis. The convergence of all these intron components on the two metal ions in DV and the close correspondence between biochemically determined contacts and the structure reported here suggest that this is a catalytically relevant structure. It is likely that this structure represents the "free retreatment" state of the intron that is capable of taking in substrate DNA for retrotransposition.

**Evolutionary implications.** The crystal structure provides a rationale for the strong phylogenetic conservation of DV. The constant separation of 5 base pairs (bp) between the catalytic triad and the bulge is required for the formation of the metal-binding platform. DV has remained conserved throughout higher organisms, and its basic form is used in the spliceosome. The intramolecular stem loop of the spliceosomal U6 small nuclear RNA (snRNA) also contains an AGC catalytic triad that is separated from a two-nucleotide bulge by 5 bp (47). Indeed, the U6 bulge binds metal ions in a manner similar to that of DV (48). DV can replace the U6 snRNA in the U12-dependent spliceosome, providing functional evidence for parity between the DV and U6 motifs (47).

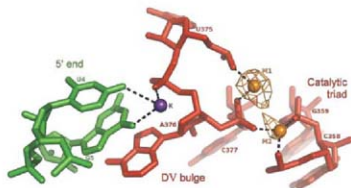
The exceptional conservation of J2/3 is now explained by the fact that it is an integral active-site motif, forming a catalytic triplex in the major groove of DV. This is evolutionarily relevant because J2/3 also has an apparent analog in the spliceosome (12): The phylogenetically invariant ACAGAGA box in U6 snRNA is refractory to mutagenesis and has been shown to interact near the bottom of the U6 stem (49). Thus, the spatial orientation of the AGA relative to the catalytic triad in U6 is very similar to that of J2/3 and DV in group II introns.

On the basis of these structural and functional analogies, it is most likely that the spliceosome is also a ribozyme and that it uses a two-metal ion mechanism for catalysis. These findings support the notion that group II introns evolved to colonize and shape the genomes of modern organisms. It has been suggested that the advent of spliceosomal introns from an ancestral group II intron resulted in the formation of the nuclear membrane and evolution of the eukaryotes (50). Introns also allowed eukaryotic genomes to breach the "one gene, one protein" barrier through alternative splicing. This crystal



**Fig. 5.** DV and its local environment. (A) Interactions between DV, DI (including the z-anchor region and  $\zeta$ - $\zeta'$ ), and J2/3. For clarity, portions of DI (green and orange) are shown without bases. Only backbone density is visible for A287 ( $\gamma$ ) and, thus, the base is not shown. Active-site  $Mg^{2+}$  ions are shown in orange and a  $K^+$  ion is shown in purple. (B) The triple helix formed by J2/3, the catalytic triad, and the bulge of DV. Hydrogen bonds are shown as yellow dashed lines. C289 forms a base triple with C358-G385 through hydrogen bonding between the O2 and N4 of C289 and the N4 and O2P of C358, respectively. G288 forms a triple with G359-U384 via the N1 and N2 of G288 bonding with the N7 and O6 of G359. The final base triple involves the O2 and 2'-OH of C377 hydrogen bonding to the N4 and O2P of C360. J2/3 residues G288 and C289 are analogous to G588 and A589 in the  $\alpha$ 5y intron, respectively. In this work, O1P is the pro- $S_{\alpha}$  oxygen and O2P is the pro- $R_{\alpha}$  oxygen.

**Fig. 6.** Metals ions in the core of the intron.  $Yb^{3+}$  anomalous density is shown contoured at 4 $\sigma$  for  $M_1$  and  $M_2$ , which are spaced 3.9 Å apart. Additionally, a  $K^+$  ion interacts with the bulge and the bases of nucleotides 4 and 5. The  $K^+$  ion is located at a distance of 8 Å from  $M_1$  and  $M_2$ . Black dashed lines indicate sites of inner-sphere coordination. Metal-binding residues C358, G359, C360, A376, and C377 from the *O. thelyensis* intron are analogous to residues A816, G817, C818, A838, and C839 from the  $\alpha$ 5y intron, respectively.



structure of a group II intron from an ancient lineage is therefore notable because it may represent a glimpse of the primordial catalyst that triggered the evolution of diverse life forms on Earth.

# References and Notes

1. A. M. Pyle, A. M. Lambowitz, *The RNA World* (Cold Spring Harbor Laboratory Press, Cold Spring Harbor, NY, ed. 3, 2006).
2. S. Zimmerly, H. Guo, P. Perlman, A. Lambowitz, *Cell* **82**, 545 (1995).
3. A. Robert, W. Seo, S. Zimmerly, *Proc. Natl. Acad. Sci. U.S.A.* **104**, 6620 (2007).
4. J. Ferat, F. Michel, *Nature* **364**, 358 (1993).
5. Y. Vallès, K. Halanay, J. Boore, *PLoS ONE* **3**, e1488 (2008).
6. P. Sharp, *Science* **254**, 663 (1993).
7. T. Cech, *Cell* **44**, 207 (1986).
8. A. Jacquier, F. Michel, *Cell* **50**, 17 (1987).
9. M. Costa, F. Michel, E. Westhof, *EMBO J.* **19**, 5007 (2000).
10. O. Fedorova, T. Nilsson, A. Pyle, *J. Mol. Biol.* **330**, 197 (2003).
11. S. Mikhayeva, H. Murray, H. Zhou, B. Turczyk, K. Jarrell, *RNA* **6**, 1509 (2000).
12. A. de Lencastre, A. Pyle, *RNA* **14**, 11 (2007).
13. H. Wank, J. Sanfilippo, R. Singh, M. Matsura, A. Lambowitz, *Mol. Cell* **4**, 239 (1999).
14. U. Schmidt, M. Podar, U. Stahl, P. Perlman, *RNA* **2**, 1161 (1996).
15. S. Boulanger et al., *Mol. Cell. Biol.* **15**, 4479 (1995).
16. A. de Lencastre, S. Hamill, A. Pyle, *Nat. Struct. Mol. Biol.* **12**, 626 (2005).
17. N. Toor, G. Hanner, S. Zimmerly, *RNA* **7**, 1142 (2001).
18. N. Toor, A. Robert, J. Christenson, S. Zimmerly, *Nucleic Acids Res.* **34**, 4443 (2006).
19. J. Rest, D. Mindell, *Mol. Biol. Evol.* **20**, 1134 (2003).
20. M. Podar, V. Chu, A. Pyle, P. Perlman, *Nature* **391**, 915 (1998).
21. M. Granlund, F. Michel, M. Norgren, *J. Bacteriol.* **183**, 2560 (2003).
22. Materials and methods are available as supporting material on Science Online.
23. W. Hendrickson, J. Smith, S. Sheriff, *Methods Enzymol.* **115**, 41 (1985).
24. A. Kent, R. Rambo, R. Baty, J. Kieft, *Structure* **15**, 761 (2007).
25. C. Harris-Kor, M. Zhang, C. Peckles, *Proc. Natl. Acad. Sci. U.S.A.* **90**, 10658 (1993).
26. A. Jacquier, F. Michel, *J. Mol. Biol.* **213**, 437 (1990).
27. M. Boudvillain, A. de Lencastre, A. Pyle, *Nature* **406**, 315 (2000).
28. M. Costa, E. Dérme, A. Jacquier, F. Michel, *J. Mol. Biol.* **267**, 520 (1997).
29. M. Boudvillain, A. Pyle, *EMBO J.* **17**, 7091 (1998).
30. M. Costa, F. Michel, *EMBO J.* **14**, 1276 (1995).
31. O. Fedorova, A. Pyle, *EMBO J.* **24**, 3906 (2005).
32. A. Pyle, O. Fedorova, C. Waldsch, *Trends Biochem. Sci.* **32**, 138 (2007).
33. M. Tamura, S. Halbrook, *J. Mol. Biol.* **320**, 455 (2002).
34. P. Adams, M. Stahley, A. Kowak, J. Wang, S. Strobel, *Nature* **430**, 45 (2004).
35. M. Podar et al., *RNA* **4**, 151 (1998).
36. R. Sigel et al., *Nat. Struct. Mol. Biol.* **11**, 187 (2004).
37. L. Zhang, J. Doudna, *Science* **295**, 2084 (2002).
38. G. Charfreau, A. Jacquier, *Science* **266**, 1383 (1994).
39. P. Gordon, J. Piccirilli, *Nat. Struct. Mol. Biol.* **8**, 893 (2001).
40. T. Steitz, J. Steitz, *Proc. Natl. Acad. Sci. U.S.A.* **90**, 6498 (1993).
41. M. Stahley, S. Strobel, *Science* **309**, 1587 (2005).
42. K. Bayens, H. De Bondt, A. Pardi, S. Halbrook, *Proc. Natl. Acad. Sci. U.S.A.* **93**, 12851 (1996).
43. N. Lonsif, E. Westhof, *RNA* **7**, 499 (2001).
44. M. Podar, S. Di-Haji, P. Perlman, *RNA* **1**, 828 (1995).
45. M. Podar, P. Perlman, *RNA* **5**, 318 (1999).
46. P. Gordon, R. Fong, J. Piccirilli, *Chem. Biol.* **14**, 607 (2007).
47. G. Shukla, R. Padgett, *Mol. Cell* **9**, 1145 (2002).
48. S. Yeon, G. Wenzschell, J. Termini, R. Lin, *Nature* **408**, 881 (2000).
49. H. Madhani, C. Guthrie, *Nes Dev.* **8**, 1071 (1994).
50. W. Martin, E. Koonin, *Nature* **440**, 41 (2006).
51. www.pymol.org
52. We thank K. Rajashankar, N. Sukumar, and I. Kourinov of Northeastern Collaborative Access Team (NE-CAT) beamline ID-24 at the Advanced Photon Source (APS) of Argonne National Laboratory. We also thank J. Osiupik and the staff at Structural Biology Center Collaborative Access Team (SBC-CAT) beamline ID-19 at APS, and C. Whalen, A. Héroux, A. Sazawa, W. Shi, and H. Robinson at X25 and X29 at the National Synchrotron Light Source at Brookhaven National Laboratory. We thank J. Cochran, M. Stahley, and P. S. Perlman for their advice and support. We thank S. A. Strobel, M. Stahley, J. Cochran, J. Cabral, J. Li-Pook-Thun, O. Fedorova, and G. P. Wagner for comments on the manuscript. R. Baty for the gift of iridium hexamine, and H. Takami for the *O. rheynisi* strain. K.S.K. was supported by NIH training grant T15 AG07056, S.D.T. was supported by the U.S. Department of Defense through the National Defense Science and Engineering Graduate Fellowship Program and by a NSF Graduate Research Fellowship. This work was supported by the Howard Hughes Medical Institute (HHMI) and NIH grant GM50313 to A.M.P., who is an investigator of the HHMI. Coordinates, structure factors, and experimental phases of the group II intron have been deposited in the Protein Data Bank (accession number 3BWP, www.pdb.org) and the Nucleic Acid Database (accession number UR0130, http://ndbserver.rutgers.edu).

## Supporting Online Material

www.sciencemag.org/cgi/content/full/320/S8/7277/DC1

Materials and Methods

Figs. S1 to S8

Table S1

References

5 December 2007; accepted 13 February 2008

10.1126/science.1153803

## REPORTS

# Revealing Magnetic Interactions from Single-Atom Magnetization Curves

Focko Meier,\* Lihui Zhou, Jens Wiebe,† Roland Wiesendanger

The miniaturization of magnetic devices toward the limit of single atoms calls for appropriate tools to study their magnetic properties. We demonstrate the ability to measure magnetization curves of individual magnetic atoms adsorbed on a nonmagnetic metallic substrate with use of a scanning tunneling microscope with a spin-polarized tip. We can map out low-energy magnetic interactions on the atomic scale as evidenced by the oscillating indirect exchange between a Co adatom and a nanowire on Pt(111). These results are important for the understanding of variations that are found in the magnetic properties of apparently identical adatoms because of different local environments.

Magnetic nanostructures consisting of a few atoms on nonmagnetic substrates (adatoms) are explored as model systems for miniaturized data storage and spintronic

devices and for the implementation of quantum computing. Because these structures are well defined and controllable on the atomic scale, they are ideally suited to study the fundamentals of magnetic interactions that are the ingredients of today's and future memory and computation technology.

Since the early days of modern research in magnetism, the magnetization in response to an external magnetic field (a magnetization curve) has been recorded to gather information on the basic properties of magnetic samples (*1*). Such curves can be used to deduce the sample's mag-

netic moment and magnetic anisotropy energy. The downsizing of samples from bulk over thin films and nanowires to nanodots requires an ever-increasing sensitivity of this method. It has been demonstrated that x-ray absorption spectroscopy with polarization analysis is able to measure magnetization curves of adatoms on a nonmagnetic substrate, albeit limited to large ensembles (*2*). Different approaches are potentially able to detect individual spins with nanometer spatial resolution ranging from magnetic resonance measurements (*3*) over magnetic exchange force microscopy (*4*) to scanning tunneling microscopy and spectroscopy (STM and STS) (*5–10*). Spin-averaged STS has been used to indirectly deduce the properties of single and coupled spins via the Kondo effect (*5*), the detection of noise (*6, 7*), or the observation of exchange splittings (*8, 9*). Inelastic electron tunneling has been adopted to measure the magnetic moments and anisotropy of individual atoms by spin-flip spectroscopy (*10*). This approach is complementary to the detection of magnetization curves but does not provide information on the dynamics of the spin and is so far restricted to adatoms on insulating layers. The method of choice for various substrates, spin-polarized STS (SP-STS), has been proven to detect single spins stabilized by direct exchange to

Institute of Applied Physics and Microstructure Research Center, University of Hamburg, Jungiusstrasse 11, D-20355 Hamburg, Germany.

\*Present address: Laboratory of Atomic and Solid State Physics, Department of Physics, Cornell University, Ithaca, NY 14853, USA.

†To whom correspondence should be addressed. E-mail: jwiebe@physnet.uni-hamburg.de



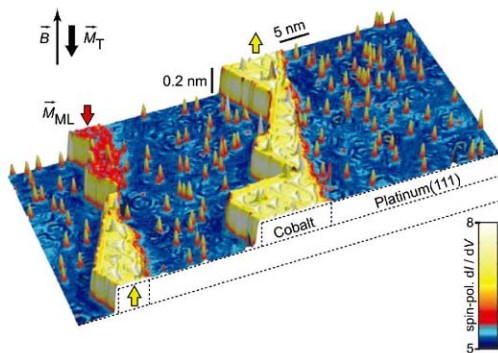
(anti)ferromagnetic layers (11, 12). However, the important step to individual spins in a nonmagnetic surrounding has been lacking because of the experimental challenge posed by spin instability.

We demonstrate the direct detection of the magnetization of single adatoms on a nonmagnetic metallic substrate as a function of an external magnetic field by SP-STs. Cobalt adatoms were used on a strongly polarizable platinum(111) substrate, forming large effective magnetic moments of about 5 Bohr magnetons ( $\mu_B$ ) with a strong out-of-plane anisotropy (2). Our intent is to measure the magnetic interaction between stripes of one atomic layer Co grown at room temperature (13) and the individual Co adatoms deposited at about 25 K on the bare Pt(111) (Fig. 1) (14, 15). The monolayer (ML) stripes, which have a magnetization,  $\vec{M}_{ML}$ , perpendicular to the surface (13), serve as the calibration standard for the magnetic properties of the SP-STM tip. When we use out-of-plane-oriented tips, the up and down domains exhibit a different spin-resolved  $dI/dV$  signal as seen in Fig. 1. It is then possible to characterize the spin polarization and magnetization,  $\vec{M}_T$ , of the foremost tip atom acting as a detector for the magnetization of the adatom,  $\vec{M}_A$  (fig. S1). The  $dI/dV$  signal recorded above a particular adatom is sensitive to the relative orientation of  $\vec{M}_T$  and  $\vec{M}_A$  (16),

$$dI/dV \propto (dI/dV)_0 + (dI/dV)_{SP} \vec{M}_T \cdot \vec{M}_A \quad (1)$$

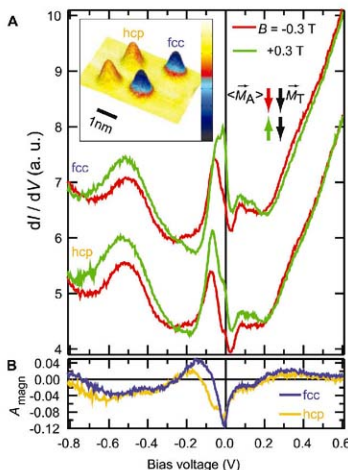
where the first term and the second term represent the bias-voltage-dependent spin-averaged and spin-resolved parts of  $dI/dV$ , respectively. The  $dI/dV$  signal is averaged over about 10 ms.  $dI/dV$  as a function of an external magnetic field,  $\vec{B}$ , is thus a direct measure for the component of the time-averaged magnetization ( $\vec{M}_A$ ) in the out-of-plane direction.

Before analyzing the  $\vec{B}$ -dependent magnetization of single adatoms, their exact location with respect to the underlying substrate has to be determined. The Co adatoms can sit on either hexagonal close-packed (hcp) or face-centered cubic (fcc) lattice sites, which are unambiguously distinguishable by their  $dI/dV$  at small negative bias voltages (Fig. 2A inset and fig. S2). In the  $dI/dV$  curves, the fcc adatoms show a characteristic peak at about  $-0.05$  V below the Fermi level  $E_F$  ( $V = 0$  V), which is shifted slightly downward for hcp adatoms. When  $\vec{B}$  is reversed from  $-0.3$  T to  $+0.3$  T, this peak strongly changes intensity because of the alignment of ( $\vec{M}_A$ ) with  $\vec{B}$ , leading to parallel and antiparallel orientation of ( $\vec{M}_A$ ) and  $\vec{M}_T$  ( $\vec{M}_T$  is constant as shown in fig. S1). Similar intensity changes can be observed in nearly the entire voltage range and can be quantified by the magnetic asymmetry  $A_{mag} = (dI/dV_p - dI/dV_{ap}) / (dI/dV_p + dI/dV_{ap})$ , where  $dI/dV_p$  and  $dI/dV_{ap}$  are the curves for parallel and antiparallel orientation, respectively (Fig. 2B). The strongest asymmetry occurs at the energy of the prominent peak below  $E_F$ , proving that this adatom state is strongly spin-polarized. Because this state is sensitive to the

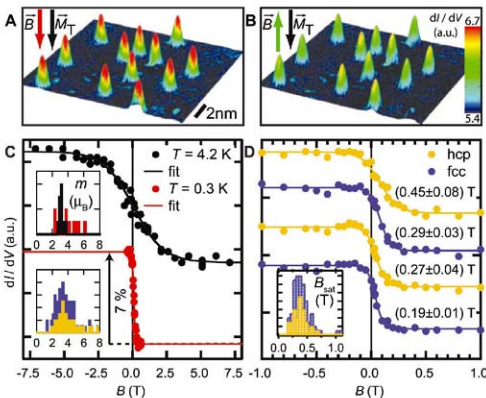


**Fig. 1.** Overview of the sample of individual Co adatoms on the Pt(111) surface (blue) and Co ML stripes (red and yellow) attached to the step edges (STM topograph colored with the simultaneously recorded spin-polarized  $dI/dV$  map measured with an STM tip magnetized antiparallel to the surface normal). An external  $\vec{B}$  can be applied perpendicular to the sample surface in order to change the magnetization of adatoms  $\vec{M}_A$ , ML stripes  $\vec{M}_{ML}$ , or tip  $\vec{M}_T$ . The ML appears red when  $\vec{M}_{ML}$  is parallel to  $\vec{M}_T$  and yellow when  $\vec{M}_{ML}$  is antiparallel to  $\vec{M}_T$ . (Tunneling parameters are as follows:  $I = 0.8$  nA,  $V = 0.3$  V, modulation voltage  $V_{mod} = 20$  mV,  $T = 0.3$  K.)

**Fig. 2.** Spin-polarized  $dI/dV$  curves from individual Co adatoms. (A) Curves measured on an hcp and on an fcc adatom by using the same tip as in fig. S1 with  $\vec{B}$  as indicated (averages from six single curves, fcc curves are offset for clarity). The time-averaged magnetization of the adatoms ( $\vec{M}_A$ ) is aligned with  $\vec{B}$ , resulting in a change in the  $dI/dV$  curve depending on the relative orientation of ( $\vec{M}_A$ ) and  $\vec{M}_T$  as indicated. a.u., arbitrary units. (Inset) Topograph colored with simultaneously recorded  $dI/dV$  map at  $V_{stab} = -0.1$  V of an area with two hcp (orange) and two fcc (blue) adatoms. (B) Magnetic asymmetry ( $A_{mag}$ ) calculated from the curves of (A). (Tunneling parameters are as follows:  $I_{stab} = 1$  nA,  $V_{stab} = 0.6$  V,  $V_{mod} = 10$  mV,  $T = 0.3$  K.)



**Fig. 3. (A and B)** Topographs of an area with several adatoms colorized with the spin-polarized  $dI/dV$  map at  $B = -0.5$  T parallel to the tip magnetization  $\vec{M}_T$  (A) and  $B = +0.5$  T antiparallel to  $\vec{M}_T$  (B) ( $T = 0.3$  K). (C) Magnetization curves from the same adatom taken at different temperatures as indicated (dots). Reversal of  $\vec{M}_T$  is corrected (fig. S3). The solid lines are fits to the data (see text). The insets show the resulting histograms of the fitted magnetic moments (in  $\mu_B$ ) for the same 11 adatoms at  $T = 4.2$  K (black) and at  $0.3$  K (red) (top histogram) and for 38 hcp (orange) and 46 fcc (blue) adatoms at  $0.3$  K (bottom histogram), fcc bars stacked on hcp. (D) Magnetization curves of four adatoms at  $0.3$  K with fit curves and resulting  $B_{sat}$  of 99% saturation. The inset shows the histogram of  $B_{sat}$  (in T) for the same adatoms used in the lower histogram in (C) (fcc bars stacked on hcp). [Curves in (C) and (D) are offset for clarity. Tunneling parameters are as follows:  $I = 0.8$  nA,  $V = 0.3$  V,  $V_{mod} = 20$  mV.]



lattice site of the adatom and to its spin orientation, it is not suited to separate structural and magnetic contributions. Instead, the  $dI/dV$  signal at  $+0.3$  V has a small but sufficient asymmetry with negligible influence of the lattice site and will be used to record ( $M_A$ ) as a function of  $B$ .

Focusing first on isolated adatoms [mean nearest neighbor distance of  $2.4 \pm 1$  nm (SEM)] that are more than 8 nm distant from the ML, Fig. 3, A and B, shows  $dI/dV$  maps recorded at  $-0.5$  T and  $+0.5$  T. As in the  $dI/dV$  curves, the  $dI/dV$  signal on the adatoms is reduced for antiparallel configuration of  $\vec{M}_A$  and  $\vec{M}_T$ . Similar  $dI/dV$  maps have been recorded at different  $B$ , which was varied in small steps from  $-7.5$  T to  $+7.5$  T and back to  $-7.5$  T. The  $dI/dV$  signal was averaged above individual adatoms (about  $0.25$  nm $^2$ ) and plotted as a function of  $B$  (Fig. 3C). The magnetization curves are shifted slightly to the right because of the residual stray field of the tip,  $B_T$  (fig. S3A).

We observed S-shaped curves for both temperatures but with strongly different saturation fields,  $B_{sat} \approx 5$  T ( $T = 4.2$  K) and  $B_{sat} \approx 0.3$  T ( $T = 0.3$  K). No signs of hysteresis are observed; that is,  $M_A$  behaves paramagnetically and statistically switches between up and down with a rate much faster than the current time resolution of the experiment ( $>100$  Hz). It has been reported that Co adatoms on Pt(111) have a large out-of-plane magnetocrystalline anisotropy of  $K = 9.3$  meV per atom (at  $5.5$  K), corresponding to an energy barrier between up- and downward pointing  $\vec{M}_A$  of about  $100$  K (2). Because our lowest temperature is  $350$  times smaller, we can exclude thermally induced switching of  $M_A$  across such a barrier (17). Thus, if the description in (2) is correct, our results imply the dominance of a temperature-independent

switching process, for example, quantum tunneling of the magnetization or current-induced magnetization switching by inelastic processes.

In order to gain information on the magnetic moment,  $m$ , we fitted the measured magnetization curves. It is interesting to evaluate whether a quasi-classical description is appropriate (2) because the magnetization is that of an individual atom averaged over a time window without ensemble averaging. We thus calculate  $M_A$  by using a magnetic energy function  $E(\theta, B) = -m(B - B_T)\cos\theta - K(\cos\theta)^2$ , where  $\theta$  is the angle between the magnetic moment and  $\vec{B}$ . We numerically fit the magnetization curves by variation of  $m$ , of the saturation magnetization,  $M_{sat}$ , and of the tip stray field,  $B_T$ . Because of the lack of a hard axis magnetization curve,  $K$  is not an appropriate independent fit parameter. Therefore, a fixed value  $K = 9.3$  meV is taken (2). The corresponding fit curves in Fig. 3C excellently reproduce the single-atom magnetization curves. Probably a strong hybridization of the adatom states with the Pt bands leads to a quasi-classical behavior of the total magnetic moment (2, 18).

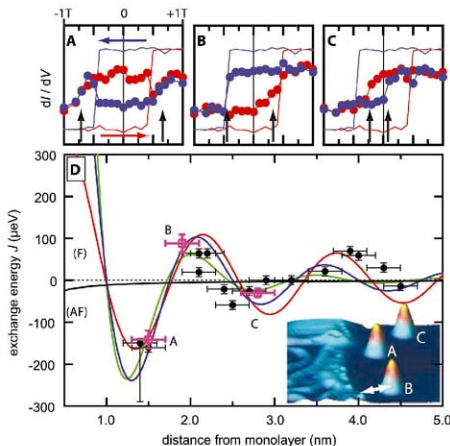
Similar magnetization curves as in Fig. 3C have been recorded by using several tips for about 80 different adatoms showing qualitatively the same paramagnetic shape. The insets contain the histograms of the fitted  $m$ . Surprisingly, the variance in  $m$  for the same adatoms increases notably at  $T = 0.3$  K. The bottom histogram indicates a broad distribution from about  $2\mu_B$  to  $6\mu_B$  with arithmetic means of  $m_{hcp} = (3.9 \pm 0.2)\mu_B$  and  $m_{fcc} = (3.5 \pm 0.2)\mu_B$ . These are larger than the  $4.2$  K values [ $m_{hcp} = (3.0 \pm 0.3)\mu_B$  and  $m_{fcc} = (3.1 \pm 0.1)\mu_B$ ] (19). Figure 3D shows the measured magnetization curves and the correspond-

ing fits of four different adatoms where the variance in  $m$  is visible as a spreading in the saturation fields  $B_{sat}$ .

Because the peculiar spreading in the fitted  $m$  is obtained similarly for hcp and fcc adatoms, we can exclude an adsorption-site-induced variance in the magnetic moment. Another reason for variance can be electronic substrate inhomogeneity because of the subsurface-defect scattering seen in Fig. 1 (20). However, this is very unlikely: (i) There is no obvious correlation between  $m$  and the scattering state distribution; (ii) the variance in  $m$  is strongly increased for lower temperature, whereas the scattering states remain unaffected. Thus, we propose that the variance in  $m$  is induced by a magnetic interaction between the adatoms with an energy scale of about  $k_B \cdot 0.3$  K =  $25$   $\mu$ eV. From the spreading of  $B_{sat}$  found in the histogram in Fig. 3D ( $0.2$  T to  $0.7$  T), we get a rough estimate for the interaction strength  $J = m(0.7 - 0.2$  T) $\approx 50$   $\mu$ eV ( $m = 3.7\mu_B$ ). This is consistent with an increased variance only at very low temperatures. Direct exchange and dipolar interactions can be neglected because of the large separation of the adatoms. Therefore, we assume that indirect exchange via the Pt substrate is responsible for the variance.

If this hypothesis is true, a long-range coupling between the adatoms and the ML is expected. Focusing on adatoms close to the right of the ML, Fig. 4A shows the magnetization curve of a particular ML stripe and of an adatom with a distance of  $d \approx 1.5$  nm. The ML shows a regular squarelike hysteresis corresponding to ferromagnetic behavior. In the down sweep (blue curve), its magnetization switches from up (high signal) to down (low signal) at  $B = -0.5$  T, and in the up sweep (red curve) it switches from down to up at

**Fig. 4.** Magnetic exchange between adatoms and ML stripe. (A to C) Magnetization curves measured on the ML (straight lines) and on the three adatoms (dots) A, B, and C visible in the inset topograph of (D). The blue circle indicates the down sweep from  $B = +1$  T to  $-1$  T (and red, the up sweep from  $-1$  T to  $+1$  T) ( $dI/dV$  signal on ML inverted for clarity). The vertical arrows indicate the exchange bias field,  $B_{ex}$ , which is converted into the exchange energy (using  $m = 3.7 \mu_B$ ) for the corresponding magenta points in the plot (D). (Tunneling parameters are as follows:  $I = 0.8$  nA,  $V = 0.3$  V,  $V_{mod} = 20$  mV,  $T = 0.3$  K) (D) Dots show measured exchange energy as a function of distance from ML as indicated by the arrow in the inset (about  $50^\circ$  to  $[112]$ ). The black line is the dipolar interaction calculated from the stray field of a 10-nm-wide stripe with saturation magnetization  $1.3 \times 10^6$  A/m. The red, blue, and green lines are fits to 1D, 2D, and 3D range functions for indirect exchange. Horizontal error bars are due to the roughness of the Co-ML stripe edge, whereas the vertical ones are due to the uncertainty in  $B_{ex}$ .



+0.5 T. The adatom behaves completely different than the previously described distant ones. In the down sweep, its magnetization switches from up to down already at large positive  $B = +0.7$  T (see arrow). It then switches back to up simultaneously with the reversal of the stripe at  $-0.5$  T. Only at  $-0.7$  T is the adatom magnetization again forced into the down state (see arrow). The same behavior is observed for the up sweep but now with the stripe magnetization pointing upward at zero field. The adatom feels an antiferromagnetic (AF) coupling to the stripe, which is broken by an exchange bias of  $B_{ex} = \pm 0.7$  T corresponding to an interaction energy of  $J = -m \cdot B_{ex} \approx -150$   $\mu$ eV ( $m = 3.7 \mu_B$ ). The magnetization curve of a more distant adatom shows a ferromagnetic (F) coupling (Fig. 4B); that is, the adatom magnetization is forced parallel to the stripe at zero field ( $J > 0$ ). An even more distant adatom (Fig. 4C) again is antiferromagnetically coupled but with a lower  $B_{ex}$  smaller than the stripe coercivity (see arrows).

The interaction energies  $J(d)$  determined from similar magnetization curves of many adatoms are plotted in Fig. 4D. A damped oscillatory behavior, which is reminiscent of Ruderman-Kittel-Kasuya-Yosida (RKKY)-like exchange, is observed (21–23). Note that dipolar coupling (black line) is always AF and negligible. Therefore, we conclude that the interaction is due to indirect exchange via the Pt electrons. In order to test whether an RKKY description is appropriate, Fig. 4D shows corresponding fits

to the data points using range functions  $J(d) = J_0 \cdot \cos(2k_F d) / (2k_F d)^2$  with different assumed dimensionalities,  $D$  (24, 25). A good agreement is found for  $D = 1$  and a wavelength of  $\lambda_F = 2\pi/k_F \approx 3$  nm, corresponding to an oscillation period of the exchange energy of 1.5 nm.

A dimensionality below 2 is indeed expected if the interaction is dominated by surface-related [two-dimensional (2D)] states and the superposition of the contributions from all Co atoms along the stripe edge attenuates the decay. This conclusion is analogous to the case of the exchange interaction between ferromagnetic layers separated by nonmagnetic metallic spacer layers, where the dominating states are bulk (3D) states, and the summation over the atoms in the layer can result in a 2D asymptotic behavior (26). Furthermore, the period of the measured oscillation leads to a  $\lambda_F$  that is a factor of 2 to 6 larger than typical Fermi wavelengths of the Pt(111) surface (20). We anticipate that effects similar to those found in layered systems explaining the long-period oscillation (26) also play a crucial role in the stripe-adatom interaction.

Our method not only reveals the magnetization of individual adatoms but also detects magnetic interactions with atomic resolution at an energy scale of 10  $\mu$ eV. An increase in the time resolution should allow for the investigation of the dynamics in single and coupled spin systems (27). Together with the STM's ability to assemble nanometer-sized objects adatom by adatom, our method may be suitable for the fabrication and investigation of magnetic nanostructures on vari-

ous substrates as metallic, semiconducting (9), or thin insulating layers (10).

## References and Notes

- See, for example, S. Chikazumi, *Physics of Magnetism* (Wiley, New York, 1964).
- P. Gambardella et al., *Science* **300**, 1130 (2003).
- D. Rugar, R. Budakian, H. J. Mamin, B. W. Chui, *Nature* **430**, 329 (2004).
- U. Kaiser, A. Schwarz, R. Wiesendanger, *Nature* **446**, 522 (2007).
- P. Wahl et al., *Phys. Rev. Lett.* **98**, 056601 (2007).
- V. Manasson, R. J. Hamers, J. E. Demuth, A. Castellano, *Phys. Rev. Lett.* **62**, 2531 (1989).
- C. Durkan, M. E. Welland, *Appl. Phys. Lett.* **80**, 458 (2002).
- H. J. Lee, W. Ho, M. Persson, *Phys. Rev. Lett.* **92**, 186802 (2004).
- D. Kitchen, A. Richardelle, J.-M. Tang, M. E. Flatté, A. Yazdani, *Nature* **442**, 436 (2006).
- C. F. Hühnerbein et al., *Science* **317**, 1199 (2007).
- S. Heinze et al., *Science* **328**, 1805 (2005).
- Y. Yagci, V. W. Brar, L. Senapati, S. C. Erwin, M. F. Crommie, *Phys. Rev. Lett.* **99**, 067202 (2007).
- J. Meier et al., *Phys. Rev. B* **74**, 195411 (2006).
- J. Wiebe et al., *Rev. Sci. Instrum.* **75**, 4871 (2004).
- Materials and methods are available as supporting material on Science Online.
- D. Wörmann, S. Heinze, P. Kurz, G. Bihlmeyer, S. Büchel, *Phys. Rev. Lett.* **86**, 4132 (2001).
- R. L. White, *J. Magn. Mater.* **209**, 1 (2000).
- However, a quantum mechanical two-level model with Zeeman splitting and off diagonal elements  $\pm I$  that couple the spin up and down configurations was also tried to fit the data. It gives identical results as long as  $I \ll k_B T$ , corresponding to a reasonable switching rate  $\Omega = I/\hbar \ll 10^{10}$  Hz.
- It has been checked that a variation of  $K$  in reasonable constraints  $1 \text{ meV} < K < 20 \text{ meV}$  will not change the fitted  $m$  at  $T = 0.3$  K because this temperature is too low to turn the magnetization considerably into hard axis direction. For the fits at  $T = 4.2$  K, we would have to



- assume  $K = 1$  meV in order to reproduce the value of  $m$  given in (2).
20. J. Wiebe *et al.*, *Phys. Rev. B* **72**, 193406 (2005).
21. M. A. Ruderman, C. Kittel, *Phys. Rev.* **96**, 99 (1954).
22. T. Kawai, *Prog. Theor. Phys.* **16**, 45 (1956).
23. K. Yoda, *Phys. Rev.* **106**, 893 (1957).
24. B. Fischer, M. W. Klein, *Phys. Rev. B* **11**, 2025 (1975).
25. Y. Yafet, *Phys. Rev. B* **37**, 3948 (1986).

26. P. Bruno, C. Chappert, *Phys. Rev. B* **46**, 261 (1992).
27. S. Krause, L. Berbil-Bautista, G. Herzog, M. Bode, R. Wiesendanger, *Science* **317**, 1537 (2007).
28. Financial support from the Deutsche Forschungsgemeinschaft (SFB668, SFB508, and GRK1286) is gratefully acknowledged. We thank M. Bode, S. Heinze, E. Vedmedenko, A. Lichtenstein, S. Blügel, S. Lounis, and A. Schwarz for fruitful discussions and F. Marczewski for assistance in illustration arts.

## Supporting Online Material

www.sciencemag.org/cgi/content/full/320/5872/DC1  
Materials and Methods  
SOM Text  
Figs. S1 to S3  
References and Notes

20 December 2007; accepted 27 February 2008  
10.1126/science.1154415

# The Roles of Subsurface Carbon and Hydrogen in Palladium-Catalyzed Alkyne Hydrogenation

Detre Teschner,<sup>1,\*</sup> János Borsodi,<sup>1,2</sup> Attila Wootsch,<sup>2</sup> Zsolt Révay,<sup>2</sup> Michael Hävecker,<sup>1</sup> Axel Knop-Gericke,<sup>1</sup> S. David Jackson,<sup>3</sup> Robert Schlögl<sup>1</sup>

Alkynes can be selectively hydrogenated into alkenes on solid palladium catalysts. This process requires a strong modification of the near-surface region of palladium, in which carbon (from fragmented feed molecules) occupies interstitial lattice sites. In situ x-ray photoelectron spectroscopic measurements under reaction conditions indicated that much less carbon was dissolved in palladium during unselective, total hydrogenation. Additional studies of hydrogen content using in situ prompt gamma activation analysis, which allowed us to follow the hydrogen content of palladium during catalysis, indicated that unselective hydrogenation proceeds on hydrogen-saturated  $\beta$ -hydride, whereas selective hydrogenation was only possible after decoupling bulk properties from the surface events. Thus, the population of subsurface sites of palladium, by either hydrogen or carbon, governs the hydrogenation events on the surface.

A fundamental understanding of catalytic reactions requires a "bottom-up" approach using surface-science experiments and theoretical calculations to provide insights into surface dynamics and adsorbed species, their coverage, and possible reaction paths. For simple heterogeneous catalytic systems (such as ammonia synthesis and CO oxidation), the level of characterization approaches the point where national insights into the design of the catalyst

become feasible (1). Experimental studies have been aided by instrumental modifications that allow many surface-science techniques that typically are used under high-vacuum conditions to be used at modest pressures of reactants over the catalysts.

The presumed simplification of most studies is that the bulk of the catalyst, the part of the active sample below the surface, is "frozen" and can be neglected. Although heterogeneous catalytic conversion is a surface process, there is accumulating evidence, particularly from experiments applying in situ functional analysis, that the bulk and especially the subsurface region (the few layers below the surface) can play a key role in surface events. Reaction conditions (such as temperature and the ambient reactive

gas) may not only reconstruct the top surface layer, but also may create added rows and valleys of atoms (2, 3) or even massively change the whole morphology of the catalytic particles (4). Atoms that are part of the catalytic feed can dissolve in metallic particles, and can change the electronic structure of the surface (5, 6), and dissolved species can even participate in the reaction (7). Here, we present a still relatively simple but industrially relevant case, alkyne hydrogenation on palladium, in which different subsurface species define which of the possible reaction paths dominates the overall reaction.

Many studies have addressed the question of how to selectively hydrogenate a certain functional group. A hydrocarbon with a carbon-carbon triple bond can be hydrogenated partially to the alkene or fully to the alkane. We have explored why palladium can selectively hydrogenate alkynes to alkenes, when Pd itself is usually even more active in hydrogenating the corresponding alkene to the alkane. The typical explanation (8) is that the difference in the heat of adsorption of the feed alkyne and of the partial hydrogenation product alkene forces the intermediate product alkene to desorb and become replaced by the incoming alkene of the feed. However, 30 years ago, Al-Ammar *et al.* (9) demonstrated that, contrary to thermodynamic factors, ethylene could be adsorbed on a catalyst of Pd supported on silica while acetylene was present in the gas phase. This is possible because the surface of catalysts is usually heterogeneous and can have discrete sites that facilitate selective adsorption. Furthermore, many research groups have suggested that carbonaceous deposits formed during reaction might substantially affect selectivity ([10, 11] and references therein). Alkyne hydrogenation usually goes through an

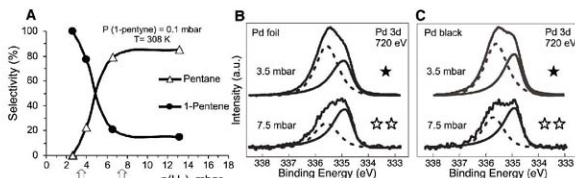
<sup>1</sup>Fritz-Haber-Institut der Max-Planck-Gesellschaft, Faradayweg 4-6, D-14195 Berlin, Germany. <sup>2</sup>Institute of Isotopes, Hungarian Academy of Sciences, Post Office Box 77, Budapest H-1525, Hungary. <sup>3</sup>WestCHEM, Department of Chemistry, University of Glasgow, Glasgow G12 8QQ, Scotland, UK.

\*To whom correspondence should be addressed. E-mail: teschner@fhi-berlin.mpg.de

**Fig. 1.** Catalytic 1-pentyne gas-phase

hydrogenation as a function of  $p(\text{H}_2)$ . (A) Selectivity for the two main reaction paths on Pd black; experiments were carried out in a closed-loop circulation setup. Hydrogenation selectivity is a strong function of  $p(\text{H}_2)$ . Solid and open stars mark pressures at which XPS experiments were carried out. P, pressure; T, temperature. (B and C) Corresponding Pd 3d<sub>5/2</sub> XP spectra recorded under hydrogenation conditions for Pd foil and black, respectively, using 720-eV excitation energy.

The Pd component at 335 eV corresponds to bulk, metallic Pd, whereas the higher binding-energy peak (dashed line) represents the sum of adsorbate-induced surface core-level shift components and PdC. The reaction selectivity



correlates with PdC: Selective hydrogenation occurs when the Pd peak is dominated by PdC, whereas total hydrogenation prevails on Pd containing much less C incorporated in the top few atomic layers. a.u., arbitrary units.

activation period (fig. S1), which strongly suggests that the catalyst is not identical to its "as-introduced" form.

We recently found that, under conditions that selectively hydrogenate 1-pentyne, the active state of Pd is a Pd-C surface phase (PdC), approximately three Pd layers thick (12). The amount of C incorporated within the top layers was 35 to 45 atomic %. This identification was mainly based on x-ray photoelectron spectroscopic (XPS) investigation under hydrogenation conditions (high-pressure XPS). Although XPS is typically used in ultrahigh-vacuum conditions, recent developments in instrumentation have made it possible to investigate catalysts under reaction conditions (13), provided that their reaction proceeds in the millibar range ( $10^{-4}$  to  $10^{-2}$  atm). Selective 1-pentyne hydrogenation, and alkyne hydrogenation in general, follows the same formal kinetics at these reduced pressures as it does at higher-pressure conditions (fig. S2); thus, in situ XPS will detect the catalytically relevant surface state. Because PdC was found to be stable only in the reaction ambient (12), its investigation requires in situ characterization techniques. To relate C incorporation into Pd to hydrogenation selectivity, we performed 1-pentyne hy-

drogenation experiments in the millibar pressure range, varying the experimental conditions to induce modification in the product pattern.

The selectivity response of unsupported Pd black (mean particle size 230 nm) to the variation of hydrogen partial pressure, as well as the XP spectra of Pd 3d core levels (Pd 3d<sub>5/2</sub>), are shown in Fig. 1. Increasing H<sub>2</sub> pressure accelerated selective hydrogenation, but above a certain pressure, total hydrogenation occurred. Pd, before contact with the hydrogenation feed, was in the metallic state (the Pd 3d component at 335 eV).

The regime of selective 1-pentyne hydrogenation was characterized by the strong peak at ~335.6 eV, which included any adsorbate-induced surface core-level shift components and the contribution from PdC. At the applied 720-eV excitation energy, the adsorbate-induced surface component should contribute ~20% to the total intensity of the peak (14); thus, the dominant part of the newly formed state corresponded to PdC. We used nondestructive depth-profile analysis (varying the energy of excitation and hence varying the depth corresponding to the detected photoelectrons) to verify that the location of the 335.6-eV component was on top, above the metallic Pd (12). However, when hydrogenation

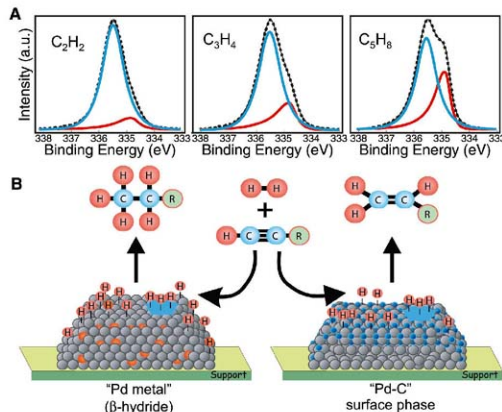
became unselective [such as at high partial pressure of H<sub>2</sub> (pH<sub>2</sub>)], much less C was incorporated into the top few layers of Pd, which decreased considerably the Pd 3d component associated with PdC. The state of palladium depended strongly on reaction temperature as well (fig. S3), when the concentration of H<sub>2</sub> in the gas phase was near the limit of the phase transition of Pd to Pd β-hydride (15). PdC appeared substantially above the decomposition temperature of β-hydride (fig. S3).

To discover whether PdC formation is a general phenomenon during any alkyne hydrogenation reaction, we carried out further investigation with other alkynes. The compilation in Fig. 2A shows that, with lower-chain alkynes, a similar dissolution of C in the near-surface region of palladium occurred and was indeed a general process of alkynes. Because it is likely that only atoms, rather than molecules, will penetrate into the metal lattice, many alkyne molecules must fragment in the early stage of the reaction, in agreement with numerous studies indicating massive irreversible C uptake at the beginning of any selective alkyne hydrogenation processes [(11) and references therein], and also in agreement with the activation period observed in such systems. The model of Pd during alkyne hydrogenation is summarized in Fig. 2B.

Carbon below the topmost layer of Pd has been observed with scanning tunneling microscopy (16), and allowing C to occupy octahedral subsurface sites was also theoretically verified to be energetically favorable (17). These studies have indicated that, in general, subsurface species can trap surface adsorbates; but, according to Yudanov *et al.* (17), subsurface C will, for example, weaken the binding energy of CO to Pd. Thus, C dissolved in the top layers modifies the surface electronic structure of Pd that apparently favors partial hydrogenation. Additionally, catalytic properties of Pd complexes in homogeneous hydrogenation are strongly affected by the coordinating ligands (18).

The rate-limiting step of alkyne hydrogenation is usually assumed to be the first H-addition step, deduced mainly from surface-science experiments in C<sub>2</sub> chemistry, but this cannot explain why selectivity should be a strong function of subsurface C content. However, the type of hydrogen involved in hydrogenation might be critically influenced by C incorporation. It was experimentally demonstrated (7), and later theoretically validated (19, 20), that bulk dissolved H, being much more energetic than adsorbed surface H, can hydrogenate surface adsorbates upon emerging to the surface. Temperature-programmed desorption experiments by Khan *et al.* (21), however, provided clear evidence that subsurface H strongly enhanced total hydrogenation of acetylene, whereas surface H alone (without any subsurface population) was much more selective toward ethylene.

Provided that the conclusion of these surface-science experiments and density functional theory



**Fig. 2.** In situ Pd 3d<sub>5/2</sub> spectra of Pd foil under acetylene, propyne, and 1-pentyne selective hydrogenation (A). The reaction mixture contained ~0.1 mbar alkyne and 0.9 mbar H<sub>2</sub>; temperature was in the range of 343 to 353 K. The red curve corresponds to Pd metal and the blue curve represents the sum of adsorbate-induced surface core-level shift components and of PdC. The dashed curve indicates the recorded spectrum. PdC forms with all three alkynes on Pd foil (but also on other Pd catalysts), rendering the Pd samples selective in the gas-phase alkyne hydrogenation processes. (B) Schematic representation of Pd catalysts operating in the selective and unselective alkyne hydrogenation regimes. Blue and orange balls indicate C in PdC and β-hydride in Pd, respectively. Green balls indicate an alkyl group or H. Blue patches symbolize carbonaceous deposits. (For clarity, no C<sub>3</sub> adsorbates are depicted on the surface.)

calculations can be transferred to real catalytic conditions, C incorporated in the top Pd layers will strongly affect the transport of hydrogen, and thus disturb the equilibrium of H between surface and deeper layers and hinder the participation of subsurface H in the catalytic process. To verify this hypothesis, the amount of H dissolved in Pd had to be quantified during the hydrogenation event. Because most of the spectroscopic methods are not sensitive for hydrogen (or cannot be applied in situ), we developed existing prompt gamma activation analysis (PGAA) (22) into an in situ technique by placing a continuous-flow reactor instead of a normal specimen into the neutron beam.

The nuclei of the chemical elements can capture neutrons, and during the de-excitation, they emit characteristic prompt gamma radiation. Hence, the H atoms dissolved in Pd could be analyzed with PGAA. When a fresh Pd black sample was introduced into flowing  $H_2$  at room temperature, the H content was 0.75 H per Pd atom (Table 1), in perfect agreement with the Pd/H phase diagram at 1 bar of  $H_2$  (15). The phase diagram indicates that  $\beta$ -hydride should contain 0.73 H (PdH<sub>0.73</sub>). However, when the H content was recorded after alkyne hydrogenation events, the ratio was slightly higher, 0.87 on average, which may indicate that carbonaceous deposits simply contain additional hydrogen. When running unselective 1-pentyne hydrogenation ( $H_2/C_5 > 7$ ), the H content is slightly higher, which means (i) that the reaction proceeds on saturated  $\beta$ -hydride and (ii) that additional deposits and adsorbates should carry even more H. This finding validates the idea that bulk-dissolved and subsurface H are very reactive but unselective

species and, furthermore, that equilibrium between surface and bulk is maintained during total hydrogenation.

However, when 1-pentyne was hydrogenated at low  $H_2/C_5$  ratios ( $<5$ ), after a room-temperature  $H_2$  pretreatment, hydrogenation was selective and the H/Pd ratio was low (0.15 on average). Thereafter, further selective 1-pentyne hydrogenation experiments always gave similar low H/Pd values. This value should arise as a sum of H in the adsorbates, hydrocarbonaceous deposits, and the low-concentration  $\alpha$ -hydride phase. However, if selective hydrogenation was achieved directly after total hydrogenation by decreasing the  $H_2$  flow (at constant 1-pentyne flow), the H/Pd ratio—measured not directly in the transient but after at least half an hour on stream—was always high (0.72, averaged from nine experiments). These higher values were not accompanied by any substantial changes in the activity or selectivity of the sample (Fig. S4), which indicates that the reaction rate in the regime of selective hydrogenation is not affected by the amount of dissolved H or by the presence of bulk  $\beta$ -hydride.

The PGAA experiments show that, during selective alkyne hydrogenation, the H content of palladium is not a direct function of the actual reaction mixture but reflects the prehistory of the sample, and also show that the surface properties are necessarily decoupled from the bulk. This separation is made possible by the propensity of Pd to fragment part of the hydrocarbon feed in the early stage of the reaction and dissolve the product C atoms in the topmost few layers. The high concentration of dissolved carbon excludes H from populating the subsurface region and hence prevents total hydrogenation of alkyne.

Having established the relation between selectivity and subsurface chemistry, and considering the metastability of PdC (12), we considered whether the system could be brought to a state sensitive enough to induce selectivity fluctuations. Activity fluctuations in simple reactions (such as CO or  $H_2$  oxidation) on the nanoscale can be observed that arise from coverage fluctuations, hence, by pure surface origin, facilitating the formation of surface chemical waves and

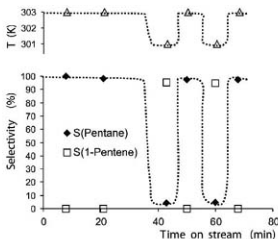
different spatiotemporal patterns (23, 24). If the kinetics of H subsurface diffusion, C dissolution, and the surface reaction comes to a period during which the population of the subsurface changes, spontaneous switching between the different hydrogenation regimes without modification of the experimental conditions is expected. Figure 3 indicates fluctuations observed during the PGAA experiments, in which the selectivity of 1-pentyne hydrogenation switched between pentane and 1-pentene formation at almost full conversion.

According to PGAA results, the H content in this experiment was PdH<sub>0.86</sub> (measured over the whole time on stream). The relatively high  $H_2$  ( $H_2/C_5 = 10$ ) ratio of the feed and the quick H diffusion to the bulk ensured that unselective hydrogenation dominated the initial period. Because C dissolution during total hydrogenation proceeds at a low rate, it takes a relatively long time until a critical amount of subsurface C accumulates to turn the hydrogenation selective. (If the rate of C dissolution is too low, no PdC will build up, because H hydrogenates away the C, and the hydrogenation remains unselective.) Because hydrogenation is exothermic, and the reaction was run adiabatically, the surface temperature when selective hydrogenation activated decreased (the thermo element reading indicated a drop of temperature from 303 to 301 K), which changed slightly the kinetics of both C and H dissolution. Because C dissolution, requiring alkyne fragmentation, is expected to be more activated, H dissolution should be more favorable at slightly lower temperatures and turn the selectivity to favor alkanes again, which makes switching back and forth possible. Considering the positive effect of defects on decreasing the switching time between possible bistable regions in pure surface-related reactions (25) and the complex parameter field of hydrogenation (such as partial pressures, temperature, surface morphology, and support effects), the possible operational window of selectivity fluctuation is likely to be narrow and requires adiabatic operation. However, kinetic discontinuities [that is, switching between two distinct activity (and sometimes selectivity) regimes] observed in a few other hydrogenation systems (26, 27) can be related to an analogous origin.

**Table 1.** Steady-state atomic H/Pd ratios of a 7-mg Pd black sample under  $H_2$  flow or under 1-pentyne hydrogenation, according to the in situ PGAA. 1-pentyne flow was kept constant at  $1.6 \text{ cm}^3 \text{ min}^{-1}$ . Temperature was near room temperature, except during high conversion, when the temperature rise of the adiabatic reactor was up to 10 K. Because the sample had low dispersion (2%), the fraction of surface atoms), and the gas-phase contribution of H has been subtracted after careful background experiments, the value in pure  $H_2$  approaches the bulk H/Pd ratio corresponding to  $\beta$ -hydride.

	H/Pd ratio ( $\pm$ absolute uncertainty)
In $H_2^*$	0.75 (0.08)
In $H_2$ after hydrogenation events	0.87 (0.09)
Unselective hydrogenation†	0.92 (0.10)
Selective hydrogenation 1‡	0.18 (0.06)
Selective hydrogenation 2§	0.72 (0.10)

\*Fresh Pd black in flowing  $H_2$ . †During 1-pentyne unselective hydrogenation (six experiments are averaged). ‡During selective hydrogenation, either directly after H treatment or thereafter (nine experiments are averaged). §During selective hydrogenation, either directly after unselective total hydrogenation events or thereafter (nine experiments are averaged).



**Fig. 3.** Spontaneous fluctuation of the reaction selectivity in 1-pentyne hydrogenation over 7 mg of Pd black during the in situ PGAA experiment with  $16 \text{ cm}^3 \text{ min}^{-1}$  of  $H_2$  and  $1.6 \text{ cm}^3 \text{ min}^{-1}$  of 1-pentyne flow. S, selectivity. Triangles indicate temperature. Conversion levels were always  $>95\%$ . The reactor was operated adiabatically, at near room temperature. (The lines are only a guide for the eyes.)



Although gas-phase alkyne hydrogenation on palladium catalysts is a surface process, we have shown that the population of the subsurface region by either C or H will determine the surface events. This result suggests that not only the surface but also the subsurface region is affected by the chemical potential of the reaction mixture. Because both H and C are part of the hydrogenation feed, the chemical potential creates feedback circles, in the form of H or C dissolution, superimposed on the surface event and performs a major role in the selectivity of hydrogenation.

We are aware that many other factors, such as promoters in the form of a second metal or selective poison, can strongly modify the hydrogenation selectivity. Our aim was to shed some light on the importance of subsurface chemistry in hydrogenation processes. We believe that to take the next step toward rational catalyst design, a critical level of understanding of both surface and subsurface dynamics in these and other complex processes of heterogeneous catalysis is required.

## References and Notes

- J. K. Nørskov *et al.*, *Science* **307**, 555 (2005).
- L. P. Nielsen, F. Besenbacher, E. Lægsgaard, I. Stenngaard, *Phys. Rev. B* **44**, 13156 (1991).
- A. R. Almozat, R. J. Madix, *Surf. Sci.* **557**, 231 (2004).
- H. Topsøe *et al.*, *Science* **295**, 2053 (2002).
- H. Blum *et al.*, *J. Phys. Chem. B* **108**, 14340 (2004).
- M. Kiskinova *et al.*, *Phys. Chem. Chem. Phys.* **9**, 3648 (2007).
- D. A. Johnson, S. P. Daley, A. L. Utz, S. T. Ceyer, *Science* **257**, 223 (1992).
- G. C. Bond, G. Webb, P. B. Wells, J. M. Winterbottom, *J. Catal.* **1**, 74 (1962).
- A. S. Al-Ammar, G. Webb, *J. Chem. Soc. Faraday Trans. 1* **74**, 3195 (1978).
- A. Molnar, A. S. Al-Ammar, M. Varga, *J. Mol. Catal. A* **173**, 185 (2003).
- A. Bondaritskiy, G. C. Bond, *Catal. Rev.* **48**, 91 (2006).
- D. Tschner *et al.*, *J. Catal.* **242**, 26 (2006).
- Additional data are available in the supporting material available on Science Online.
- The inelastic mean free path of Pd 3d photoelectrons at 720-eV excitation is 9 Å. Hence, the topmost Pd atoms should contribute approximately 20 to 25% to the whole intensity of the Pd 3d core level. Assuming that not every surface atom can interact with 1-pentene adsorbates because it is a relatively bulky species, the maximum contribution of adsorbate-induced surface core-level shift should be ~20%.
- H. Frische, E. Wicke, *Ber. Bunsenges.* **77**, 48 (1973).
- M. K. Rose, A. Borg, T. Mitsui, D. F. Ogletree, M. Salmeron, *J. Chem. Phys.* **115**, 10927 (2001).
- I. V. Yudanov, K. M. Neyman, N. Rösch, *Phys. Chem. Chem. Phys.* **6**, 116 (2004).
- J. G. de Vries, C. J. Elsevier, Eds., *Handbook for Homogeneous Hydrogenation* (Wiley-VCH, Weinheim, Germany, 2007).
- V. Ledentu, W. Dong, P. Sautet, *J. Am. Chem. Soc.* **122**, 1796 (2000).
- A. Michaelides, P. Hu, A. Alavi, *J. Chem. Phys.* **111**, 1343 (1999).
- N. A. Khan, S. Shaikhutdinov, H.-J. Freund, *Catal. Lett.* **108**, 159 (2006).
- G. L. Molnar, Ed., *Handbook of Prompt Gamma Activation Analysis with Neutron Beams* (Kluwer Academic Publishers, Dordrecht, Netherlands, 2004).
- R. Imbühl, G. Ertl, *Chem. Rev.* **95**, 697 (1995).
- H. Rotermund *et al.*, *Science* **292**, 1357 (2001).
- J. Ullrich *et al.*, *Science* **304**, 1639 (2004).
- S. D. Jackson *et al.*, *J. Catal.* **162**, 10 (1996).
- R. Marshall, G. Webb, S. D. Jackson, D. Lemmon, *J. Mol. Catal. A* **226**, 227 (2003).
- Support for this work was provided through the ATHENA project, which is funded by the Engineering and Physical Sciences Research Council, UK, and Johnson Matthey. The authors acknowledge the cooperation project between the Fritz-Haber Institute and the Institute of Isotopes founded by the Max-Planck Gesellschaft. For the PIGA experiments, we acknowledge the Integrated Infrastructure Initiative for Neutron Scattering and Muon Spectroscopy European Union Framework Programme (contract no. RI3-CT-2003-505925), the International Research and Development Project of the Hungarian National Office for Research and Technology OS project (contract no. OMFB-00384/2006), and the assistance of László Szendrői. Furthermore, we thank the Berliner Elektronenbeschleuniger-Gesellschaft für Synchrotronstrahlung staff for their continuing support during the XPS measurements.

## Supporting Online Material

www.sciencemag.org/cgi/content/full/320/SB782/6/DC1

Materials and Methods

Figs. S1 to S5

References

14 January 2008; accepted 29 February 2008

10.1126/science.1155200

# The Electrical Conductivity of Post-Perovskite in Earth's D'' Layer

Kenji Ohta,<sup>1</sup> Suzue Onoda,<sup>2</sup> Kei Hirose,<sup>1,3,\*</sup> Ryosuke Sinmyo,<sup>2</sup> Katsuya Shimizu,<sup>2</sup> Nagayoshi Sata,<sup>3</sup> Yasuo Ohishi,<sup>4</sup> Akira Yasuhara<sup>5</sup>

Recent discovery of a phase transition from perovskite to post-perovskite suggests that the physical properties of Earth's lowermost mantle, called the D'' layer, may be different from those of the overlying mantle. We report that the electrical conductivity of (Mg<sub>0.9</sub>Fe<sub>0.1</sub>)SiO<sub>3</sub> post-perovskite is >10<sup>2</sup> siemens per meter and does not vary greatly with temperature at the conditions of the D'' layer. A post-perovskite layer above the core-mantle boundary would, by electromagnetic coupling, enhance the exchange of angular momentum between the fluid core and the solid mantle, which can explain the observed changes in the length of a day on decadal time scales. Heterogeneity in the conductivity of the lowermost mantle is likely to depend on changes in chemistry of the boundary region, not fluctuations in temperature.

Geomagnetic observations have shown that the electrical conductivity of the upper to middle part of the lower mantle is 1 to 10 S/m (1), consistent with the laboratory measurements of the conductivity of silicate perovskite (2–4). The possible existence of a highly

conductive layer has been often suggested in the deepest mantle from geophysical modeling (5, 6), where the recently discovered post-perovskite phase is dominant (7, 8). Ono *et al.* (9) speculated that post-perovskite had a high conductivity from the results of shock-wave experiments on Al<sub>2</sub>O<sub>3</sub>, which may be an analog. Here, we report direct measurements of the conductivity of (Mg, Fe)SiO<sub>3</sub> post-perovskite at pressures and temperatures corresponding to the conditions at the D'' layer of the mantle.

We measured the dc electrical conductivity in a laser-heated diamond-anvil cell (DAC) (10, 11) (Fig. 1) (see supporting material). In the first run, we compressed a (Mg<sub>0.9</sub>Fe<sub>0.1</sub>)SiO<sub>3</sub> amorphous sample to 37 GPa in a DAC at room temperature and then heated it to about 1800 K to synthesize

perovskite. The resistance of untransformed material was ~10<sup>3</sup> Ω, and it dropped by two orders of magnitude after the synthesis of perovskite. Subsequently, the sample resistance was measured with increasing temperature; it decreased from 21 MΩ at 300 K to 20 kΩ at 1940 K. The conductivity was estimated to be about 1 S/m at high temperatures (Fig. 2). This value is substantially higher than that determined in (12) in a DAC but is reasonably consistent with the measurements on (Mg<sub>0.9</sub>Fe<sub>0.1</sub>)SiO<sub>3</sub> perovskite at 23 GPa in a multi-anvil apparatus by Katsura *et al.* (3). Next, we further compressed this sample to 58 GPa and carried out the measurements between 1580 and 2290 K (Fig. 2).

Similarly, in the second set of experiments, perovskite was first synthesized, and then the high-temperature conductivity measurements were performed up to 2700 K at 104 GPa and to 2660 K at 117 GPa (Fig. 2). The conductivity was about 10<sup>-1</sup> to 10<sup>-2</sup> S/m at high temperatures, considerably lower than that measured at 37 to 58 GPa in the first run. We further squeezed this sample to 143 GPa and reheated it to ~2000 K for 20 min. During laser heating, the sample resistance drastically dropped by four orders of magnitude. This pressure is well within the stability field of iron-bearing post-perovskite (13, 14), suggesting that such a drastic change in the resistance was a result of the perovskite to post-perovskite phase transformation. The sample resistance remained almost constant at ~7 kΩ as the temperature was increased from 300 to 2000 K, which corresponds to a conductivity of 1.4 × 10<sup>2</sup> S/m

<sup>1</sup>Department of Earth and Planetary Sciences, Tokyo Institute of Technology, 2-26-1 Ookayama, Meguro, Tokyo 152-8551, Japan. <sup>2</sup>Center for Quantum Science and Technology under Extreme Conditions, Osaka University, 1-3 Machikaneyama, Toyonaka, Osaka 560-8531, Japan. <sup>3</sup>Institute for Research on Earth Evolution, Japan Agency for Marine-Earth Science and Technology, 2-15 Natushima, Yokosuka, Kanagawa 237-0061, Japan. <sup>4</sup>Japan Synchrotron Radiation Research Institute, 1-1-1 Koto, Sayo, Hyogo 679-5198, Japan. <sup>5</sup>ISOL Ltd., 3-1-2 Musashino, Akishima, Tokyo 196-8558, Japan.

\*To whom correspondence should be addressed. E-mail: kei@geo.titech.ac.jp (K.H.)

(Fig. 2). Pressure should have increased at higher temperatures because of thermal expansion of the sample. If such an increase is considered, temperature may have a small negative effect on the electrical conductivity of post-perovskite.

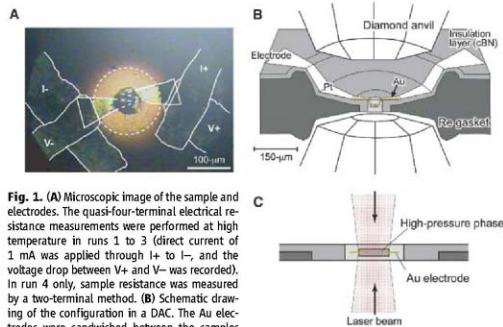
In a third run, we synthesized post-perovskite by heating the starting material to 2000 K for 30 min at 129 GPa. The x-ray diffraction (XRD) pattern indicated that the sample was dominated by post-perovskite but included lesser amount of perovskite. The sample resistance changed little from 31 k $\Omega$  at 300 K to 24 k $\Omega$  at 2500 K. The conductivity was estimated to be  $4.9 \times 10^7$  S/m at 2500 K, with a small temperature dependence

(Fig. 2). During decompression of this sample to 102 GPa at room temperature, the resistance increased slightly. After the complete pressure release, the sample was examined under both transmission electron microscope (TEM) and field-emission-type scanning electron microscope (FE-SEM, HITACHI SU-70), with a spatial resolution of 1.0 nm. No metal-like phase was observed throughout the sample (fig. S1). In addition, the chemical composition of post-perovskite was analyzed by energy-dispersive spectroscopy (EDS) and electron energy-loss near-edge structure (ELNES) spectroscopy equipped with the TEM (fig. S2). The results show that post-perovskite

has a Mg/(Mg + total Fe) molar ratio of  $0.89 \pm 0.10$ , consistent with those of the starting material (table S1). This indicates that the Fe<sup>2+</sup> abundance in the sample remained unchanged during experiments, although we did not control the oxygen fugacity specifically. A fourth experiment corroborated the low conductivity of perovskite. We synthesized perovskite from the amorphous sample by heating to 2000 K for 30 min and then performed the conductivity measurements at 121 GPa. The conductivity was low between 1450 and 1950 K, pretty consistent with the results of run 2 (Fig. 2).

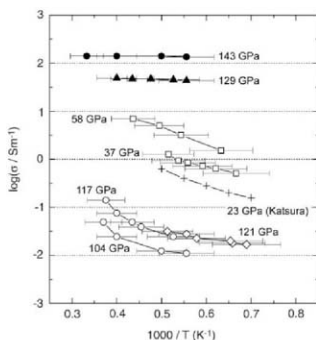
These results indicate that the electrical conductivity of (Mg, Fe)SiO<sub>3</sub> post-perovskite is much higher than that of perovskite (Fig. 2). The post-perovskite phase has a stacked SiO<sub>4</sub> octahedral sheet structure with interlayer (Mg, Fe) ions (7, 8). The high conductivity likely reflects the short Fe-Fe distance in the (Mg, Fe) layer, which is shorter than that in perovskite (15). The lower conductivity of perovskite at 104 to 121 GPa than at 37 to 58 GPa could be due to the high-spin to low-spin transition of iron in perovskite (16). A recent theoretical study (17) suggests that ferric iron in perovskite undergoes spin transition above 76 GPa at 0 K, although the pressure range of transition has been controversial. The conduction in the high-spin perovskite is dominated by a small-polaron process of electron hopping between ferrous and ferric iron sites (2, 3). The unpaired electrons in the 3d orbital play important roles in this process, but the number of unpaired electrons of ferric iron decreases from five to one at this spin-pairing transition, thus resulting in a marked reduction in the conductivity. Similar reduction in the electrical conductivity has been observed for (Mg, Fe)O ferropentacalcite between 50 and 70 GPa at room temperature (11, 18), and it has been attributed to the iron spin-pairing transition as well (19).

A layer with a high electrical conductivity above the core-mantle boundary would enhance the electromagnetic (EM) coupling between the fluid core and solid mantle. It has been suggested that if the conductivity of this layer is  $>10^7$  S (at least  $3 \times 10^7$  S), the resultant exchange of angular momentum between the core and the mantle would be sufficient to change the length of a day on decadal time scales by a few milliseconds, as has been observed (5), although several other mechanisms have been proposed (20). Post-perovskite is a primary mineral of the D'' layer below about a 2600-km depth (7, 8, 21). Our measurements on (Mg, Fe)SiO<sub>3</sub> post-perovskite indicate that the conductance of the D'' layer may be  $4 \times 10^7$  S (the conductance is related to the conductivity and thickness of the layer). The post-perovskite phase in the D'' region actually includes a certain amount of Al<sub>2</sub>O<sub>3</sub>, which increases the Fe<sup>3+</sup>/(Fe<sup>2+</sup>+Fe<sup>3+</sup>) ratio in post-perovskite (22) and hence should further enhance the electrical conductivity. In perovskite, experiments (4) showed that inclusion of 2.89 weight percent Al<sub>2</sub>O<sub>3</sub> increased the conductivity by a factor of 3.5. The



**Fig. 1.** (A) Microscopic image of the sample and electrodes. The quasi-four-terminal electrical resistance measurements were performed at high temperature in runs 1 to 3 (direct current of 1 mA was applied through I+ to I-, and the voltage drop between V+ and V- was recorded). In run 4 only, sample resistance was measured by a two-terminal method. (B) Schematic drawing of the configuration in a DAC. The Au electrodes were sandwiched between the samples and connected to Pt leads outside the sample hole. The sample and electrodes were insulated against Re gasket by a cubic-BN layer. (C) Close-up view of the sample during heating by laser. The sample and gold electrodes were heated from both sides by laser, which had a beam diameter of 30 or 50 μm. Only the high-temperature part of the sample transformed to the high-pressure phase (see fig. S4 for a TEM image of the recovered sample).

**Fig. 2.** Electrical conductivity ( $\sigma$ ) of perovskite and post-perovskite as a function of reciprocal temperature. Squares, run 1; circles, run 2; triangles, run 3; diamonds, run 4. Open and closed symbols indicate measurements of perovskite and post-perovskite, respectively. Previous data on perovskite by Katsura *et al.* (3) are also presented by crosses. The measured variations in temperature between the electrodes are shown by error bars.



conductance of the D' layer therefore may be high enough ( $>10^8$  S) to account for the decadal variations in the length of a day. In addition, the EM coupling also affects the periodic precession of the Earth's axis of rotation (nutation). The high conductance of the post-perovskite-rich D' layer may explain the retrograde 18.6- and 1.0-year nutations that have been observed (6). A 200-m-thick metallic solid layer at the top of the core has been proposed as the source of these changes (6), but a ~300-km-thick post-perovskite layer provides an alternative explanation.

Heterogeneity in electrical conductivity also has been inferred in the deep lower mantle from observations of geomagnetic jerks (23). The inferred higher conductivity underneath Africa and southern Pacific has been attributed to higher temperatures there, corresponding to the regions with large low shear-wave velocity anomalies in the D' layer (24). Our measurements, however, show a minimal or even negative temperature dependence of the electrical conductivity of post-perovskite (Fig. 2). Thus, such conductivity heterogeneities in the D' layer, if any, could have a chemical origin rather than a thermal origin (25).

# References and Notes

- N. Olsen, *Geophys. J. Int.* **138**, 179 (1999).
- T. J. Shankland, J. Peyronneau, J. P. Poirier, *Nature* **366**, 453 (1993).
- T. Katsura, K. Sato, E. Ito, *Nature* **395**, 493 (1998).
- Y. Xu, C. McCammon, B. T. Poe, *Science* **282**, 922 (1998).
- R. Hahné, in *The Core-Mantle Boundary Region*, M. Gurnis, M. E. Wyssoc, E. Knittle, B. A. Buffett, Eds. (American Geophysical Union, Washington, DC, 1999), pp. 139–151.
- B. A. Buffett, E. J. Garnero, R. Jeanloz, *Science* **290**, 1338 (2000).
- M. Murakami, K. Hirose, K. Kawamura, N. Sata, Y. Ohishi, *Science* **304**, 855 (2004).
- A. R. Oganov, S. Ono, *Nature* **430**, 445 (2004).
- S. Ono, A. R. Oganov, T. Koyama, H. Shimizu, *Earth Planet. Sci. Lett.* **246**, 326 (2006).
- K. Shimizu, H. Ishikawa, D. Takao, T. Yagi, K. Amaya, *Nature* **419**, 597 (2002).
- K. Ohira, K. Hirose, S. Onoda, K. Shimizu, *Proc. Jpn. Acad. Ser. B* **83**, 97 (2007).
- X. Y. Li, R. Jeanloz, *J. Geophys. Res.* **95**, 5067 (1990).
- W. L. Mao et al., *Proc. Natl. Acad. Sci. U.S.A.* **102**, 9751 (2005).
- S. Tazawa, K. Hirose, N. Sata, Y. Ohishi, *Phys. Earth Planet. Inter.* **160**, 319 (2007).
- T. Itaka, K. Hirose, K. Kawamura, M. Murakami, *Nature* **430**, 442 (2004).
- J. Badro et al., *Science* **305**, 383 (2004).
- F. W. Zhang, A. R. Oganov, *Earth Planet. Sci. Lett.* **249**, 436 (2006).
- J. F. Lin et al., *Geophys. Res. Lett.* **34**, L16305 (2007).
- J. Badro et al., *Science* **300**, 789 (2003).
- J. Blochman, *Annu. Rev. Earth Planet. Sci.* **26**, 501 (1998).
- M. E. Wyssoc et al., in *The Core-Mantle Boundary Region*, M. Gurnis, M. E. Wyssoc, E. Knittle, B. A. Buffett, Eds. (American Geophysical Union, Washington, DC, 1998), pp. 273–297.
- R. Shimizu, K. Hirose, H. S. O'Neill, E. Okunishi, *Geophys. Res. Lett.* **33**, L25513 (2006).
- H. Nagao, T. Iyemori, T. Higuchi, T. Araki, *J. Geophys. Res.* **108**, 2524 (2003).
- N. Takeuchi, *Geophys. J. Int.* **169**, 1153 (2007).
- T. Lay, E. J. Garnero, in *The State of the Planet: Frontiers and Challenges in Geophysics*, R. S. J. Sparks, C. J. Hawkesworth, Eds. (American Geophysical Union, Washington, DC, 2004), pp. 25–41.
- We thank H. Tsunakawa, K. Kawamura, M. Ichiki, and H. Nagao for thoughtful comments, and T. Komabayashi, Y. Komayama, and H. Otsawa for technical supports. Comments from three reviewers helped to improve the manuscript. XRD measurements were conducted at Spring 8 (proposal no. 2007AC099). The TE-SEM study was done at the Hitachi High-Technologies Co.

## Supporting Online Material

www.sciencemag.org/cgi/content/full/320/SB789/DC1

Materials and Methods

Figs. S1 to S4

Table S1

References

11 January 2008; accepted 22 February 2008

10.1126/science.1155148

## Graphite Whiskers in CV3 Meteorites

Marc Fries\* and Andrew Steele

Graphite whiskers (GWs), an allotrope of carbon that has been proposed to occur in space, have been discovered in three CV-type carbonaceous chondrites via Raman imaging and electron microscopy. The GWs are associated with high-temperature calcium-aluminum inclusion (CAI) rims and interiors, with the rim of a dark inclusion, and within an inclusion inside an unusual chondrule that bears mineralogy and texture indicative of high-temperature processing. Current understanding of CAI formation places their condensation, and that of associated GWs, relatively close to the Sun and early in the condensation sequence of protoplanetary disk materials. If this is the case, then it is a possibility that GWs are expelled from any young solar system early in its history, thus populating interstellar space with diffuse GWs. Graphite whiskers have been postulated to play a role in the near-infrared (near-IR) dimming of type Ia supernovae, as well as in the thermalization of both the cosmic IR and microwave background and in galactic center dimming between 3 and 9 micrometers. Our observations, along with the further possibility that GWs could be manufactured during supernovae, suggest that GWs may have substantial effects in observational astronomy.

Carbon allotropes known to exist in carbonaceous meteorites—ranging from simple organic compounds, to macromolecular carbon, to graphite, to diamond—cover a range of formation temperatures (1). Adding to this list, we report the discovery of high-temperature, vapor-grown GWs in different mineralogical settings in three CV-type carbonaceous chondrites. The identification and mineralogical context of this phase are indicative of carbon condensation in a higher-temperature regime than that asso-

ciated with the other carbon allotropes, with the possible exception of diamond.

Graphite whiskers are essentially needle-like morphologies formed of rolled graphite spindles. Graphite whiskers have been reported in two natural settings (2, 3), and several laboratory synthesis methods of GWs have been described (4–6). All known GW synthesis methods involve deposition from a carbon-containing gas at relatively high temperatures, ranging up to 2273 K in a furnace (4) and up to ~3900 K by arc discharge (5). Although the stability field for GWs is crudely understood, Sears (7) showed on the basis of thermodynamics arguments that GW growth is favorable at high temperatures.

The primary tool we used to locate GWs is confocal Raman imaging spectroscopy (CRIS),

supplemented with scanning electron microscopy (SEM). The Raman spectrum of GWs is distinctive among carbon allotropes (8–10), allowing the detection of individual whiskers even in the presence of other carbon phases. The GW spectrum is characterized by narrow G and D Raman peaks (~1585 and ~1345  $\text{cm}^{-1}$ , respectively) and an unusually intense D\* overtone mode (~2690  $\text{cm}^{-1}$ ) that is diagnostic of this species (Fig. 1).

Graphite cones exhibit a spectrum very similar to that of GWs (6). These polymorphs are also composed of rolled graphite but taper to a point instead of forming a long needle-like morphology (11). The primary means of distinguishing between the two forms is by the intensity of the D\* Raman band and direct observation (Figs. 1 and 2).

Pure whiskers, as produced by Tan et al. (8), exhibited a Raman D\*/D band intensity ratio of about 16, whereas the GWs we found have a ratio of about 3 to 6 (Fig. 1). This effect may arise from elemental impurities in the natural system that are absent in the laboratory setting, which would alter the Raman spectrum through the addition of substitution defects and/or graphene edge functionalization. Another possibility is that meteorite matrix carbon is adding intensity to the overall G and D bands. Additionally, the GWs could be damaged by sample preparation or partially masked from the Raman excitation laser. Saito (12) reports a continuum of GW morphologies—ranging from columnar shapes to frustums, spindles, and even hourglass shapes—in whiskers produced by anoxic heat treatment of wood samples in excess of 2273 K. This indicates that naturally derived systems produce a wide range of whisker morphol-

Geophysical Laboratory, Carnegie Institution of Washington, 5251 Broad Branch Road N.W., Washington, DC 20015, USA.

\*To whom correspondence should be addressed. E-mail: Marc.D.Fries@jpl.nasa.gov

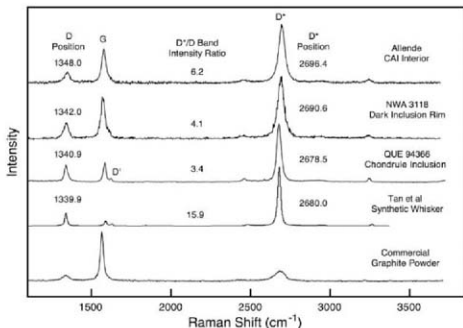


ogies, which is consistent with our Raman observations. In any event, the fundamental Raman spectral property of a high  $D^*/D$  ratio is emblematic of whisker-like graphite morphologies.

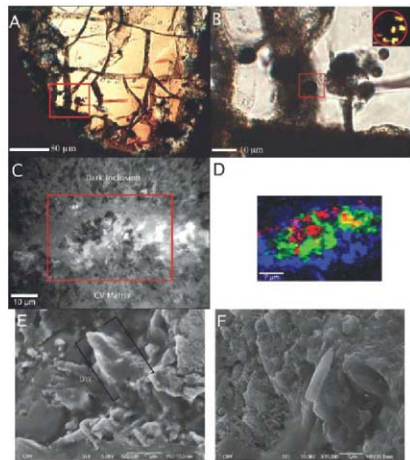
We found GWs in three meteoritic settings. The GWs found in the QUE 94366 CV meteorite reside within an inclusion in a type I FeO-poor chondrule that appears to have cooled from an atypically high temperature, as evidenced by refractory mineral inclusions and its nearly single-crystal composition (Fig. 2, A and B). The GW-bearing inclusion includes a sulfide phase, chromite, and void space within a ~10- $\mu\text{m}$ -diameter spherical body. No other carbon allotropes are in evidence, and the whiskers present are apparently hundreds of nanometers in length, because most of them appear to be confined within one or two 360-nm<sup>2</sup> image pixels. Whisker formation in this case must have occurred within the parent inclusion as the chondrule cooled from high temperature, fed by a carbon-rich gas trapped within the inclusion. CRIS allows imaging within transparent minerals, and this example of a meteoritic GW is within an intact chondrule inclusion entirely contained within the host matrix. These GWs do not breach the surface of this section and therefore cannot be contaminants, but it is also unlikely that in this setting would be ejected from chondrule interiors into interstellar space and so participate in modifying astronomical observations of distant objects.

The second example of GWs is within compacted carbonaceous material in the alteration rim of a type A dark inclusion (DI) in the NWA 3118 CV3 meteorite (Fig. 2, C and D). Dark inclusions (13–15) are composed of CV meteoritic material that has been subjected to strong heating followed by aqueous alteration. The discontinuous and porous DI rim includes andradite and hedenbergite grains, with proposed formation temperatures greater than 1273 K (15). Although collisions on the CV parent body could conceivably spall a small number of these GWs into interplanetary space, the rarity of such an event and uncertainties about the formation mechanism of DIs render these GWs unlikely to participate in affecting astronomical observations of distant objects.

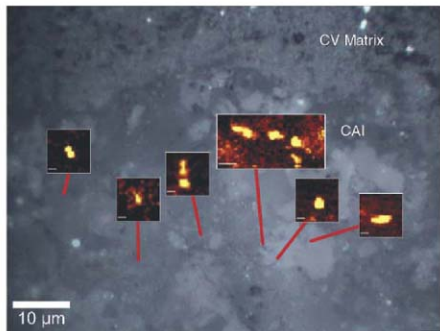
A third example of GWs found in CAI rims and interiors is the most likely candidate for subsequent ejection into the interstellar medium. We examined nine CAIs in thin sections, fresh fracture surfaces, and a potted butt in the Allende meteorite (Fig. 2, E and F). One yielded a Raman signature of GWs at the CAI/ CV matrix boundary, and five yielded GWs within the CAI interior. Of a total of 37 Raman images, each ~200  $\mu\text{m}^2$  in area, 9 yielded Raman signatures of GWs with a  $D^*/D$  Gaussian fit intensity ratio of at least 3. One CAI yielded multiple whiskers that generally appear to be distributed in a band, although this distribution bears no immediately obvious connection with the mineralogy of the CAI (Fig. 3). The discovery of GWs incorporated into CAIs implies that GWs condensed during and immediately after CAI formation in



**Fig. 1.** Raman spectra of GWs from examples found in an Allende CAI, a DI rim from NWA 3118, a chondrule inclusion in QUE 94366, and synthetic examples as compared against graphite. Note the prominent  $D^*$  Raman peak around 2690  $\text{cm}^{-1}$ , which is twice the Raman shift of the D band. See text for discussion of the peak intensity variation.



**Fig. 2.** (A) Transmitted light image of chondrule in QUE 94366, showing nearly single-crystal morphology and opaque inclusions. (B) Image from boxed area in (A). The inclusion in the center, which is also shown in a Raman image (inset), contains sulfide, chromite, and GWs. Inset scale bar, 1  $\mu\text{m}$ . (C) NWA 3118 DI rim showing the boundary between DI and meteorite matrix containing porous andradite and hedenbergite grains. (D) Raman composite image from boxed area in (C) showing GWs (red), andradite (green), and hedenbergite (blue). (E) SEM image of a tip of a GW exposed at a fresh fracture surface in a CAI. (F) A second whisker-like object with the "halved spindle" morphology described by Saito (12). Energy-dispersive x-ray spectroscopy shows that the objects in (E) and (F) are composed of carbon.



**Fig. 3.** Reflected light image of a polished Allende CAI surface with overlaid Raman images of the intensity of a Gaussian fit to the  $D^+$  GW band. Scale bars for the inset images are 1  $\mu\text{m}$ , except for the scale bar in the largest inset, which is 2  $\mu\text{m}$ . Note the elongated nature of most of the whiskers. Whiskers that appear rounded may be truncated by polishing, may be oriented perpendicular to the sample surface, or may actually have a conical morphology.

the protoplanetary disk, very near the young Sun (16) and during a period when its polar and X-wind outflow may have been active (17, 18). From here, these GWs could have been ejected from the young stellar system into interstellar space, producing an example of GW production and expulsion that may be extrapolated onto other young stellar systems. Furthermore, condensation of material ejected during supernovae may also produce GWs in a mechanism similar to that shown in meteorites.

In astronomy, whisker (or needle) morphologies of carbon, silicates, or iron have been invoked to explain several phenomena. They have been used to model the observed attenuation of IR light in the 3- to 9- $\mu\text{m}$  range in observations of the galactic center and Cassiopeia A (19–22) that cannot be adequately explained by populations of polycyclic aromatic hydrocarbons and spherical silicates, iron, and graphite grains (23, 24). Whiskers have been proposed to explain the apparent dimming of type Ia supernovae (SN Ia) and also for attenuating cosmic microwave background radiation (21, 22, 25–27), although the latter interpretation has been challenged (28). In the case of IR dimming of SN Ia, models invoking spherical (or “gray”) dust show that the extinction of light in visible wavelengths would occur before dimming in the near IR (29, 30). However, it has been calculated that inclusion of GWs at a concentration as low as 0.1% would produce the observed dimming without obstructing visible wavelengths (31, 32). With the discovery of GWs in a meteoritic setting, their physical properties are now available for testing against these models and observa-

tions. Optical effects from these whiskers may have implications for interpreting data on supernova brightness that have been used to support the notion of dark energy (33, 34).

#### References and Notes

1. T. Henning, *F. Salama, Science* **282**, 2204 (1998).
2. J. A. Jaszczak et al., *Can. Mineral.* **45**, 379 (2007).
3. J. A. Jaszczak et al., *Carbon* **41**, 2085 (2003).
4. S. Amelind et al., *J. Cryst. Growth* **121**, 543 (1992).
5. R. Bacon, *J. Appl. Phys.* **31**, 283 (1960).
6. Y. Gogotsi et al., *Science* **290**, 317 (2000).

7. G. Sears, *J. Chem. Phys.* **31**, 358 (1959).
8. P. H. Tan et al., *Phys. Rev. B* **64**, 214031 (2001).
9. P. H. Tan et al., *Philos. Trans. R. Soc. London Ser. A* **362**, 2289 (2004).
10. J. Dong et al., *Appl. Phys. Lett.* **80**, 3733 (2002).
11. S. Dimovski, Y. Gogotsi, in *Nanotubes and Nanofibers*, Y. Gogotsi, Ed. (Taylor and Francis, New York, 2006), pp. 109–134.
12. Y. Saito, T. Arima, *Carbon* **45**, 248 (2007).
13. C. A. Johnson et al., *Geochim. Cosmochim. Acta* **54**, 819 (1990).
14. A. N. Krot, E. R. D. Scott, M. E. Zolensky, *Meteoritics* **30**, 748 (1995).
15. F. E. Brenker, A. N. Krot, *Am. Mineral.* **89**, 1280 (2004).
16. L. Grossman, *Geochim. Cosmochim. Acta* **36**, 597 (1972).
17. F. Shu et al., *Astrophys. J.* **429**, 781 (1994).
18. F. Shu et al., *Science* **277**, 1475 (1997).
19. E. Dwek, *Astrophys. J.* **607**, 848 (2004).
20. E. Dwek, *Astrophys. J.* **611**, L109 (2004).
21. A. N. Aguirre, *Astrophys. J.* **512**, L19 (1999).
22. A. N. Aguirre, *Astrophys. J.* **525**, 383 (1999).
23. A. U. B. T. Draine, *Astrophys. J.* **550**, L213 (2001).
24. V. Zubko et al., *Astrophys. J. Suppl. Ser.* **152**, 211 (2004).
25. J. V. Natfika et al., *Publ. Astron. Soc. Pac.* **114**, 1092 (2002).
26. N. C. Wickramasinghe, F. Hoyle, *Astrophys. Space Sci.* **213**, 143 (1994).
27. A. N. Aguirre, *Astrophys. J.* **533**, 1 (2000).
28. C. Sivaaram, G. A. Shah, *Astrophys. Space Sci.* **117**, 199 (1985).
29. A. U. B. T. Draine, *Astrophys. J.* **584**, 593 (2003).
30. A. R. Robins, J. Cepa, *Astron. Astrophys.* **464**, 465 (2007).
31. N. C. Wickramasinghe, D. H. Wallis, *Astrophys. Space Sci.* **240**, 157 (1996).
32. F. Hoyle et al., *Astrophys. Space Sci.* **103**, 371 (1984).
33. S. Perlmutter et al., *Astrophys. J.* **517**, 565 (1999).
34. A. G. Reiss et al., *Astron. J.* **116**, 1609 (1998).
35. We thank A. Boss, G. Cody, T. Gooding, M. Hudson, A. Roberge, V. Rubin, A. Ruzicka, T. McCoy, E. Vornoi, S. Rinehart, A. Weinberger, L. Wenzelbach, and P. Tan for assistance; the NASA Sample Return Laboratory Instrument and Data Analysis Program, Astrobiology Science and Technology for Exploring Planets, and Astrobiology Institute programs for funding this work; the Antarctic Search for Meteorites expedition; and the RRIFF database project.

29 November 2007; accepted 14 February 2008

Published online 28 February 2008

10.1126/science.1153578

Include this information when citing this paper.

## Covariant Glacial-Interglacial Dust Fluxes in the Equatorial Pacific and Antarctica

Gisela Winckler,<sup>1,\*</sup> Robert F. Anderson,<sup>1,2</sup> Martin Q. Fleisher,<sup>1</sup> David McGee,<sup>1,2</sup> Natalie Mahowald<sup>3</sup>

Dust plays a critical role in Earth's climate system and serves as a natural source of iron and other micronutrients to remote regions of the ocean. We have generated records of dust deposition over the past 500,000 years at three sites spanning the breadth of the equatorial Pacific Ocean. Equatorial Pacific dust fluxes are highly correlated with global ice volume and with dust fluxes to Antarctica, which suggests that dust generation in interhemispheric source regions exhibited a common response to climate change over late-Pleistocene glacial cycles. Our results provide quantitative constraints on the variability of aeolian iron supply to the equatorial Pacific Ocean and, more generally, on the potential contribution of dust to past climate change and to related changes in biogeochemical cycles.

Dust affects climate, both directly by altering the radiation budget of the atmosphere (1) and indirectly by influencing the biological uptake of  $\text{CO}_2$  by the oceans (2)

and the exchange of radiatively active gases with the atmosphere (3). Thus, dust may have been an important player in climate change in the past and is potentially one in the future. Polar ice core

records [e.g., (4)] provide evidence that glacial dust deposition at high latitudes was as much as a factor of 25 higher than during interglacial periods. However, research on the role of dust in the past has been hampered by the scarcity of well-resolved internally consistent records of dust deposition at low latitudes (5), where changes may have important impacts on marine biogeochemistry (6), surface radiation (7), and the hydrological cycle (8).

Because of the potential importance of dust in forcing climate change, considerable effort is now devoted to including dust-generating processes in climate models (9–11). Complementary modeling endeavors to simulate the impact of dust deposition on marine biota, nutrient cycles, and atmospheric  $\text{CO}_2$  (6, 12). These impacts appear to be particularly important in high nutrient-low chlorophyll regions (HNLC) such as the equatorial Pacific Ocean, where concentrations of nutrients are high, yet chlorophyll, or primary production, is low. Phytoplankton growth in the equatorial Pacific has been shown to be limited by iron supply (13). Because aeolian dust is a substantial source of iron, changes in dust input have the potential to affect the ecosystem structure and carbon cycle in this iron-limited region.

Efforts to quantify dust-related impacts on climate and ocean biogeochemistry in the equatorial Pacific region have been limited by uncertainty as to the magnitude and even sign of glacial-interglacial dust flux changes. Several studies have reported increased dust fluxes during interglacial periods (14) or dust fluxes unrelated to glacial-interglacial cycles (15). Others have found dust accumulation maxima during glacial periods, as recently shown along short meridional transects in the eastern (16) and central (17) equatorial Pacific Ocean.

Here, we present a reproducible and self-consistent reconstruction of the aeolian dust flux across the equatorial Pacific from marine sediments deposited over the past 500,000 years. Our transect spans from the eastern equatorial Pacific [Ocean Drilling Program (ODP) site 849; 110.5°W, 0.2°N], across the central equatorial Pacific (TIN013-PC72; 0.1°N, 139.4°W), to the western equatorial Pacific (ODP site 806; 159.3°E, 0.3°N, RC17-177; 159.5°E, 1.75°N) (Fig. 1) (18). We use common thorium ( $^{232}\text{Th}$ ), a trace element enriched in continental crust and low in basaltic volcanic material, as a tracer for lithogenic material, which, in remote regions in the Pacific Ocean, is predominantly derived from aeolian dust supply (14). A survey of circum-Pacific dust and loess data (16) shows that  $^{232}\text{Th}$  concentrations in potential dust source areas fall within 1 part per million (ppm) of the average concentration of

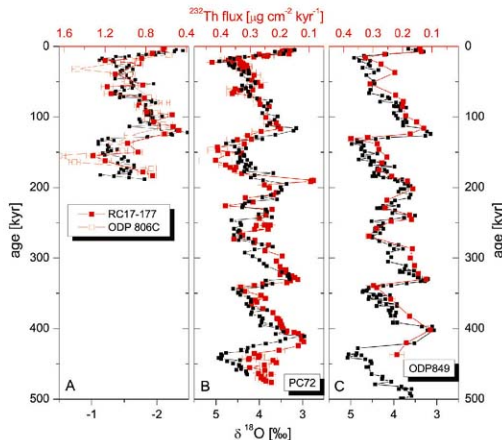
upper continental crust (10.7 ppm) (19). The validity of  $^{232}\text{Th}$  as a dust proxy is supported by the linear relationships at three of our sites between  $^{232}\text{Th}$  and terrigenous  $^{10}\text{Be}$  (fig. S1), an independent proxy for the lithogenic component that has been successfully used to reconstruct dust fluxes in marine sediments (20, 21). Because  $^{232}\text{Th}$  data are available at much higher resolution than  $^{10}\text{Be}$  in our cores, we focus here on  $^{232}\text{Th}$ .

We evaluated dust fluxes by normalizing  $^{232}\text{Th}$  concentrations to  $^{230}\text{Th}$ . This approach relies on the observation that the flux of  $^{230}\text{Th}$  to the sea floor approximately equals its known production rate from U decay in the overlying water column, thereby allowing the flux of any sedimentary constituent to be estimated from the ratio of the concentration of the constituent to that of  $^{230}\text{Th}$  [corrected for decay and detrital  $^{230}\text{Th}$  (18)]. There is currently an intense debate over the best approach to determine fluxes in marine sediments (22, 23). Equatorial Pacific dust fluxes presented here exhibit excellent internal consistency across a wide geographical region and very different productivity regimes, as well as consistency with global ice volume and with dust fluxes from Antarctica. The lack of consistency among earlier records reflects, in part, the limited age resolution of many

previous records. In addition, variable preservation of  $\text{CaCO}_3$  in equatorial Pacific sediments may have introduced systematic errors in  $\delta^{18}\text{O}$ -based age models. The use of  $^{230}\text{Th}$ -normalization greatly reduces the sensitivity of derived fluxes to such errors and this contributes to the consistency among the dust flux records presented here.

After conversion to dust mass fluxes by dividing by the average  $^{232}\text{Th}$  concentration of upper continental crust (10.7 ppm) (19), our  $^{232}\text{Th}$ -based Holocene dust fluxes can be cross-calibrated with modern observations from sediment trap studies (Table 1). Agreement between our estimates of Holocene dust fluxes and the sediment trap fluxes, derived from independent proxies, is excellent, with respect to both absolute fluxes and the observed west-east gradient. The west-east gradient in dust fluxes is also consistent with in situ observations of dust fluxes by aerosol collection (24).

Dust fluxes in the central and eastern equatorial Pacific are comparable, with slightly higher fluxes at the central Pacific location (Table 1 and Fig. 1). Dust fluxes at two locations in the western Pacific, both on (ODP site 806) and off (RC17-177) the equator, are similar to one another and are consistently a factor of 3.5 higher than in the central and eastern regions.



**Fig. 1.** Correlation of  $^{232}\text{Th}$  fluxes (red, reverse scale) with global ice volume, as traced by the oxygen isotopic composition of foraminifera (black), for (A) ODP site 806C and RC17-177 in the western equatorial Pacific [Th isotope data from (34); planktonic  $\delta^{18}\text{O}$  from (35)]; (B) TIN013-PC72 in the central equatorial Pacific [Th isotope data from (27) and from this study; benthic  $\delta^{18}\text{O}$  from (15)]; (C) ODP site 849 from the eastern equatorial Pacific [Th isotope data from this study; benthic  $\delta^{18}\text{O}$  from (33)].  $^{232}\text{Th}$  fluxes are highest at maximum glacial conditions (as indicated by maximum  $\delta^{18}\text{O}$ ) and lowest at minimal ice coverage. The limited resolution of the records does not allow us to decipher a lead-lag relationship between dust flux and ice volume change at terminations.

<sup>1</sup>Lamont-Doherty Earth Observatory of Columbia University, Palisades, NY 10964, USA. <sup>2</sup>Department of Earth and Environmental Sciences, Columbia University, New York, NY 10027, USA. <sup>3</sup>Department of Earth and Atmospheric Sciences, Cornell University, Ithaca, NY 14853, USA.

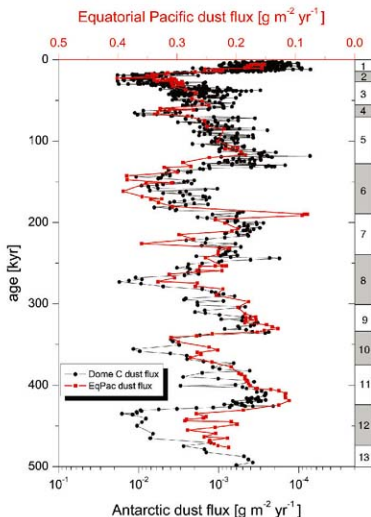
\*To whom correspondence should be addressed. E-mail: winckler@ldeo.columbia.edu

**Table 1.** Observation- and model-based estimates of dust fluxes to the Equatorial Pacific.

Source of dust flux estimate	Western Eq. Pac. (160°E) [g m <sup>-2</sup> yr <sup>-1</sup> ]	Central Eq. Pac. (140°W) [g m <sup>-2</sup> yr <sup>-1</sup> ]	Eastern Eq. Pac. (110°W) [g m <sup>-2</sup> yr <sup>-1</sup> ]	Reference
<b>MODERN</b>				
<i>Observations</i>				
<sup>232</sup> Th-derived dust flux (Holocene)	0.55	0.16	0.13	This study
Sediment trap*	0.84			(37)
Sediment trap†		0.15		(38)
<i>Model simulations</i>				
ECHAM3	0.0098	0.0037	0.0089	(9)
ECHAM4	0.0325	0.0196	0.0211	(10)
MATCH	0.059	0.05	0.043	(39)
Composite‡	0.107	0.123	0.116	(3)
CCSM-SOMB	0.098	0.34	0.59	(11)
<b>LGM</b>				
<i>Observations</i>				
<sup>232</sup> Th-derived dust flux (LGM)	1.37	0.40	0.30	This study
<i>Model simulations</i>				
ECHAM3	0.119	0.39	0.71	(9)
ECHAM4	0.049	0.056	0.106	(10)
CCSM-SOMBLGMS	0.060	0.336	0.411	(11)

\*Calculated using terrigenous = total - carbonate - opal - 1.8\*organic C (organic matter). †Calculated from Ti fluxes, assuming [Ti] = 0.3% in terrigenous fraction. ‡Composite model, based on several dust models. §LGM, Last Glacial Maximum total source.

**Fig. 2.** Covariance of dust fluxes to the equatorial Pacific (TTN013-PC72, red) and Antarctica (European Project for Ice Coring in Antarctica (EPICA) site Dome C (EDC), black). Dust fluxes at Dome C have been compiled from dust concentration data (4) and accumulation rates, derived from the new time scale EDC3 (36). Both records are plotted on their individual time scales [EDC3 (36) for the Dome C record;  $\delta^{18}\text{O}$ -derived age model (15) for TTN013-PC72]. MIS indicated along the right age axis.



Throughout the past five glacial cycles, dust fluxes at all sites show striking correlation with  $\delta^{18}\text{O}$  of foraminifera, which primarily tracks global ice volume (25). The amplitude of glacial-interglacial variations in dust fluxes, derived by comparing maximum (glacial) to minimum (interglacial)  $^{232}\text{Th}$  fluxes (table S3), is consistent among all four locations, with glacial dust fluxes about a factor of 2.5 higher than interglacial fluxes. This indicates relatively uniform glacial/interglacial changes in dust regimes throughout the entire equatorial Pacific region, independent of the absolute dust flux levels.

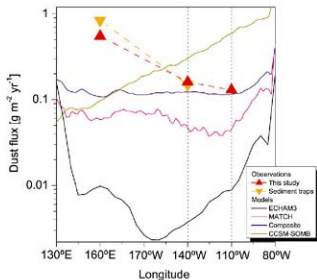
The dust flux record from the equatorial Pacific is closely correlated to the dust flux reconstruction from Dome C in Antarctica (4) (Fig. 2). While the dust flux levels are much lower in Antarctica than in the tropics, and the relative glacial-interglacial variability of the tropical records is an order of magnitude smaller than for the polar record, the records show very similar behavior over five glacial cycles. Both records show the same rapid changes, such as the dust flux decrease over the last glacial termination. Even suborbital signals such as increased dust flux during marine isotope stage (MIS) 4 and the reversal in MIS 7 co-vary in the tropics and Antarctica.

The excellent correlation between dust fluxes recorded in the tropics and in Antarctica is particularly stunning given that the records from the two regions are based on different paleoarchives, and consequently independent age models, as well as different dust measures. Furthermore, the records represent at least three distinct source areas. Previous studies have found that most of the dust deposited in the western and central equatorial Pacific originates in Asia (24, 26, 27), whereas the dust deposited in the eastern equatorial Pacific is predominantly derived from sources in northern South America (27, 28). Support for this source distribution comes from the regional patterns in the  $^{4}\text{He}_{\text{env}}$ - $^{232}\text{Th}$  characteristics (fig. S1), which point to similar dust sources for the west and central Pacific but suggest a distinct dust source for the eastern Pacific. The lower  $^{4}\text{He}_{\text{env}}$ / $^{232}\text{Th}$  ratios at the eastern site are consistent with a dominant influence from a younger ( $^3\text{He}$ -poor) dust source of northern South America. The dominant source for dust reaching Antarctica is Patagonia (29).

The similar glacial-interglacial amplitude in deposition of dust from Asia (as seen in the western and central equatorial Pacific) and northern South America (as recorded in the eastern equatorial Pacific site) indicates quantitatively similar environmental responses to climate variability by dust mobilization processes in these low- and mid-latitude climate regions. Local processes affecting dust production appear to be subsidiary. In contrast, the much larger glacial dust flux increase in Antarctica (i.e., increase by a factor of 25 in Antarctica versus a factor of 2.5 in the tropical Pacific) suggests that local processes in Patagonia may have amplified dust generation in this source region. Specifically, the advance of



**Fig. 3.** Zonal gradients in dust fluxes across the equatorial Pacific from various recent model simulations (solid lines) and observations from sediment cores and traps (triangles). Model results are listed in chronological order of their publication: European Centre Hamburg Model 3 (ECHAM3) [black, (9)], Model of Atmospheric Transport and Chemistry (MATCH) [pink, (39)], Composite [blue, (3)], and Community Climate System Model-Slab Ocean Model with Biome3 sources (CCSM-SOM3) [olive, (11)]. The west-east decrease in the observations is not reflected by most dust models and is the reverse of the strong west-east increase in the most recent model simulation (11).



the Patagonian ice sheet during glacial periods, which increased glacial erosion and deposition of fine-grained glaciogenic sediments in extensive outwash plains, provided enhanced availability of dust to be exported to Antarctica (30). This ice sheet-driven amplifier of dust production is less relevant for tropical and mid-latitude dust sources because of the absence or limited size of ice sheets in these regions.

Three factors have been identified to explain higher dust fluxes in glacial periods compared with interglacials: a less vigorous hydrological cycle resulting in reduced washout, increased glacial wind intensities leading to increased dust entrainment, and expanded dust source areas [see (31) for a review]. Although there is uncertainty concerning the complex interplay of the factors influencing dust generation in any particular region, we infer from the synchronous changes in dust fluxes seen in our records that in each of the source areas, that is, Asia, northern South America, and Patagonia, the dominant processes regulating dust generation experienced a coherent response to global climate change. This response is consistent with other substantial glacial-interglacial environmental changes, such as the near-synchronous interhemispheric termination of the last glaciation inferred from temperate mountain glacial records (32). By this scenario, the consistent dust flux variations among different source regions suggests that the interhemispheric synchronicity is not limited to the last termination but extends back over at least the last five glacial cycles.

The need for deeper understanding of the processes that regulate dust generation and transport is demonstrated by the discrepancies between measured dust fluxes and several state-of-the-art model simulations (Table 1 and Fig. 3). Improvement to models over the past decade have brought modeled dust fluxes into the appropriate magnitude ranges for the equatorial Pacific. However, most models predict dust fluxes that are either relatively uniform zonally or, as for the most recent simulation (11), increase from west

to east, in stark contrast to the strong west-to-east decrease by a factor of 3.5 in  $^{232}\text{Th}$ -based dust fluxes.

Discrepancies are even more apparent for the models simulating climate conditions at the Last Glacial Maximum (LGM). Earlier models (9) inferred LGM/modern dust flux ratios ranging from 12 to 105, greatly exceeding our glacial/interglacial dust flux ratio of 2.5, while a more recent dust simulation (11) produced dust fluxes during the LGM that are lower than under modern conditions, at odds with greater glacial dust fluxes inferred from the sediment records. The newer model (11) also produces LGM dust fluxes that increase from west to east by about a factor of 6, in strong contrast to the observed decrease by a factor of 3.5 in our  $^{232}\text{Th}$ -based reconstruction.

Research on the role of tropical dust in climate variability, as well as in climate-related changes in marine ecosystems and biogeochemical cycles, has been limited until now by the lack of internally consistent well-resolved records of dust flux. Results presented here should help to better constrain models of dust generation and transport. In addition, the coherent responses of dust fluxes from widespread source regions will serve as a basis for new hypotheses linking dust fluxes to climate change.

#### References and Notes

1. Tegen, A. A. Lacs, L. *Fung*, *Nature* **380**, 419 (1996).
2. J. Martin, *Paleoceanography* **5**, 1 (1990).
3. T. D. Jickells *et al.*, *Science* **308**, 67 (2005).
4. EPICA Community Members, *Nature* **429**, 623 (2004).
5. K. E. Kohfeld, S. P. Harrison, *Earth Sci. Rev.* **54**, 81 (2001).
6. J. K. Moore, S. C. Doney, K. Lindsay, *Global Biogeochem. Cycles* **18**, 10.1029/2004GB002220 (2004).
7. N. M. Mahowald *et al.*, *Geophys. Res. Lett.* **33**, 10.1029/2006GL026124 (2006).
8. R. L. Miller, I. Tegen, J. Rotz, *J. Geophys. Res.* **109**, 10.1029/2003JD004005 (2004).
9. N. Mahowald *et al.*, *J. Geophys. Res.* **104**, 15895 (1999).
10. M. Werner *et al.*, *J. Geophys. Res.* **107**, 10.1029/2002JD002365 (2002).

11. N. M. Mahowald *et al.*, *J. Geophys. Res.* **111**, 10.1029/2003JD006653 (2006).
12. A. J. Watson, D. C. E. Bakker, A. J. Ridgwell, P. W. Boyd, C. S. Law, *Nature* **407**, 730 (2000).
13. K. H. Coale *et al.*, *Nature* **383**, 495 (1996).
14. D. K. Rea, *Rev. Geophys.* **32**, 159 (1994).
15. R. W. Murray, M. Leinen, D. W. Murray, A. C. Mix, C. W. Knowlton, *Global Biogeochem. Cycles* **9**, 667 (1995).
16. D. McGee, F. Marantoni, J. Lynch-Stieglitz, *Earth Planet. Sci. Lett.* **257**, 215 (2007).
17. R. F. Anderson, M. Q. Fleisher, Y. Luo, *Earth Planet. Sci. Lett.* **242**, 406 (2006).
18. Materials and methods are available as supporting material on Science Online.
19. S. R. Taylor, S. M. McLennan, *The Continental Crust: Its Composition and Evolution* (Blackwell, Oxford, 1985).
20. D. B. Patterson, K. A. Farley, M. D. Norman, *Geochim. Cosmochim. Acta* **63**, 615 (1999).
21. G. Winkler, R. F. Anderson, P. Schlosser, *Paleoceanography* **20**, 10.1029/2005PA001177 (2005).
22. M. Lyle *et al.*, *Paleoceanography* **20**, 10.1029/2004PA001019 (2005).
23. R. Francois *et al.*, *Paleoceanography* **22**, 10.1029/2005PA002353 (2007).
24. J. M. Prospero, M. Uematsu, D. L. Savoie, in *Chemical Oceanography*, J. P. Riley, Ed. (Academic Press, New York, 1989), pp. 187–218.
25. W. F. Ruddiman, *Earth's Climate: Past and Present* (W. H. Freeman, New York, 2001).
26. L. A. Krissek, T. R. Jancsek, *Proc. ODP Sci. Res.* **130**, 471 (1993).
27. S. Nakai, A. N. Halliday, D. K. Rea, *Earth Planet. Sci. Lett.* **119**, 343 (1993).
28. M. A. Stancin *et al.*, *Earth Planet. Sci. Lett.* **248**, 840 (2006).
29. I. Basile *et al.*, *Earth Planet. Sci. Lett.* **146**, 573 (1997).
30. A. J. Ridgwell, A. J. Watson, *Paleoceanography* **17**, 10.1029/2001PA000729 (2002).
31. S. P. Harrison, K. E. Kohfeld, C. Roelandt, T. Claquin, *Earth Sci. Rev.* **54**, 43 (2001).
32. J. M. Schaefer *et al.*, *Science* **312**, 1510 (2006).
33. A. C. Mix *et al.*, *Proc. ODP Sci. Res.* **138**, 371 (1995).
34. S. M. Higgins, R. F. Anderson, F. Marantoni, M. Schlosser, M. Stute, *Earth Planet. Sci. Lett.* **203**, 383 (2002).
35. D. W. Lea, D. K. Pak, H. J. Spero, *Science* **289**, 1719 (2000).
36. F. Parrenin *et al.*, *Clim. Past* **3**, 19 (2007).
37. H. Kawahata, A. Suzuki, H. Ohta, *Deep Sea Res.* **47**, 2061 (2000).
38. J. Dymond, R. Collier, J. McManus, S. Hono, S. Manganini, *Paleoceanography* **12**, 586 (1997).
39. C. Luo, N. M. Mahowald, J. del Corral, *J. Geophys. Res.* **108**, 10.1029/2003JD003483 (2003).
40. We thank U. Ruth for compiling the dust flux data from Dome C on the new ED3 time scale, M. Werner for making the data for the ECHAM run available, and J. Schaefer and W. Broecker for constructive comments. This research used samples provided by the Ocean Drilling Program (ODP site 849) and the University of Rhode Island core repository (T7N013-P722). Funding for this study was provided by the National Science Foundation (grant OCE 02-21333 to R.F.A. and G.W.). We thank the Earth Institute Advance Program for supporting N.M.'s visit to Columbia University through a Marie-Tharp Fellowship. This is L-DEO contribution 7143.

#### Supporting Online Material

www.sciencemag.org/cgi/content/full/111/5055

Materials and Methods

Fig. S1

Tables S1 to S3

References

17 September 2007; accepted 19 February 2008

Published online 28 February 2008

10.1126/science.1150595

Include this information when citing this paper.

# Selective Blockade of MicroRNA Processing by Lin28

Srinivas R. Viswanathan,<sup>1</sup> George Q. Daley,<sup>1,2\*</sup> Richard I. Gregory<sup>1\*</sup>

MicroRNAs (miRNAs) play critical roles in development, and dysregulation of miRNA expression has been observed in human malignancies. Recent evidence suggests that the processing of several primary miRNA transcripts (pri-miRNAs) is blocked posttranscriptionally in embryonic stem cells, embryonic carcinoma cells, and primary tumors. Here we show that Lin28, a developmentally regulated RNA binding protein, selectively blocks the processing of pri-let-7 miRNAs in embryonic cells. Using *in vitro* and *in vivo* studies, we found that Lin28 is necessary and sufficient for blocking Microprocessor-mediated cleavage of pri-let-7 miRNAs. Our results identify Lin28 as a negative regulator of miRNA biogenesis and suggest that Lin28 may play a central role in blocking miRNA-mediated differentiation in stem cells and in certain cancers.

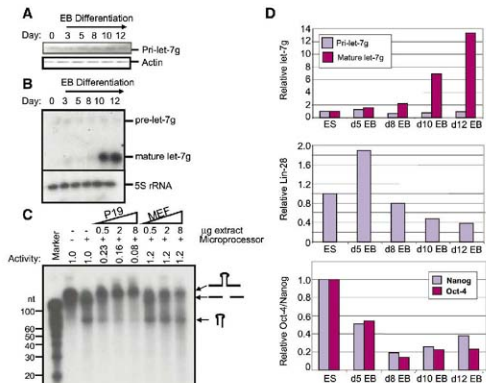
MicroRNAs (miRNAs) constitute a large family of short, noncoding RNAs that posttranscriptionally repress gene expression in metazoans. Mature miRNAs are produced from primary miRNA transcripts (pri-miRNAs) through sequential cleavages by the Microprocessor, comprising the ribonuclease III Drosha component and the double-stranded RNA (dsRNA) binding protein DGCR8 (1, 2) and Dicer (3, 4) enzyme complexes, to release pre-miRNA and mature miRNA species, respectively. Posttranscriptional control of miRNA expression has been reported to occur in a tissue-specific (5) and developmentally regulated fashion (6–8). The processing of several pri-miRNAs is blocked in embryonic tissues, with activation of processing occurring only as development proceeds. In addition, it has been reported that certain pri-miRNAs are highly expressed in human (9) and mouse embryonic stem (ES) cells, mouse embryonic carcinoma (EC) cells, and human primary tumors; however, the corresponding mature species are not detectable (7). This suggests that there may be a posttranscriptional block in miRNA biogenesis, the mechanism of which has remained unknown. In ES and EC cells, the magnitude of the Microprocessor processing block is greatest for members of the let-7 family of miRNAs, although it has been proposed that the processing of all miRNAs may be regulated at the Microprocessor step (7).

We observed that the pri-let-7 transcript is readily detectable in ES cells and remains at relatively constant levels over the course of differentiation into embryoid bodies (Fig. 1A). In contrast, mature let-7g is undetectable in undifferentiated ES cells but is strongly induced after day 10 of

differentiation (Fig. 1B). A posttranscriptional induction of let-7g expression has also been reported during the differentiation of P19 EC cells with retinoic acid (7). We sought to understand the mechanism for the posttranscriptional block in miRNA processing in EC and ES cells. We first compared cell extracts from different cell types for their ability to inhibit Microprocessor-mediated cleavage of pri-miRNA substrates to the corre-

sponding pre-miRNAs *in vitro* (Fig. 1C). Radio-labeled pri-miRNA substrates were preincubated with cell extract and were then subjected to processing by affinity-purified Microprocessor complex. Whereas extracts from undifferentiated P19 cells readily inhibited Microprocessor-mediated cleavage of pri-let-7g to pre-let-7g, cell extracts from differentiated mouse embryonic fibroblasts (MEFs) did not inhibit cleavage. Thus, the cell-type specificity of the *in vivo* Microprocessor processing block was recapitulated in our *in vitro* assay.

We surmised that a protein factor or factors present in ES and EC cells might be inhibiting Microprocessor-mediated processing of pri-miRNAs, and we used a biochemical approach to identify this factor. Electrophoretic gel mobility shift assays using a labeled pre-let-7g probe identified a specific band shift present in P19 EC and ES extract but not with MEF extract (Fig. S1). This finding suggested that pre-let-7g could be used as an effective affinity reagent for purification of the factor(s) responsible for the Microprocessor processing block. Pre-let-7g was conjugated to agarose beads and incubated with whole-cell extract from P19 cells. The affinity eluate was subjected to SDS-polyacrylamide gel electrophoresis (SDS-PAGE) followed by colloidal staining. Bands were excised



**Fig. 1.** Posttranscriptional control of pri-let-7g processing.

(A) Reverse transcription PCR for pri-let-7g transcript as described in (7) during ES differentiation to embryoid bodies. Actin serves as control. (B) Northern blot showing posttranscriptional induction of mature let-7g during embryoid body formation; 5S rRNA serves as loading control. (C) *In vitro* pri-miRNA processing reaction using radiolabeled pri-let-7g as substrate. Pri-miRNA was preincubated with various amounts of P19 cell extract or mouse embryonic fibroblast (MEF) extract before processing reaction with Flag-Drosha immunoprecipitate (see supporting online material). The ratio of pre-miRNA to pri-miRNA was quantitated by densitometry and values were normalized to the Microprocessor-only lane. (D) Quantitative PCR analysis of gene expression during embryoid body formation of a feeder-free mouse ES line (1 ES). Data are the average of experimental triplicates performed on the RNA samples from (B). Top, Pri-let-7g and mature let-7g; middle, Lin28; bottom, pluripotency factors Oct-4 and Nanog.

<sup>1</sup>Stem Cell Program, Children's Hospital Boston, Department of Biological Chemistry and Molecular Pharmacology, Harvard Medical School, Harvard Stem Cell Institute, Boston, MA 02115, USA. <sup>2</sup>Division of Pediatric Hematology/Oncology, Children's Hospital Boston and Dana-Farber Cancer Institute; and Howard Hughes Medical Institute, Division of Hematology, Brigham and Women's Hospital, Boston, MA 02115, USA.

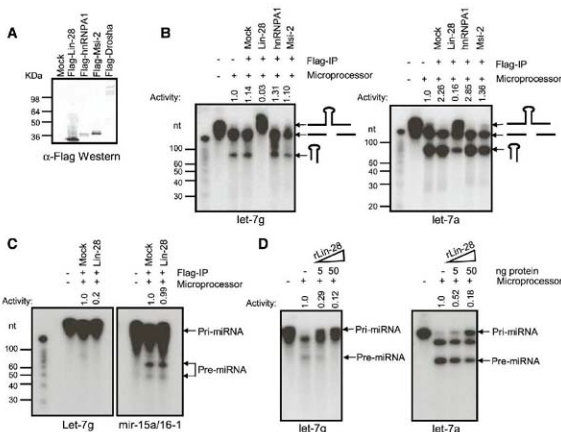
\*To whom correspondence should be addressed. E-mail: rgregory@enders.ich.harvard.edu (R.I.G.); george.daley@childrens.harvard.edu (G.Q.D.)

and subjected to mass spectroscopic sequencing in three segments (fig. S2). Sequencing revealed several RNA binding proteins copurifying with pre-

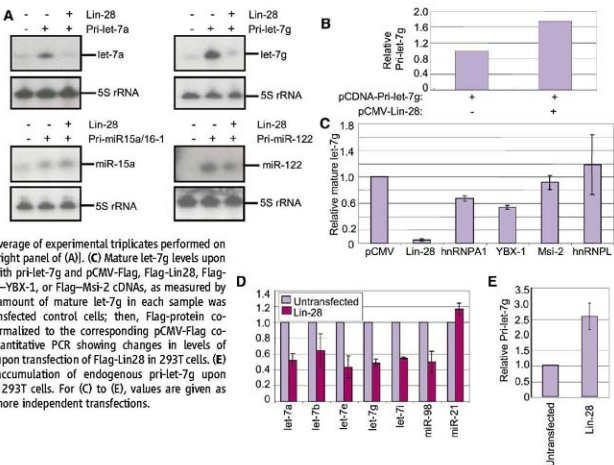
let-7g. A number of these proteins were previously identified as members of a large Drosophila-containing protein complex (2) (fig. S2).

One of the pre-let-7g-interacting proteins was the small, highly conserved RNA binding protein Lin28. Lin28 was an attractive candidate for the

**Fig. 2.** Lin28 inhibits pri-miRNA processing in vitro. **(A)**  $\alpha$ -Flag-Western blot to confirm expression of Flag-tagged proteins for use in *in vitro* assays. **(B)** *In vitro* pri-miRNA processing reaction on pri-let-7g (left panel) and pri-let-7a (right panel) substrates in the presence of mock, Flag-Lin28, Flag-hnRNP1, or Flag-Msi-2 immunoprecipitate. Quantitation was normalized to the Microprocessor-only lane. **(C)** *In vitro* pri-miRNA processing reaction on pri-let-7g (left panel) and pri-miR-15a/16-1 (right panel) substrates in the presence of either mock or Flag-Lin28 immunoprecipitate and competitor tRNA. Quantitation was normalized to the mock-IP lane. **(D)** *In vitro* pri-miRNA processing reaction on pri-let-7g (left panel) and pri-let-7a (right panel) substrates in the presence of rhis-Lin28. Quantitation was normalized to the Microprocessor-only lane.



**Fig. 3.** Ectopic expression of Lin28 selectively inhibits pri-miRNA processing in vivo. **(A)** In each panel, 293T cells were untransfected (lane 1), cotransfected with the indicated pri-miRNA and 0.5  $\mu$ g of pCMV-Flag empty vector (lane 2), or cotransfected with the indicated pri-miRNA and 0.5  $\mu$ g of Flag-Lin28 cDNA (lane 3). Total RNA was collected 40 hours after transfection and subjected to Northern blotting for the indicated miRNA. **(B)** Quantitative PCR analysis of pri-let-7g levels [average of experimental triplicates performed on the RNA samples from upper right panel of (A)]. **(C)** Mature let-7g levels upon cotransfection of 293T cells with pri-let-7g and pCMV-Flag, Flag-Lin28, Flag-hnRNP1, Flag-hnRNP1, Flag-YBX-1, or Flag-Msi-2 cDNAs, as measured by quantitative PCR. First, the amount of mature let-7g in each sample was calculated relative to untransfected control cells; then, Flag-protein cotransfected samples were normalized to the corresponding pCMV-Flag cotransfected samples. **(D)** Quantitative PCR showing changes in levels of endogenous mature miRNAs upon transfection of Flag-Lin28 in 293T cells. **(E)** Quantitative PCR showing accumulation of endogenous pri-let-7g upon transfection of Flag-Lin28 in 293T cells. For (C) to (E), values are given as average  $\pm$  SEM from two or more independent transfections.



following reasons: (i) Mutations within its RNA binding domain have been shown to impair developmental timing regulation in *Caenorhabditis elegans* (10); (ii) it is expressed specifically in undifferentiated P19 cells, mouse ES cells (11), and human ES cells (12) and is down-regulated upon differentiation; (iii) a mammalian Lin28 homolog, Lin28B, is overexpressed in hepatocellular carcinoma, and overexpression of this gene promotes cancer cell proliferation in vitro (13); (iv) it has been reported that Lin28 is expressed in embryonic muscle, neurons, and epithelia in a stage-specific fashion, and Lin28 is crucial for appropriate skeletal muscle differentiation (11); and (v) Lin28 was recently used with three other factors to reprogram human somatic fibroblasts to pluripotency (14).

We examined the kinetics of Lin28 expression during embryoid body formation (Fig. 1D). Lin28 is down-regulated upon ES cell differentiation, with kinetics that are delayed relative to the known pluripotency factors Oct4 and Nanog. This down-regulation of Lin28 temporally coincides with activation of pri-let-7 processing (Fig. 1D).

To explore the possibility that Lin28 may regulate pri-let-7 processing, we confirmed that Lin28 is capable of binding both pre-let-7g and pri-let-7g in a cosedimentation assay (Fig. S3). We then tested the ability of Lin28 to functionally block pri-miRNA processing in vitro. We observed that a Flag immunoprecipitate containing Flag-Lin28 potentially inhibited the processing of both pri-let-7a and pri-let-7g in vitro. Flag immunoprecipitates containing the control RNA binding proteins Flag-hnRNP1 and Flag-Msi2 had no effect on pri-let-7a and pri-let-7g processing (Fig. 2, A and B). Flag-Lin28 immunoprecipitate did not impair the processing of pri-miR-15a/16-1, which demonstrates the selectivity of the miRNA processing block (Fig. 2C). We next purified bacterially expressed His-Lin28 (Fig. 2D) and tested this

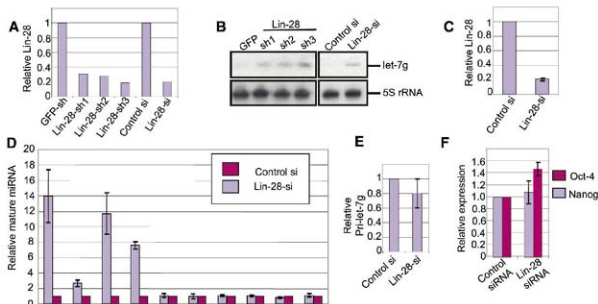
recombinant Lin28 (rLin28) for its ability to block pri-miRNA processing in vitro. rLin28 inhibited the processing of both pri-let-7a and pri-let-7g (Fig. 2D). Therefore, Lin28 is sufficient to inhibit miRNA processing at the Microprocessor step.

To determine whether Lin28 is capable of blocking miRNA processing in vivo, we introduced four pri-miRNAs in either the presence or absence of mouse Lin28 cDNA into 293T cells, a transformed human cell line that lacks Lin28. In the absence of Lin28, all ectopic pri-miRNAs were efficiently processed to their mature form (Fig. 3A and Fig. S4). However, ectopic expression of Lin28 completely blocked processing of both pri-let-7a and pri-let-7g, whereas processing of pri-miR-15a and pri-miR-122 was largely unaffected (Fig. 3A and Fig. S4). Cotransfection of pri-let-7g and Lin28 led to accumulation of pri-let-7g (Fig. 3B), consistent with the notion that Lin28 blocks miRNA processing at the Microprocessor step. We performed these cotransfection experiments with four control RNA binding proteins (YBX1, Msi2, hnRNP1, and hnRNP1) to confirm that this block in processing of pri-let-7 miRNAs is specific to Lin28 (Fig. 3C and Fig. S5). Finally, to test whether Lin28 is capable of blocking endogenous miRNA processing (as opposed to only blocking the processing of ectopically expressed pri-miRNAs), we transfected Lin28 cDNA into 293T cells and measured levels of several mature miRNAs after 4 days by quantitative polymerase chain reaction (PCR). We observed decreased endogenous levels of mature let-7 family members; levels of endogenous mature miR-21 were unaffected (Fig. 3D). Decreased mature let-7g upon Lin28 overexpression was accompanied by a corresponding increase in levels of pri-let-7g (Fig. 3E).

We sought to determine whether Lin28 is an endogenous blocker of miRNA processing in embryonic cells. We used three different short hairpin

RNAs (shRNAs) and a small interfering RNA (siRNA) targeting Lin28 to knock down endogenous Lin28 in P19 EC cells (Fig. 4A) and ES cells (Fig. S6). Knockdown of Lin28 led to an induction of mature let-7g in both P19 cells (Fig. 4B) and ES cells (Fig. S4B), indicating that Lin28 serves to inhibit miRNA processing in vivo (Fig. 4B). All let-7 family members tested were substantially up-regulated upon knockdown of Lin28, whereas levels of other miRNAs were unchanged (Fig. 4D and Fig. S7). Induction of mature let-7 miRNAs occurred within 60 hours of Lin28 knockdown, whereas let-7 miRNAs were normally induced only after 10 days of ES and P19 differentiation, when endogenous Lin28 levels fell (Fig. 1A) (7). Therefore, the induction we observed likely represents a direct effect of Lin28 on pri-miRNA processing rather than an indirect consequence of cell differentiation. In support of this notion, we observed no decrease in levels of the pluripotency markers Oct4 and Nanog upon knockdown of Lin28 over the time course of our experiment (Fig. 4F). Furthermore, global miRNA profiling detected up-regulation of only let-7 miRNAs upon Lin28 knockdown, underscoring the specificity of Lin28 in regulating let-7 miRNAs (Fig. S7).

A Lin28 homolog, Lin28B, is overexpressed in human hepatocellular carcinoma as well as in several cancer cell lines (13). Two isoforms of Lin28B, differing in their 5' exons, have been reported. The short isoform (Lin28B-S) preserves the two retroviral-type CCHC zinc-finger motifs present in the long isoform (Lin28B-L) but contains a truncated cold-shock domain. Lin28B-L overexpression induces cancer cell proliferation, whereas Lin28B-S overexpression has no effect (13). We found that Lin28B-L potentially inhibited the processing of pri-let-7g (Fig. S8), whereas Lin28B-S did not. Hence, the previously reported oncogenic properties of Lin28B may be mediated, at least in part, through



**Fig. 4.** Knockdown of Lin28 relieves the miRNA-processing block. P19 cells were transfected with control hairpin (GFP), pXO1-shRNA hairpins targeting Lin28, control siRNA (scrambled sequence), or Lin28 siRNA. Total RNA was collected 60 hours after transfection for analysis. (A) Quantitative PCR analysis of Lin28 expression, normalized to Lin28 expression with control hairpin or control siRNA (average of experimental triplicates performed on the RNA samples from (B)). (B) Northern blot for mature let-7g. (C) Confirmation of Lin28 knockdown using Lin28-Si2 on samples analyzed in (D). (D) Changes in mature miRNA levels upon knockdown of Lin28 as analyzed by quantitative PCR. (E) Levels of pri-let-7g upon knockdown of Lin28 in P19 cells. (F) Levels of the pluripotency markers Oct-4 and Nanog in P19 cells transfected with either control siRNA or Lin28-si. In (C) to (F), error bars represent SEM with  $N = 3$ .



blockade of let-7 processing. It is possible that Lin28 and Lin28B may require both the cold-shock domain and CCHC zinc fingers for blocking activity. Lin28 and Lin28B are the only animal proteins known to contain both of these domains (15).

Our results show that Lin28 is necessary and sufficient for blockade of pri-miRNA processing of let-7 family members both in vitro and in vivo. There are several possible reasons why ES and EC cells possess a mechanism for post-transcriptional regulation of let-7 miRNA expression. First, posttranscriptional activation of miRNA processing would allow for rapid induction of several let-7 miRNAs by down-regulation of a single factor. Second, disruption of DGCR8, a dsRNA binding protein and essential component of the Microprocessor complex, interferes with ES cell differentiation, which suggests that activation of miRNAs may be important for silencing the self-renewal machinery (16). It has been suggested that posttranscriptional control could prevent even small amounts of let-7 from being produced in ES and EC cells, tightly maintaining the undifferentiated state (7). Third, posttranscriptional control of miRNA expression could serve as a means for dissociating expression patterns of intronic miRNAs from expression patterns of their host transcripts.

The precise mechanism by which Lin28 blocks miRNA processing as well as the range and determinants of its substrate selectivity are unknown. Our data suggest that Lin28 has a preference for selectively blocking the processing of let-7 family pri-miRNAs at the Microprocessor step. However, we cannot rule out the possibility that Lin28, alone or in concert with other factors, may block other pri-miRNAs in different physiological contexts. Others have reported that miRNA processing can also be regulated at the Dicer step, when pre-miRNAs are cleaved to their mature

form (5, 8). Additional factors may yet be discovered that posttranscriptionally regulate miRNA processing. Lin28 is predominantly localized to the cytoplasm, although it can also be found in the nucleus (10, 11); Lin28B is translocated into the nucleus in a cell cycle-dependent fashion (13). Lin28 may posttranscriptionally regulate miRNA processing in embryonic cells in a cell cycle-specific manner.

Recently, Lin28 was used in conjunction with Nanog, Oct-4, and Sox2 to reprogram human fibroblasts to pluripotency (14). Our data thus suggest that modulating miRNA processing may contribute to the reprogramming of somatic cells to an embryonic state. Additionally, global inhibition of miRNA processing by knockdown of the Drosha component of the Microprocessor was shown to promote cellular transformation and tumorigenesis; this phenotype was found to be, in large part, due to loss of let-7 expression (17). Let-7 has been reported to play a tumor suppressor role in lung and breast cancer by repression of oncogenes such as *Hmga2* (18) and *Ras* (19, 20). We suggest that disruption of let-7 processing by activation of Lin28 could promote the oncogenic phenotype. Notably, several human primary tumors show a general lack of correlation between expression of pri-miRNAs and the corresponding mature species (7, 21). This suggests that a block in miRNA processing may contribute to the low miRNA expression observed in many human cancers (22). Future study of Lin28 promises to reveal how miRNA processing contributes to the dedifferentiation that accompanies both somatic cell reprogramming and oncogenesis.

#### References and Notes

1. A. M. Denli, B. J. Tops, R. H. A. Plasterik, R. F. Ketting, G. J. Hannon, *Nature* **432**, 231 (2004).
2. R. L. Gregory et al., *Nature* **432**, 235 (2004).
3. T. P. Chendrimada et al., *Nature* **436**, 740 (2005).

4. R. L. Gregory, T. P. Chendrimada, N. Cooch, R. Shiekhattar, *Cell* **123**, 633 (2005).
5. G. Obermayer, P. J. F. Leuschner, M. Alenius, J. Martinez, *RNA* **12**, 1361 (2006).
6. J. Mineno et al., *Nucleic Acids Res.* **34**, 1765 (2006).
7. J. M. Thomson et al., *Genes Dev.* **20**, 2202 (2006).
8. F. G. Wulczyn et al., *FASEB J.* **21**, 415 (2007).
9. M. R. Suh et al., *Dev. Biol.* **270**, 488 (2004).
10. E. G. Moss, R. C. Lee, V. Ambros, *Cell* **88**, 637 (1997).
11. A. Polesky et al., *Genes Dev.* **21**, 1125 (2007).
12. M. Richards, S. P. Tan, J. H. Tan, W. K. Chan, A. Bongso, *Stem Cells* **22**, 51 (2004).
13. Y. Guo et al., *Gene* **384**, 51 (2006).
14. J. Yu et al., *Science* **318**, 197 (2007); published online 20 November 2007 (10.1126/science.1151260).
15. E. Balzer, E. G. Moss, *RNA Biol.* **4**, 16 (2007).
16. Y. Wang, R. Medvid, C. Melton, R. Jernisch, R. Blobel, *Mot. Genet.* **3**, 380 (2007).
17. M. S. Kumar, J. Lu, K. L. Mercer, T. R. Golub, T. Jacks, *Mot. Genet.* **3**, 673 (2007).
18. C. Maye, M. T. Herman, D. Bartel, *Science* **315**, 1576 (2007); published online 21 February 2007 (10.1126/science.1137999).
19. S. M. Johnson et al., *Cell* **120**, 635 (2005).
20. F. Yu et al., *Cell* **131**, 1109 (2007).
21. G. A. Calin et al., *Proc. Natl. Acad. Sci. U.S.A.* **99**, 15524 (2002).
22. J. Lu et al., *Nature* **435**, 834 (2005).
23. We thank H. Steen of the Proteomics Center at Children's Hospital Boston for expertise in the microcapillary HPLC/MS spectrometry, L. Skellington and R. LaPiere for technical support, and D. Bloch for providing Flag-Yb-1 plasmid. Supported by ILS Startup funds from Children's Hospital Boston and a Harvard Stem Cell Institute grant (R.G.) and by NIH grant DC00705, the NIH Director's Pioneer Award of the NIH Roadmap for Medical Research, and a Burroughs Wellcome Fund Clinical Scientist Award in Translational Research (G.D.).

#### Supporting Online Material

[www.sciencemag.org/cgi/content/full/1154040/DC1](http://www.sciencemag.org/cgi/content/full/1154040/DC1)

Materials and Methods

Figs. S1 to S8

Table S1

References

11 December 2007; accepted 14 February 2008

Published online 21 February 2008

10.1126/science.1154040

Include this information when citing this paper.

## Bacteria Subsisting on Antibiotics

Gautam Dantas,<sup>1\*</sup> Morten O. A. Sommer,<sup>1,2,\*</sup> Rantimi D. Oluwasegun,<sup>1</sup> George M. Church<sup>1†</sup>

Antibiotics are a crucial line of defense against bacterial infections. Nevertheless, several antibiotics are natural products of microorganisms that have as yet poorly appreciated ecological roles in the wider environment. We isolated hundreds of soil bacteria with the capacity to grow on antibiotics as a sole carbon source. Of 18 antibiotics tested, representing eight major classes of natural and synthetic origin, 13 to 17 supported the growth of clonal bacteria from each of 11 diverse soils. Bacteria subsisting on antibiotics are surprisingly phylogenetically diverse, and many are closely related to human pathogens. Furthermore, each antibiotic-consuming isolate was resistant to multiple antibiotics at clinically relevant concentrations. This phenomenon suggests that this unappreciated reservoir of antibiotic-resistance determinants can contribute to the increasing levels of multiple antibiotic resistance in pathogenic bacteria.

The seemingly unchecked spread of multiple antibiotic resistance in clinically relevant pathogenic microbes is alarming. Furthermore, an important environmental reservoir of antibiotic-resistance determinants, termed the antibiotic resistome, has been discovered (1, 2). The primary microbial antibiotic-resistance mechanisms

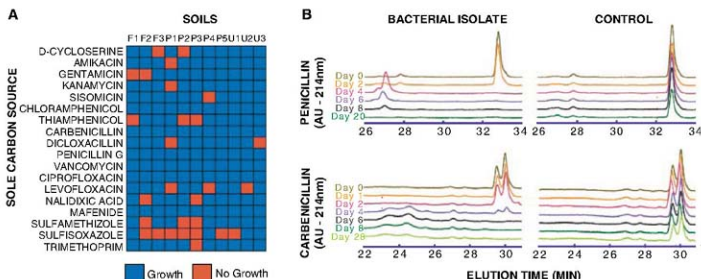
include efflux pumps, target gene-product modifications, and enzymatic inactivation of the antibiotic compound (3, 4). Many of the mechanisms are common to several species of pathogens and spread by lateral gene transfer (5). Although enzymatic inactivation is often sufficient to annul the antimicrobial activity of these chemicals, the

biochemical processing of these compounds is unlikely to end there, and we hypothesize that the soil microbiome must include a substantial reservoir of bacteria capable of subsisting on antibiotics. Although many bacteria growing in extreme environments (6) and capable of degrading toxic substrates (7) have been previously reported, only a few organisms have been shown to subsist on a limited number of antibiotic substrates (8–10).

We cultured clonal bacterial isolates from 11 diverse soils (table S2) that were capable of using one of 18 different antibiotics as their sole carbon source. These antibiotics included natural, semisynthetic, and synthetic compounds of different ages and from all major bacterial target classes. Every antibiotic tested was able to support bacterial

<sup>1</sup>Department of Genetics, Harvard Medical School, Boston, MA 02115, USA. <sup>2</sup>Program of Biophysics, Harvard University, Cambridge, MA 02138, USA.

\*These authors contributed equally to this work.  
†To whom correspondence should be addressed. E-mail: [http://arep.harvard.edu/gmc/email.html](mailto:http://arep.harvard.edu/gmc/email.html)



**Fig. 1.** Clonal bacterial isolates subsisting on antibiotics. **(A)** Heat map illustrating growth results from all combinations of 11 soils with 18 antibiotics, where blue squares represent the successful isolation of bacteria from a given soil that were able to use antibiotic as their sole carbon source at an antibiotic concentration of 1 g/liter. Soil samples labeled F1 to F3 are farm soils

and those labeled U1 to U3 are urban soils. P1 to P5 are pristine soils, collected from non-urban areas that had minimal human exposure over the past 100 years (table S2). **(B)** HPLC traces at 214 nm of representative penicillin- and carbenicillin-catabolizing clonal isolates and corresponding un-inoculated media controls for different time points over 20 or 28 days of growth, respectively.

growth (Fig. 1A and fig. S1). Six out of 18 antibiotics supported growth in all 11 soils, covering five of the eight classes of antibiotics tested. Appropriate controls were performed to ensure that carbon source contamination of the source media or carbon fixation from the air were insignificant (11). We obtained clonal isolates capable of subsisting on penicillin and carbenicillin from all the soils tested, and isolates from 9 out of 11 soils that could subsist on dicloxacillin. Representative isolates capable of growth on penicillin and carbenicillin were selected for subsequent analysis by high-performance liquid chromatography (HPLC) (11). Removal of the antibiotics from the media was observed within 4 and 6 days, respectively (Fig. 1B). Mass spectrometry analysis of penicillin cultures has indicated the existence of a penicillin catabolic pathway (9) that is initiated by hydrolytic cleavage of the beta-lactam ring. Beta-lactam ring cleavage, followed by a decarboxylation step, is the dominant mode of clinical resistance to penicillin and related beta-lactam antibiotics (fig. S3) (11).

We isolated bacteria from all the soils tested that grew on ciprofloxacin (Fig. 1A), a synthetic fluoroquinolone and one of the most widely prescribed antibiotics. Clonal isolates capable of catabolizing the other two synthetic quinolones tested, levofloxacin and nalidixic acid, were also isolated from a majority of the soils (Fig. 1A). Previous studies have highlighted the strong parallels between antibiotic-resistance determinants harbored by soil-dwelling microbes and human pathogens (5, 12, 13). The lateral transfer of genes encoding the enzymatic machinery responsible for subsistence on quinolone antibiotics from soil-dwelling microbes to human pathogens could introduce a novel resistance mechanism so far not observed in the clinic.

Phylogenetic profiling of the clonal isolates (11) revealed a diverse set of species in the Proteobac-

**Fig. 2.** Phylogenetic distribution of bacterial isolates subsisting on antibiotics. 16S ribosomal DNA (rDNA) was sequenced from antibiotic-catabolizing clonal isolates with the use of universal bacterial rDNA primers. High-quality nonchimeric sequences were classified using the Greengenes database (16), with consensus annotations from Ribosomal Database Project II (17) and National Center for Biotechnology Information taxonomies (18). Phylogenetic trees were constructed using the neighbor-joining algorithm in the ARB program package (19) using the Greengenes-aligned 16S rDNA database. Placement in the tree was confirmed by comparing automated Greengenes taxonomy to the annotated taxonomies of the nearest neighbors of each sequence in the aligned database. Branches of the tree are color-coded by bacterial orders, and clonal isolates are represented as squares.

teria (87%), Actinobacteria (7%), and Bacteroidetes (6%) (Fig. 2 and fig. S2). These phyla all include many clinically relevant pathogens. Of the 11 orders represented, *Burkholderiales* constitute 41% of the species isolated. The other major orders (>5%) are *Pseudomonadales* (24%), *Enterobacteriales* (13%), *Actinomycetales* (7%), *Rhizobiales* (7%), and *Sphingobacteriales* (6%).

One explanation for the widespread catabolism of both natural and synthetic antibiotics may relate to organic substrates found in nature. Microbial metabolic mechanisms exist for processing those substrates and may allow for the utilization of the parent synthetic antibiotic molecule. It is interesting that more than half of the bacterial isolates identified in this study belong to the orders *Burkholderiales* and *Pseudomonadales*. Organisms in these orders typically have large genomes of

approximately 6 to 10 megabases, which has been suggested to be positively correlated to their metabolic diversity and multiple antibiotic resistance (14). These organisms can be thought of as scavengers, capable of using a large variety of single carbon sources as food (15).

We determined the magnitude of antibiotic resistance for a representative subset of 75 clonal isolates (table S3). Each clonal isolate was tested for resistance to all 18 antibiotics used in the subsistence experiments at antibiotic concentrations of 20 mg/liter and 1 g/liter in rich media (11). The clonal isolates tested were on average resistant to 17 out of 18 antibiotics at 20 mg/liter and 14 out of 18 antibiotics at 1 g/liter (Fig. 3). Furthermore, for 74 of the 75 isolates, we found that if a bacterial isolate was able to subsist on an antibiotic, it was also resistant to all antibiotics in that class at 20 mg/liter.

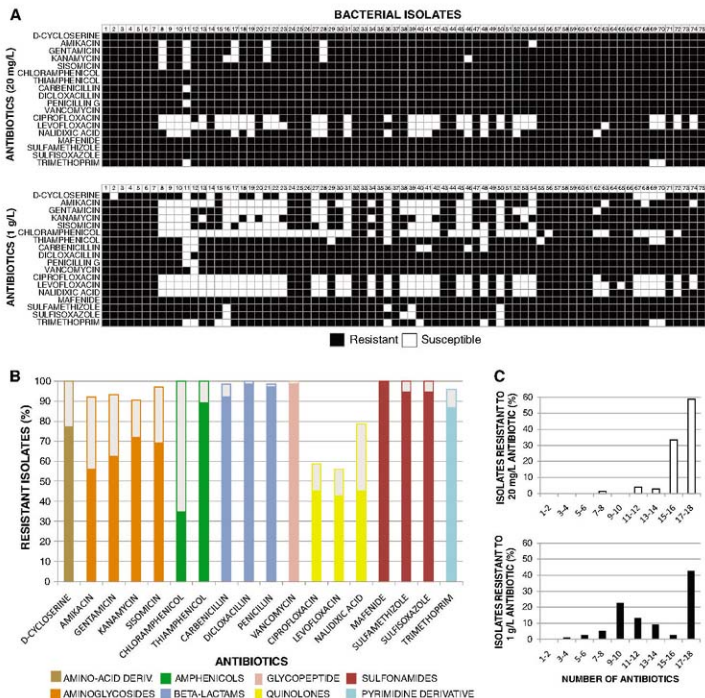
Previous work showing that strains from the genus *Streptomyces* are on average resistant to seven to eight antibiotics at 20 mg/liter has highlighted the importance of producer organisms as a reservoir of antibiotic resistance (2). Here we describe bacteria subsisting on antibiotics as a substantial addition to the antibiotic resistance in terms of both phylogenetic diversity and prevalence of resistance. The bacteria isolated in this study were super-resistant, because they tolerated concentrations of antibiotics >1 g/liter, which is 50 times higher than the

antibiotic concentrations used to define the antibiotic resistance (2).

The Greengenes database (16) identified isolates among the bacteria subsisting on antibiotics that are closely related to known pathogens, such as members of the *Burkholderia cepacia* complex and *Serratia marcescens*. In principle, relatedness allows for easier transfer of genetic material, because codon usage, promoter binding sites, and other transcriptional and translational motifs are likely to be similar. It is therefore possible that pathogenic microbes can more readily use resist-

ance genes originating from bacteria subsisting on antibiotics than the resistance genes from more distantly related antibiotic producer organisms.

To date, there have been no reports describing antibiotic catabolism in pathogenic strains. However, because most sites of serious infection in the human body are not carbon-source-limited, it is unlikely that antibiotic catabolism confers a strong selective advantage on pathogenic microbes as compared to just resisting them. Therefore, it is likely that only the resistance-conferring part of the catabolic machinery would be selected for in pathogenic strains.



**Fig. 3.** Antibiotic-resistance profiling of 75 clonal isolates capable of subsisting on antibiotics. (A) Heat map illustrating the resistance profiles of a representative subset of 75 clonal isolates capable of using antibiotics as their sole carbon source (table S3). Resistance was determined as growth after 4 days at 22°C in Luria broth media containing antibiotic at concentrations of 20 mg/liter (top) and 1 g/liter (bottom). (B) Percentage of clonal isolates resistant to each of

the 18 antibiotics. Antibiotics are color-coded by class; the full height of each bar corresponds to the percentage of clonal isolates resistant at a concentration of 20 mg/liter and the solid colored section of each bar corresponds to the percentage of clonal isolates resistant at 1 g/liter. (C) Histogram depicting the distribution of the number of antibiotics that the clonal isolates were resistant to at 20 mg/liter (top) and 1 g/liter (bottom).

In addition to the finding that bacteria subsisting on natural and synthetic antibiotics are widely distributed in the environment, these results highlight an unrecognized reservoir of multiple antibiotic-resistance machinery. Bacteria subsisting on antibiotics are phylogenetically diverse and include many organisms closely related to clinically relevant pathogens. It is thus possible that pathogens could obtain antibiotic-resistance genes from environmentally distributed super-resistant microbes subsisting on antibiotics.

## References and Notes

- C. S. Riesenfeld, R. M. Goodman, J. Handelsman, *Environ. Microbiol.* **6**, 981 (2004).
- V. M. D. Costa, K. M. McGrann, D. W. Hughes, G. D. Wright, *Science* **311**, 374 (2006).
- C. Walsh, *Nature* **406**, 775 (2003).
- M. N. Atkinson, S. B. Levy, *Cell* **128**, 1037 (2007).
- J. Davies, *Science* **264**, 375 (1994).
- J. K. Fredrickson, H. M. Kostandarithes, S. W. Li, A. E. Plymale, M. J. Daly, *Appl. Environ. Microbiol.* **66**, 2006 (2000).
- K. A. McAllister, H. Lee, J. T. Trevors, *Biodegradation* **7**, 1 (1996).
- Y. Kameda, E. Toyoura, Y. Kimura, T. Omori, *Nature* **191**, 1322 (1961).
- J. Johnson, *Arch. Microbiol.* **115**, 271 (1977).
- Y. Adl-Madek, A. Hazem, M. Momb, *Nature* **189**, 775 (1961).
- Materials and methods are available as supporting material on Science Online.
- C. G. Marshall, L. A. D. Lessard, I. S. Park, G. D. Wright, *Antimicrob. Agents Chemother.* **42**, 2215 (1998).
- V. M. D. Costa, E. Griffiths, G. D. Wright, *Curr. Opin. Microbiol.* **10**, 481 (2007).
- S. J. Projan, *Antimicrob. Agents Chemother.* **51**, 1133 (2007).
- J. L. Parke, D. Gurian-Sherman, *Annu. Rev. Phytopathol.* **39**, 225 (2001).
- T. Z. DeSantis et al., *Appl. Environ. Microbiol.* **72**, 5069 (2006).
- J. R. Cate et al., *Nucleic Acids Res.* **35**, D169 (2007).
- D. L. Wheeler et al., *Nucleic Acids Res.* **28**, 10 (2000).
- W. Ludwig et al., *Nucleic Acids Res.* **32**, 1363 (2004).
- We acknowledge the expert assistance of N. Soares and H. Henderson for microbial culturing; P. Girgis and H. White for HPLC analysis; D. Bang for HPLC; W. Haas for mass spectrometry; D. Elson and W. Curtis for sample collection; J. H. Lee, R. Kötter, and J. Shendure for general discussion; J. Aach for helpful discussions regarding the manuscript; and the U.S. Department of Energy Gen. Program, the Harvard Biophysics Program, The Hartmann Foundation, and Det Kongelige Danske Videnskabsnævnet for funding. 165 ribosomal RNA gene sequences were deposited in GenBank with accession numbers EU151534 to EU151623.

## Supporting Online Material

www.sciencemag.org/cgi/content/full/320/5872/100/D1  
Materials and Methods  
Figs. S1 to S3  
Tables S1 to S3  
References

11 January 2008; accepted 3 March 2008  
10.1126/science.1155157

# Reversible Compartmentalization of de Novo Purine Biosynthetic Complexes in Living Cells

Songon An,\* Ravindra Kumar, Erin D. Sheets,\* Stephen J. Benkovic\*

Purines are synthesized de novo in 10 chemical steps that are catalyzed by six enzymes in eukaryotes. Studies in vitro have provided little evidence of anticipated protein-protein interactions that would enable substrate channeling and regulation of the metabolic flux. We applied fluorescence microscopy to HeLa cells and discovered that all six enzymes colocalize to form clusters in the cellular cytoplasm. The association and dissociation of these enzyme clusters can be regulated dynamically, by either changing the purine levels of or adding exogenous agents to the culture media. Collectively, the data provide strong evidence for the formation of a multi-enzyme complex, the "purinosome," to carry out de novo purine biosynthesis in cells.

Purines are not only essential building blocks of DNA and RNA, but, as nucleotide derivatives, they also participate in a multitude of pathways in both prokaryotes and eukaryotes (1, 2). Biochemically, adenosine and guanosine nucleotides are derived from inosine monophosphate (IMP), which is synthesized from phosphoribosyl pyrophosphate (PRPP) in both the de novo and salvage pathways (Fig. 1). The salvage pathway catalyzes the one-step conversion of hypoxanthine to IMP by hypoxanthine phosphoribosyl transferase (HPRT), whereas the de novo pathway consists of 10 chemical reactions that transform PRPP to IMP. In higher eukaryotes (such as humans), the de novo pathway uses six enzymes, including three multifunctional enzymes: a trifunctional protein, TrtGART, that has glycineamide ribonucleotide (GAR) synthetase (GARS) (step 2), GAR transformylase (GAR Tfase) (step 3), and aminimidazole ribonucleotide synthetase (AIRS) (step 5) activities; a bifunctional enzyme, PAICS,

that has carboxyaminoimidazole ribonucleotide synthetase (CAIRS) (step 6) and succinylaminoimidazolecarboxamide ribonucleotide synthetase (SAICARS) (step 7) activities; and a bifunctional enzyme, ATIC, that has aminimidazolecarboxamide ribonucleotide transformylase (AICAR Tfase) (step 9) and IMP cyclohydrolase (IMPCH) (step 10) activities. In contrast, prokaryotes, such as *Escherichia coli*, use only monofunctional enzymes throughout this pathway, except for the bifunctional ATIC.

Although studies of the individual enzymes in vitro have revealed much about their respective mechanisms of action, a number of in vitro attempts using kinetic analysis and/or binding measurements to demonstrate protein-protein interactions have not been fruitful, with few exceptions (3–6). In addition, there is scant evidence from in vivo cellular studies for the hypothesis that these enzymes act in concert within a multi-enzyme complex (7). In this study, we used fluorescence microscopy to investigate whether functional multi-enzyme complexes involved in de novo purine biosynthesis form in living mammalian cells under purine-rich and purine-depleted conditions, which affect the rate of metabolic flux (8–10).

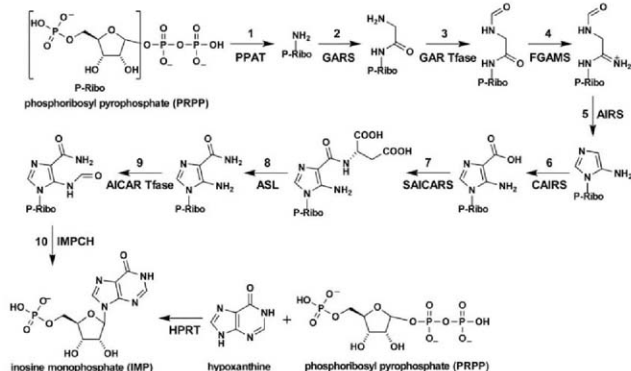
We selected for study two human (h) enzymes involved with de novo purine biosynthesis as initial candidates for involvement in a multi-enzyme complex in vivo: the nonsequential hTrtGART protein, which catalyzes steps 2, 3, and 5, and formylglycinamide ribonucleotide synthetase (hFGAMS), which catalyzes step 4. These proteins were fused to either a green fluorescent protein (GFP) or an orange fluorescent protein (OPF) and were transiently expressed in HeLa cells that had been cultured in either purine-rich [minimum essential medium and 10% fetal bovine serum (FBS)] or purine-depleted (RPMI 1640 and dialyzed 5% FBS) media (9, 11). When expressed individually in cells grown in purine-rich media, both the hTrtGART (Fig. 2A) and hFGAMS (Fig. 2C) proteins exhibited diffuse cytoplasmic distributions, as previously found in 293T fibroblast cells and with their prokaryotic counterpart, *E. coli* cells (7). However, when these constructs were expressed in purine-depleted cells, we observed cytoplasmic clustering, estimated at ~27% of the hTrtGART-GFP (Fig. 2B) and ~77% of the hFGAMS-GFP (Fig. 2D) proteins. To determine whether the two enzymes colocalized into these clusters in low-purine conditions, we transiently coexpressed hTrtGART-GFP and hFGAMS-OPF in HeLa cells (Fig. 2, G, H, and I); ~60% of the transfected cells exhibited colocalization within the clusters (Fig. 2J).

Z-scan imaging with confocal laser-scanning microscopy confirmed that the hTrtGART-GFP and the hFGAMS-OPF proteins were co-clustered in the cytoplasm (fig. S1). We also observed co-clustering between hFGAMS-GFP and hTrtGART-OPF after we reversed the fusion of the fluorescent probes in HeLa cells that were maintained in purine-depleted media (fig. S2). Additionally, similar cellular localization experiments were carried out with hTrtGART-GFP and hFGAMS-GFP in two additional human cell lines, HTB-125 and HTB-126; the results suggested that the purine-dependent clustering appears to occur in other human cell lines [supporting online material (SOM) Text]. These findings, when combined with the imaging results described

Department of Chemistry, The Pennsylvania State University, University Park, PA 16802, USA.

\*To whom correspondence should be addressed. E-mail: sja1@psu.edu (S.J.B.); eds11@psu.edu (E.D.S.); sua13@psu.edu (S.A.)





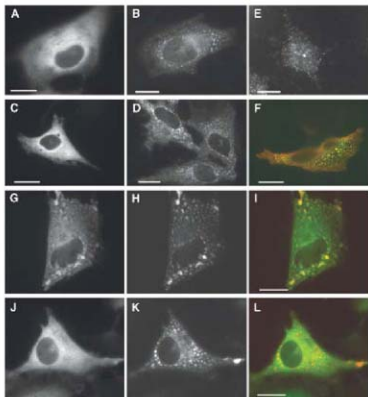
**Fig. 1.** The de novo purine biosynthetic and salvage pathways. The de novo pathway transforms PRPP to IMP in 10 steps. Steps 2, 3, and 5 are catalyzed by a trifunctional enzyme, TrifGART; steps 6 and 7 are catalyzed by a bifunctional enzyme, PAICS; and steps 9 and 10 are catalyzed by a bifunctional enzyme, ATIC.

for HeLa cells, suggest that the formation of this multienzyme complex involved in the de novo purine biosynthetic pathway may be functionally relevant in mammalian cells, particularly those challenged with minimal media.

To verify that the clustering we observed was not due to an artifact of expressing the fluorescent fusion constructs but was in fact present with endogenously expressed protein, we conducted immunofluorescence imaging of endogenous hTrifGART protein in HeLa cells grown in purine-depleted media; clustering was clearly observed (Fig. 2E), similar to what we found for the hTrifGART-GFP protein under the same conditions (Fig. 2B). We also identified some clustering of endogenous hTrifGART in the presence of purine-rich media (Fig. S3), which we attribute either to the sensitivity of immunofluorescence in detecting protein expression or to the loss of cytosolic materials during fixation. We further demonstrated that endogenous hTrifGART co-clustered with hTrifGART-GFP in HeLa cells that were maintained in purine-depleted media (Fig. 2F), which supports our initial observations with the GFP fusion constructs. Taken together, these results suggest that multienzyme complexes form to satisfy the cellular demand for de novo purine biosynthesis.

We expanded our studies to include all six human enzymes of the pathway (Fig. 1): PRPP amidotransferase (hPPAT) (step 1), hTrifGART, hFGAMS, hPAICS, adenylosuccinate lyase (hASL) (step 8), and hATIC. As a control, we also included a tetrahydrofolate ( $H_4F$ )-utilizing trifunctional enzyme, hC1THF, that possesses 5,10-methylene- $H_4F$  dehydrogenase, 5,10-methylene- $H_4F$  cyclohydrolase, and 10-formyl- $H_4F$  synthetase activities. hC1THF is not directly involved in the de novo purine pathway but is responsible for synthesizing a key cofactor, 10-formyl- $H_4F$ , for both hTrifGART and

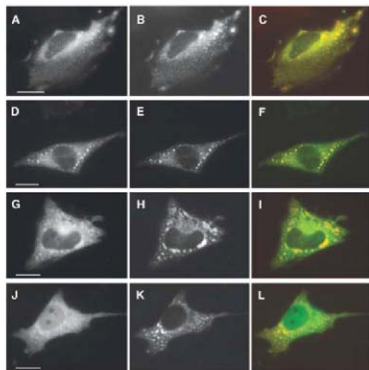
**Fig. 2.** Cellular localization of enzymes participating in the de novo purine biosynthetic pathway. (A to D) hTrifGART-GFP [(A) and (B)] and hFGAMS-GFP [(C) and (D)] transiently expressed in HeLa cells in purine-rich [(A) and (C)] and purine-depleted [(B) and (D)] media. (E) Immunofluorescence of endogenous hTrifGART protein expressed in HeLa cells cultured under low-purine conditions. (F) Merged image by immunofluorescence of hTrifGART-GFP (green) and endogenous hTrifGART (red) expressed in HeLa cells grown in purine-depleted media. (G to I) hTrifGART-GFP [(G) and (H)] co-localize with hFGAMS-GFP [(H) and (I)] in HeLa cells under purine-depleted conditions. (J to L) The control hC1THF-GFP [(J) and (K)], which does not participate directly in de novo purine biosynthesis, does not form clusters or colocalize with hFGAMS-GFP [(K) and (L)] in HeLa cells grown in purine-depleted media. Scale bar, 10  $\mu$ m.



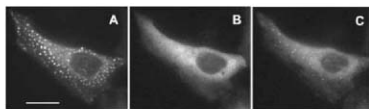
hATIC activities (5, 12). We found that all six enzymes that directly participate in the de novo purine biosynthetic pathway co-clustered with hFGAMS-GFP in the cytoplasm of cells maintained in purine-depleted media (Fig. 2, G to I, and Fig. 3); however, hC1THF-GFP was diffuse throughout the cytoplasm, and thus did not co-cluster with hFGAMS-GFP (Fig. 2, J to L).

When the individual fluorescent protein constructs were transiently expressed in purine-depleted HeLa cells, the frequency of clustering was generally very low: ~5 to 8% for hPPAT-GFP, hPAICS-GFP, hASL-GFP, and GFP-hATIC, but ~27% for hTrifGART-GFP and ~77% for hFGAMS-GFP. However, when co-transfected with hFGAMS-GFP under these conditions, the

**Fig. 3.** Colocalization of GFP fusion proteins with hFGAMS-OPF in HeLa cells grown in purine-depleted media. hPPAT-GFP (A), hPAICS-GFP (D), hASL-GFP (G), and GFP-hATIC (J) were co-transfected with hFGAMS-OPF (B, E, H, and K, respectively). (C, F, I, and L) Green channels correspond to the GFP-fusion constructs, and red channels correspond to hFGAMS-OPF in the merged images. Scale bar, 10  $\mu$ m.



**Fig. 4.** Reversible formation of clusters by hFGAMS-GFP. (A) hFGAMS-GFP clusters when HeLa cells are exposed to purine-depleted medium. (B) Clusters disperse within ~0.5 to 1.5 hours upon incubation with purine-rich medium. (C) The clusters begin to re-form within ~1 to 2 hours after purine-depleted medium is restored. Scale bar, 10  $\mu$ m.



clustering frequency increased substantially to ~22 to 32% for hPPAT-GFP, hPAICS-GFP, hASL-GFP, and GFP-hATIC, and ~60% for hTriGART-GFP. The percentage of colocalization of GFP-fusion proteins with hFGAMS-OPF was calculated by dividing the number of pixels that showed both green and red colors by the total number of pixels that showed either green or red colors (11, 13). Colocalization analysis collectively revealed that  $78 \pm 6\%$  of GFP-fusion proteins co-clustered with hFGAMS-OPF. However, the analysis for hATIC-GFP and hFGAMS-OPF exhibited  $21 \pm 5\%$  colocalization, which suggests that these proteins do not colocalize in clusters. The representative image (Fig. 2L) clearly shows hFGAMS-OPF clusters on a diffuse background of hATIC-GFP. Scattergram analysis was carried out as an alternative means of examining colocalization, and it showed the compartmentalization of all six enzymes participating in the de novo purine biosynthesis (table S1 and Fig. S4). The varying percentage of cells exhibiting clustering under low-purine conditions may be attributed to cells not being synchronized with respect to the cell cycle. The G<sub>1</sub> and S phases require more purines to support RNA and DNA synthesis than the other phases of the cell cycle (14); thus, we speculate that the population of the cells exhibiting clustering may represent cells in the G<sub>1</sub> or S phases. This rationale is

further supported by the previously measured ~five- to sixfold increase in the level of mRNAs for PPAT and SAICARS in the G<sub>1</sub> and S phases over those in the G<sub>0</sub> phase of synchronized rat 3Y1 fibroblasts (15).

To assess the reversibility of the multienzyme complexes, we imaged the cellular distribution of hFGAMS-GFP while purine-depleted medium was exchanged for purine-rich medium, and observed that the hFGAMS-GFP clusters dispersed within ~0.5 to 1.5 hours of HeLa cells being incubated with purine-rich medium (Fig. 4, A and B). When purine-depleted medium was subsequently restored, clusters began to re-form in ~1 to 2 hours (Fig. 4, B and C). Additionally, we performed fluorescence recovery after photobleaching on hFGAMS-GFP in HeLa cells that had been incubated in purine-depleted medium. We clearly observed mobility of the clusters through the rapid fluorescence recovery as a function of time (Fig. S5). Collectively, the predominance of clustering appears to be linked to insufficient levels of purines, which suggests that there is a cellular sensor of the external purine conditions and that the mobile clusters represent functional complexes.

Furthermore, we imaged the effects of introducing either an exogenous purine source, hypoxanthine, or a well-known antagonist of hFGAMS, azaserine, to inhibit the metabolic flux in the de

novo pathway of HeLa cells grown under purine-depleted conditions (8). Hypoxanthine, when added to fibroblast cultures in concentrations as low as 1 to 10  $\mu$ M, significantly inhibits (>50%) de novo purine biosynthesis through its effect on adenosine and guanosine nucleotides in the cellular pools (16, 17), and the increased levels of adenosine and guanosine nucleotides modulate activities of PPAT as well as PRPP synthetase (8). In addition, cells grown in purine-depleted media are deficient in adenosine 5'-triphosphate, with both the restoration of cellular growth rates and the timing of the G<sub>1</sub>-to-S transition dependent on both the de novo and salvage pathways (14). We propose that the initial increased clustering is a response to hypoxanthine-induced inhibition of the de novo pathway and that the retention of the clusters reflects demand for purines in cellular growth (Fig. S6, A, B, and solid squares in E). When we incubated azaserine with purine-depleted cells, we anticipated that hFGAMS clusters would at least be maintained because of the greater demand for purine biosynthesis. An azaserine block increases the rate of the early steps of de novo purine biosynthesis in fibroblasts that lack HPRT activity (17), which is consistent with our observed maintenance of the clusters (Fig. S6, C, D, and open circles in E). Collectively, the association and dissociation of the multienzyme complex reflected changes in cellular purine levels that were imposed by the addition of external reagents that regulate purine metabolic flux.

From our studies, the various roles that the multienzyme complex plays in cells are not yet clear. These functional complexes may produce efficient substrate channels that link the 10 catalytic active sites. To date, extensive kinetic analyses of *E. coli* PPAT and GARS (6), *Acetobacter aceti* purE and purK (bacterial counterparts of CAIRS) (3), and recent crystal structures of octameric hPAICS (18) have revealed putative substrate channels for individual steps in the de novo pathway. Additionally, clustering of the 10 active sites may provide an efficient means of globally regulating purine flux under varying environmental conditions. However, we have not yet identified a specific subcellular compartment with which these multienzyme complexes associate, in contrast to, for example, the actin cytoskeletal association observed for aldolase (19). However, our cross-linking experiments with formaldehyde on living cells grown in purine-depleted media, and subsequent Western blot analysis, revealed that endogenous hTriGART proteins produced a cross-linked adduct of molecular weight greater than 500 kDa (Fig. S7), which suggests that hTriGART is indeed compartmentalized in close proximity with other proteins, whose identities are under investigation. Moreover, recent proteomic studies suggest that hTriGART and hFGAMS are probably phosphorylated at binding motifs recognized by 14-3-3 proteins that play important roles in many biological processes, including cell-cycle regulation and signal transduction (20), which raises the intriguing possibility that phosphorylation is involved in regulation of the complex.

Although the association of metabolic enzymes has been claimed for enzymes involved in the glycolytic pathway (21, 22), to our knowledge this complex, the glycosome, has not been identified in living mammalian cells. By analogy, the present clusters observed in the *de novo* purine biosynthesis pathway may constitute a "purinosome." The formation of the purinosome appears to be dynamically regulated by stimulation of *de novo* purine biosynthesis in response to changes in purine levels. The purinosome may be a general phenomenon in all cell types during specific stages of the cell cycle, along with posttranslational modifications. Because of the relevance of *de novo* purine biosynthesis in human diseases, the purinosome may represent a new pharmacological opportunity for therapeutic intervention.

#### References and Notes

- C. Stasolla, K. Kishida, T. A. Thorpe, H. Adhikari, *J. Plant Physiol.* **160**, 1271 (2003).
- R. Zrenner, M. Stitt, U. Sonnewald, R. Boldt, *Annu. Rev. Plant Biol.* **57**, 805 (2006).
- C. Z. Constantinou et al., *Biochemistry* **45**, 8193 (2006).
- C. A. Caparelli, P. A. Benkovic, G. Chettur, S. J. Benkovic, *J. Biol. Chem.* **255**, 10885 (1980).
- G. K. Smith, W. T. Mueller, G. F. Wasserman, W. D. Taylor, S. J. Benkovic, *Biochemistry* **19**, 4313 (1980).
- J. Rudolph, J. Stubbs, *Biochemistry* **34**, 2241 (1995).
- L. T. Goolarysingh, J. Ramcharan, S. Gilroy, S. J. Benkovic, *Proc. Natl. Acad. Sci. U.S.A.* **98**, 6565 (2001).
- M. A. Becker, M. Kim, *J. Biol. Chem.* **262**, 14531 (1987).
- T. Yamazaki et al., *J. Biol. Chem.* **272**, 17719 (1997).
- T. Yamazaki et al., *J. Biol. Chem.* **276**, 21285 (2001).
- Materials and methods are available as supporting material on Science Online.
- G. F. Wasserman, W. T. Mueller, S. J. Benkovic, W. S. Liao, *J. Taylor, Biochemistry* **23**, 6704 (1984).
- M. Howarth, K. Takao, Y. Hayashi, A. Y. Ting, *Proc. Natl. Acad. Sci. U.S.A.* **102**, 7583 (2005).
- M. Kondo et al., *J. Biochem. (Tokyo)* **128**, 57 (2000).
- H. Iwashina et al., *Biochim. Biophys. Acta* **1261**, 369 (1995).
- L. F. Thompson, R. C. Willis, J. W. Stoop, J. E. Seegermiller, *Proc. Natl. Acad. Sci. U.S.A.* **75**, 3722 (1978).
- M. A. Becker, M. J. Losman, M. Kim, *J. Biol. Chem.* **262**, 5596 (1987).
- S. X. Li et al., *J. Mol. Biol.* **366**, 1603 (2007).
- L. Pagliaro, D. L. Taylor, *J. Cell Biol.* **107**, 981 (1988).
- M. Ponzeto Rubio et al., *Biochem. J.* **379**, 395 (2004).
- M. E. Campanella, H. Chu, P. S. Low, *Proc. Natl. Acad. Sci. U.S.A.* **102**, 2402 (2005).
- F. R. Oppenheimer, P. Borst, *FEBS Lett.* **80**, 340 (1977).
- We thank K. Kyoung (Pennsylvania State University) for valuable suggestions on data collection, imaging analysis, and statistics; E. Kamez (Pennsylvania State University) for assistance with confocal laser-scanning microscopy; A. A. Heikal (Pennsylvania State University) for sharing HTB-125 and 326 cell lines; and R. Y. Tsien (University of California, San Diego) for providing the pRSET-mOrange plasmid as a gift. This work was supported, in part, by Pennsylvania State University and the Center for Optical Technologies (E.D.S.). Additional acknowledgment is made to the Donors of the American Chemical Society Petroleum Research Fund, for partial support of this research (E.D.S.).

#### Supporting Online Material

www.sciencemag.org/cgi/content/full/320/S872/103/DC1  
Materials and Methods

SOM Text

Figs. S1 to S9

Table S1

References

26 October 2007; accepted 21 February 2008  
10.1126/science.1152241

## Single-Molecule DNA Sequencing of a Viral Genome

Timothy D. Harris,<sup>1,2</sup> Phillip R. Buzby,<sup>1</sup> Hazen Babcock,<sup>1</sup> Eric Beer,<sup>1</sup> Jayson Bowers,<sup>1</sup> Ido Braslavsky,<sup>2</sup> Marie Causey,<sup>1</sup> Jennifer Colonell,<sup>1</sup> James DiMeo,<sup>1</sup> J. William Efcavitch,<sup>1</sup> Eldar Giladi,<sup>1</sup> Jaime Gill,<sup>1</sup> John Healy,<sup>1</sup> Mirna Jarosz,<sup>1</sup> Dan Lapan,<sup>1</sup> Keith Moulton,<sup>1</sup> Stephen R. Quake,<sup>1</sup> Kathleen Steinmann,<sup>1</sup> Edward Thayer,<sup>1</sup> Anastasia Tyurin,<sup>1</sup> Rebecca Ward,<sup>1</sup> Howard Weiss,<sup>3</sup> Zheng Xie<sup>1</sup>

The full promise of human genomics will be realized only when the genomes of thousands of individuals can be sequenced for comparative analysis. A reference sequence enables the use of short read length. We report an amplification-free method for determining the nucleotide sequence of more than 280,000 individual DNA molecules simultaneously. A DNA polymerase adds labeled nucleotides to surface-immobilized primer-template duplexes in stepwise fashion, and the asynchronous growth of individual DNA molecules was monitored by fluorescence imaging. Read lengths of >25 bases and equivalent phred software program quality scores approaching 30 were achieved. We used this method to sequence the M13 virus to an average depth of >150× and with 100% coverage; thus, we resequenced the M13 genome with high-sensitivity mutation detection. This demonstrates a strategy for high-throughput low-cost resequencing.

DNA sequencing and the attendant genetic manipulation it enables have fundamentally altered life science, with the completion of the human genome sequence as a major milestone of this work (1, 2). However, large sample sets—thousands of genomes—are required to analyze many phenomena in which genetics plays a role. With current sequencing technologies, the cost and complexity of such experiments remains limiting (3). Having the consensus human genome sequence in hand fundamentally changes the technology requirements for resequencing human genomes. In particular, one can use low-cost techniques with

much shorter read lengths and higher parallelism than found with the Sanger capillary electrophoresis methods used to generate the reference genome (4).

Several recent reports emphasize the progress in short-read sequencing strategies (5–8). Although those methods have been used successfully to sequence microbial genomes, their current cost of sequencing, the complexity associated with DNA library preparation, and their use of polymerase chain reaction (PCR) amplification may limit broad application to human genome resequencing. The use of PCR is problematic for three reasons. First, because amplification efficiencies vary as a function of template properties, PCR introduces an uncontrolled bias in template representation. Second, short-read techniques require many more templates than conventional sequencing, and the *in vitro* manipulations to create libraries with defined sequences at the ends of templates are onerous and expensive in terms of DNA manipulation. Third, errors can be

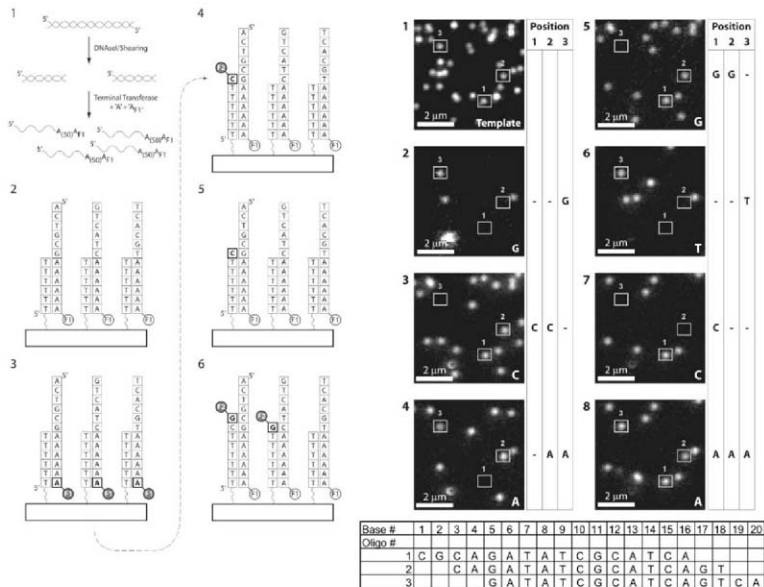
introduced; in a recent large-scale cancer resequencing effort, PCR errors alone accounted for about one-third of initially detected "mutations" (9). The fidelity of PCR polymerases is widely reported at 0.5 to 1.0 × 10<sup>-4</sup> (9), a substantial error rate for amplification of single-molecule targets. These limitations can be ameliorated by single-molecule sequencing approaches.

Single-molecule sequencing was proposed as early as 1989 (10). Recent work, however, has demonstrated the feasibility of single-molecule sequencing using DNA polymerase to sequence by synthesis (11), and a subsequent study of single-RNA polymerase activity shows DNA sequence can be inferred from the serial observation of four identical single-molecule templates (12). We have used single-molecule DNA sequencing to resequence the M13 phage genome (13). Our sequencing-by-synthesis scheme is diagrammed in Fig. 1. The library preparation process is simple and fast and does not require the use of PCR; it results in single-stranded, poly(dA)-tailed templates. Poly(dT) oligonucleotides are covalently anchored to glass coverslips at random positions. These oligomers are first used to capture the template strands, and then either as a primer for the template-directed primer extension that forms the basis of the sequence reading (Fig. 1) or, optionally, for a template replication step before sequencing (Fig. 2A). Up to 224 sequencing cycles are performed; each cycle consists of adding the polymerase and labeled nucleotide mixture (containing one of the four bases), rinsing, imaging multiple positions, and cleaving the dye labels. For the M13 data reported below, this sequencing process was performed simultaneously on more than 280,000 primer-template duplexes.

This single-molecule sequencing method allows a number of innovations that are not possible with bulk sequencing by synthesis (5, 8). Most of these are related to the principle of asynchronous synthesis; that is, because each template molecule

<sup>1</sup>Helicos BioSciences Corporation, One Kendall Square, Cambridge, MA 02139, USA. <sup>2</sup>Department of Physics and Astronomy, Ohio University, Athens, OH 45701, USA. <sup>3</sup>Department of Bioengineering, Stanford University, and Howard Hughes Medical Institute, Stanford, CA 94305, USA.

\*To whom correspondence should be addressed. E-mail: tharris@helicosbio.com



**Fig. 1.** Single-molecule sequencing sample preparation and imaging of single-nucleotide incorporation. (Left) Illustration of the single-molecule sequencing by synthesis process for single-pass sequencing. (1) Genomic DNA is prepared for sequencing by fragmentation and 3' poly(A) tail addition, labeling, and blocking by terminal transferase. (2) Hybridization capture of these templates onto a surface with covalently bound 5' "down" dT(50) oligonucleotide. (3) Imaging of the captured templates to establish sites for sequencing by synthesis. (4) Incubation of this surface with one labeled nucleotide and polymerase mixture, followed by rinsing of the synthesis mixture and direct imaging of the Cys labels exciting at 647 nm. (5) Chemical cleavage of the dye-nucleotide linker to release the dye label. (6) Addition of

the next nucleotide and polymerase mixture. (Right) Image series illustrating template-specific base addition, successful rinsing, and successful linker cleavage. A mix of three templates is used to allow visual sequence assignment. Template complementary sequences are shown in the table (bottom). One example of each template is outlined in the figure. Each frame is a  $6.6\text{-}\mu\text{m}$  square image of the same sample position, and shows  $\sim 35$  of the  $1.8 \times 10^6$  imaged templates in this experiment. Frame 1 is the image of the template labels. Template activity in three positions is shown in the columns to the right. Frame 2 is after the first synthesis and rinse cycle. Frames 3 to 8 show the effect of six more consecutive cleave, synthesis, and image cycles, using the base identity shown in the lower right corner of the frame.

is monitored individually, there is no need to keep each step of synthesis in phase. Thus, it is not necessary to drive each enzymatic incorporation step to completion. The principal benefit is that mis-incorporations are rare; their slow kinetics do not compete appreciably with the time to incorporate 80 to 90% of the correct base. A corollary is that this allows greater flexibility in the choice of reagents and synthesis chemistries, because the requirements on incorporation kinetics are relaxed. Asynchronicity is also used to facilitate reading of base-repeat sequences, homopolymers.

The use of a single-molecule method also enabled us to resequence each individual template

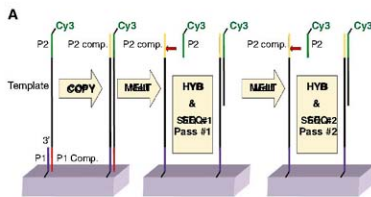
**Table 1.** M13 genome alignment statistics. The average read length was 23 bases, increasing to 27 bases after homopolymers were deconvolved.

Alignment	Coverage				Coverage (%)		No. of reads
	Average	Voting	Max.	Min.	>10x	>20x	
Forward	96x	75x	283x	3x	99.4	97.2	32,473
Reverse	105x	83x	301x	5x	99.5	95.8	34,109

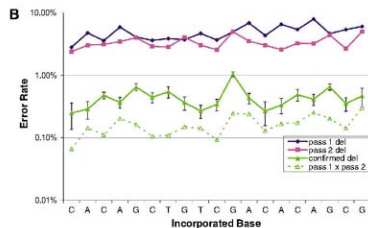
in situ, which greatly reduced the ensemble error rate. This "two-pass" sequencing process is illustrated in Fig. 2A. Captured oligonucleotide templates were copied using a high-fidelity polymerase to yield covalently attached templates with a distal

primer hybridization sequence. In the first pass, templates were primed and sequenced as described above (pass 1). The extended primers were then melted off using hot water, and the templates were primed again and sequenced a second time (pass 2).

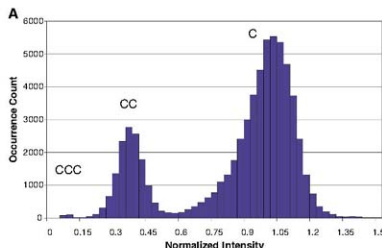




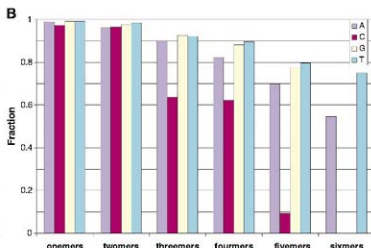
**Fig. 2.** Methodology for two-pass sequencing and deletion statistics. **(A)** Process for two-pass sequencing. As with one pass, the DNA sample is hybridized to the surface capture oligomer. A copy of the DNA is made, which results in covalent anchoring of the template copy to the surface. Library construction is described in fig. S1 and provides for a primer site at the distal end of the template. This primer



site is used for sequencing by synthesis, as before. After a sequencing run, the synthesized strand is melted off, and a new primer is hybridized, which allows the template to be sequenced a second time. **(B)** Average deletion rate for a single synthetic oligonucleotide, sequenced twice, from a data set of 35,000 reads; error bars show 3x the shot noise. See text and (I3) for quantitative details.



**Fig. 3.** Intensity calling for homopolymer length. **(A)** Histogram of observed intensities for C incorporation cycles across all C after A contexts in M13. By using known sequences and the incorporation cycle count required to observe the base following the poly(C) motif, the intensity of single, double, and triple incorporations can be determined. The group centered at normalized intensity ~1.0 is single incorporations; the group at normalized intensity 0.35 is incorporation of two labeled dCTP-Cy5 analogs in a single cycle; the small peak near normalized intensity 0.10 is incorporation of three labeled dCTP-Cy5 analogs in a single cycle. The magnitude of the quenching can be adjusted by addition of



nonpolar solvents to the imaging medium, in this case acetonitrile. By using thresholds chosen from plots similar to those in (A) for all four bases, an intensity-based counting process can be used. **(B)** The accuracy for confirmed two-pass length calling for all M13 homopolymer motifs except for a single 8A/8T occurrence. Monomer, dimer, and so on is short for one-nucleotide oligomer, two-nucleotide oligomer, and so forth. All contexts have a correct majority vote, exceeding 80% up to four-nucleotide oligomers, for all contexts except 5C. The 5C case and the strategy to achieve minimal false-positive-mutation calling is discussed in detail in (I3).

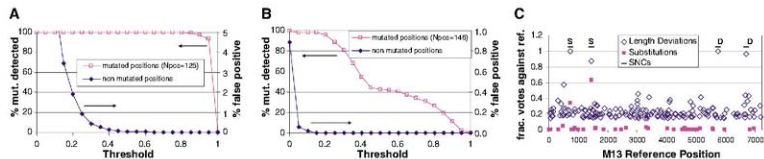
The combined or two-pass error rate was defined as follows [discussed in more detail in (I3)]: The reads from both passes of each template were separately aligned to the oligonucleotide reference. Only reads that were in agreement on both passes were given a "vote" at that position; ~80% of the bases meet this criterion. The error rate is the ratio of votes disagreeing with the reference divided by the total number of templates considered. The dominant error was deletion. Deletion errors varied from 3 to 7% in pass 1 and 2 to 5% in pass 2; the confirmed (seen in both passes) deletion error rate range was 0.2 to 1.0% (Fig. 2B). The calculated product of the first- and second-pass deletion error rates varied from 0.1 to 0.3% and is shown for comparison in Fig. 2B as open triangles. The confirmed deletion rate is roughly the same magnitude as this product, the expected result for substantially random errors.

The ultimate lower limit for single-molecule single-pass error rates is not clear, but this two-pass process produces error rates low enough to assemble contigs if adequate read length is considered (I4). The equivalent phred software program quality of these single-molecule reads ranges from 20 to 28 (I5).

To demonstrate the performance of single-molecule sequencing, we resequenced the M13 phage genome. A double-stranded M13 sample, prepared as shown in fig. S1, was sequenced for a total of 224 cycles; two passes with 112 cycles of synthesis were made in each pass; each pass was 28 "quadrant cycles" of successive CTAG additions. The average and median read lengths were ~23 bases for this run. Increasing the cycle count increases the average read length, and we have performed sequencing runs with average read lengths as high as 30. The forward and reverse genome coverage

for the M13 data here averaged  $96\times$  and  $105\times$ , respectively. We aligned the data against the known M13 reference. The alignment statistics for this run are shown in Table 1.

It is a challenge for all sequencing by synthesis methods to detect base repeats, homopolymers. Because we operate the chemistry asynchronously, we can limit incorporations in base repeats to primarily two or three bases. For example, a template with a sequence segment TGGGAT may incorporate zero, one, two, or three C's in a single synthesis cycle when reading the GGG template sequence (see the statistics in fig. S2). We observed that fluorophores in multiple incorporations interact and thus yield reduced emission. Intensity distributions from all C after A incorporations in the M13 experiment described above (Fig. 3A) show that separation between single and double incorporations is



**Fig. 4.** Demonstration of mutation detection by alignment of experimental data against mutated M13 references. We show two single-nucleotide-change response curves. (A) Statistics for false-positive and mutation detection for insertions causing increase to homopolymer length. (B) Statistics for false-positive and mutation detection for substitutions creating all classes of sequence change. These curves show the fraction of positions in M13 that voted against the reference on both forward and reverse strands, as a function of the voting threshold. A vote against the reference is a mutation call. (C) A voting plot showing the results for all positions for the error types plotted in (A) and (B) against a reference with four mutations, two each for the mutation types in (A)

**Table 2.** Mutation detection with synthetic mutations in the M13 reference genome (hp, homopolymer). We tested 500 randomly chosen positions in 10 separately modified references; four of these positions had less than 10 $\times$  coverage and were disqualified.

Mutation type	Number		Success (%)
	Tested	Found	
Insertion into hp	125	125	100
Deletion from hp	42	41	98
Deletion from non-hp	49	45	92
Deletion creating hp	34	33	97
Non-hp insertion	100	100	100
Substitution	146	143	98
Total mutations	496	487	98

very good and can be counted with only a small fraction of ambiguous calls. Triple incorporations are weak emitters, and a significant fraction fall below the system detection limit. Incorporation of more than three nucleotides is rare. Longer homopolymer runs were measured by adding the results of individual incorporation cycles, almost all made up of one-, two-, or three-base incorporations.

Normalized intensity thresholds delineating incorporations of one, two, or three nucleotides were determined for all four nucleotides by finding the minima between the distributions (Fig. 3A and Fig. S4). For each base read in each strand, an incorporation count is generated on the basis of its intensity relative to the threshold. As with our accounting for deletion errors, we accept votes only from positions where the two passes agree on the length of a homopolymer position and ignore votes from positions where the passes disagree. The success rate for length calling for all positions in the M13 genome is shown in Fig. 3B; homopolymers range from two to six bases except for a single 8A/8T. For homopolymers with just two bases, the calling was accurate, with >95% of the homopolymer calls correct, but there was a significant fraction of incorrect length calls for longer homo-

polymers, particularly for C. We imposed a constraint that the called length must agree on the forward and reverse strands for our double-stranded sample, which requires sequence depth on both sense strands. Difficulties in calling C homopolymers were compensated on the complementary strand, because the corresponding positions are G homopolymers, which are called more accurately (Fig. 3B and Fig. S5). For a single-stranded target, these C homopolymer length errors would result in a false-positive mutation call. The demonstrated homopolymer call accuracy is sufficient to achieve sensitive detection of mutations in the M13 genome, as described below.

To determine the M13 sequence quality, we explored how well mutations in the reference sequence could be detected. When single-nucleotide changes (6) are created in the reference genome, one expects to find poor agreement with the sequence read alignments at those positions, and they therefore serve as an unbiased test of the alignment quality and sensitivity. We aligned the data to 10 mutated M13 reference genomes, each with 50 sequence changes representing all classes of single-nucleotide change (insertions, deletions, and substitutions in varying contexts). Using these alignments, we measured the fraction of votes against the reference; locations where the aligned reads vote significantly against the reference are possible mutations. Single-nucleotide-change response curves indicated true-positive mutation detection and false-positive detection for various choices of vote thresholds (Fig. 4, A and B, and Fig. S10). To score a positive, we stipulated that the read sequence must have above-threshold votes against the reference on both the forward and reverse strands. The curves show that it is possible to achieve excellent mutation detection with very low false-positives for every class of mutation. We found thresholds that gave zero false-positives and enabled discovery of more than 98% of all mutations (Table 2). The error rate and homopolymer run-through in the sequencing chemistry reported here do limit the mutation detection sensitivity—i.e., the thresholds need to be set low. Large genomes, heterogeneous

and (B). Length mutations, those two points in the upper right, have a high false-positive rate (only votes >0.15 are plotted for clarity) but a near 100% mutation detection efficiency (A). Substitutions have a much lower false-positive rate, all votes against the reference were plotted, but as reflected in (B), the result was lower mutation-detection efficiency. As seen in (C), substitutions are reported directly (red violet solid squares) and as length changes (open diamonds), upper left. S and D show positions for, respectively, substitution and deletion SNC changes to the reference. These curves demonstrate that it is possible to choose voting thresholds that enable successful mutation detection with very low false-positive rates. SNCs, single-nucleotide changes.

samples, and genomic structural variations will likely require longer reads, reduced homopolymer run through, and enhanced alignment tools.

In summary, we report a method to sequence single molecules of genomic DNA. The consensus alignment of this sequence data is able to accurately recapitulate the M13 phage genome with 100% coverage, while demonstrating robust and efficient detection of all single base-mutation types. The simplicity of the methods described here, the freedom from cloning or amplification, and the low reagent volumes used to produce sequence from over 280,000 strands simultaneously opens a path to very high throughput sequencing.

#### References and Notes

1. E. S. Lander et al., *Nature*, **409**, 860 (2001).
2. J. C. Venter et al., *Science*, **291**, 1304 (2001).
3. T. Sjodahl et al., *Science*, **314**, 268 (2006).
4. J. Shendure, R. D. Mitra, C. Varma, G. M. Church, *Nat. Rev. Genet.*, **5**, 335 (2004).
5. M. Margulies et al., *Nature*, **437**, 374 (2005).
6. J. Shendure et al., *Nat. Methods*, **5**, 183 (2008).
7. J. Ju et al., *Proc. Natl. Acad. Sci. U.S.A.*, **103**, 19635 (2006).
8. W. M. Barnes, *Genet.*, **112**, 29 (1992).
9. J. H. Jett et al., *Biomol. Struct. Dyn.*, **7**, 301 (1989).
10. I. Braslavsky, B. Hebert, E. Kartalov, S. R. Quake, *Proc. Natl. Acad. Sci. U.S.A.*, **100**, 3960 (2003).
11. W. J. Greenleaf, S. M. Block, *Science*, **313**, 801 (2006).
12. Materials and methods are available as supporting material on Science Online.
13. R. Staden, *Nucleic Acids Res.*, **6**, 2601 (1979).
14. B. Ewing, L. Hillier, M. C. Wendt, P. Green, *Genome Res.*, **8**, 175 (1998).
15. We thank M. Nishikawa, G. Church, D. Groves, S. Chu, P. Rombregue, N. Aloyan, P. Nikos, E. Lindner, and S. Lipidopoulos for many valuable discussions. This work was supported in part by NIH grant R01 HG004144-01. S.R.Q. and I.B. are paid consultants for and own equity in HelicosBioSciences Corp. S.R.Q. and I.B. are also inventors of a licensed patent on single-molecule sequencing that may yield royalty payments.

#### Supporting Online Material

www.sciencemag.org/cgi/content/full/320/S872/106/DC1

Materials and Methods

SOM Text

Figs. S1 to S10

Tables S1 and S2

12 September 2007; accepted 29 February 2008  
10.1126/science.1150427

# Entrainment of Neuronal Oscillations as a Mechanism of Attentional Selection

Peter Lakatos,<sup>1,2</sup> George Karmos,<sup>2,3</sup> Ashesh D. Mehta,<sup>4</sup> Istvan Ulbert,<sup>2,3</sup> Charles E. Schroeder<sup>1,5\*</sup>

Whereas gamma-band neuronal oscillations clearly appear integral to visual attention, the role of lower-frequency oscillations is still being debated. Mounting evidence indicates that a key functional property of these oscillations is the rhythmic shifting of excitability in local neuronal ensembles. Here, we show that when attended stimuli are in a rhythmic stream, delta-band oscillations in the primary visual cortex entrain to the rhythm of the stream, resulting in increased response gain for task-relevant events and decreased reaction times. Because of hierarchical cross-frequency coupling, delta phase also determines momentary power in higher-frequency activity. These instrumental functions of low-frequency oscillations support a conceptual framework that integrates numerous earlier findings.

Neuronal oscillations reflect rhythmic shifting of neuronal excitability over a wide range of spatial and temporal scales (1–3). These oscillations play a role in a variety of brain operations including stimulus processing (2–4), neuronal interactions across areas (2, 4), memory formation (5), and cognitive control of input processing (6–8). To date, gamma-band (30 to 70 Hz) oscillations have been linked most clearly to active, attentive processes (8, 9). However, recent evidence suggests that lower-frequency (theta and alpha) oscillations also contribute to active processing (10, 11) and that during rhythmic stimulation, oscillatory entrainment in various frequency bands can be enhanced by attention (12–14). We therefore hypothesized that if relevant stimuli appear in a rhythmic and predictable pattern, neuronal oscillations would entrain (phase-lock) to the structure of the attended stimulus stream (3, 12–16) and thus serve as instruments of sensory selection.

Our hypothesis makes four key predictions: (i) When attention is allocated to one of several rhythmic event streams, oscillations in the sensory cortices will entrain (phase-lock) to the events in the attended stream. (ii) Because of entrainment, rhythmic fluctuations in neuronal excitability will be aligned so that high-excitability phases will tend to coincide with events in the attended stream. Given some variability in stimulation rhythm and entrainment, (iii) neuronal response amplitude and (iv) reaction time will be systematically related to the phase of the entrained oscillation.

To test these predictions, we analyzed the effects of selective attention on the visual event-related response and the prestimulus activity obtained during 24 experimental sessions in the primary visual cortex (V1) of two macaque monkeys (17).

Monkeys were trained to perform an intermodal selection task, as described previously (18). In this task (Fig. 1), interdigitated auditory and visual stimuli (beeps and flashes) were delivered with random stimulus onset asynchronies (SOAs) varying between 500 and 800 ms (Gaussian distribution), with a mean of 650 ms (1.5-Hz delta frequency) within each stream (mean combined stimulus rate of 3 Hz). Despite the variability in SOA, visual and auditory stimulus streams stayed, on average, 180° out of phase over all trials. This paradigm combines the rhythmic structure and variability characteristic of natural event patterns. In alternate trial blocks, the monkey had to attend to either the visual or the auditory stimulus stream and make a manual response to an infrequently presented “oddball” stimulus.

Laminar profiles of field potentials and concomitant multiunit activity (MUA) were recorded with linear array microelectrodes positioned to straddle the layers of V1 during each recording session. Instead of analyzing the field potentials, we calculated current-source density (CSD) profiles, which allow for better localization and more direct physiological interpretation of transmembrane currents that cause excitability changes and generate the local field potential profile. As in previous studies (18, 19), the comparison of response amplitudes within each experiment revealed a significantly larger response to attended visual stimuli: On average, CSD response amplitude was 62% higher and MUA was 46% larger in the attend visual (AV) condition, as compared with the attend auditory (AA) condition (Fig. S1).

To illustrate differential entrainment by attention [prediction (i)], we compared averaged CSD profiles in the AV and AA conditions (Fig. 2A). Whereas the relatively long time frame shown extends over a number of successive stimuli, response averaging is time-locked to visual stimuli presented at time zero; because of the jitter in SOA, responses to prior and succeeding stimuli (red and blue brackets) appear “smeared” in the CSD plot. Along with a clear attentional enhancement of the visual response, a noteworthy pattern of underlying oscillatory entrainment is also evident. At the time of stimulus presentation (dotted line), supragranular baseline CSD activity (along with activity in the infragranular

layers) is opposite in sign in the AV and AA conditions, whereas the sign of granular-layer prestimulus CSD activity is the same for each condition (this pattern was consistent across sessions) (Fig. S2). Overlay of the CSD waveforms from the selected supragranular electrode “S” (Fig. 2B) shows that the baseline effect is not a result of a direct current shift in excitability; instead it is a cyclical delta-band oscillation with a period matching the rate of visual stimulation, which is 180 degrees out of phase in the AV and AA conditions. Supragranular entrainment by attention is confirmed by the single-trial delta-phase distribution at 1.55 Hz (visual stimulation frequency) (Fig. 2C) and mean delta phase at visual stimulus onset across all experiments (Fig. 2D). Whereas delta phase at visual stimulus onset was close to the negative peak ( $\phi$  mean = 2.7 rad,  $\phi$  dev = 0.61,  $n$  = 24 experiments) in the AV condition, it was in the opposite phase around the positive peak ( $\phi$  mean = 0.23 rad,  $\phi$  dev = 0.87,  $n$  = 24) in the AA condition. Because of entrainment, the delta-phase distribution was significantly biased (i.e., nonrandom) in both conditions in all experiments (Rayleigh’s uniformity tests,  $P$  < 0.01). However, intertrial coherence values—indexing phase similarity across trials—were always larger for relevant versus irrelevant stimuli (12), independent of modality (supporting online material), which indicates that phase alignment/entrainment is controlled by attention. The fact that oscillations in V1 entrain to attended auditory stimuli just as well as to attended visual stimuli reinforces the view that the primary cortices are not the exclusive domain of a single-input system (20) and confirms the role of attention in modulating the impact of heteromodal stimuli in the primary cortical regions (21, 22).

In both monkeys (3) and humans (6), neuronal oscillations in the neocortex tend to couple hierarchically, with the phase of lower-frequency oscillations modulating the amplitudes of higher-frequency ones. Excitability is also coupled to oscillatory phase [prediction (ii)] (1–3). These related types of coupling are both observed in the present results. Time-frequency plots (Fig. 2E, left and right) and spectrograms (Fig. 2E, middle) computed for the supragranular site (S) in the AV and AA conditions show that the amplitude of oscillations above 4 Hz (including activity in both the theta and gamma bands) is modulated in counterphase in the two attention conditions, at the period of the entrained delta oscillation (Fig. 2F). As a consequence of their coupling to delta oscillations, these higher-frequency oscillations display increasing amplitude near visual stimulus onset in the AV condition but decreasing amplitude near visual stimulus onset in the AA condition. This “counterstream modulation” of prestimulus gamma oscillations was present in all 24 experimental sessions, and the same was true for the prestimulus MUA (Fig. 2G). Gamma amplitude and MUA, which have both been linked to excitability previously (8, 23–25), are thus larger in the AV condition around the time of visual stimulus onset, smaller around the time of auditory stimulus onset, and vice versa in the AA condition.

<sup>1</sup>Cognitive Neuroscience and Schizophrenia Program, Nathan Kline Institute, Orangeburg, NY 10962, USA. <sup>2</sup>Institute for Psychology, Hungarian Academy of Sciences, Budapest, Hungary 1394. <sup>3</sup>Faculty of Information Technology, Péter Pázmány Catholic University, Budapest, Hungary 1083. <sup>4</sup>Comprehensive Epilepsy Center, Long Island Jewish Medical Center, New Hyde Park, NY 11040, USA. <sup>5</sup>Department of Psychiatry, Columbia University College of Physicians and Surgeons, New York, NY 10032, USA.

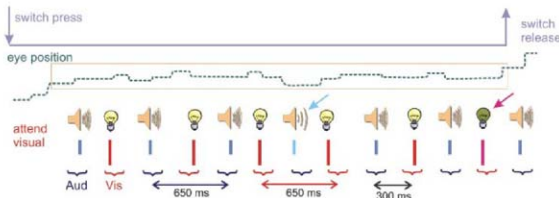
\*To whom correspondence should be addressed. E-mail: schroeder@nki.kfn.org

The above findings suggest that delta-band entrainment can account for the large visual-response amplitude difference in the two attention conditions [prediction (iii)]. To verify this, we measured the influence of prestimulus delta phase on single-trial event-related responses. Figure 3A shows visual event-related laminar CSD amplitude and MUA profiles from an additional experiment, with a typical attention-related response amplitude difference. Figure 3B shows that the single-trial amplitude of the visual response is

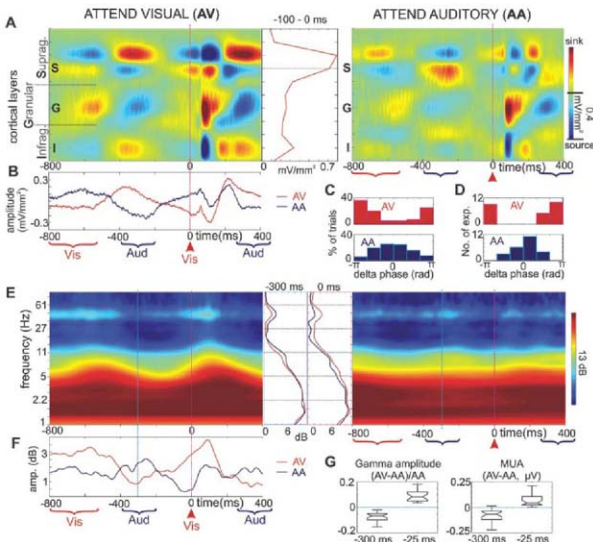
systematically related to the phase of prestimulus delta oscillation in both attention conditions. Moreover, because amplitudes are measured from signals that are baseline corrected to the immediate prestimulus period, the enhancement reflects modulation of response gain, rather than superposition of an unmodulated response on a modulated background signal. In all of our experiments, the largest CSD and MUA amplitudes occur around the negative peak (high-excitability phase), whereas the smallest response amplitudes occur around

the positive peak (low-excitability phase) of delta oscillations. Given this dependence of response amplitude on delta phase (Fig. 3B), the strong counterphase entrainment of delta oscillation in the AV and AA conditions (Fig. 3D) can account for most of the attentional modulation of the visual-response amplitude. As in Fig. 3B, there is an amplitude offset between the AV and AA functions in most of our experiments, indicating larger response amplitudes for attended versus nonattended visual stimuli with the same prestim-

**Fig. 1.** Intermodal selective-attention task. Light bulbs and speakers represent visual and auditory stimuli in the mixed stimulus stream. Visual and auditory deviants are marked by light blue and magenta arrows, respectively. Stimulation began when the monkey depressed a switch and maintained a gaze (dashed line) within an eye position "window" (orange box). SOA within modality was jittered (Gaussian distribution) around a mean of 650 ms. SOA between modalities was 300 ms, on average.



**Fig. 2.** Entrainment and the oscillatory hierarchy. (A) Color maps show CSD profiles related to standard visual stimuli in the AV and AA conditions for the  $-800$  to  $+400$  ms time frame from a representative experiment. Traces between the CSD maps show the laminar profile of prestimulus oscillation amplitude based on the Hilbert transform of the CSD ( $-100$  to  $0$  ms). The red arrowhead indicates the visual event used as trigger ( $0$  ms). Blue and red brackets indicate the time frames in which adjoining auditory and visual events occur, respectively. (B) CSD from supragranular electrode "S" in the AV and AA conditions. (C) Distribution of single-trial supragranular prestimulus ( $0$  ms) delta oscillatory phases in the same experiment. (D) Pooled prestimulus mean (across trials) delta phase for all experiments ( $n = 24$ ). (E) Time-frequency plots display the average oscillatory amplitude of the wavelet-transformed single trials in the selected supragranular site in (A). Traces in the middle show prestimulus amplitude spectra in the AV and AA conditions at  $-300$  and  $0$  ms. (F) Time courses of the averaged ( $37$  to  $57$  Hz) gamma amplitudes. (G) Pooled ( $n = 24$ ) normalized gamma-amplitude and MUA differences between AV and AA conditions [(AV-AA)/AA] for the  $-325$  to  $-275$  and  $-50$  to  $0$  ms time frames. Notches in the boxes indicate a 95% confidence interval about the median of each distribution. Whiskers extend to the most extreme values.



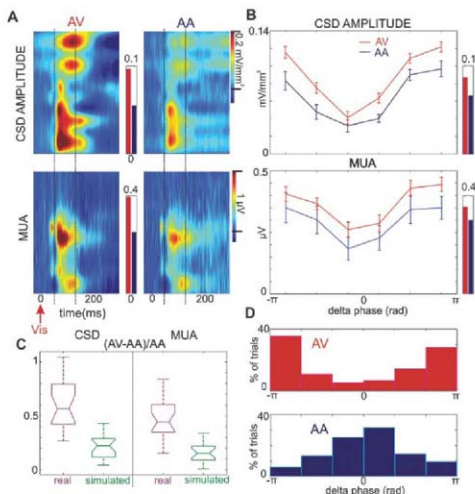


ulus delta phase. This offset suggests that there may be some attentional modulation independent of local delta entrainment (Fig. 3C).

Enhanced prestimulus neuronal gamma-band synchronization (amplitude) in V4 is related to shorter reaction times (25). Because delta phase

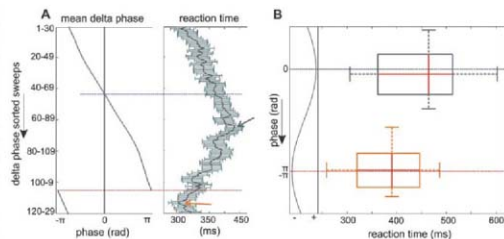
controls gamma amplitude (Fig. 2F) (5), it should also affect reaction time (prediction (iv)). Figure 4 shows a systematic relation between delta phase at the time of visual target onset (0 ms) and reaction time. For each experiment, we then determined the 25% of trials with the fastest (orange arrow) and slowest (green arrow) reaction times and the corresponding mean delta phases. These two groups of trials were not overlapping in any of the 24 experiments. We found the fastest reaction times around the negative peak of prestimulus delta oscillations ( $\phi$  mean = 2.96 rad,  $\phi$  dev = 0.49,  $n = 24$ ), whereas the slowest group was always around the positive peak ( $\phi$  mean = 0.44 rad,  $\phi$  dev = 0.53,  $n = 24$ ), as shown in Fig. 4B. Reaction times were significantly different for the “fast” and “slow” 25% of trials in all 24 cases (Wilcoxon rank sum,  $P < 0.05$ ); on average, they were 14.3% ( $SD = 7$ ) faster in the fast group. Thus, there is a strong relation between prestimulus delta phase and reaction time.

Overall, our findings suggest that when the brain can detect a rhythm in a task, attention enforces phase resetting and entrainment of neuronal excitability oscillations to the relevant stimulus stream, thus changing response gain and amplifying neuronal responses to the events in that stream. A similar predictive effect operating with single-trial coding may underlie “orienting of attention in time” (26). An associated event-related potential effect, the “contingent negative variation” (27), may reflect a low-frequency frontal cortical oscillation, reset by a warning cue. Whereas slow excitability oscillations can be useful when stimulus timing is predictable, their cost is “downtime,” and random inputs arriving during extended low-excitability phases are less likely to be detected, as in the case of an “inhibition of return” (28). Thus, when the brain cannot detect a rhythm in stimulus occurrence, a continuous processing mode is initiated, and low-frequency oscillations are suppressed (8). Rhythmic processing is not uniquely linked to delta oscillations because oscillations in numerous frequency ranges can entrain to rhythmic stimulation (3, 12–16). Although earlier studies suggest that the entrained oscillations we report may represent spontaneously occurring neural oscillations aligned by phase resetting to the structure of attended stimulus streams (3, 20), we



**Fig. 3.** Prestimulus delta phase and its effect on the visual event-related response. (A) Laminar CSD (top) and MUA (bottom) profiles elicited by standard visual stimuli in a representative experiment. Red and blue bars between the color maps represent response amplitudes for the 50 to 135 ms time interval in the AV and AA conditions, respectively (“real” average). (B) Response amplitudes sorted into six bins on the basis of prestimulus delta phase. Red and blue bars at right represent response amplitudes averaged across the bins using the mean of each bin (“simulated” average). Error bars indicate SE. (C) Pooled ( $n = 24$ ) normalized CSD and MUA response amplitude differences between AV and AA conditions [(AV-AA)/AA] for real and simulated averages [see (A) and (B)]. Notches in the boxes indicate a 95% confidence interval about the median. Whiskers extend to the most extreme values. (D) Distribution of single-trial supragranular prestimulus (0 ms) delta phases in the same experiment.

**Fig. 4.** Delta phase and reaction time. (A) Deviant trials with correct responses were sorted on the basis of delta phase at 0 ms from  $-\pi$  to  $\pi$  rad on the selected supragranular electrode in a representative experiment. After sorting, we calculated the mean phase (left) and mean reaction time (green line on the right; error bars denote SE) in groups of trials corresponding to 25% of all trials starting with each consecutive trial. Blue and red dotted lines denote the groups of trials corresponding to the positive and negative peak of prestimulus delta oscillation. Green and orange arrows point to groups with the slowest and fastest reaction times, respectively. (B) Two-dimensional box plots show pooled mean reaction time (x axis) and pooled mean prestimulus delta phase (y axis) for all experiments ( $n = 24$ ). Red lines in the boxes denote the medians, whereas boxes extend to the lower- and upper-quartile values. Whiskers extend to the most extreme values.



cannot yet differentiate this account from alternative interpretations.

# References and Notes

- G. Buzsáki, *A. Draguhn*, *Science* **304**, 1926 (2004).
- P. Fries, *Trends Cogn. Sci.* **9**, 474 (2005).
- P. Lakatos et al., *J. Neurophysiol.* **94**, 3804 (2005).
- T. Womelsdorf et al., *Science* **314**, 1609 (2007).
- P. Fries, G. Fernandez, O. Jensen, *Trends Neurosci.* **26**, 123 (2003).
- R. T. Canolty et al., *Science* **313**, 1626 (2006).
- A. K. Engel, P. Fries, W. Singer, *Nat. Rev. Neurosci.* **2**, 704 (2001).
- P. Fries, J. H. Reynolds, A. E. Rorie, R. Desimone, *Science* **291**, 1560 (2001).
- J. Fell, G. Fernández, P. Klaver, C. E. Elger, P. Fries, *Brain Res. Rev.* **42**, 265 (2003).
- G. Buzsáki, *Hippocampus* **15**, 827 (2005).
- S. Palva, J. M. Palva, *Trends Neurosci.* **30**, 150 (2007).
- J. Ding, G. Sponring, R. Srinivasan, *Cereb. Cortex* **16**, 1016 (2006); published online 12 October 2005, 10.1093/cercor/bhl044.
- Y. K. Kim, M. Grabowicz, K. A. Poller, K. Marhu, S. Suzuki, *Nat. Neurosci.* **10**, 117 (2007); published online 17 December 2006, 10.1038/nn1821.
- S. T. Morgan, J. C. Hansen, S. A. Hillyard, *Proc. Natl. Acad. Sci. U.S.A.* **93**, 4770 (1996).
- R. Galambos, S. Makeig, P. J. Talmachoff, *Proc. Natl. Acad. Sci. U.S.A.* **78**, 2643 (1981).
- D. Regan, *J. Opt. Soc. Am.* **67**, 1475 (1977).
- Materials and methods are available as supporting material on Science Online.
- A. D. Mehta, I. Ulbert, C. E. Schroeder, *Cereb. Cortex* **10**, 343 (2000).
- C. J. McAdams, J. H. Maunsell, *J. Neurosci.* **19**, 431 (1999).
- P. Lakatos, C. M. Chen, M. N. O'Connell, A. Mills, C. E. Schroeder, *Neuron* **53**, 279 (2007).
- M. Brosch, E. Seleneva, H. Scheich, *J. Neurosci.* **25**, 6797 (2005).
- A. L. Jack, G. L. Shulman, A. Z. Snyder, M. McAvoy, M. Corbetta, *Neuron* **51**, 135 (2006).
- T. Womelsdorf, P. Fries, P. P. Mitra, R. Desimone, *Nature* **439**, 733 (2006).
- C. Zelazo, E. K. Miller, J. Duncan, R. Desimone, *Nature* **363**, 345 (1993).
- S. J. Luck, L. Chelazzi, S. A. Hillyard, R. Desimone, *J. Neurophysiol.* **77**, 24 (1997).
- C. Minussi, E. L. Wilding, J. T. Coull, A. C. Nobre, *Brain* **122**, 1507 (1999).
- W. G. Walter, R. Cooper, V. J. Aldridge, W. C. McCallum, A. L. Winter, *Nature* **203**, 380 (1964).
- R. Klein, *Nature* **334**, 430 (1988).
- This work was supported by National Institute of Mental Health grant MH-60358. We thank T. McGinnis for her invaluable assistance in organizing the data set used in this study, R. Desimone, A. Faldutier, Y. Kajikawa, and A. Barczak for helpful comments on earlier versions of the manuscript; and D. Javitt for his support and advice during this project.

## Supporting Online Material

www.sciencemag.org/cgi/content/full/320/5872/110C1

Materials and Methods

Figs. S1 and S2

References

31 December 2007; accepted 22 February 2008

10.1126/science.1154735

## Episodic-Like Memory in Rats: Is It Based on When or How Long Ago?

William A. Roberts,<sup>1,\*</sup> Miranda C. Feeney,<sup>1</sup> Krista MacPherson,<sup>1</sup> Mark Petter,<sup>2</sup> Neil McMillan,<sup>1</sup> Evanya Musolino<sup>1</sup>

Recent experiments with rats suggest that they show episodic-like or what-where-when memory for a preferred food found on a radial maze. Although memory for when a salient event occurred suggests that rats can mentally travel in time to a moment in the past, an alternative possibility is that they remember how long ago the food was found. Three groups of rats were tested for memory of previously encountered food. The different groups could use only the cues of when, how long ago, or when + how long ago. Only the cue of how long ago food was encountered was used successfully. These results suggest that episodic-like memory in rats is qualitatively different from human episodic memory.

Although Tulving (1) initially defined episodic memory as a person's ability to remember a personal past event (what) including where and when it happened, he later amended this definition to include autonoetic consciousness or the feeling of retrieving a personal episode (2). It was argued further that episodic memory is found only in humans (3). However, recent research with birds and rodents has brought this position into question. By using Tulving's original criteria of what-where-when, it has been shown in behavioral experiments that scrub jays (4–6) and rats (7–10) remember where and when they cached or discovered foods of differing palatability. Because these experiments could not involve an assessment of autonoetic consciousness, their findings have been taken as evidence for episodic-like memory, a form of memory in animals that may have some of the properties of human episodic memory (11).

Of particular importance in these studies was the discovery that animals could remember when

they had cached or encountered a favored food. Memory for when suggests that animals can mentally travel in time or locate a past event within a temporal framework of hours and days (12). An alternative possibility is that, instead of remembering when an event happened within a framework of past time, animals are keeping track of how much time has elapsed since caching or encountering a particular food item at a particular place and are using elapsed time to indicate return to or avoidance of that location (12). The cues of when and how long ago are typically confounded in studies of episodic-like memory. Thus, animals might be remembering how long ago an event occurred by keeping track of elapsed time using accumulators, circadian timers, their own behavior, or the strength of a decaying memory trace (13–17). If this is the case, then episodic-like memory in animals may be quite different from human episodic memory in which people can reconstruct past experiences within an absolute temporal dimension (18–20).

In two experiments, we asked whether the temporal cues used by rats to show episodic-like memory were when the study phase occurred, how long ago it occurred, or whether rats needed both when and how long ago cues. Three groups of 10 Long-Evans hooded rats each were tested

(21), in one procedure in which the cue of when was relevant and the cue of how long ago was made irrelevant, a second in which how long ago was relevant and when was irrelevant, and a third in which rats could use when + how long ago (Fig. 1). Within daily trials, rats were allowed to enter four randomly chosen arms of an eight-arm radial maze during a study phase that could occur at 9 a.m. or 12:30 p.m. Three of the arms contained two Noyes 45-mg reward pellets, and the fourth arm contained the highly preferred reward of a cube of cheese (10). The rats were returned to the maze for a test phase at 9:30 a.m., 1 p.m., or 4:30 p.m. On the test phase, all eight arms were open, and rats could choose freely among them. The four arms closed during the study phase now contained two reward pellets, and the three arms that contained pellets during the study phase were empty.

Groups When and How Long Ago (HLA) had study phase trials at either 9 a.m. or 12:30 p.m. and test phase trials at 9:30 a.m., 1 p.m., or 4:30 p.m. (Fig. 1). On the arm where a rat consumed cheese in the study phase, another piece of cheese was placed on the same arm to replenish (R) it or the arm was empty, as the cheese had been pilfered (P); these conditions were found at different times for subgroups A and B within each group. Notice that the When group always had the cheese arm replenished after entering it at 9 a.m. (subgroup B) or at 12:30 p.m. (subgroup A) and pilfered after entering it at 12:30 p.m. (subgroup B) or at 9 a.m. (subgroup A). These rats then could only consistently return to the replenished cheese arm early on the appropriate trials if they used "when" as a cue and not how long ago the cheese arm had been encountered. The opposite arrangement was in effect for rats in the HLA group; subgroups A and B always had the cheese arm replenished after 30 min or 4 hours, and when the rats first encountered the cheese arm was made irrelevant. Rats in the When + HLA condition were tested under a standard procedure (10) in which both the time of the study phase and the interval until testing could indicate whether the

<sup>1</sup>Department of Psychology, University of Western Ontario, London, Ontario, N6A 5C2, Canada. <sup>2</sup>Department of Psychology, Dalhousie University, Halifax, Nova Scotia, B3H 4J1, Canada.

\*To whom correspondence should be addressed. E-mail: roberts@uwo.ca

cheese arm would be replenished or pilfered in both subgroups. It should be further noted in this design that tests at 1 p.m. provide the most important data. When tested at 9:30 a.m. or 4:30 p.m., rats in both When and HLA groups could use time of day as a cue to indicate replenishment of the cheese reward. At 1 p.m. tests, however, time of test is irrelevant as a cue, and only when or how long ago cues can be used to determine whether the cheese reward will be replenished or pilfered.

Training trials in which the cheese reward was always replenished or always pilfered were presented initially in blocks of 16 days. Over the initial 16 days, only trials in which cheese was replenished were presented, and, over the next 16 days, only trials in which the cheese was pilfered were presented. Over a final block of 40 days, both replenished and pilfered trials at 30-min and 4-hour retention intervals were randomly mixed together. Sequences of rats' entrances into the arms of the maze during test phase trials were recorded. Rats showed a strong preference for the arms that had been closed during the study phase and that now contained pellets (table S1). Their readiness to return to the arm where cheese had been found during study was evaluated by two measures: the probability of returning to the cheese arm in the first four arms visited, and the mean rank of entry into the cheese arm during successive arm choices. Early return to the cheese arm is indicated by a high probability of visiting it in the first four choices and by a low rank of entry.

Performance over the last 20 trials of training is shown in Fig. 2, with the proportion of cheese arm entries in the first four visits shown in 2A and the mean rank of entry into the cheese arm shown in 2B. Both measures show the same pattern. When tests at all times of day are analyzed, all three groups show a significant tendency to enter the cheese arm earlier when cheese is replenished than when it is pilfered [ $t(9) \geq 2.48$  for proportion;  $t(9) \geq 3.21$  for mean rank of entry]. When tests at 1 p.m. are considered, however, the When group shows no difference between replenish and pilfer trials ( $t(9) = 0.29$  for proportion;  $t(9) = 0.9$  for mean rank of entry), but the HLA and When + HLA groups show significant effects [ $t(9) \geq 2.72$  for proportion;  $t(9) \geq 2.67$  for mean rank entry].

The first experiment indicated that rats used how long ago cheese was encountered as a cue but not when during the day it was encountered. It is possible that rats might be sensitive to when a preferred reward was found if the encounter occurred on the previous day. In experiment 2, we examined memory for when versus how long ago over an interval longer than 24 hours (Fig. 3). The When, HLA, and When + HLA groups ( $n = 5$ ) were tested again. In the When and HLA groups, rats were given the study trial at 9 a.m. or 12 p.m. The short retention interval was 1 hour, with test trials given at 10 a.m. or 1 p.m. of the same day. The long retention interval was 28 hours, with test trials given at 1 p.m. or 4 p.m. of the next day. As in experiment 1, the time of day at which cheese was encountered was the relevant cue for the When group, the time

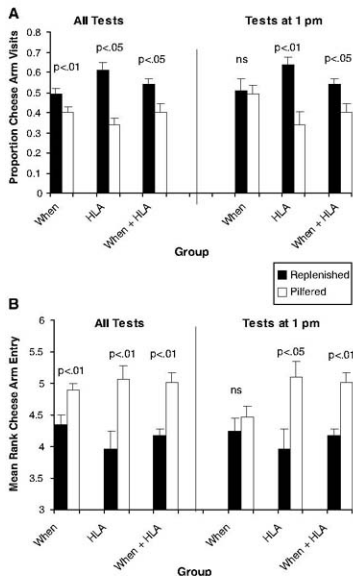
that elapsed between the study and test phases was the relevant cue for the HLA group, and both cues were relevant for the When + HLA group. From the start of training, the different types of trials were presented in random order over days; each group received 56 total trials, 28 on which cheese was replenished and 28 on which cheese was pilfered.

Again, tests at 1 p.m. were most important because they controlled for time of day as a cue for cheese replenishment.

Data for the final 28 trials of training are shown in Fig. 4. The findings of experiment 2 largely replicated those of experiment 1. When tests at all times of day were considered, both the

Study→Test Interval	Group					
	When		HLA		When + HLA	
	A	B	A	B	A	B
9 am → 9:30 am	P	R	P	R		
9 am → 1 p.m.	P	R	R	P	R	P
12:30 pm → 1 p.m.			R	P	P	R
12:30 pm → 4:30 pm			R	P		

**Fig. 1.** Design of experiment 1 for the study of the temporal basis of episodic-like memory in rats. Three groups (When, HLA, and When + HLA; each  $n = 10$ ) explored, in the study phase, four randomly chosen arms at 9 a.m. or 12:30 p.m. and were given a choice in the test phase among all eight arms at 9:30 a.m., 1 p.m., or 4:30 p.m. Subgroups (A and B;  $n = 5$ ) found that the cheese on one arm in the study phase was either replenished (R) or pilfered (P) in the test phase.



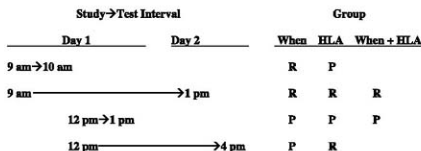
**Fig. 2.** Results of experiment 1. (A) Proportion of visits to the cheese arm in the first four visits. (B) Mean rank of entry into the cheese arm. All error bars are SEM.

proportion of cheese arm visits in the first four arm entries and the mean rank entry show no significant effect of when cheese was found in the maze [ $t(4) = 0.2$  for proportion;  $t(4) = 0.48$  for mean rank entry]. However, the HLA and When + HLA groups showed significantly earlier visits to the cheese arm on replenish trials than on pilfer trials [ $t(4) \geq 2.32$  for proportion;  $t(4) \geq 2.73$  for mean rank entry]. The same results appear when tests at 1 p.m. only are

examined, with no effects of when the cheese arm was visited [ $t(4) = 0.75$  for proportion;  $t(4) = 0.12$  for mean rank entry], but significant effects of HLA and When + HLA [ $t(4) \geq 2.63$  for proportion;  $t(4) \geq 3.00$  for mean rank entry].

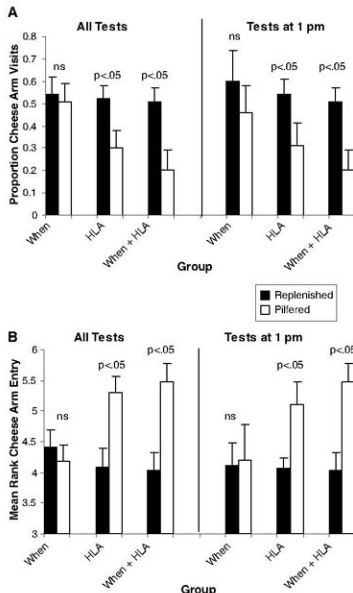
The findings of two experiments indicate that rats were not sensitive to when during the day they first discovered cheese on an arm of the radial maze. By contrast, they were able to use elapsed time or

how long ago the cheese was found to indicate that it would be replenished or pilfered on the test phase. The difference between the When and HLA groups suggests that the success of the When + HLA group and rats tested in previous episodic-like memory experiments (7–10) was caused by animals keeping track of the time between study and test phases and not by memory for when the study phase occurred. Rats have been shown to be able to track the time that has elapsed between a signal and the delivery of food over both short and long time intervals, and several possible mechanisms may account for this ability, including internal accumulators (15), circadian oscillators (14, 15), the animal's own behavior (16), and the strength of a memory trace (17). Although humans may reconstruct the timing of a past experience using memory for absolute time, order of events, and elapsed time (20), the implication of the studies reported here is that rats do not need to remember when a food was encountered within a day or between days in order to show episodic-like memory. These findings then cast into doubt any similarity between episodic-like memory in rats and episodic memory in humans. Humans can specify when an event occurred within a past temporal framework of hours, days, and years (20), but rats appear to remember only how much time has gone by since an important event occurred.



**Fig. 3.** Design of experiment 2 for the study of the temporal basis of episodic-like memory in rats between days. Three groups (When, HLA, and When + HLA; each  $n = 5$ ) explored, in the study phase, four randomly chosen arms at 9 a.m. or 12 p.m., and were given a choice in the test phase among all eight arms at 10 a.m., 1 p.m., or 4 p.m. Tests between days made the retention interval 28 hours long. Rats found that the cheese on one arm in the study phase was either replenished (R) or pilfered (P) in the test phase.

**Fig. 4.** Results of experiment 2. (A) Proportion of visits to the cheese arm in the first four visits. (B) Mean rank of entry into the cheese arm. All error bars are SEM.



## References and Notes

1. E. Tulving, in *Organization of Memory*, E. Tulving, W. Donaldson, Eds. (Academic Press, San Diego, 1972), pp. 381–403.
2. E. Tulving, *Am. Psychol.* **40**, 385 (1985).
3. E. Tulving, *Elements of Episodic Memory* (Clarendon Press, Oxford, 1983).
4. N. S. Clayton, A. Dickinson, *Nature* **395**, 272 (1998).
5. N. S. Clayton, A. Dickinson, *J. Comp. Psychol.* **113**, 403 (1999).
6. N. S. Clayton, K. S. Yu, A. Dickinson, *J. Exp. Psychol. Anim. Behav. Proc.* **27**, 17 (2001).
7. J. J. Babb, J. D. Crystal, *Learn. Mem.* **36**, 177 (2005).
8. J. J. Babb, J. D. Crystal, *Learn. Behav.* **34**, 124 (2006).
9. J. J. Babb, J. D. Crystal, *Curr. Biol.* **16**, 1317 (2006).
10. M. Nazghbandi, M. C. Feeney, T. L. B. McKenzie, W. A. Roberts, *Behav. Proc.* **74**, 217 (2007).
11. D. Griffiths, A. Dickinson, N. Clayton, *Trends Cogn. Sci.* **3**, 74 (1999).
12. W. A. Roberts, *Psychol. Bull.* **128**, 473 (2002).
13. J. Gibbon, *Learn. Mem.* **22**, 3 (1991).
14. K. M. Church, H. A. Broadbent, *Cognition* **37**, 55 (1990).
15. J. D. Crystal, *Behav. Proc.* **72**, 149 (2006).
16. R. R. Kilian, J. G. Fetterman, *Psychol. Rev.* **95**, 274 (1988).
17. J. E. R. Staddon, J. J. Higa, I. M. Chelaru, *J. Exp. Anal. Behav.* **71**, 215 (1999).
18. T. Suddendorf, M. C. Corballis, *Genet. Soc. Gen. Psychol. Monogr.* **123**, 133 (1997).
19. T. Suddendorf, M. C. Corballis, *Behav. Brain Sci.* **30**, 299 (2007).
20. W. J. Friedman, *Psychol. Bull.* **113**, 44 (1993).
21. Materials and methods are available as supporting material on Science Online.
22. Support for this research was provided by a Discovery Grant from the Natural Sciences and Engineering Research Council of Canada.

## Supporting Online Material

www.sciencemag.org/cgi/content/full/320/5872/113/DC1  
Materials and Methods  
SOM Text  
Table S1

7 November 2007; accepted 15 February 2008  
10.1126/science.1152709



## GENOTYPING TECHNOLOGY: SNP-ING OUT INFORMATION

Researchers from academia and industry continue to make new technologies and tools to learn more from single nucleotide polymorphisms (SNPs). As expected, some of the advances come from higher density microarrays. Nevertheless, ancillary technologies, such as microfluidics, deliver additional advances. Moreover, researchers are also exploring variations beyond SNPs.

by Mike May

**D**espite ongoing discussions of the data overload, researchers still want more, especially from SNPs. “We really need to have high throughput techniques,” says Lise Lotte Hansen, associate professor of human genetics at the University of Aarhus in Denmark. Beyond just gathering more genotyping data, however, Hansen wants data that include more content. In some cases, any content would help. As Hansen says, “You look through databases and there is no information on some SNPs.”

In fact, some of the current data turn out to be wrong. “Sometimes, the SNP is not really located where the database places it,” Hansen says. “Also, the frequencies for the various genotypes can simply be wrong.” This arises from either methodological problems or because genotype frequencies vary considerably between populations.

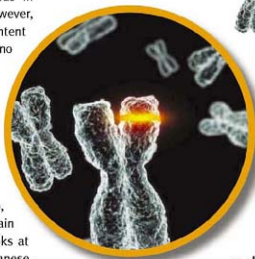
To get better information on SNPs, scientists need more data, such as that gathered by the International HapMap Project ([www.hapmap.org](http://www.hapmap.org)). This organization focuses on making a catalog of the human haplotype map, or HapMap, which is basically the variation in human genotypes. To obtain a representative sampling of human variation, the HapMap project looks at SNPs from 270 people from four populations: European, Han Chinese, Japanese, and Nigerian.

It will take even more information on SNPs to correlate them with diseases. Scientists need to look through tens of thousands of SNPs to find the one or two disease-related ones. So researchers need faster and more-accurate approaches to genotyping.

### Expanding the View

Although scientists need more SNP data, part of today's challenge in genotyping ironically comes from simply having too much to consider. “There are 10 million or so SNPs in public databases,” says Carsten Rosenow, senior marketing manager of DNA analysis products at Illumina in San Diego, California. “Researchers don't have the array density—or the money—to look at all 10 million.” Still, companies want to give scientists more SNPs on a chip—but no one can jam every SNP on one microarray. Instead, scientists at Illumina look for the SNPs that make what Rosenow calls “the best proxies for the others.”

Illumina's tools depend on the company's BeadChip design, which relies on beads of silica covered with DNA probes. “With enhancements to the beads and the slides,” says Rosenow, “we were able to make even higher density products.” Specifically, Illumina recently released its Infinium High-Density Human1M-Duo and Human610-Quad BeadChips, which run two [continued >](#)



“We really need to have high throughput techniques. You look through databases and there is no information on some SNPs.”

### Look for these Upcoming Articles

RNAi — June 6

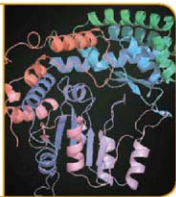
Proteomics 2 — August 1

Genomics 2 — September 19

*Inclusion of companies in this article does not indicate endorsement by either AAAS or Science, nor is it meant to imply that their products or services are superior to those of other companies.*

## Genomics

"It is very clear that not only SNPs, but the combination of all known types of variants need to be discovered and typed—fast and cost efficiently."



and four samples per chip, respectively. "These include up to 2.4 million markers on each chip," says Rosenow. About 2.3 million of the markers are for typing SNPs and copy-number variation. The approximately 100,000 other markers improve the analysis of copy-number variation, because they increase the uniformity of probe distribution, reducing the number of large gaps without any probe coverage in the genome.

Rosenow sees these products used in many ways, such as studying the causes of complex diseases. When using Illumina chips to look for SNP-related diseases, though, Rosenow says that it's not likely that the SNP causing the disease is on the chip. "But once you know that a SNP on the chip shows an association with the disease," he says, "then you know where to go on a hunt."

Other companies also look for more flexible ways to study SNPs. For example, the GenomeLab SNPStream Genotyping System from Beckman Coulter in Fullerton, California, works with nucleic acid samples in 384-well plates. Each well can contain 12 or 48 SNPs. "We can analyze 4,000 to 3.2 million SNP genotypes per day," says Rene M. Oda, senior scientist at Beckman Coulter. "It's very scalable."

Moreover, this instrument does not limit scientists to a list of SNPs. Instead, says Oda, "We give them the design tools, and they can design any type of SNP or insertion or deletion." This includes nucleic acids from humans or other mammals as well as bacteria, plants, or viruses.

The SNP analysis performed by this instrument can be used in many ways. For example, **DNAPrint Genomics** in Sarasota, Florida, uses the GenomeLab SNPStream to provide law enforcement agencies with ancestry information about suspects and victims, based on samples taken from crime scenes. In addition, **MMI Genomics** in Davis, California, markets a SNP-based kit to consumers that reports the genetic makeup of a dog from among 38 breeds, providing insight into behavioral characteristics and predisposition to genetic-based diseases that afflict some breeds.

Moreover, scientists are searching for signs of human health risks in other features of chromosomes. "Somatic mutations, for example, cannot be seen through genotyping," says James Wang, president of **TrimGen** in Sparks, Maryland. His company, though, uses a form of real-time polymerase chain reaction, called eQ-PCR, which uses a proprietary probe design and chemistry that the company says enhances the detection of the fluorescent signal. According to Wang, eQ-PCR can find somatic mutations at levels of just 1 percent. In other words, TrimGen's technology could find a mutation composed

of one base in 100. "For cancers, that could mean earlier detection," Wang says. "Our eQ-PCR is sensitive and accurate. So you could use this to predict risks based on somatic mutations."

This technology can also be used to detect a virus in a sample. Using just 1 milliliter of blood, TrimGen's eQ-PCR can detect as few as 10 copies of a virus. "Most technologies can only get down to 50–100 copies," says Wang.

TrimGen already puts this technology to many uses. For example, the company is running a leukemia project. "In Europe," says Wang, "physicians already use genetic testing to select the treatment for leukemia and to predict relapse." Consequently, TrimGen developed leukemia panels for its eQ-PCR. "This tells you which patients are likely to relapse fast and which are likely to be stable," says Wang, "and it has already been proven that there is a gene related to this." The eQ-PCR test results, Wang says, will provide supportive genetic evidence and valuable information to transform traditional medicine into personalized medicine.

### Controlling the Flow

Making SNP technology work depends in many ways on getting the right sample materials to the right detectors. **Fluidigm** in South San Francisco meets this challenge with integrated fluidic circuits (IFCs). "It's a chip that incorporates a network of elements: inlets, chambers, channels, and valves," explains Michael Y. Lucero, Fluidigm's executive vice president of sales and marketing. "It's like an electrical circuit, except that instead of channeling electrons, IFCs manipulate fluids. The IFCs include the logic that controls the flow with 10,000 or more valves."

Fluidigm recently introduced its BioMark system, which uses IFCs for various applications, including real-time PCR and genotyping analysis. "With IFCs," says Lucero, "we can load many samples and test them against many different SNP assays in the same run." The current version can run 48 samples against 48 assays—for a total of 2,304 reactions in one run. In the near future, says Lucero, the company will increase the throughput to 96 x 96. "That will be 9,216 parallel PCR reactions for genotyping," he says.

The BioMark system runs its 2,304 PCR reactions in about 75 minutes, which Lucero says is the same time as is required for running PCR using conventional 384-well plates. Moreover, the system lowers running costs because IFCs require far less sample, reagents, and pipetting steps to set up reactions, according to Lucero. "These factors also make IFCs ideal for analyses of many single-cell samples as each cell can be efficiently assayed for 48 genes at once," he says.

**Science Applications International Corporation (SAIC)**—a contractor for the US National Cancer Institute in Frederick, Maryland—recently installed a BioMark system at its core genotyping facility (CGF) to use genotyping to track down cancer susceptibility genes. With the BioMark, scientists at the CGF will be able to use TaqMan assays that they've already developed, including more than 5,000 SNP assays to look for potentially cancer-related genotypes.

The TaqMan assays, which were developed by Applied Biosystems in Foster City, California, are used by many scientists for PCR-based research. The TaqMan assays continue to expand to new instruments,

including being used on the OpenArray Platform from **BioTrove** in Woburn, Massachusetts. “Researchers using this integrated platform can experience an end-to-end genotyping workflow of less than five hours, enabling them to analyze thousands of samples in days, in contrast to weeks on alternative genotyping platforms,” says Phoebe A. White, senior director genotyping applications at **Applied Biosystems**. She adds, “The platform offers a flexible range of assay configurations, allowing researchers to interrogate as few as 16 and as many as 3,072 SNPs within one array across hundreds to thousands of samples.” Moreover, a customer can pick the SNPs from **Applied Biosystems’** 4.5 million **TaqMan SNP Genotyping Assays**, **Custom TaqMan SNP Genotyping Assays**, or **TaqMan DME Genotyping Assays**.

Beyond focusing **TaqMan** assays on cancer, IFCs can also tackle environmental questions. Alaska fisheries, for example, are using **Fluidigm’s** IFCs to genotype salmon populations in the ocean. “A panel of SNP assays,” says Lucero, “is used to determine which stream head the salmon will return to for spawning, allowing controlled harvesting.”

### Targeting Mutations

Instead of screening an ocean of possibilities, scientists sometimes prefer to focus genotyping on specific chromosomal regions. According to Rob van Miltenburg, director, global marketing, **Roche Applied Science** in Penzberg, Germany, “With the development of high-resolution melting, or HRM, Roche is now offering a method that can be used to scan for mutations in selected gene regions.” Roche put this technology in its **LightCycler 480** real-time PCR. Running this HRM method is easy and cost effective, according to van Miltenburg. “In addition,” he says, “mutation scanning by HRM can be performed in high throughput, only requiring approximately 90 minutes to analyze a 96-well or 384-well plate.”

The **LightScanner** made by **Idaho Technology** in Salt Lake City, Utah, uses a similar technology. “Using a new double-stranded DNA binding dye that is included in the PCR reaction, it can monitor the

thermal denaturation—the melting—of a sample,” explains Rachel Jones, marketing manager for life science at **Idaho Technology**. “It can detect very subtle differences in DNA melting behavior and identify sequence variants or genotype samples based on the unique melting profile.” It works with both 96- and 384-well plates.

The latest application using the **LightScanner** can genotype a small amplicon generated from primers placed immediately adjacent to a SNP. However, if SNPs of interest melt at very similar temperatures, they can be difficult to discriminate. “Our Master Mix,” says Jones, “includes normalizing, temperature-calibrator probes that allow more accurate differentiation of the melting temps of SNPs whose  $T_m$  differs by less than 0.5 degree Celsius.”

Moreover, melting a sample is nondestructive. As a result, a researcher could go back to a plate and collect samples for further processing. “Lots of customers identify novel SNPs by using sequencing as a second step,” says Jones, “but by using the **LightScanner** as a prescreen, they can reduce the amount of sequencing by more than 90 percent in most cases.” This technology currently is most widely used for gene scanning, such as looking at entire exons for rare or novel mutations. For products that are 400 bases in length or less, says Jones, the **LightScanner’s** sensitivity and specificity are 95–99 percent.

In addition to exploring specific regions or small amplicons from a chromosome, researchers want to look across wider areas and for a variety of differences in genotypes. “With the **Roche/454 Genome Sequencer FLX System**,” says Marcus Droege, director, global marketing, **Roche Applied Science**, “it is possible to discover and analyze the whole spectrum of different types of mutations, from a SNP to smaller insertions and deletions to large structural variations of the genome.” As a result, this next-generation sequencer can be used to determine both sequences and genotypes. Other sequencers can also be used this way. In the April 2007 *Journal of Clinical Microbiology*, for instance, Donald Murphy of the Institut National de Santé Publique du Québec, and his colleagues used **Applied Biosystems’** **Prism 3100** genetic analyzer to genotype variants of the hepatitis C virus.

Whether genotyping in selected regions or across the genome, scientists need a range of tools, as do companies. For example, **Roche’s** acquisition of **NimbleGen** (Madison, Wisconsin) adds to the company’s variety of analytical capabilities, according to Janti Masani, vice president marketing at **NimbleGen**. He says, “Now, **Roche** will also be able to offer an optimized workflow composed of enrichment and sequencing of targeted gene regions or the complete human exome.”

Beyond the growing range of applications of genotyping, even its definition continues to evolve. “It is very clear that not only SNPs, but the combination of all known types of variants need to be discovered and typed—fast and cost efficiently,” says Droege. “This will lead to a wider definition of ‘genotyping,’ which is still often used with respect to SNP analysis only.” As scientists study ever-more variations, the very meaning of genotyping will expand over the next few years.

*Mike May is a publishing consultant for science and technology.*

DOI: 10.1126/science.opms.p0800025

### Featured Participants

#### Applied Biosystems

[www.appliedbiosystems.com](http://www.appliedbiosystems.com)

#### Beckman Coulter

[www.beckmancoulter.com](http://www.beckmancoulter.com)

#### BioTrove

[www.biotrove.com](http://www.biotrove.com)

#### DNAPrint Genomics

[www.dnaprint.com](http://www.dnaprint.com)

#### Fluidigm

[www.fluidigm.com](http://www.fluidigm.com)

#### Idaho Technology

[www.idahotech.com](http://www.idahotech.com)

#### Illumina

[www.illumina.com](http://www.illumina.com)

#### MMI Genomics

[www.mmigenomics.com](http://www.mmigenomics.com)

#### NimbleGen

[www.nimblegen.com](http://www.nimblegen.com)

#### Roche Applied Science

[www.roche-applied-science.com](http://www.roche-applied-science.com)

#### Science Applications

**International Corporation**  
[www.saic.com](http://www.saic.com)

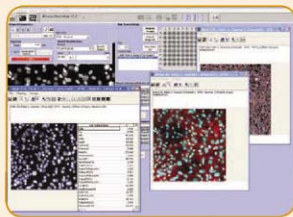
#### TrimGen

[www.trimgen.com](http://www.trimgen.com)

#### University of Aarhus

[www.au.dk/en](http://www.au.dk/en)

## New Products



ThermoFisher

For information 828-365-1205  
[www.thermofisher.com](http://www.thermofisher.com)

## Gene Expression and Function Studies

The EZ-Tn5 Transposomes are tools for gene expression and function studies in microorganisms. The user simply electroporates the EZ-Tn5 Transposome complex into a microorganism and screens for the transposon-encoded resistance marker. The EZ-Tn5 Transposome inserts in a highly random manner into bacterial chromosomes or endogenous plasmids. Uses of the tool include development of new bacterial strains, location of specific genetic markers on chromosomes and plasmids, and creation of gene knockouts.

**Epicentre Biotechnologies**

For information 800-284-8474  
[www.epicentre.com](http://www.epicentre.com)

## Improved Amplification of Difficult Samples

PCRboost is a reagent that enhances polymerase chain reaction (PCR) and reverse transcription (RT) PCR performance by five times or more by improving sensitivity and specificity during amplification of genomic DNA or RNA templates. PCRboost makes it easy for scientists to amplify templates that are traditionally difficult to amplify and present in limited quantities. At the same time, the number of cycles and amount of polymerase used are reduced, resulting in time and cost savings. The reagent enhances the yield, specificity, and consistency of the final product in difficult samples. It requires no changes to existing PCR and RT-PCR protocols—users simply replace the water in the reaction with PCRboost.

**Biomatrica**

For information 858-550-0308  
[www.biomatrica.com](http://www.biomatrica.com)

## Automated Capillary Electrophoresis

The QIAxcel system makes analysis of DNA fragments, such as single and multiplex polymerase chain reaction products, and qualitative and quantitative RNA analysis easier and faster than ever. The QIAxcel system automates sensitive, high-resolution capillary electrophoresis of up to 96 samples per run. The system provides: safety and convenience with ready-to-use gel cartridges; analysis of up to 96 samples without manual intervention; robust results for nucleic acid concentrations as low as 0.1 ng/μl; confident data interpretation with resolution down to 3 bp to 5 bp; and standardized processing with digital data collection and documentation.

**Qiagen**

For information 49-2103-29-13884  
[www.qiagen.com](http://www.qiagen.com)

## Screening Platform Enhancements

Four enhancements to the High Content Screening (HCS) Platform include HCExplorer informatics software, new functionality for its image analysis software, expanded capability of the HCS Analysis Platform, and a brightfield module that adds white light imaging to its fluorescent imaging capabilities. The HCExplorer software makes use of web-based technology to enable rapid and easy enterprisewide data access and analysis. It provides powerful analytical, data visualization, and image comparison tools that can be used with any data store. The Bioapplications image analysis algorithms allow scientists to easily make complex measurements. The new version can measure larger image sizes and more objects within any given field. Version 6.1 of the HCS Analysis Platform provides new image display features and can analyze data from a wide range of third-party microscopes and HCS readers. The Brightfield module, by combining the use of white light with the existing fluorescent channels, enables users to broaden their assay capabilities, which is particularly important for toxicological live-cell assays and novel formats using stem cells, tissues, and whole organisms.

## Plasmid Mapping Software

The beta release of an enhanced version of the DNA plasmid mapping software, Gene Construction Kit 3.0, is available for download at Textco's website. The new version includes new modules for polymerase chain reaction analysis, automated shotgun cloning, and integrated web searching for performing biologically related searches across multiple internet data repositories. Compatible with Mac OS 10.2 and higher, Windows XP, and Windows Vista, the new release integrates numerous enhancements and user-requested upgrades into a powerful tool.

**Textco BioSoftware**

For information 603-643-1471  
[www.textco.com](http://www.textco.com)

## Fluorescent Dye

Amersham HyPer5 fluorescent dye for gene expression and array-based comparative genomic hybridization applications delivers reproducible results, regardless of environmental conditions and number of scans. Amersham HyPer5 fluorescent dyes are photostable and ozone stable. The ozone stability makes the dye consistent year round, even in warmer months when ozone levels rise. The dyes are available as the NHS active ester for coupling to aminoalkyl modified complementary DNA or amplified RNA in postlabeling experiments, or as the dCTP analog for spiking the dye-nucleotide in direct enzymatic incorporation and probe-labeling reactions. The dye allows a direct comparison with Cy3 signal levels in expression analysis from both direct and postlabeling experiments.

**GE Healthcare**

For information 732-457-8149  
[www.gelifesciences.com](http://www.gelifesciences.com)

Electronically submit your new product description or product literature information! Go to [www.sciencemag.org/products/newproducts.dtl](http://www.sciencemag.org/products/newproducts.dtl) for more information.

Newly offered instrumentation, apparatus, and laboratory materials of interest to researchers in all disciplines in academic, industrial, and governmental organizations are featured in this space. Emphasis is given to purpose, chief characteristics, and availability of products and materials. Endorsement by Science or AAAS of any products or materials mentioned is not implied. Additional information may be obtained from the manufacturer or supplier.